

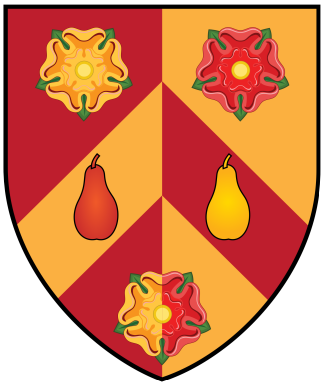

High rate properties of particulate composites

Author:

Akash R. Trivedi

Wolfson College

Supervisor:

Prof. Clive R. Siviour

Pembroke College

Thesis submitted in partial fulfilment of the requirements for the degree of Doctor of Philosophy in the

Solid Mechanics and Materials Engineering Group

Department of Engineering Science

University of Oxford

Trinity 2020

Abstract

The main aim of the research presented in this thesis was to better understand the high strain rate mechanical properties of particulate composites. As the mechanical response of these materials is sensitive to rate and temperature, they must be experimentally characterised at various strain rates and temperatures, interrogating their dependences. In polymer composite materials, the rate and temperature dependence originates from the polymeric binder, which motivated the starting place for this research.

Preliminary modelling frameworks were developed, based on observed rate-temperature equivalence in the mechanical properties, and the time-temperature superposition principle. By suitably representing the viscoelasticity, hyperelasticity, and viscoplasticity, the modelling frameworks enabled the high rate behaviour of neoprene rubber and (plasticised) poly(vinyl chloride) to be captured.

It was shown that in order to better capture the high rate response, the temperature rise from self-heating must be related to the thermal relaxation of the elastic modulus. By calibrating the model parameters with data from quasi-static experiments performed at different temperatures, the stress-strain response at high strain rates was *predicted* and validated with carefully conducted experiments.

The insights developed from the initial modelling frameworks were used in the latter part of the project to model the behaviour of particulate composites. These composites were based on a vulcanised, natural rubber binder filled with different grades of glass microspheres. This allowed the effect of filler volume fraction and mean particle diameter to also be investigated. These materials were chosen as their varied (rubbery through to glassy) response provided an interesting challenge for its experimental characterisation under dynamic loading.

The dataset generated, partly as a result of experimental technique development, enabled the resulting insights and data to be used to develop modelling frameworks allowing the high strain rate response of unfilled and filled natural rubber to be predicted above the glass transition temperature.

Acknowledgements

Without the support, guidance, and intellectual input of Clive Siviour, this research would not have been possible and so I thank him wholeheartedly. Many other people have supported me during my time at the University of Oxford, and I would like to also thank them for their help in enabling me to do the best research that I can do: Igor Dyson, for inducting me into the mechanical testing laboratory and training me on how to use the Instron machine, liquid nitrogen dewers, and environmental chamber; Marzena Tkaczyk, for inducting me into the thermomechanical laboratory and training me on how to use the DSC, DMA and rheometer; Nick Hawkins, for advice and help troubleshooting any (and many) issues I have had in this laboratory with the apparatus; and Richard Duffin, with the rest of the workshop team, for producing the required specimens and components necessary for experimental testing.

I would also like to thank the generous support of the Air Force Office of Scientific Research, and specifically Jason Foley, with whom I have had the opportunity for many intellectually stimulating and amusing conversations. A further thanks to: Wolfson College; the Department of Engineering Science; the American Physical Society; the Armourers' and Brasiers' Company; the Royal Aeronautical Society; the Society for Experimental Mechanics; and the British Society of Strain Measurement. They have all contributed financially to enable me to attend conferences around the world, enabling me to present my research to colleagues in the field, and make the most of the networking opportunities.

I would not be here without the love and support of my family, friends and Neha; thank you for being with me every step of the way.

This material is based upon work supported by the Air Force Office of Scientific Research, Air Force Materiel Command, USAF under Award No. FA9550-15-1-0448.

List of Publications

Trivedi, A.R. & Siviour, C.R., 2020. *A simple rate and temperature dependent hyperelastic model applied to capture the high strain rate behaviour of neoprene rubber.* Dynamic Behaviour of Materials. https://doi.org/10.1007/s40870-020-00252-w

Chen, H., Trivedi, A.R. & Siviour, C.R., 2020. *Application of linear viscoelastic continuum damage theory to the low and high strain rate response of thermoplastic polyurethane.* Experimental Mechanics, 60, 925936. https://doi.org/10.1007/s11340-020-00608-2

Trivedi, A.R. & Siviour, C.R., 2020. *Experimentally Characterising the High Strain Rate Behaviour of Natural Rubber Particulate Composites.* Proceedings of the 2020 Annual Conference on Experimental and Applied Mechanics.

Trivedi, A.R. & Siviour, C.R., 2020. *A novel methodology for predicting the high rate mechanical response of polymers from low rate data: application to (plasticised) poly(vinyl chloride).* Mechanics of Time Dependent Materials.
https://doi.org/10.1007/s11043-020-09450-4

Trivedi, A.R. & Siviour, C.R., 2019. *Predicting the large strain high strain rate mechanical response of plasticised PVC using an improved fractional model.* Challenges in Mechanics of Time-Dependent Materials: Proceedings of the 2019 Annual Conference on Experimental and Applied Mechanics.

Trivedi, A.R. & Siviour, C.R., 2019. *Predicting the high rate mechanical response of (un)filled natural rubber.* Proceedings of the 2019 Annual Conference on Experimental and Applied Mechanics.

Trivedi, A.R. & Siviour, C.R., 2018. *Predicting the high strain rate response of plasticised poly(vinyl chloride) using a fractional derivative model.* EPJ Web of Conferences, 183, p.01013.

Trivedi, A.R. & Siviour, C.R., 2018. *Framework for analyzing hyper-viscoelastic polymers.* In AIP Conference Proceedings (Vol. 1979, No. 1, p. 090013). AIP Publishing.

Babra, T.S., Trivedi, A.R. et al., 2017. *Fluoride degradable and thermally debondable polyurethane based adhesive.* Polymer Chemistry, 8(46), 7207-7216.
https://doi.org/10.1039/C7PY01653K

Trivedi, A.R. & Siviour, C.R., 2017. *A framework for analyzing hyper-viscoelastic polymers.* Constitutive Models for Rubber X: Proceedings of the European Conference on Constitutive Models for Rubbers X (Munich, Germany, 28-31 August 2017). CRC Press, pp. 529–535.

Responsibilities:

First author: drafted manuscripts, completed experiments, conducted simulations, submissions and revisions.

Second author: contributed to experiments, simulations and conceptualisation.

Contents

Abstract **i**

Acknowledgements **iii**

List of publications **v**

List of Figures **xiii**

List of Tables **xxiii**

1 Introduction **1**
1.1 Context . . . 1
1.2 Scope . . . 3

2 Background **5**
2.1 History of polymers and composites . . . 5
2.2 Rate and temperature dependence of amorphous polymers . . . 8
2.3 Experimental techniques . . . 11
2.3.1 Low strain rates . . . 12
2.3.1.1 Analysis of data . . . 12
2.3.2 Intermediate strain rates . . . 14
2.3.2.1 Analysis of data . . . 15
2.3.3 High strain rates . . . 15
2.3.3.1 Analysis of data . . . 17
2.3.3.2 Challenges . . . 20
2.3.4 Calorimetry . . . 21
2.3.5 Thermomechanical characterisation . . . 24
2.4 Time temperature superposition . . . 26
2.4.1 Isothermal frequency sweep data . . . 27
2.4.2 Shifting process . . . 28
2.4.3 Calculating the shift factors . . . 29
2.4.4 Master curve . . . 31
2.5 Constitutive modelling . . . 32
2.5.1 Hyperelasticity . . . 33
2.5.1.1 Ogden model . . . 33
2.5.1.2 8-chain Langevin model . . . 34
2.5.2 Linear viscoelasticity . . . 36
2.5.2.1 Prony series . . . 37
2.5.2.2 Fractional derivative model . . . 38
2.5.3 Hyper-viscoelastic models . . . 39
2.5.4 Viscoplasticity . . . 40
2.5.4.1 Mulliken-Boyce model overview . . . 40
2.6 Summary . . . 43

2.7 Outline of remaining thesis 44

3 Preliminary experiments and proposed modelling framework 47
3.1 Introduction 48
3.2 Material 48
3.3 Compression experiments 49
3.3.1 Specimen geometry 49
3.3.2 Low rate experiments 50
3.3.2.1 Varying temperature experiments 51
3.3.2.2 Results and analysis 53
3.3.3 Medium rate experiments 55
3.3.3.1 Results and analysis 55
3.3.4 High rate experiments 57
3.3.4.1 Results and analysis 57
3.4 Dynamic Mechanical Analysis 59
3.4.1 Experimental method 59
3.4.2 Results and analysis 59
3.5 Discussion of rate and temperature dependence 61
3.5.1 Varying rate experiments 61
3.5.2 Varying temperature experiments 62
3.5.3 Rate-temperature equivalence 63
3.5.4 Time-temperature superposition 64
3.6 Modelling framework 66
3.6.1 Requirements 66
3.6.2 Modelling results 67
3.6.3 Rate and temperature dependence 69
3.6.4 Enhancing predictability with DMA results 75
3.6.5 Sensitivity analysis 77
3.7 Conclusions 79
Modelling framework overview 81
Ogden fits to varying rate experiments 81
Ogden fits to varying temperature experiments 81
Refitting based on a constant strain hardening exponent 81
Invoke rate-temperature equivalence 82
Find equivalent temperatures for analogues 82
Enhance predictability with DMA results 82

4 Modelling framework for (plasticised) poly(vinyl chloride) 85
4.1 Introduction 86
4.2 Material 87
4.3 Compression experiments 89
4.3.1 Results and analysis 89
4.4 Dynamic Mechanical Analysis 91
4.4.1 Experimental method 91
4.4.2 Results and analysis 91
4.4.2.1 Activation energies 93
4.4.3 Time-temperature superposition 95
4.5 Differential Scanning Calorimetry 97

4.5.1 Method . . . 97
4.5.2 Results . . . 98
4.5.3 Characterisation of self-heating . . . 100
4.6 Modelling framework . . . 103
4.6.1 Requirements . . . 103
4.6.1.1 Hyperelasticity . . . 103
4.6.1.2 Viscoelasticty . . . 104
4.6.1.3 Viscoplasticity . . . 104
4.6.2 Modifications to the Mulliken-Boyce model . . . 105
4.6.2.1 Fractional derivative model . . . 105
4.6.2.2 Thermal relaxation of the modulus . . . 109
4.6.3 Enhanced Fractional Thermo-Visco-Hyperelasto-Plastic (FTVHEP) model . . . 111
4.6.3.1 Langevin component . . . 111
4.6.3.2 α component . . . 112
4.6.3.3 β component . . . 113
4.7 Modelling results . . . 116
4.7.1 High rate predictions . . . 116
4.7.2 Peak stresses . . . 118
4.7.3 Effect of heating . . . 119
4.7.4 Simulating adiabatic experiments . . . 119
4.8 Conclusions . . . 122
Modelling framework overview . . . 124
Quasi-static and thermomechanical experiments . . . 124
Obtaining E(t) . . . 124
Error mitigation in master curve construction . . . 125
Obtaining E(t,T) . . . 127
Obtaining Langevin parameters . . . 128
Obtaining α parameters . . . 128
Obtaining β parameters . . . 128
Predicting and validating high strain rate response . . . 129

5 Experimental characterisation of unfilled and filled natural rubber 131
5.1 Introduction . . . 132
5.2 Materials . . . 133
5.3 Compression experiments . . . 135
5.3.1 Varying temperature experiments . . . 135
5.3.2 Varying rate experiments . . . 139
5.3.3 Rate-temperature equivalence . . . 142
5.3.4 Varying strain experiments . . . 144
5.3.5 Low temperature, high rate experiments . . . 146
5.3.5.1 Development of new experimental capability . . . 146
5.3.5.2 Results and analysis . . . 147
5.3.5.3 *Post-mortem* damage analysis . . . 150
5.3.6 Discussion of results . . . 155
5.3.6.1 Variation of peak stress . . . 155
5.3.6.2 Enhancement of the apparent modulus . . . 156

5.4 Dynamic Mechanical Analysis . . . 158
5.4.1 Initial method . . . 158
5.4.2 Initial results and analysis . . . 158
5.4.3 Updated method . . . 162
5.4.4 Updated results and discussion . . . 164
5.4.4.1 Complex moduli and loss tangents . . . 164
5.4.4.2 Master curves . . . 166
5.4.4.3 Shift factor relationships . . . 168
5.4.4.4 Activation energies . . . 171
5.5 Differential Scanning Calorimetry . . . 173
5.5.1 Method . . . 174
5.5.2 Results and analysis . . . 174
5.6 Conclusions . . . 177

6 Modelling framework for natural rubber particulate composites 179
6.1 Introduction . . . 180
6.2 Model requirements . . . 181
6.2.1 Models considered . . . 182
6.2.2 Viscoelasticity . . . 183
6.2.2.1 Hyperviscoelastic (HV) model . . . 183
6.2.2.2 Mulliken-Boyce (MB) model . . . 184
6.2.3 Hyperelasticity . . . 185
6.2.3.1 Hyperviscoelastic (HV) model . . . 185
6.2.3.2 Mulliken-Boyce (MB) model . . . 185
6.2.4 Viscoplasticity . . . 186
6.2.5 Filler enhancement . . . 186
6.2.6 Strain activated damage . . . 187
6.2.6.1 Hyperviscoelastic (HV) model . . . 187
6.2.6.2 Mulliken-Boyce (MB) model . . . 189
6.3 Modelling results and analysis: Ambient, high rate . . . 190
6.3.1 Unfilled natural rubber . . . 190
6.3.1.1 Quasi-static calibration: U-NR . . . 191
6.3.1.2 Predictions of high rate response: U-NR . . . 192
6.3.2 Filled natural rubber . . . 194
6.3.3 Quasi-static calibration of model . . . 195
6.3.3.1 Quasi-static, ambient calibration . . . 195
6.3.3.2 Quasi-static, low temperature calibration . . . 198
6.3.4 Predictions of high rate response . . . 201
6.4 Modelling results and analysis: Sub-ambient, high rate . . . 204
6.4.1 Unfilled natural rubber . . . 204
6.4.1.1 Mulliken-Boyce (MB) model calibration . . . 205
6.4.1.2 Results: U-NR . . . 206
6.4.2 Filled natural rubber . . . 210
6.4.2.1 Results: F-NR, −40 °C . . . 210
6.4.2.2 Results: F-NR, −60 °C . . . 213
6.5 Conclusions . . . 216

7 Conclusions **219**
7.1 Thesis objectives 219
7.2 Summary of accomplishments 220
7.2.1 Experimental contributions 220
7.2.1.1 Technique development for Dynamic Mechanical Analysis experiments 220
7.2.1.2 Low temperature capability enhancement for the split-Hopkinson pressure bar 221
7.2.1.3 Generation of new data for unfilled and filled natural rubbers 221
7.2.2 Modelling contributions 222
7.2.2.1 Development of a hyper-viscoelastic model to capture the high rate behaviour of neoprene rubber 222
7.2.2.2 Time-Temperature Superposition based modified Mulliken-Boyce model to *predict* the high rate response of (plasticised) poly(vinyl chloride) 222
7.2.2.3 Development of hyper-viscoelastic model with strain activated damage to *predict* the high rate behaviour of natural rubber based particulate composites 223
7.3 Recommendations for future work 224
7.4 Closing remarks 226

Bibliography **227**

List of Figures

2.1 Relative importance of materials throughout history, from Ashby et. al. [24]. 6
2.2 Strain rate regimes and experimental techniques typically used in investigations (adapted from [77]). 11
2.3 Hydraulic press for medium rate compression experiments. 14
2.4 SHPB diagram illustrating the set-up for high rate compression experiments. 16
2.5 (a) Examples of raw strain gauge signals obtained from the incident and transmitter bars, (b) individual pulse signals for the incident, reflected and transmitted waves, and (c) comparison of the inferred forces on each bar-specimen interface. These data are from a high strain rate experiment on neoprene rubber. 18
2.6 (a) Examples of stress-time and strain-time curves obtained from the analysis and (b) the resultant stress-strain relationship for the experiment on neoprene rubber at $\dot{\varepsilon} = 1900\ \mathrm{s}^{-1}$. 19
2.7 Examples of data obtained for calorimetry experiments on LDPE using (a) a conventional DSC experiment with a linear temperature ramp of 3 °C /min and (b) a modulated DSC experiment, which also superposes a sinusoidal modulation of amplitude 0.5 °C and period 1 min (±0.5 °C /min). 22
2.8 Example of data for a DMA experiment on natural rubber in single cantilever configuration showing the dependence of (a) storage and loss moduli, and (b) the loss tangent, on temperature for a variety of frequencies. 24

2.9 (a) Isotherms showing the frequency and temperature dependence of storage modulus, (b) a schematic of the isotherm shifting process, (c) the master curve generated at a reference of 20 °C by shifting these isotherms (inset highlights experimentally relevant frequencies), and (d) the shift factors required to move the isotherms. 28
2.10 Depicting the broadly different mechanical responses of polymers. . . . 32
2.11 Schematic illustration of the unit cell deformation for the 8-chain model [139]. 35
2.12 Top: Kelvin-Voigt in series with a spring. Bottom: Maxwell in parallel with a spring. 37
2.13 Generalised Kelvin-Voigt model. 37
2.14 Generalised Maxwell model. 37
2.15 Schematic of the Mulliken-Boyce model. 41

3.1 Molecular structure of neoprene rubber. 49
3.2 (a) Specimen that can be produced by careful machining, and (b) deformed specimen that results from the punching process. 50
3.3 Environmental chamber set-up on the Instron apparatus for low strain rate, varying temperature experiments. 51
3.4 (a) Liquid nitrogen dewar used for the Instron environmental chamber, and (b) gaseous nitrogen fed into the chamber. 52
3.5 (a) Results from three varying rate quasi-static experiments, with three repeats, conducted on neoprene rubber at a constant temperature (20 °C), and (b) results from varying temperature experiments conducted at a constant strain rate (10^{-2} s^{-1}). 53
3.6 True strain versus time profiles for constant temperature, varying rate experiments, identifying the average true strain rate. 54
3.7 True strain versus time profiles for varying temperature, constant rate experiments. 55
3.8 Results from varying rate hydraulic experiments conducted at a constant temperature (20 °C), highlighting the difference between intended and achieved strain rates. 56

3.9 Comparison of the intended and measured strain rates. 56
3.10 Results from the SHPB experiments on neoprene rubber at 20 °C. . . . 58
3.11 True strain versus time profiles for high rate experiments, identifying the true strain rate. 58
3.12 (a) Results from the DMA experiments conducted for neoprene rubber at 0.5, 2, 5 and 10 Hz for a temperature range from −50 °C to 80 °C, and (b) loss tangent ($\tan\delta$) as a function of temperature and frequency. 60
3.13 Results from compression experiments for varying strain rates at a constant temperature (20 °C). 61
3.14 Results from varying temperature experiments conducted at a constant strain rate (10^{-2} s^{-1}). 62
3.15 Equivalence between ambient, high strain rate and sub-ambient, low strain rate experiments. 64
3.16 (a) Isotherms showing the frequency and temperature dependence of storage modulus and (b) shift factors required to move these to construct a master curve for neoprene rubber. 65
3.17 (a) Master curve for neoprene rubber at a reference temperature of 20 °C, and, inset, highlighting experimentally relevant frequencies; and (b) comparing the rate-temperature equivalence for the modulus with the characteristic stresses in Figure 3.15. 65
3.18 (a) Ogden model fits to the full response of varying strain rate experiments conducted at 20 ± 1 °C, and (b) to fit varying temperature experiments at 10^{-2} s^{-1}. 67
3.19 Implied shift factor relationship for μ. 69
3.20 The rate and temperature dependence of Ogden parameters, with fits describing the dependences. 70
3.21 (a) Updated Ogden model fits to varying strain rate experiments conducted at 20 °C using a fixed α and (b) updated fits to the varying temperature experiments at 10^{-2} s^{-1}. 71
3.22 The rate and temperature dependence of the fixed α Ogden parameters, with fits describing the dependences. 72

3.23 Comparing optimised Ogden fits as in Figure 3.18a and their analogues obtained by considering the response at 10^{-2} s^{-1} and an equivalent lower temperature. 75
3.24 (a) Highlighting the similarity between E' and the equivalent Young's modulus, E, (b) Comparison of $\mu_{\dot{\varepsilon}}$ as obtained from the master curve with that from varying rate fits (Figure 3.20). 76
3.25 Predictions of the response using these μ values and the α obtained in varying temperature fits (also Figure 3.20). 76
3.26 Sensitivity analysis for the fits to varying rate experiments where the model parameters are varied: (a) $\mu \pm 25\%$ and (b) $\alpha \pm 25\%$. Solid blue lines are experimental, solid black are the analogue fits using μ values based on T_{eq}, red dashed lines are the simulations with +25% values and red dotted lines are simulations with −25% values. 77
3.27 Flowchart to describe the preliminary modelling framework. 83

4.1 (a) Molecular structure for PVC and (b) for DINP. 87
4.2 (a) True stress-strain curves from the uniaxial compression experiments at varying strain rates for PVC, (b) for PPVC, and (c) varying temperature experiments at a rate of 10^{-2} s^{-1} for PVC, and (d) for PPVC: from [3]. 90
4.3 (a) Storage and loss moduli DMA results for PVC and (b) for PPVC. (c) Loss tangent ($\tan\delta$) as a function of temperature and frequency for PVC and (d) for PPVC: from [3]. 92
4.4 Plotting the temperature dependence of the shift factor for each transition process in order to find their activation energies. 95
4.5 (a) Results of the DMA experiments, (b) isotherms showing the rate and temperature dependence of the modulus, (c) which are shifted laterally to construct a master curve at a reference temperature of 25 °C, (d) using the shift factors as described. 96
4.6 MDSC results for the PVC with descriptions of the heat capacity either side of the α transition. 98

4.7 MDSC results for the PPVC with descriptions of the heat capacity either side of the α transition. 99
4.8 (a) Calculated temperature rise due to self heating for PVC and (b) for PPVC. 102
4.9 (a) The relaxation modulus with an FDM fit to the DMA results and (b) of the combined model as used in this research. 105
4.10 Fitting traditional Prony series and FDM to the DMA master curve. . 106
4.11 (a) Graphical representation of shifting the master curve for an increasing temperature and (b) highlighting the additional relaxation of the modulus due to temperature rise. 110
4.12 Obtaining the Langevin limiting chain extensibility, $\sqrt{N}$ parameter. . . 111
4.13 Obtaining the α parameters from the low strain rate experiments. . . . 112
4.14 (a) Obtaining the β parameters from the low rate varying temperature experiments, and (b) illustrating what the modelled curves would look like without the β component. 113
4.15 (a) Predictions and comparisons with experimental results for the entire mechanical response for PVC and (b) for PPVC. 117
4.16 (a) Predictions and comparisons with experiments for the peak stresses for PVC and (b) for PPVC. 118
4.17 Comparing adiabatic and isothermal model predictions for PVC at high rate. 119
4.18 Using the model to simulate adiabatic conditions for PPVC with low rate low temperature experiments using an increasing temperature profile. 120
4.19 Comparison of master curves constructed with either three PPT or ten PPT. For completeness, the original master curve is also provided. . . . 126
4.20 Flowchart to describe the modelling framework. 130

5.1 Molecular structure for cis-1,4-polyisoprene. 133
5.2 Highlighting the different grades of F-NR composites for easy identification (not to scale). 134
5.3 Low rate, varying temperature results for U-NR. 136
5.4 Low rate, varying temperature results for (a) F-NR2 and (b) F-NR3. . 136

5.5 Low rate, varying temperature results for (a) F-NR4 and (b) F-NR5. . 137
5.6 (a) Highlighting selected low rate, varying temperature experiments for all NR grades, and (b) better illustrating the higher temperature behaviour. 138
5.7 Varying strain rate data at 25 °C for U-NR. 139
5.8 Varying strain rate data at 25 °C for (a) F-NR2 and (b) F-NR3. 139
5.9 Varying strain rate data at 25 °C for (a) F-NR4 and (b) F-NR5. 140
5.10 Highlighting selected varying strain rate data for all grades of NR. . . . 140
5.11 Highlighting the rate-temperature equivalence between high strain rate experiments at 25 °C and low rate experiments at −40 °C for U-NR. . 142
5.12 Highlighting the rate-temperature equivalence between high strain rate experiments at 25 °C and low rate experiments at −40 °C for (a) F-NR2 and (b) F-NR3. 142
5.13 Highlighting the rate-temperature equivalence between high strain rate experiments at 25 °C and low rate experiments at −45 °C for (a) F-NR4 and (b) F-NR5. 143
5.14 Showing that experimentally simulating the high rate response of all grades of NR is possible with the use of low temperature quasi-static analogue experiments. 143
5.15 Results of varying strain quasi-static compression experiments at 10^{-2} s^{-1} and 25 °C for (a) all grades of rubber and (b) only 50% F-NRs to focus on strain activated damage. 144
5.16 Results of varying strain quasi-static compression experiments at 10^{-2} s^{-1} for 50% F-NRs at (a) −40 °C and (b) −50 °C. 145
5.17 (a) Liquid nitrogen immersion chiller for nitrogen gas and (b) a bespoke fixture for the SHPB to conduct low temperature, high rate experiments. 146
5.18 Comparison of high strain rate data from SHPB experiments at −40 °C for all grades of NR. 148
5.19 Preliminary high strain rate data from SHPB experiments at −60 °C and at (a) c. 1000 s^{-1} and (b) c. 2000 s^{-1} for all grades of NR. 148
5.20 Evolution of strain and strain rate for U-NR. 149
5.21 Evolution of strain and strain rate for (a) F-NR2 and (b) F-NR3. . . . 150

5.22 Evolution of strain and strain rate for (a) F-NR4 and (b) F-NR5. . . . 150
5.23 *Post-mortem* examination for high strain rate experiments at −60 °C for U-NR at (a) c. 1000 s^{-1} and (b) c. 2000 s^{-1}. 151
5.24 *Post-mortem* examination for high strain rate experiments at −60 °C for F-NR2 at (a) c. 1000 s^{-1} and (b) c. 2000 s^{-1}. 152
5.25 *Post-mortem* examination for high strain rate experiments at −60 °C for F-NR3 at (a) c. 1000 s^{-1} and (b) c. 2000 s^{-1}. 152
5.26 *Post-mortem* examination for high strain rate experiments at −60 °C for F-NR4 at (a) c. 1000 s^{-1} and (b) c. 2000 s^{-1}. 153
5.27 *Post-mortem* examination for high strain rate experiments at $T \approx -55$ °C for F-NR5 at c. 1000 s^{-1}. 153
5.28 Strain rate and temperature dependence on the peak stress for U-NR. . 155
5.29 Strain rate and temperature dependence on the peak stress for (a) F-NR2 and (b) F-NR3. 155
5.30 Strain rate and temperature dependence on the peak stress for (a) F-NR4 and (b) F-NR5. 156
5.31 DMA results for U-NR with major clamping artefacts. 159
5.32 DMA results for F-NR2 with (a) substantial clamping artefacts and (b) poor temperature control. 159
5.33 Comparison of old (left) and new (right) clamp screens for the DMA. . 160
5.34 DMA results for F-NR3 with mild clamping artefacts. 161
5.35 DMA results for (a) F-NR4 and (b) F-NR5 with significant clamping artefacts. 162
5.36 Diagram showing new clamping method, placing rubber supports either side of the sample, ensuring even distribution of the clamping pressure and an improved contact area through T_g. 162
5.37 DMA results for U-NR highlighting (a) temperature dependent viscoelasticity and (b) loss tangents. 164
5.38 DMA results for F-NR2 highlighting (a) temperature dependent viscoelasticity and (b) loss tangents. 164
5.39 DMA results for F-NR3 highlighting (a) temperature dependent viscoelasticity and (b) loss tangents. 165

5.40 DMA results for F-NR4 highlighting (a) temperature dependent viscoelasticity and (b) loss tangents. 165
5.41 DMA results for F-NR5 highlighting (a) temperature dependent viscoelasticity and (b) loss tangents. 166
5.42 (a) Isotherms from the DMA results for U-NR and (b) the master curve generated by shifting these at a reference temperature of 25 °C. 167
5.43 Master curve for each material generated at a reference temperature of 25 °C. 167
5.44 Shift factors used to construct the master curve follow an (a) Arrhenius form below T_g and (b) WLF form above T_g. 168
5.45 Shift factors used to construct the master curve for F-NR2 follow an (a) Arrhenius form below T_g and (b) WLF form above T_g. 169
5.46 Shift factors used to construct the master curve for F-NR3 follow an (a) Arrhenius form below T_g and (b) WLF form above T_g. 169
5.47 Shift factors used to construct the master curve for F-NR4 follow an (a) Arrhenius form below T_g and (b) WLF form above T_g. 170
5.48 Shift factors used to construct the master curve for F-NR5 follow an (a) Arrhenius form below T_g and (b) WLF form above T_g. 170
5.49 Using the loss tangent peaks to find the activation energy. 171
5.50 Using the loss tangent peaks to find the activation energy for (a) F-NR2, (b) F-NR3, (c) F-NR4, and (d) F-NR5. 172
5.51 MDSC results for U-NR with model fits either side of the T_g. 174
5.52 MDSC results for (a) F-NR2, (b) F-NR3, (c) F-NR4, and (d) F-NR5, with model fits either side of T_g. 175
5.53 Shifted MDSC results for all grades of NR to compare T_g, heat capacity rise and breadth of transition. 176

6.1 Experiments highlighting the three distinct responses: (a) Hyper-viscoelastic response under ambient, varying rate conditions, (b) viscoplastic response under sub-ambient conditions at a rate of 10^{-2} s^{-1} and (c) also featuring strain activated damage under sub-ambient, high rate conditions at −40 °C. 181

6.2 Diagrams of the (a) hyper-viscoelastic (HV) model and (b) modified Mulliken-Boyce (MB) model. 182
6.3 (a) Prony series representation of the viscoelasticity in the HV model and (b) using the Prony and Fractional Derivative (FD) models to fit the U-NR DMA data. 183
6.4 SLS + Ogden proof-of-concept for U-NR at (a) 1900 s^{-1} and (b) 2600 s^{-1}. 190
6.5 SLS + Ogden proof-of-concept for U-NR at the lowest strain rate: 10^{-3} s^{-1}. 190
6.6 Calibrating the hyperelastic convexity, α using data at -50 °C and 10^{-2} s^{-1}. 192
6.7 High rate HV model results for U-NR at (a) 1900 s^{-1} and (b) 2600 s^{-1}. 193
6.8 HV model results for (a) F-NR2 at 2500 s^{-1} and (b) F-NR3 at 2400 s^{-1}, (c) F-NR4 at 2700 s^{-1}, and (d) F-NR5 at 2600 s^{-1}. 194
6.9 Results from the quasi-static (10^{-1} s^{-1}), ambient (25 °C) calibration of the model parameters for (a) F-NR2, (b) F-NR3, (c) F-NR4, and (d) F-NR5. 196
6.10 Predictions of the high rate response for (a) F-NR2, (b) F-NR3, (c) F-NR4, and (d) F-NR5 using the parameters calibrated under quasi-static, ambient conditions. 197
6.11 Results from the quasi-static (10^{-2} s^{-1}) calibration of the model parameters: (a) F-NR2 and (b) F-NR3 at -40 °C; (c) F-NR4 and (d) F-NR5 at -45 °C. 198
6.12 Predictions of the high rate response for (a) F-NR2, (b) F-NR3, (c) F-NR4, and (d) F-NR5 using the parameters calibrated under quasi-static, low temperature conditions. 200
6.13 Predictions of the high rate response for (a) F-NR2, (b) F-NR3, (c) F-NR4, and (d) F-NR5: f and w_0 calibrated under quasi-static, ambient conditions; α and R calibrated under quasi-static, low temperature conditions. 202
6.14 Calibration of the limiting chain extensibility, N, for U-NR with an experiment conducted at 25 °C and 10^{-3} s^{-1}. 205

6.15 (a) Calibration of MB parameters for U-NR with sub-ambient experiments and (b) using the MB model to predict the ambient varying rate response for U-NR. 206
6.16 Using the MB model to predict the sub-ambient high rate response for U-NR and highlighting its temperature sensitivity at (a) −40 °C and (b) −60 °C. 207
6.17 Using the MB model with an incorporated damage definition to capture the sub-ambient high rate response for U-NR. 208
6.18 Using the MB model with an incorporated damage definition to capture the high rate response at −40 °C for (a) F-NR2, (b) F-NR3, (c) F-NR4 and (d) F-NR5. 211
6.19 Using the MB model with an incorporated damage definition to capture the high rate response at −60 °C for (a) F-NR2, (b) F-NR3, (c) F-NR4 and (d) F-NR5 (−55 °C). 214

List of Tables

3.1 Ogden parameters required for fitting. 68
3.2 Updated Ogden parameters for fits in Figure 3.21. 71
3.3 Equivalent temperatures and associated parameters for analogue fits as shown in Figure 3.23. 74

4.1 Parameters used for the Prony and Fractional fits to the DMA data. . . 108
4.2 Parameters for the enhanced FTVHEP modelling framework and how they were obtained. 114

5.1 Material properties for U-NR and glass microsphere fillers. 133
5.2 Theoretical densities of the F-NR based on a simple rule of mixtures. . 134
5.3 Additional information for the shift factor relationships presented in Figures 5.44 through 5.48. 170
5.4 Comparison of the glass transition activation energies resulting from analysing the shifting of the loss tangent peaks (Method A), and from the empirical storage modulus shift factor relationship below T_g (Method B). 172
5.5 Parameters for the model fits to the MDSC results. 175

6.1 Parameters used for the Prony and Fractional fits to the DMA data. . . 184
6.2 Fitting parameters used in the SLS + Ogden HV model as a proof-of-concept. 191
6.3 Fitting parameters used in the HV model for the particulate composites. 195
6.4 Fitting parameters used in the quasi-static (10^{-1} s^{-1}), ambient (25 °C) calibration of the HV model for the particulate composites. 196
6.5 Fitting parameters used in the quasi-static (10^{-2} s^{-1}), low temperature (-40 and -45 °C) calibration of the HV model for the particulate composites. 199

6.6 Combined HV model parameters used in the predictive modelling of the high rate response for the particulate composites. 201
6.7 Fitting parameters used in the MB model for U-NR. 206
6.8 Fitting parameters for the damage implementation in the MB model for U-NR. 209
6.9 Fitting parameters for the damage implementation in the MB model for F-NRs at −40 °C. 212
6.10 Fitting parameters for the damage implementation in the MB model for F-NRs at −60 °C. 214

1 Introduction

1.1 Context

Polymers are used extensively in engineering applications where they are subjected to impact loading at a wide range of temperatures, leading to deformation at large strain rates. In order to improve the mechanical performance of these materials, they are commonly filled with small particulates (among other reinforcements). It is therefore of utmost importance for researchers and engineers to understand the mechanical properties of polymers and their composites. Fillers may also be used for functional purposes, such as altering the materials' electromagnetic properties or transport of the filler itself, as is the case with polymer bonded explosives (PBX). However, the focus of this research is not on specific applications.

Considering that many polymers are used in impact load mitigation and energy dissipating components, it is necessary to investigate their impact resistance and high strain rate mechanical response. However, polymer response depends on both strain rate and temperature, and a single polymer can therefore exhibit behaviour ranging from glassy and brittle to rubbery and hyperelastic [1–7]. This makes accurate measurement and modelling both necessary and difficult.

This project aims to develop a greater understanding of the high strain rate mechanical response of particulate composites. These composites often use rate and temperature dependent polymeric materials in the matrix. Furthermore, they are often low-impedance materials, making the dynamic characterisation of their mechanical properties challenging.

The focus of this research is to develop a modelling framework, fully calibrated using the results of simple quasi-static experiments, that utilises the time-temperature superposition principle to enable the prediction of the full stress-strain response of

particulate composite under a variety of loading conditions. In order to achieve this overarching goal, experimental techniques and constitutive models will be developed, analytical procedures improved, and novel datasets generated.

In future, the contributions presented in this thesis will ultimately allow researchers to predict the high rate behaviour of any polymer system from knowledge of its composition and the results of simple, quasi-static characterisation experiments. This will enable design of polymer structures optimised to work efficiently in any impact application.

1.2 Scope

A brief summary of the contents in this thesis is as follows:

Chapter 1 introduces the context and scope of the research.

Chapter 2 provides a background to the content discussed in this thesis and critically reviews the current progress in understanding the high rate mechanical behaviour of polymers and composites. Additionally, the experimental, analytical and modelling techniques employed in this research are described.

Chapter 3 details preliminary experiments validating a rate-temperature equivalence and proposed modelling framework that developed using a neoprene rubber as a model material.

Chapter 4 presents a different, predictive modelling framework for amorphous polymers, applying it to (plasticised) poly(vinyl chloride). Here it is shown that the model can be calibrated using data obtained at low strain rates and then used to predict high rate response.

Chapter 5 provides data and analysis from the experimental characterisation of unfilled and filled natural rubber.

Chapter 6 discusses the use of two modelling frameworks, calibrated using the experimental data from Chapter 5, to capture and predict the high rate response of the unfilled and filled natural rubber.

Chapter 7 evaluates the findings of this project, providing conclusions and recommendations for future investigations.

2 Background

2.1 History of polymers and composites

For millenia, mankind has made use of wood, which consists mainly of cellulose, a natural polymer, as an engineering material [8]. Another natural polymer that has been used for thousands of years includes the rubber balls of the Mesoamerican Olmecs, used for games and made with rubber latex and a solvent from the morning glory plant [9]. However, it was not until the 1840s that Goodyear and Hancock improved the properties of natural rubber through the process of vulcanisation [10]. In Britain, the first instance of artificial manufactured plastics was Alexander Parkes's creation of Parkesine in around 1855, marketed as a substitute for ivory, but this material was not commercially viable until the process was improved and made scalable to industrial quantities by the Hyatt brothers [11], who produced a material called celluloid, also used as photography film. For decades, this was the only man-made plastic, until the first synthetic thermoset polymer, Bakelite, was produced by Leo Baekeland [12] in 1910, used in the moulding of various goods. The subsequent three decades saw the synthetic polymerisation of polystyrene (PS) [13], poly(vinyl chloride) (PVC) [14], Nylon [15], polyethelyne (PE) [16], and polyester [17]. An increased research effort into these materials was supported by investment during World War II, and since then has led to many advances including the invention of Teflon, Kevlar and other advanced polymers.

One of the earliest references to engineering with composite materials was the Mesopotamian insight of gluing pieces of wood at different angles to make plywood [18]. Even the Bible references an ancient use of composite materials in Exodus 5:7, *"Ye shall no more give the people straw to make brick, as heretofore: let them go and*

gather straw for themselves" [19]. The ancient Egyptians' use of straw as a reinforcement in mud bricks is widely reported from archeological studies and historical accounts [20]. Other examples of the historical use of composite materials include an early recipe for making concrete that can be found in an ancient Roman architectural manual by Vitruvius [21], the use of various forms of papier mâché [22], and the Mongol composite bow that played a significant role in creating one of the largest empires humanity has seen [23].

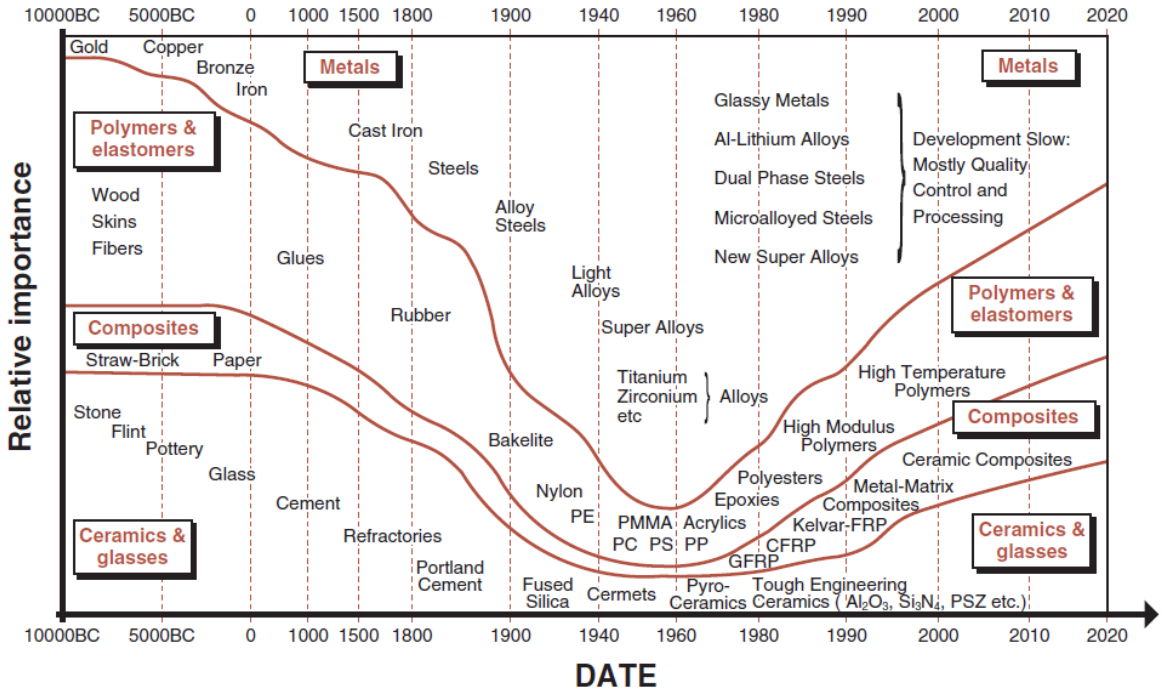

FIGURE 2.1: Relative importance of materials throughout history, from Ashby et. al. [24].

In the modern era, synthetic composite materials first appeared alongside polymers with the patent for the large scale production of glass fibres [25]. As can be seen in Figure 2.1, the relevance and importance of polymers and composites went hand in hand, and their proliferation was sparked during the inter-war years, with the advent of World War II acting as a further catalyst for growth in these fields. Resins to be used as a matrix material to bind with fibrous reinforcements were also developed in the late 30s and early 40s: namely unsaturated polyester resins [26, 27] and epoxy resins [28]. The earliest uses for the glass fibre reinforced plastics (GFRP) were in marine applications [29], and this later spread to the fields of aeronautics [30] and automotive

engineering [31]. Unsurprisingly, due to GFRP being the first synthetic composite, it still forms the majority of the industry, and these composites are estimated to grow from USD 44.10 Bn in 2016 to USD 83.63 Bn by 2026 [32].
Carbon fibre reinforced plastics (CFRP) form another important class of composites. An early driver for stronger, stiffer and lighter materials was the Space Race in the 60s, which led to the development of graphite and boron fibres [33]. Although boron fibres are stronger than their graphite counterparts, they are not as easy to process and are comparatively expensive [24]. In the early 70s, Kevlar was produced by DuPont [34], based on an aramid fibre (belonging to the Nylon group). Different matrix constituents, other than polymers, can also be used, most notably metals [35–37] and ceramics [38, 39]; however these are outside the scope of this current research.

All of the aforementioned composites have been fibrous, however there is another class of composites – the focus of the current research – particulate composites. Concrete provides an early example of a particulate composite — one in which an aggregate of gravel or coarse rock is added to a matrix of cement. Many different types of particulate composites exist, including those with micro-scale and nano-scale reinforcements [40–42], platelets [43–45], nanofibres [46–48], spherules [49–52], Buckminster fullerene [53–55], carbon nanotubes (CNT) [56–58], explosives (PBX) [4, 59], and sugar (PBS) as a simulant for PBX [60, 61].

Many particulate composites are used in systems where they can be subjected to impact loading, leading to high strain rate deformation. Therefore, the current research aims to better understand the high rate properties of particulate composites, but in order to achieve this, the following precursor materials were studied: neoprene rubber, (plasticised) PVC, and natural rubber. These polymers are mainly amorphous, though natural rubber can crystallise when held at low temperatures or under large strain deformation. To subsequently investigate the properties of particulate composites, the natural rubber was filled with different grades of glass microspheres. Overall, therefore, this research forms a coherent exploration of the relevant responses of both the polymer binder and the filled materials.

2.2 Rate and temperature dependence of amorphous polymers

Amorphous polymers lack significant order in their microstructure: the polymer macromolecules are randomly oriented. Alongside the weak van der Waals interaction holding chains together, they may also have physical chain entanglements and/or chemical cross-links (as in the case for vulcanised rubber).

Since polymers are formed of many repeating units, they have the capability to undergo various motions based on the chain structure. Their cooperative segmental mobility [62] gives rise to the (α) transition between glassy and rubbery behaviour, amongst other transitions. The ability of chain segments to move is governed by their thermal energy and the potential barrier that needs to be overcome to enable the motion. The probability that a segment has the energy to overcome such a barrier is described by a Boltzmann factor: $\exp(-Q/RT)$. This probability increases with increasing temperature, giving rise to the polymer's temperature dependent behaviour. When the temperature decreases past a threshold, most of these motions will effectively be frozen, which describes the glassy state. Depending on how broad the glass transition process is in the polymer, above this glass transition temperature (T_g), the polymer is in a rubbery state. Here, the polymer has a reduced strength, but shows non-linearly elastic stretching to large deformation prior to failure.

The theory of segmental mobility also asserts that any process which inhibits the various motions (rotations, translations, etc.) of the polymeric chain will lead to glassy behaviour. This is typically defined by the following mechanical response: linear viscoelastic rise to a peak, yield stress; post-yield softening to a lower yield point; and subsequent strain hardening. Beyond changes in temperature, the rate of loading is another such process. As the rate increases, the time-scale allowed for molecular motions is reduced. Above a certain rate, there is insufficient time during the experiment for motions to occur, thus leading to observed glassy polymer behaviour. In this state, the

polymer shows high strength and low strain to failure. Therefore, there is an underlying physical explanation for similar mechanical responses observed at low temperature and high strain rates.

This observed rate-temperature equivalence of material strengths has been investigated since the early 70s [63, 64] and has been shown for many amorphous polymers including poly(methyl methacrylate) (PMMA) [65], PVC [66] and polycarbonate [1]. One of the challenges with using the results of low temperature experiments to replicate the high strain rate behaviour is that under dynamic loading conditions, there is evidence of specimen self-heating [67, 68]. This originates from the applied mechanical work converting to heat, which does not diffuse out of the specimen on the time scale of the high rate experiment. Various approaches including interrupted experiments [69] and manual alteration of the temperature during testing [70] have been proposed to better replicate high rate response using low rate, low temperature experiments, however they too have limitations. In the interrupted experiments, a series of strain rate jump tests were conducted to form a locus of isothermal flow stresses. The interrupted experiments do not compare quasi-static tests directly with high rate ones and the manual input of the temperature rise requires the measurement of the temperature rise during high rate experiments, a significant challenge due to their short duration. Furthermore, the assumption that all applied mechanical work is converted to heat is not true for all polymers [71]. The current research aims to improve the predictive replication of the high rate response.

In the aforementioned investigations of amorphous polymers, it has often been observed that at higher strain rates (c.1000 s^{-1}), the measured strength shows an increased strain rate sensitivity. This is attributed to the secondary (β) transition in the material [72]: typically the motions of side branches in the polymer. Care must be taken in interpreting the results from experiments investigating this high rate sensitivity as the stress induced by inertial effects becomes increasingly significant [73, 74]. Additionally, the change in rate dependence occurs at around the same strain rates at which the experimental technique is changed, so the potential exists for experimental

artefacts to mask the true response of the polymer. These challenges are some of the drivers that motivate the current research and the use of alternative, complementary techniques to investigate the high rate response of polymers. One such method uses the time-temperature superposition (TTS) principle, described later in §2.4.

Although the strength of polymers exhibits a notable pressure dependence [75], the investigation of this is outside the scope of the current research as unconfined samples are tested under uniaxial loading here. This pressure dependence can be characterised experimentally through relations comparing the compressive and tensile yield strengths of the polymer at a constant temperature and loading rate [76]. In this study, only uniaxial compression experiments are conducted under various loading conditions.

2.3 Experimental techniques

In §2.2, the rate and temperature dependence of the properties of amorphous polymers was described. In this section, the techniques used to experimentally characterise these dependences in the compressive response of polymers and particulate composites are discussed.

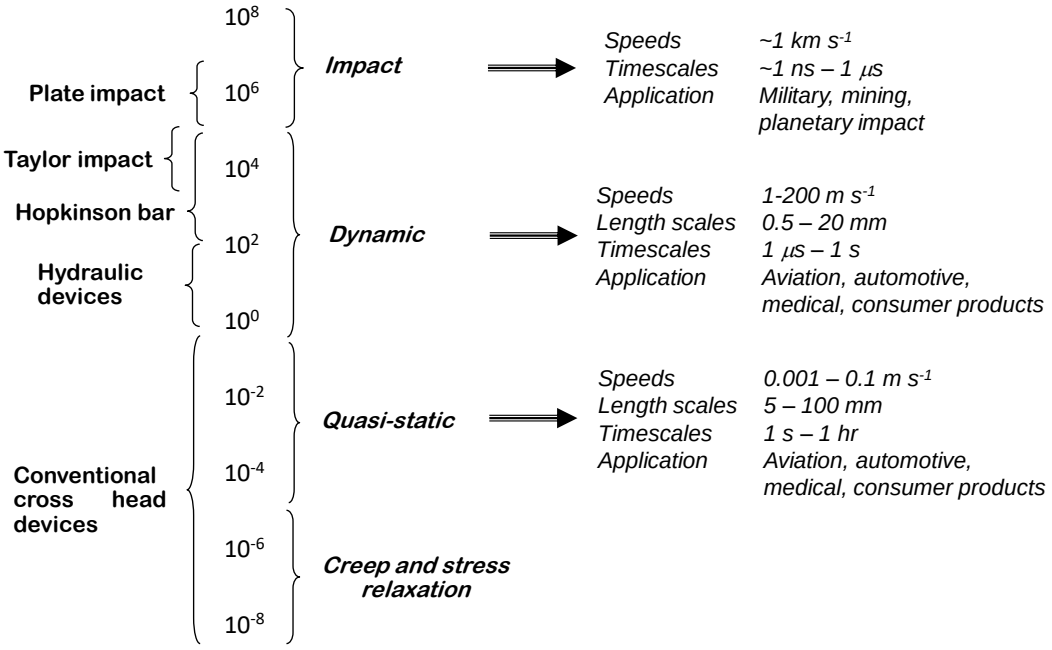

FIGURE 2.2: Strain rate regimes and experimental techniques typically used in investigations (adapted from [77]).

The primary objective of this research is to predict the high strain rate behaviour of amorphous polymers and their particulate composites by using experimental data obtained, and models calibrated, at low strain rates. Based on the divisions shown in Figure 2.2, this research is interested in the properties in the *dynamic* range. However, in order to characterise this behaviour, experimental techniques from below this range will also be required. Therefore, in terms of the uniaxial response, three apparatus will be detailed: conventional cross-head devices at low strain rates, hydraulic devices at intermediate strain rates and the split-Hopkinson pressure bar (SHPB) at high strain rates.

2.3.1 Low strain rates

The quasi-static uniaxial investigation of material mechanical properties may have their roots in the analysis by Da Vinci, who studied the dependence of length on the tensile strength of wires [78]. In England, the pioneer of this research was Hooke, who first investigated linear elasticity at small deformations [79]. Large scale testing machines for the uniaxial testing of materials were only developed in the latter part of the Industrial Revolution to analyse the properties of wrought iron, a popular engineering material of the time for applications in railways and machinery [80]. Nowadays, these servo-hydraulic or screw-driven testing machines feature advanced electronics and controllers.

An advantage of conducting experiments at quasi-static strain rates is that a range of diagnostic tools exist to make *in-situ* measurements during the time-scale of these experiments (e.g. X-ray tomography and diffraction techniques, Scanning Electron Microscopy, thermography, etc). Furthermore, with the use of an environmental chamber, conditions such as the temperature during the compression experiment can be varied. This offers a simple tool to investigate the temperature dependence at these low strain rates.

2.3.1.1 Analysis of data

The outputs of quasi-static experiments are typically the displacements, ΔL and the loads, F. To measure the displacement, a number of techniques exist, including cameras or lasers for optical visualisation, apparatus cross-head displacement or extensometers. The force is measured using the apparatus load cell. If the original specimen length is L_0, the engineering or nominal strain, e, is:

$$e = \frac{\Delta L}{L_0} \tag{2.1}$$

In compressive experiments, $\Delta L = L_0 - L$, where L is the current length of the specimen. So, in order to get a positive value, compressive true strain, ε, is defined as:

$$\begin{aligned} \varepsilon &= -\log\Big(\frac{L}{L_0}\Big) \\ &= -\log\Big(\frac{L_0 - L}{L_0}\Big) \\ &= -\log(1-e) \end{aligned} \tag{2.2}$$

The original specimen cross-sectional area is A_0, and so the engineering or nominal stress, s, is:

$$s = \frac{F}{A_0} \tag{2.3}$$

Assuming conservation of volume ($AL = A_0L_0$), the true stress, σ, is:

$$\begin{aligned} \sigma &= \frac{F}{A} \\ &= \frac{F}{A_0}\frac{L}{L_0} \\ &= s\Big(\frac{L_0 - \Delta L}{L_0}\Big) \\ &= s(1-e) \end{aligned} \tag{2.4}$$

Volume conservation is valid when there is no damage, plasticity is independent of hydrostatic stress and there are no structural changes leading to irrecoverable volume changes. After using Equations 2.2 and 2.4 to calculate the true strains and stresses, they can then be plotted on a suitable set of axes to facilitate further analyses.

2.3.2 Intermediate strain rates

As the strain rate increases beyond the quasi-static regime, accurate measurements can become challenging. Not only is the frequency at which experimental data are to be measured similar to the natural frequency of the loading system, it is also necessary overcome inertial effects in the apparatus [81].

Many experimental techniques have been used to investigate the material response at intermediate strain rates: cam plastometers [82, 83], fly-wheel systems [84, 85], expanding rings [86, 87], long Hopkinson bars [88, 89] and the drop-weight [90, 91]. In this study, a custom-built hydraulic press was used as depicted in Figure 2.3.

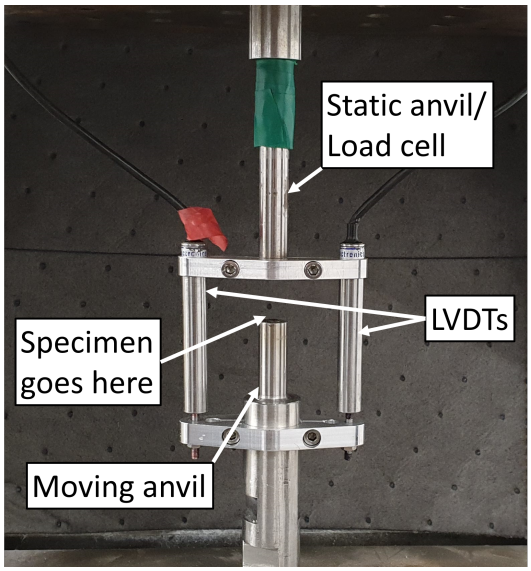

FIGURE 2.3: Hydraulic press for medium rate compression experiments.

The displacement of the moving anvil was measured using linear variable differential transformers (LVDTs), and the true strain was again calculated assuming the conservation of volume. The force was measured using a load cell built into the upper static anvil. Prior to starting the experiment, this anvil is carefully positioned to rest on the specimen with a light pre-load. The piston of the hydraulic system drives the lower anvil upwards to compress the specimen at a pre-set speed and displacement.

2.3.2.1 Analysis of data

The outputs of the hydraulic experiments are the time varying voltage signals from three channels representing the two LVDTs and the load cell. In order to calculate the load, F, and displacements from the left and right LVDTs, ΔL_l and ΔL_r, the voltage readings are divided by the individual calibration factors (pre-determined from calibrations conducted in the linear regions of the load cell and LVDTs). The two individual LVDT displacement readings are converted to displacements using their calibration factors and subsequently averaged. The true strains and stresses can then be calculated using Equations 2.2 and 2.4 as above.

2.3.3 High strain rates

For the high strain rate characterisation of materials, many different methods are used, including some of those mentioned in the previous section [77]. Other techniques involve the use of modified drop weight towers [92], Taylor (rod) impact [6, 93], plate impact [94, 95] and transverse impact [96, 97] experiments. Hopkinson formulated a method in 1914 measuring the momentum change when a bullet strikes a metal bar to understand the pressure exerted by a bullet [98]. The bar was used as a mechanical waveguide to transmit momentum to a recording system. However, this method was not able to capture the actual pressure-time profile, and it was only in 1949 that the method was refined by Kolsky to achieve this [99]. The compressive Kolsky bar, or SHPB, is used for the highest strain rates considered in this research and is shown schematically in Figure 2.4. Several books have been published to guide the user through the experimental set-up and processing of data to obtain meaningful stress-strain relationships [100–102], but a brief outline of the apparatus and analysis is shown below, using exemplar data from an experiment performed on neoprene rubber.

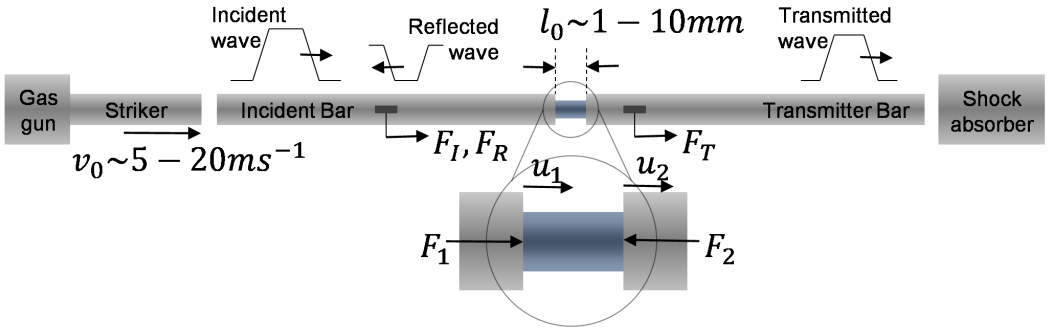

FIGURE 2.4: SHPB diagram illustrating the set-up for high rate compression experiments.

The device consists of two large bars, the incident and transmitter bar, which are designed to remain elastic for the duration of the experiment. These bars have diameters around 25 mm or less and their lengths are in the order of metres. One end of the incident bar is impacted by a striker bar, which is usually a third bar of the same material and diameter as the others. This results in a compressive stress wave propagating down the incident bar and into the specimen, which is sandwiched between the incident and transmitter bars. This wave reverberates several times within the specimen; during which time a transmitted wave also propagates into the transmitter bar. The length of the striker bar determines the duration of the loading pulse and hence the strain achievable; this is normally set to be a little less than half the length of the incident bar to prevent wave overlap at the incident bar strain gauge (typically centrally mounted).

The strain rate possible can be altered by the use of varying the bar geometry. From the conservation of momentum, it can be observed that the strain rate in the specimen is inversely proportional to the bar cross-sectional area, so smaller diameters mean a higher strain rate can be achieved. Lower strain rates can be achieved on the SHPB using a longer striker bar, producing a loading pulse long enough to deform the specimen to large strains. In order to avoid overlapping of the stress waves, due to the longer loading pulse, longer input and transmitter bars would also be required.

The incident and transmitter bars are each instrumented with strain gauges: each gauge location usually has two or four gauges arranged diametrically opposed to each other; these are typically calibrated so that the gauge output can be directly converted

to the force in the bar owing to the stress wave passing along it. With this set-up of gauges, only the longitudinal component of the stress is measured as the flexural components cancel out. The incident bar gauge is positioned halfway down the bar, to better isolate the incident and reflected waves, simplifying later analysis. The transmitter bar gauge, on the other hand, is positioned as close to the edge as possible to achieve longer loading pulses without overlap. However, due to the dynamic St Venant's principle, it is generally agreed that the gauge should be positioned no closer than around two to four bar diameters from the edge [103].

The specimen in these SHPB experiments is typically a right, circular cylinder, with lengths and diameters of the order 1 to 10 mm, typically with ratios from 1:1 to 1:2. These are constrained by the need to reduce time to reach static equilibrium and the adverse effects of inertia [74].

2.3.3.1 Analysis of data

In a conventional two-gauge set up, the measured experimental outputs are the incident and transmitter bar signals. Figure 2.5a shows these for an experiment on neoprene rubber. There are countless reverberations of the waves in the bars, but only the first is typically used, and so only this is displayed for clarity. The incident and reflected stress waves are recorded with the incident bar gauge, and the transmitted wave with the transmitter bar gauge. These are decomposed and time-shifted to the bar-specimen interface, as shown in Figure 2.5b. These pulse signals are converted to forces by dividing by the pre-determined gauge calibration factors. In this manner, F_I, F_R, and F_T are obtained. In order to continue with the analysis, a force equilibrium check must be conducted to ensure the forces at the two bar-specimen interfaces are the same. Figure 2.5c shows that this is true for the majority of the experimental duration barring the early transient effects due to Pochhammer-Chree dispersion [104, 105]. This demonstrates that enough wave oscillations have occurred in the specimen (i.e. it has 'rung up') for it to be in a state of static equilibrium. This is necessary if the

specimen response is to be representative of the true material properties, as the stress and strain need to be the same everywhere.

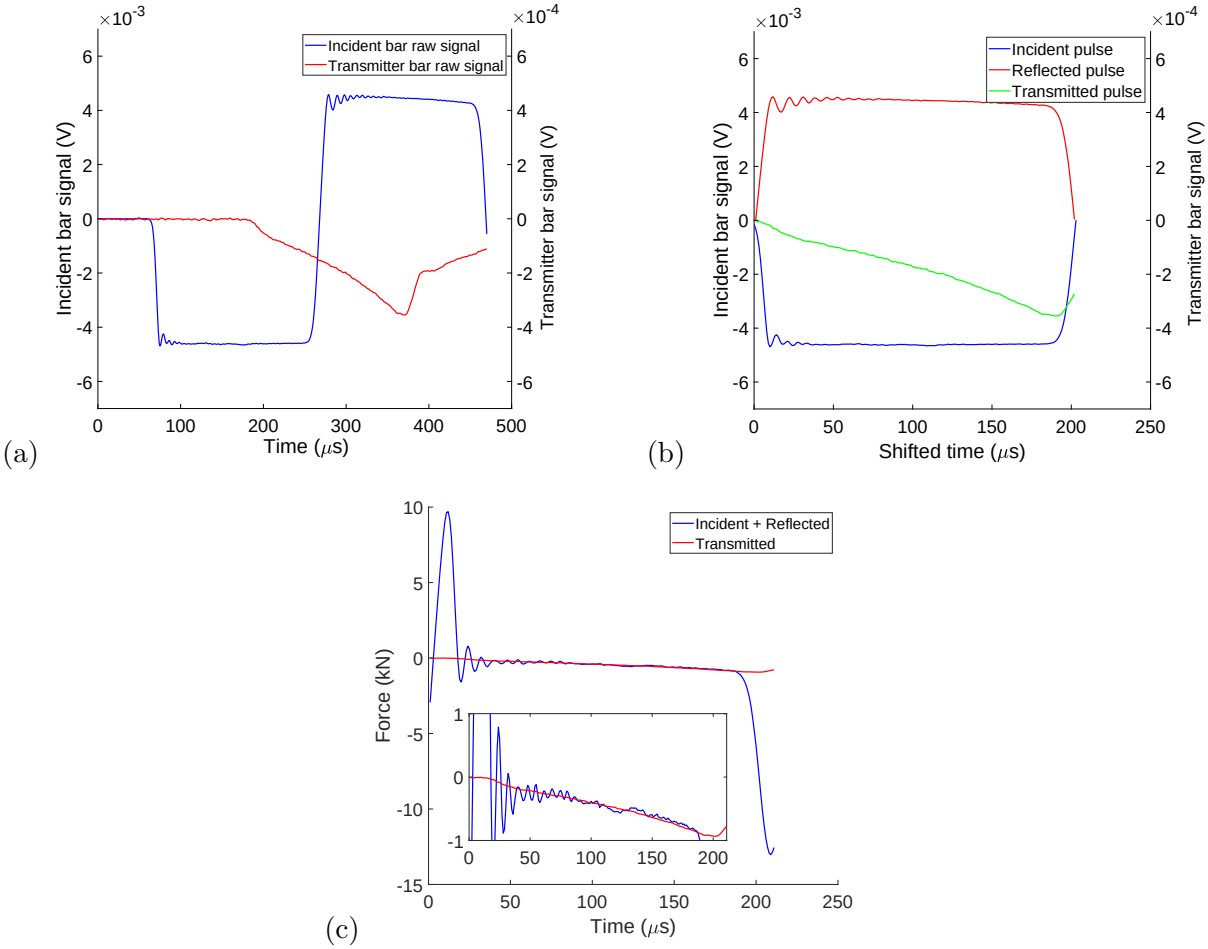

FIGURE 2.5: (a) Examples of raw strain gauge signals obtained from the incident and transmitter bars, (b) individual pulse signals for the incident, reflected and transmitted waves, and (c) comparison of the inferred forces on each bar-specimen interface. These data are from a high strain rate experiment on neoprene rubber.

Once the forces are known, and equilibrium has been validated, the deformation velocities of the bar-specimen interface can be obtained. These are expressed by Equation 2.5, where ρ_b, c_b and A_b are the bar density, wavespeed and cross-sectional area respectively.

$$u_1 = \frac{F_I - F_R}{\rho_b c_b A_b} \tag{2.5a}$$

$$u_2 = \frac{F_T}{\rho_b c_b A_b} \tag{2.5b}$$

The instantaneous length of the specimen can be inferred incrementally from the relative bar velocity $(u_1 - u_2)$, as in Equation 2.6, where $\Delta t = t_{k+1} - t_k$ is the time increment.

$$L_{k+1} = L_k - (u_{1,k} - u_{2,k})\Delta t \tag{2.6}$$

Once the instantaneous length is known, the true strain can be calculated using Equation 2.2 presented earlier. The true stress can also be calculated using Equation 2.4, where the force is either F_1 $(= F_I - F_R)$ or F_2 $(= F_T)$, as the force acting on each bar-specimen interface should be the same. However, F_T is typically used for data presentation as it is less affected by high frequency interference than $F_I - F_R$. This is since the measurements in the input bar are influenced more by high frequency components in the loading pulse, as can be seen in Figure 2.5c. Stress-time and strain-time graphs can be plotted as shown in Figure 2.6a. The strain-time curve shows that a constant true strain rate has been achieved for the majority of the test duration. Here, this is calculated from $0.2\varepsilon_{max}$ to $0.8\varepsilon_{max}$ as $\dot{\varepsilon} = 1900$ s^{-1}, where ε_{max} is the maximum strain during the experiment. Finally, the stress-strain relationship can be plotted for this high rate experiment on neoprene rubber as shown in Figure 2.6b.

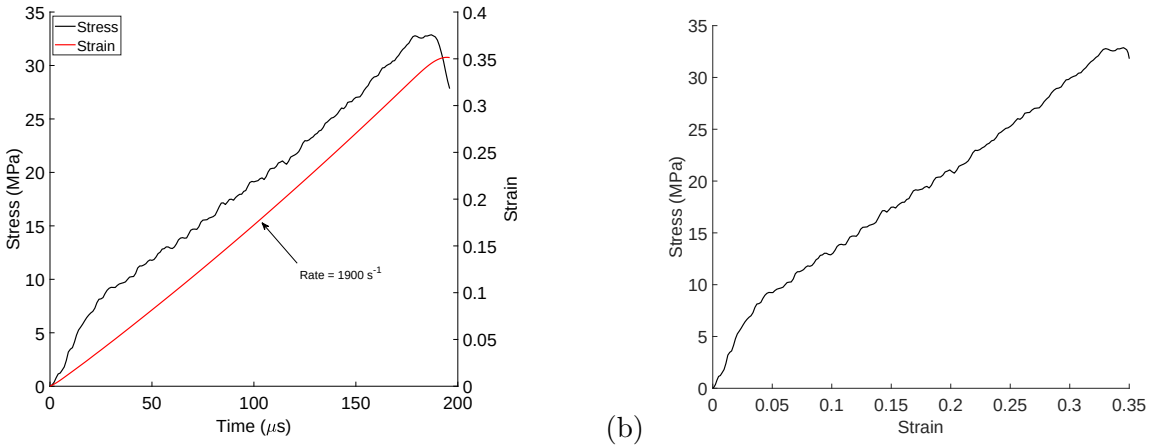

FIGURE 2.6: (a) Examples of stress-time and strain-time curves obtained from the analysis and (b) the resultant stress-strain relationship for the experiment on neoprene rubber at $\dot{\varepsilon} = 1900$ s^{-1}.

2.3.3.2 Challenges

The SHPB technique can present difficulties when trying to obtain results for soft materials. For materials with very low mechanical impedances, the transmitted signal may be too weak to be accurately measured (the transmitted signal is ten times smaller than the incident and reflected signals in Figure 2.5b), with a poor signal to noise ratio [106]. The analysis of an SHPB experiment also requires the specimen to be uniformly loaded and in a quasi-static stress equilibrium [107]. The low wavespeeds of soft polymers means that the static equilibrium takes longer to be reached. The time to equilibrium may be similar to, or sometimes even greater than, the experimental duration. This means that structural vibrations may mask the material response, as the natural frequency of the specimen is similar to frequencies in the loading pulse. Since a square stress wave is preferred, frequencies can be significantly large, though typically are below c.100 kHz [102]. Constant strain rates are also desired since the material is rate dependent, so the measured response must be correlated with a particular strain rate: this is difficult to achieve for all specimens at large strains and may require careful pulse shaping to modify the incident stress wave. Additionally, inertia induced stresses must be minimised to ensure that the stress state is 1D and the calculated stresses are representative of the underlying material response [108].

Methods have been proposed to mitigate these issues: the reduction of bar cross-sectional area [106] or modulus (including polymeric) bars [109] and/or measuring the force directly using piezoelectric pressure transducers [110] or X-cut quartz crystal discs [107]. Furthermore, the use of pulse shapers [111] and a varied geometry striker bar [112] can be used to better control the loading history. The specimen geometry also plays a key role in minimising inertial effects [113].

In this research, the force (specifically the transmitted) is measured more accurately using piezoelectric gauges, paper or copper pulse shapers are used to remove high frequencies from the loading pulse, and a geometry favouring thin circular cylindrical samples is chosen to reduce inertial contribution to stresses.

2.3.4 Calorimetry

Calorimetry is the science of understanding the heat transfer associated with changes of state including physical or phase transitions and chemical reactions [114]. One of the most popular contemporary calorimetric techniques is the use of a Differential Scanning Calorimeter (DSC).

Conventional DSC experiments measure the difference in heat flow between the sample and an inert reference as a function of time and temperature, whilst they are both subjected to the same linear heating or cooling rate and environmental conditions [115]. Since the heat flow required to maintain a constant temperature ramp depends on the heat capacity of the material and changes due to endothermic and exothermic processes, the difference in heat flow between the sample and reference can be used to identify and characterise thermal transitions of interest in the material. Exemplar data for a conventional DSC experiment on low density polyethylene (LDPE) are shown in Figure 2.7a, where a linear temperature ramp of 3 °C /min is used from −90 °C to 200 °C.

One of the biggest disadvantages with using this conventional DSC approach is that it is often difficult to discern individual transitions, as DSC sums or averages the heat flow rate from overlapping processes into a single heat flow signal from a single heating/cooling rate. This is clearly observed in Figure 2.7a, where the major melting transition for LDPE is masked by other smaller transitions.

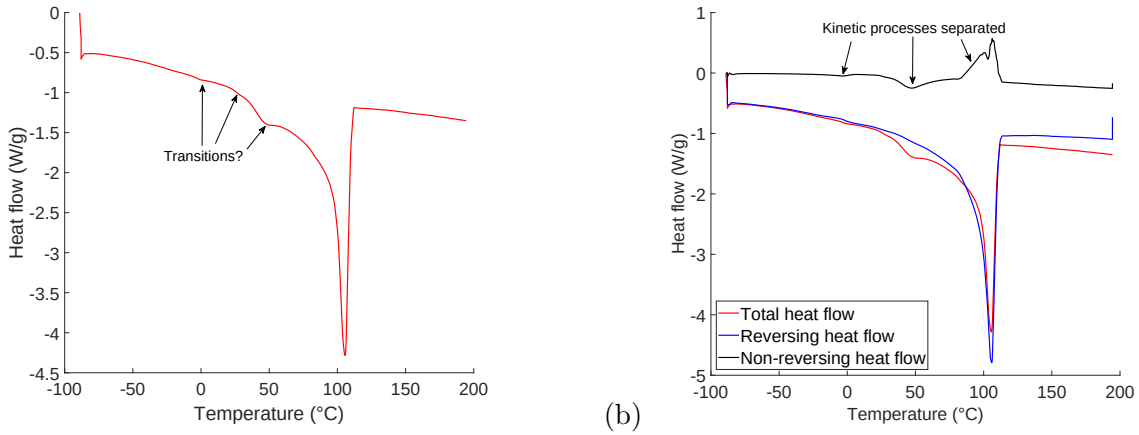

(a) (b)

FIGURE 2.7: Examples of data obtained for calorimetry experiments on LDPE using (a) a conventional DSC experiment with a linear temperature ramp of 3 °C /min and (b) a modulated DSC experiment, which also superposes a sinusoidal modulation of amplitude 0.5 °C and period 1 min (±0.5 °C /min).

In order to separate complex transitions into the desired processes, modulated DSC (MDSC) experiments can be performed. In MDSC experiments, a sinusoidal temperature oscillation is superposed onto the conventional temperature ramp and the difference in heat flow required to maintain this temperature profile is again monitored between the empty reference pan and the pan containing the specimen. MDSC data for an experiment on LDPE are shown in Figure 2.7b, which superposes an oscillatory temperature profile of amplitude 0.5 °C and period 1 min (±0.5 °C /min) onto the same linear ramp of 3 °C /min as used to obtain the data in Figure 2.7a.

Often, the DSC measurements associated with a glass transition may have similar characteristics to those of a melting transition, due to an endothermic enthalpic relaxation, which can take place around T_g, or other kinetic processes such as crystallisation. MDSC experiments allow these transitions to be discerned more clearly as it is more sensitive to the heating rate than conventional DSC, allowing for weaker transitions to be resolved. It also allows for more accurate measurements of the degree of crystallinity to be made, and can be used to directly determine thermal conductivity. In this study, MDSC experiments allowed the separation of the desired thermodynamic effects (namely the temperature dependent heat capacity) from the undesired kinetic processes, such as crystallisation, molecular relaxations or any chemical reactions.

$$\frac{\mathrm{dH}}{\mathrm{dt}} = \mathrm{C_p}\frac{\mathrm{dT}}{\mathrm{dt}} + f(\mathrm{T},\mathrm{t}) \tag{2.7}$$

In order to separate these two effects, in MDSC experiments, the total heat flow is split into reversing and non-reversing components, which sum to give the total heat flow according to Equation 2.7. This total is the value given by a standard DSC, but by superposing a sinusoidal profile on top of a linear one, it is now possible to separate the total heat flow into the reversing ($\mathrm{C_p}\frac{\mathrm{dT}}{\mathrm{dt}}$) and non-reversing ($f(\mathrm{T},\mathrm{t})$) components. The reversing heat flow is the product of the heat capacity and the total heating rate, which has a linear and modulated component. The non-reversing heat flow is the component associated with kinetic processes such as enthalpic recovery or crystallisation. In Figure 2.7b, this separation can be observed for LDPE, where the non-reversing heat flow contains information about the kinetic processes and the reversing heat flow shows the underlying thermodynamic response.

2.3.5 Thermomechanical characterisation

Polymers are viscoelastic materials, and show rate and temperature dependence to their mechanical properties: thermomechanical characterisation is therefore essential. This is normally performed by imposing an oscillating strain on a sample and measuring its stress response, or vice versa, under specific environmental conditions. One of the earliest attempts to obtain the elastic properties of a material through oscillatory testing was by Poynting in 1909 [116], who was able to deduce the Young's modulus from the lengthening of a loaded wire under torsion. Collectively, these techniques on solids are often referred to as Dynamic Mechanical Analysis (DMA). A review of oscillatory tests for DMA based characterisation is given in [117].

Many loading configurations can be used to conduct DMA experiments: shear sandwich, tension, compression, three or four point bend, single or dual cantilever, torsion, etc. With each configuration, a different sample geometry is utilised. In the current research, single/dual cantilever configurations were used and a typical sample geometry is $40\times5\times2$ mm for single, and $60\times10\times5$ mm for dual, cantilever experiments.

The main outputs of the DMA experiments are the temperature, T, storage modulus, E', loss modulus, E'' and frequency, f. Exemplar data for a DMA experiment on unfilled natural rubber (from Chapter 5) are shown in Figure 2.8a.

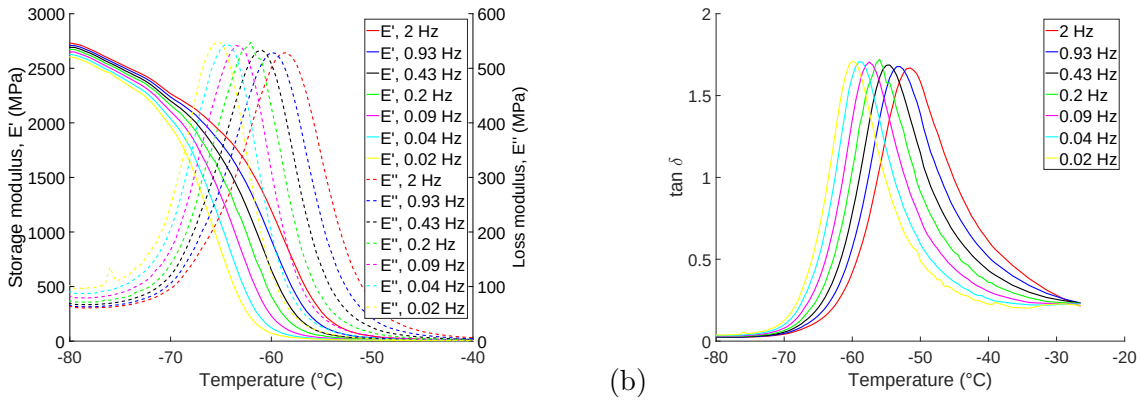

FIGURE 2.8: Example of data for a DMA experiment on natural rubber in single cantilever configuration showing the dependence of (a) storage and loss moduli, and (b) the loss tangent, on temperature for a variety of frequencies.

The oscillations at a given frequency applied to a viscoelastic material will give in-phase

(elastic) and out-of-phase (viscous) components of the modulus; the storage (E') and loss (E'') moduli characterise these components. Together they can be characterised by the dynamic or complex modulus:

$$E^* = E' + iE'' \tag{2.8}$$

Another important quantity that can be deduced is the loss tangent, which is defined as the ratio of the loss modulus to the storage modulus:

$$\tan\delta = \frac{E''}{E'} \tag{2.9}$$

The loss tangent, or tan delta, represents the ratio of energy dissipated to energy stored per deformation cycle. It is also the phase shift between the applied strain and the resultant stress. Its value ranges from zero, for a pure elastic solid, to infinity, for pure liquid. The loss tangents for unfilled natural rubber are shown in Figure 2.8b.

By performing these experiments at a variety of frequencies and temperatures, valuable insights on material transitions, and how they shift with these conditions, can be found. For example, the temperature of each loss tangent peak in Figure 2.8b can give an indication of the T_g at that frequency, whilst, by investigating the lateral shift of these curves with frequency, the frequency and temperature dependence of the transition can be explored.

Although the DMA experiments give the frequency dependence, it is often the strain rate dependence that is of interest to researchers in the field of dynamic mechanics of materials. To make comparisons between the frequency and strain rate dependence of materials based on the results of different experiments, the Cox-Merz rule [118] may be applied: $\dot{\varepsilon} \approx 2\pi f$. These strain rates are only approximations as, depending on the configuration used for DMA experiments, the strain rate can vary through the volume of the sample. Many researchers plot mechanical properties against logarithms of frequency or strain rate as it is physically realistic, and better represents constitutive laws (i.e. the Eyring plot [119–121]), so non-zero variations in the strain rate through

the specimen volume can become less significant.

DMA is a very popular technique, as indicated by its prevalence in recent publications [59, 70] and the number of books written on the subject [122–125]. It forms the quantitative basis for the time-temperature superposition technique in this study.

2.4 Time temperature superposition

The early basis of the time-temperature superposition principle was in the observation of rate and temperature dependence of the complex modulus [126]. The rate and temperature dependence of larger strain properties (as described in §2.2), such as the yield stress, documented by Bauwens-Crowet [64, 127], further extended this technique. TTS has been well documented in many books [128–130], and is particularly useful in the current research as it enables high frequency material properties to be accessed.

For some thermorheologically simple polymers, the relation between time and temperature can be described by simple models. In these models, the effect of reducing the temperature is the same as increasing the relaxation time (or decreasing the frequency). The physical basis of this has been described earlier (in §2.2) with the cooperative segmental mobility theory. Relating this to the DMA experiments from the previous section, this is akin to shifting the modulus vs log f curve horizontally to lower frequencies (Figure 2.9b, discussed later, illustrates this concept). Similarly, the effect of an increase in temperature would see this curve shift horizontally to higher frequencies. This is to say that at lower temperatures, lower frequencies can result in the same observed modulus values as at higher temperatures and higher frequencies. The amount of shifting is quantified by the shift factor, $\log a_T$, which is dependent on temperature.

Williams, Landel and Ferry (WLF) provided a comprehensive method for obtaining these shift factors for TTS near or above the T_g [131]. The WLF formula provides an expression for the temperature dependence of these shift factors:

$$\log a_T = \frac{-C_1(T - T_{ref})}{C_2 + (T - T_{ref})} \tag{2.10}$$

where C_1 and C_2 are constants, and T_{ref} is often set as T_g. Based on the thermodynamic theory governing transitions, an Arrhenius expression can also be used to obtain the shift factors [119], typically away from the T_g:

$$\log a_T = \frac{Q}{R}\Big(\frac{1}{T} - \frac{1}{T_{ref}}\Big) \tag{2.11}$$

where Q is the activation energy and R is the gas constant. A theoretical explanation of TTS was later proposed using molecular models [132]. The use of Group Interaction Modelling [133] has also been used to obtain thermomechanical insights from a theoretical basis [134, 135].

In order to illustrate the process used to derive the shift factors from experimental data, and produce a master curve of modulus against the logarithm of frequency, the results from a preliminary investigation of neoprene rubber (as detailed in Chapter 3) are used to show the TTS process in a step-by-step manner.

2.4.1 Isothermal frequency sweep data

Instead of plotting the temperature dependence of the moduli for each frequency, as in the standard output from DMA experiments (see Figure 2.8a), it is possible to plot the frequency dependence at a given temperature. When plotted on a log frequency scale, each of these isotherms is broadly linear, as shown in Figure 2.9a. The isotherms may be non-linear in other cases, in which case they can be fitted with higher order polynomials, or other appropriate functions to facilitate the shifting process. The glassy nature of the material at the lowest temperatures can be noted in the all-round stiffer response. Likewise, the rubbery nature at higher temperatures is clear from the low stiffness. The frequency dependence of the modulus is more noticeable as the temperature approaches T_g, as made evident by the increase in slope for the isotherms

approaching −50 °C. The sensitivity of the isotherms to temperature is also clear from the greater spacing between adjacent isotherms as the temperature approaches T_g.

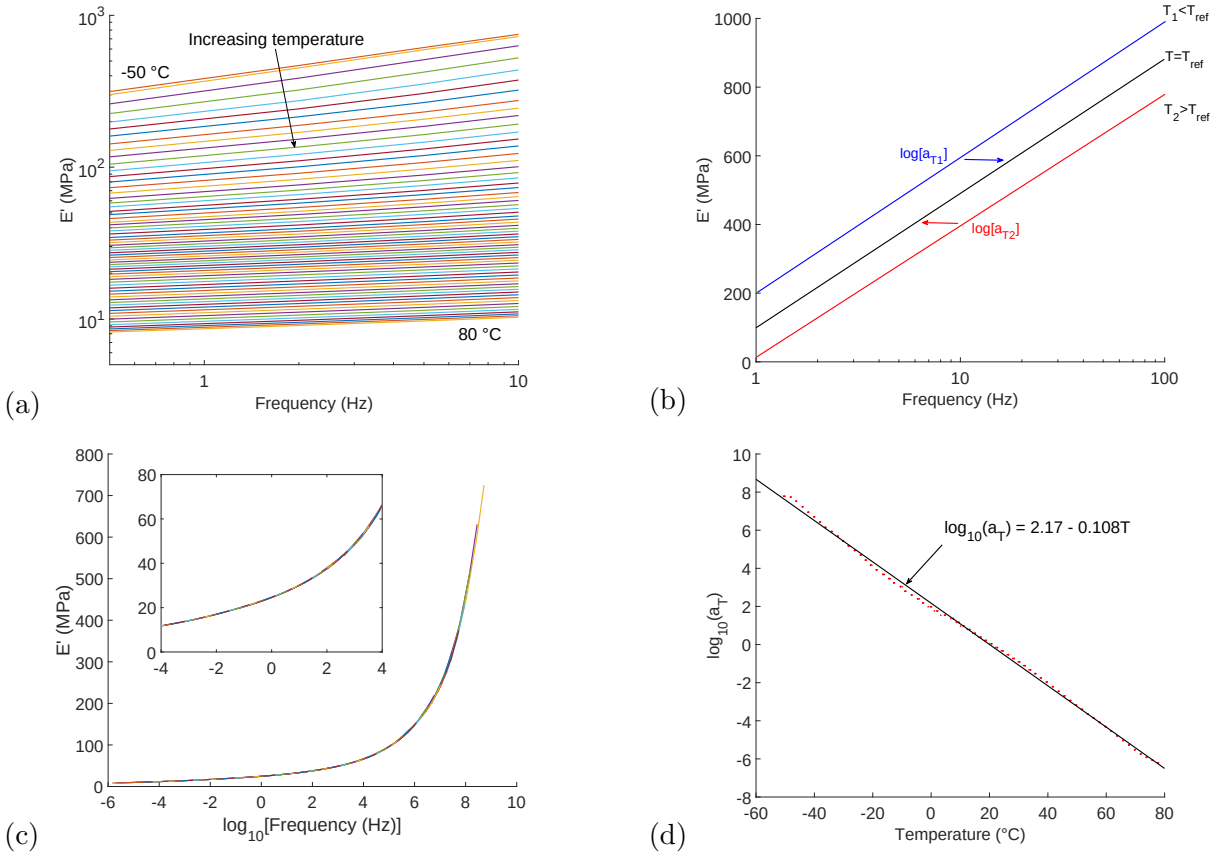

FIGURE 2.9: (a) Isotherms showing the frequency and temperature dependence of storage modulus, (b) a schematic of the isotherm shifting process, (c) the master curve generated at a reference of 20 °C by shifting these isotherms (inset highlights experimentally relevant frequencies), and (d) the shift factors required to move the isotherms.

2.4.2 Shifting process

Based on the linearity of the isotherms, it is possible to employ a horizontal shifting algorithm to construct the master curve. Figure 2.9b shows how this shifting process is conducted. Once a reference temperature, T_{ref}, is selected (in this study, this is usually chosen to be the same as the temperature of the compression experiments) other isotherms can be shifted accordingly to form a continuous curve starting from this reference isotherm.

The direction of the shifting depends on the temperature of the adjacent isotherms. For example, the isotherm for $T_1 < T_{ref}$ is shifted in the positive (to the right) direction

such that it overlaps with the isotherm for the reference temperature. Similarly, the isotherm for $T_2 > T_{ref}$ is shifted in the negative direction to overlap the same reference isotherm. The amount of shift required is called the shift factor and is described as $\log[a_T]$. Here, the T_1 isotherm requires a positive shift factor $\log[a_{T1}]$ and the T_2 isotherm requires a negative shift factor $\log[a_{T2}]$.

Generalising, all isotherms hotter than the reference have a negative shift factor and isotherms colder than the reference have a positive shift factor. This implies that an experiment at a lower frequency and lower temperature would have the same modulus as that for the reference temperature and frequency. Equally, an experiment at a higher frequency and higher temperature would have the same modulus. This time-temperature equivalence forms the basis of the time-temperature superposition technique and gives the ability to perform these shifts to construct a master curve.

2.4.3 Calculating the shift factors

Once all the isotherms are shifted, a master curve as shown in Figure 2.9b is obtained. To calculate the value of the shift factor required to translate each isotherm, let us refer back to Figure 2.9b. Each isotherm is represented by a first order polynomial fitted through the data points: $E' = m\log[f(\mathrm{Hz})] + c$. In order to shift the adjacent isotherms to overlap the reference, we consider the fact that the y-value (here the storage modulus) must be the same. The local shift factor is hence the difference in x-values (here the logarithm of the frequency), calculated as:

$$\begin{aligned} \log a_{(T_1 \to T_{ref})} &= \log[f_{ref}] - \log[f_1] \\ &= \frac{E'_{ref} - c_{ref}}{m_{ref}} - \frac{E'_{ref} - c_1}{m_1} \end{aligned} \tag{2.12}$$

where E'_{ref} is the storage modulus, which is the same for adjacent isotherms in this process; c_{ref} is the y-intercept, and m_{ref} is the gradient, for the linear fit to the reference isotherm. Likewise, c_1 and m_1 are y-intercept and gradient for the adjacent isotherm.

For the case above, where the isotherm shifted was adjacent to the reference isotherm, the local shift factor would be the total shift factor. However, for the majority of isotherms, the total shift factor would be the cumulative sum of each local shift factor that overlap the isotherm with its neighbour and thereby incrementally take it closer to the reference isotherm:

$$\log a_{(T_n \to T_{ref})} = \sum_{i=ref}^{n} \left[\frac{E'_{i+1} - c_{i+1}}{m_{i+1}} - \frac{E'_{i+1} - c_i}{m_i} \right] \tag{2.13}$$

The total shift factor values for shifting each isotherm can then be plotted against the temperature of the isotherms as shown in Figure 2.9c. Each data point corresponds to the total shift required for the isotherm at that temperature to be translated laterally such that it forms part of a continuous curve – the master curve – that goes through the reference isotherm. For neoprene rubber, a linear relationship within the temperature domain, $T : [-100, 120]$, describes the temperature dependence of the shift factors well.

No matter how far an isotherm is from the reference, this same procedure can be employed incrementally to get it to overlap the reference curve. For example, still considering the shifting process in Figure 2.9b, imagine the isotherm for a temperature T_3 where $T_3 > T_2 > T_{ref}$. In order to get the isotherm for T_3 to overlap the one for T_{ref}, it is first shifted leftwards to overlap the isotherm for T_2. This combined curve comprising of the two isotherms is then shifted further leftwards to overlap with the isotherm for T_{ref}. This cumulative shifting process works for all isotherms whether above or below the reference temperature.

If the master curve is to be constructed at a temperature that does not form part of the experimental temperature range, a final *zeroing* shift factor can be added, such that the master curve formed at a temperature within the experimental range can be taken to another desired reference. Although not ideal, it is a useful approximation to overcome experimental limitations preventing data acquisition at particular temperatures. A check that can be performed to ensure this is accurate is to validate that the total shift factor is zero for the desired reference temperature.

2.4.4 Master curve

Once all of the individual isotherms are shifted using this cumulative shifting algorithm, a master curve is produced at the desired reference temperature as seen in Figure 2.9b. Regardless of relatively short isotherms consisting of few data points being used to construct the master curve, the fact that a smooth, continuous master curve has been produced as a result of the shifting process provides confidence in the method employed. A more detailed analysis into the accuracy of master curves constructed with short segment isotherms is provided in Chapter 4, §4.8.

2.5 Constitutive modelling

The constitutive modelling of polymers and their composites is challenging. Their rate and temperature dependence alone gives rise to several different mechanical responses. Above T_g the material exhibits rubbery behaviour, around T_g it is leathery and below T_g it is glassy, with potentially a ductile to brittle transition. Figure 2.10 shows the extent to which the polymer response can vary with temperature and strain rate, with vulcanised, unfilled natural rubber used as an example.

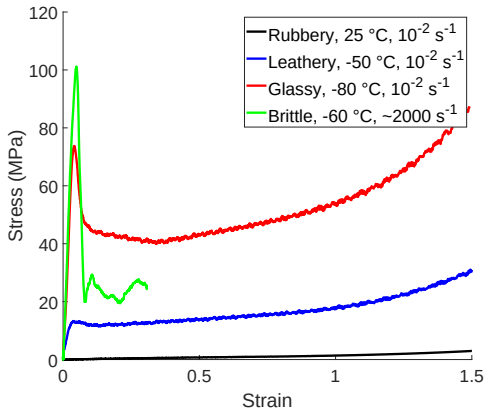

FIGURE 2.10: Depicting the broadly different mechanical responses of polymers.

Due to this, constitutive models describing the response must feature large strain rubber hyperelasticity, small strain viscoelasticity, viscoplasticity for the post-yield softening in glassy polymers and a suitable damage definition. Since the high rate response is adiabatic, the effect of self-heating on the mechanical properties must also be accounted for. When dealing with particulate composites, the enhancement of properties due to the presence of the filler needs to be described. This section outlines the models used in this thesis; chosen primarily for their simplicity in capturing the observed phenomenological behaviour, whilst lending themselves to facile calibration.

2.5.1 Hyperelasticity

For certain polymers, such as elastomers, or those showing a large strain non-linear elasticity, a linear elastic model like that of Hooke [79] does not capture the response well. In order to describe this behaviour, several non-linear hyperelastic models have been developed, including phenomenological models such as those of Mooney and Rivlin [136, 137] or those based on underlying macromolecular physics such as the tube model by Heinrich and Kaliske [138]. Many other models exist, broadly split into the phenomenological or mechanistic category, and are reviewed in [139, 140]. The two models considered in this study are the phenomenological Ogden model [141, 142] and the mechanistic 8-chain Langevin model [143]. These were selected for their simple numerical implementation and small number of parameters.

2.5.1.1 Ogden model

Ogden proposed a strain energy density function for incompressible, isotropic materials deformed under isothermal conditions. The function is then differentiated with respect to the strain in order to obtain stress-strain relations. The simplest version of this function is the so-called one term model in which the energy density is given by:

$$\phi = \frac{2\mu}{\alpha^2}(\mathrm{e}^{\alpha\varepsilon_1} + \mathrm{e}^{\alpha\varepsilon_2} + \mathrm{e}^{\alpha\varepsilon_3} - 3) \tag{2.14}$$

where μ relates to the shear modulus and α, the strain hardening exponent, reflects the hyperelastic convexity. The three principal strains are given by ε_i, where $i = 1, 2, 3$. Since most of the results in this research will be presented in terms of true stresses and strains, the strain energy density (Equation 2.14) is expressed in terms of true strain, as opposed to the stretch ratio, λ, as originally proposed [144]. The true strain and the stretch ratio are related by: $\varepsilon = \ln\lambda$. The true stress response for each principal strain is obtained by:

$$\sigma_i = \frac{d\phi}{d\varepsilon_i} - p \tag{2.15}$$

where p is the pressure. Although the pressure is unknown, it can be deduced by noting that for a uniaxial stress state, the principal stresses along the other two axes are zero, therefore:

$$\begin{aligned} \frac{2\mu}{\alpha}\mathrm{e}^{\varepsilon_2} - p &= \frac{2\mu}{\alpha}\mathrm{e}^{\varepsilon_3} - p \\ \mathrm{e}^{\varepsilon_2} &= \mathrm{e}^{\varepsilon_3} \end{aligned} \tag{2.16}$$

Furthermore, due to incompressibility, $\mathrm{e}^{\varepsilon_1}\mathrm{e}^{\varepsilon_2}\mathrm{e}^{\varepsilon_3} = 1$. Since $\mathrm{e}^{\varepsilon_2} = \mathrm{e}^{\varepsilon_3}$, it follows that $\mathrm{e}^{\varepsilon_2} = \mathrm{e}^{-\varepsilon_1/2}$. The strain energy function in Equation 2.14 therefore simplifies to:

$$\begin{aligned} \phi &= \frac{2\mu}{\alpha^2}(\mathrm{e}^{\alpha\varepsilon_1} + \mathrm{e}^{\alpha\varepsilon_2} + \mathrm{e}^{\alpha\varepsilon_3} - 3) \\ &= \frac{2\mu}{\alpha^2}(\mathrm{e}^{\alpha\varepsilon_1} + 2\mathrm{e}^{\alpha\varepsilon_2} - 3) \\ &= \frac{2\mu}{\alpha^2}(\mathrm{e}^{\alpha\varepsilon_1} + 2\mathrm{e}^{-\frac{1}{2}\alpha\varepsilon_1} - 3) \end{aligned} \tag{2.17}$$

The uniaxial stress can be obtained by differentiating this expression with respect to the strain:

$$\sigma_1 = \frac{d\phi}{d\varepsilon_1} = \frac{2\mu}{\alpha}\left(\mathrm{e}^{\alpha\varepsilon_1} - \mathrm{e}^{-\frac{1}{2}\alpha\varepsilon_1}\right) \tag{2.18}$$

The initial Young's modulus can then be found by:

$$E_\infty = \lim_{\varepsilon\to 0}\frac{d\sigma}{d\varepsilon} = 3\mu \tag{2.19}$$

2.5.1.2 8-chain Langevin model

Arruda and Boyce proposed a mechanistic model (shown diagrammatically in Figure 2.11) in which polymeric chains are located along the diagonals of the unit cell and deform with the cell. The chains meet at an interior junction point that remains centrally located.

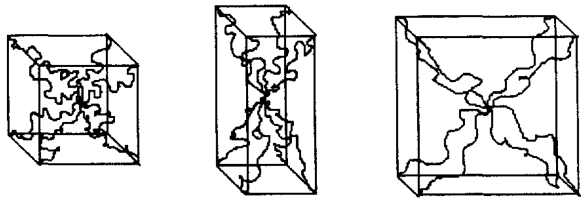

FIGURE 2.11: Schematic illustration of the unit cell deformation for the 8-chain model [139].

In this model, the stretch experienced by each chain is the root mean square of the stretch applied to the cell: $\lambda_{chain} = \sqrt{I_1/3}$, where $I_1 = \lambda_1^2 + \lambda_2^2 + \lambda_3^2$

Following the original theory of Kuhn on the Gaussian treatment of a randomly jointed chain [145], the strain energy function is given as:

$$\phi = \frac{1}{6} E_\infty (I_1 - 3) \tag{2.20}$$

where E_∞ is the long-term rubbery modulus. However, Gaussian chain statistics assume that the deformations are much smaller than the total chain length, and so models based on this treatment are only accurate to moderate levels of strain. To extend this to large strains, a non-Gaussian treatment was proposed [146], which forms the basis of the 8-chain model. In this case, the strain energy function is given as:

$$\phi = E_\infty \sqrt{N} \left[\beta_{chain} \lambda_{chain} + \sqrt{N} \ln \left(\frac{\beta_{chain}}{\sinh \beta_{chain}} \right) \right] \tag{2.21}$$

where $\sqrt{N}$ is the limiting chain extensibility based on random walk statistics. β_{chain} is given by the inverse Langevin function:

$$\beta_{chain} = \mathcal{L}^{-1} \left(\frac{\lambda_{chain}}{\sqrt{N}} \right) \tag{2.22}$$

where $\mathcal{L}^{-1}(x) = \coth x - x^{-1}$. The stress is subsequently given as:

$$\sigma = \frac{E_\infty}{3} \frac{\sqrt{N}}{\lambda_{chain}} \beta_{chain} \left(\mathrm{e}^{2\varepsilon} - \mathrm{e}^{-\varepsilon} \right) \tag{2.23}$$

where the term within the parentheses is based on the stress expression that would be obtained with the chain stretch described above and a 1D Neo-Hookean energy density function as shown in Equation 2.20.

2.5.2 Linear viscoelasticity

When a stress or strain is imposed on a solid material, if the internal structure is able to reorganise instantaneously, then it is said to be purely elastic. If the response is time dependent, then the material is described as viscoelastic. The phenomenological theory of linear viscoelasticity [147] well describes the models that will be used in the current research.

In terms of modelling linear viscoelasticity, the stress is decomposed into the elastic and viscous components through their representations as either springs or dashpots. A spring element has the constitutive equation $\sigma = E\varepsilon$, and the dashpot element $\sigma = \eta\dot{\varepsilon}$. Therefore the most basic equation for linear viscoelasticity is $\sigma = E\varepsilon + \eta\dot{\varepsilon}$; this was presented as early as 1874 by Meyer [148] and is commonly referred to as the Kelvin or the Voigt model, described symbolically as a spring element and dashpot element in parallel.

Other models are used, most notably the Maxwell model, which is a spring and dashpot in series. In isolation, the Maxwell model is not able to capture creep or recovery behaviour and the Kelvin-Voigt model is unable to capture stress relaxation behaviour. The simplest model that is able to achieve both of these is called the Standard Linear Solid (SLS) model, sometimes called the Zener model [149].

There are two variants of the Zener model: one is a Kelvin-Voigt model in series with a spring (see Figure 2.12: Top) and the other is a Maxwell element in parallel with a spring (see Figure 2.12: Bottom). They are both identical in their ability to capture the phenomenological viscoelastic effects, although their parameters differ.

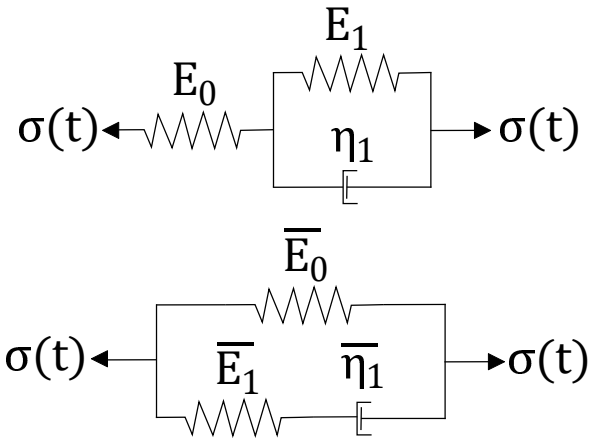

FIGURE 2.12: Top: Kelvin-Voigt in series with a spring. Bottom: Maxwell in parallel with a spring.

2.5.2.1 Prony series

Generalisations can be made to both of the above models by adding more Maxwell or Kelvin-Voigt elements. This is useful when the material response to be captured exhibits multiple relaxations, or often, a relaxation with a broad time spectrum. In Figure 2.13, a generalised Kelvin-Voigt model is shown in which more Kelvin-Voigt elements can be added in series. Likewise, Figure 2.14 shows more Maxwell elements can be added in parallel to the existing model.

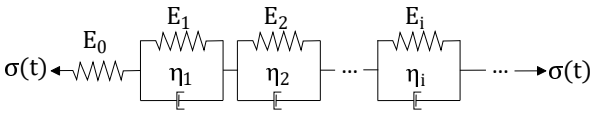

FIGURE 2.13: Generalised Kelvin-Voigt model.

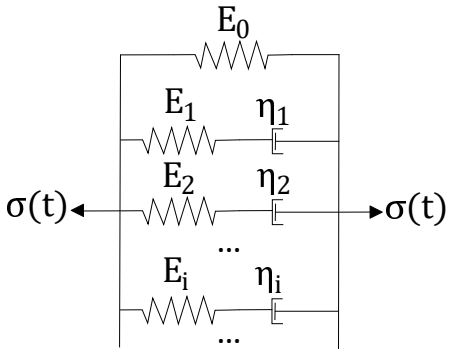

FIGURE 2.14: Generalised Maxwell model.

In order to define the modulus when using multiple elements chained together as above, a Prony series is conventionally used. Here, the modulus is defined as the sum of elements according to:

$$E = E_\infty + \sum_{i=1}^{N} E_i \mathrm{e}^{-t/\tau_i} \tag{2.24}$$

where E_∞ is the long term modulus, E_i is the modulus for an individual element, and τ_i (typically $= \eta_i/E_i$) is the relaxation time for that element. In this research, this type of definition would be fit to the master curve produced from the results of DMA experiments. The disadvantage with using this definition is that in order to get an accurate depiction of the modulus as it varies over a significant range of frequencies, a very large number of elements is needed. An alternative approach is to use a fractional definition.

2.5.2.2 Fractional derivative model

As mentioned in the previous section, one can use generalised SLS models with multiple Kelvin-Voigt or Maxwell chains in what is often called a Prony series. This is effective at allowing multiple relaxations to be captured easily, and in fact has been used by many of the previously mentioned researchers [150–153]. However, it is not desirable to use an increasing number of elements in the model to try and fit the experimental data better. In fact, with more elements, whilst the data may be more closely matched, the physical meaningfulness of the model is diluted and non-uniqueness of parameters becomes an issue. For this reason a fractional derivative model is a possible alternative.

The earliest progenitor of the idea that fractional time derivatives could be used for the purpose of modelling viscoelasticity was Nutting in 1921 [154]. In the 30s, Gemant observed that the stiffness and damping of viscoelastic materials were proportional to fractional derivatives of frequency [155] and could therefore be modelled with fractional time derivatives [156]. Applications of this were developed in the 60s by Caputo with his generalisation of the Kelvin-Voigt model to include fractional time derivatives [157, 158]. This was then extended in 1971 to the SLS model by Caputo and Mainardi [159].

Previously, the stress for a spring was given as $\sigma = E\varepsilon$, and the stress for a dashpot was $\sigma = \eta\dot{\varepsilon}$. In fractional viscoelastic models, a *springpot* is used instead of

a dashpot, with the following relation between stress and strain:

$$\sigma = \eta \frac{d^\beta}{dt^\beta} \varepsilon \tag{2.25}$$

The resulting constitutive relations can be solved using Laplace transforms or numerically using the Caputo integral definition [157] alongside a Mittag-Leffler function of order β [159]. Further information on fractional viscoelasticity can be found in the seminal text by Mainardi [160].

Linking this definition to physical underpinnings of macromolecular behaviour and thermodynamics was then presented by Bagley and Torvik in the 80s enhancing the credibility of the model [161, 162]. In 1999, Welch *et. al.* provided a numerical method to obtain solutions in the time domain for fractional time derivatives and compared results to various pre-existing models [163]. Numerical methods have since been further developed as observed in [164]. Simplifications to the model using half derivatives [165] and approximations to aid with obtaining solutions [166, 167] have also been proposed. Recently, applications to FEA have also been developed [168].

2.5.3 Hyper-viscoelastic models

If the material has rate and temperature dependence, but also large strain non-linear elasticity, then a model that has both hyperelastic and viscoelastic components can be used. Considering an additive case, the overall stress is the superposition of the hyperelastic stress (from say an Ogden or Mooney-Rivlin model) and the viscoelastic stress (from say an SLS or K-BKZ [169, 170] model). This seperability of the rate and large strain dependence has been applied to polyurea [150, 171], rubbers [172–174], foams [175, 176], other polymers [151, 177], and PBX [178, 179].

Indeed, an additive superposition of stresses from any combination of models is possible, to give simple representations of different material behaviours. This approach assumes that the models are situated in parallel, and that the strain in each is the same.

2.5.4 Viscoplasticity

To describe large strain, glassy behaviour, viscoplasticity must be included in the model. Haward and Thackray were amongst the first to model the post-yield flow behaviour of glassy polymers [180], albeit under isothermal conditions. Robertson [181] and Argon [182] both presented theories based on thermally activated processes. Richeton et. al. [120] added further degrees of freedom to allow the properties through a range of rates and temperature to be captured. Rate dependent plasticity has also been implemented with the Mulliken-Boyce (MB) model [183, 184], which is capable of relating the behaviour to underlying material transitions. This aspect makes it an ideal candidate to form the basis of viscoplasticity in this study as it has a good synergy with the results of the DMA experiment.

The MB model also includes the effects of thermal softening through adiabatic heating by explicitly increasing the temperature based on theoretical calculations [185]. However, its seamless integration into a framework with predictive capabilities at high strain rates, entirely calibrated at low strain rates, has not been fully explored and is therefore one focus of the current project.

2.5.4.1 Mulliken-Boyce model overview

In the approach initially proposed by Mulliken, the frequency dependence of each transition is used to shift modulus-temperature data obtained from DMA experiments at low frequencies to reconstruct the expected modulus-temperature curves at high strain rates. The materials studied by Mulliken and Boyce – much like those in the current study – had two transitions: the α (glass) transition, and the β (secondary) transition. Each transition is shifted independently to room temperature and then reconstructed to obtain the high rate behaviour at this temperature. The model then considers the contributions to the stress to be an additive sum of α and β components and the hyperelastic limiting behaviour: $\sigma = \sigma_\alpha + \sigma_\beta + \sigma_\ell$.

The α and β components themselves are both represented by a spring and viscoplastic dashpot, which correspond to the intermolecular resistance for each of these processes. The hyperelasticity is represented by a non-linear, non-Gaussian Langevin spring (as described in §2.5.1.2); one that requires extra stress to stretch out an incrementally larger amount, and corresponds to the entropic resistance to chain alignment (as shown diagrammatically in Figure 2.15). Not only is this an appropriate form as it captures the phenomenological hyperelastic behaviour observed experimentally, its basis on the physical limitation a polymeric chain can extend given its covalently bonded backbone is realistic.

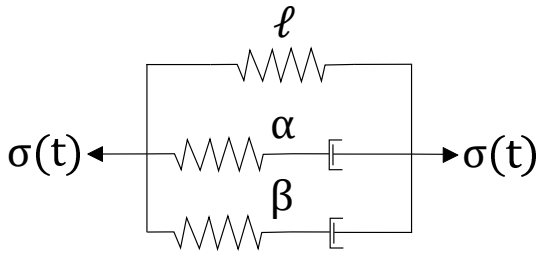

FIGURE 2.15: Schematic of the Mulliken-Boyce model.

The hyperelastic Langevin stress is calculated based on the network back-stress approach used in the Arruda-Boyce model [143] and shown above by Equation 2.23.

To work out the stress in either α or β component, one can consider the stress in the linear spring portion. In this manner, each of the α and β stress is given by $(i = \alpha, \beta)$:

$$\sigma_i = E_i \varepsilon^e \tag{2.26}$$

where E_i is the modulus and ε^e is the elastic strain. The total strain across each of the elements is identical for compatibility reasons, and a constant strain rate is assumed, which is decomposed into elastic and plastic components: $\dot{\varepsilon} = \dot{\varepsilon}_i^e + \dot{\varepsilon}_i^p$. Taking time derivatives of Equation 2.26, it is possible to obtain the total stress rate as: $\dot{\sigma}_i = E_i(\dot{\varepsilon} - \dot{\varepsilon}_i^p) + \dot{E}_i(\varepsilon - \varepsilon_i^p) \approx E_i(\dot{\varepsilon} - \dot{\varepsilon}_i^p)$. Though the modulus is time-dependent, the stress rate is dominated by the first term as the product of the rate

of change of modulus (in the range of experimental interest) and the strain is several orders of magnitude smaller. In any case, the model will take into account the temporal relaxation of the modulus. The plastic shear strain rate in the viscoplastic dashpots can be given by:

$$\dot{\gamma}_i^p = \dot{\gamma}_{0,i}^p exp\left[-\frac{Q_i}{k\theta}\left(1 - \frac{\tau_i}{s_i + \alpha_{p,i}p}\right)\right] \tag{2.27}$$

where $\dot{\gamma}_0^p$ is the pre-exponential factor proportional to the attempt frequency; Q is the activation energy; k is Boltzmann's constant; θ is the absolute temperature; τ is the shear stress in the dashpot; s is the athermal shear strength, an internal variable that models the post-yield strain softening behaviour; α_p is the pressure coefficient dictating the pressure (p) dependence. The rate at which the athermal shear strength evolves is given by:

$$\dot{s}_i = h_i \dot{\gamma}_{0,i}^p \left(1 - \frac{s_i}{s_{ss,i}}\right) \tag{2.28}$$

where h is the softening slope and s_{ss} is the preferred steady state value. The initial value is defined as: $s_{0,i} \equiv 0.077\mu_i(1-\nu)^{-1}$, where μ is the shear modulus; and ν is the Poisson's ratio. In this research, the Poisson's ratio is assumed to be 0.5 due to an incompressibility assumption. This is valid in the majority of cases in the current study, breaking down only at larger strains, where damage and irrecoverable volume changes can occur. The plastic normal strain rate can be calculated by: $\dot{\varepsilon}_i^p = \dot{\gamma}_i^p/\sqrt{3}$, based on the von Mises equivalent strain under shear loading.

2.6 Summary

In this chapter, contextual information was provided about the nature of this project, the current state of the art, and more importantly, where improvements can be made. Experimental techniques for characterising the high rate response can be enhanced for understanding the behaviour of soft polymers and their composites under a variety of loading conditions. Furthermore, novel modelling frameworks can be introduced avoiding high rate parameter calibration, and allowing features such as the effect of adiabatic self-heating on the modulus to be better integrated into a predictive approach.

One of the major aims of this project is to calibrate as many of parameters as possible for constitutive modelling of high strain rate behaviour using the results of simple, low strain rate experiments. This would enable the use of time-temperature superposition based modelling frameworks to enhance the predictive capability of the model, whilst minimising the number of apparatus and experiments required at high strain rates. Another desire is to make the modelling process as simple as possible, minimising the number of parameters in the model. The chapters that follow will discuss the progress in implementing the enhancements proposed and the research achievements so far in understanding the high rate behaviour of particulate composites.

2.7 Outline of remaining thesis

The main aim of the research presented in this thesis is to better understand the high strain rate mechanical properties of particulate composites. As the mechanical response of these materials is sensitive to rate and temperature, they must be experimentally characterised at various strain rates and temperatures, interrogating their dependences. In polymer composite materials, the rate and temperature dependence originates from the polymeric binder, which motivates the starting place for this research.

Chapter 3 presents the experimental characterisation for a typical soft polymer that may be used as a binder: neoprene rubber. The chapter also presents a preliminary hyper-viscoelastic modelling framework, based on the observed rate-temperature equivalence in mechanical properties, that enables the high rate behaviour of neoprene to be captured.

Limitations of this modelling framework include: that it only captures the elastic loading of the material; and that an isothermal compression is assumed, so the temperature rise that accompanies high rate deformation is not included.

Chapter 4 shows how plasticity and the effects of adiabatic self-heating can be addressed in the modelling framework, with applications to (plasticised) PVC. A Mulliken-Boyce model is used as a base to incorporate viscoplasticity, as it is based on the superposition of stresses arising from individual polymer processes. This formulation of the model has synergies with the DMA experiments used to characterise the viscoelasticity, which also breaks down the response into contributions from individual processes: the glass (α) and the secondary (β) transitions. To exploit this synergy, a fractional derivative model is used to describe the viscoelasticity instead of the classic Prony series, so that each material transition can be mapped directly to each element in the Mulliken-Boyce model.

The temperature dependent heat capacity is measured, which is subsequently used to characterise the temperature rise due to self-heating, assuming a complete conversion of plastic mechanical work to heat. This temperature rise is then related to the thermal

relaxation of the elastic modulus. Accompanying the temporal relaxation, this $E(t, T)$ allows the high rate response to be better captured.

In order to enhance the predictive capability of the modelling framework, its parameters are all calibrated with data from quasi-static experiments performed at different temperatures. In this manner, the modelling framework presented in Chapter 4 can be used to *predict* the high rate behaviour of (plasticised) PVC. The model is also useful in the simulation of adiabatic experiments, by artificially inputting a temperature rise to the response of quasi-static, low temperature simulated responses.

Limitations to the research presented in this chapter are: that the modelling framework does not take into account any damage; and that as it stands, it would not be able to predict the response of particulate composites. Suitable modifications to the modelling framework would be required.

To move towards the modelling of particulate composites, the mechanical response of the binder polymer and the composites need to be experimentally characterised. **Chapter 5** presents the results of, and insights derived from, experiments performed on unfilled and glass filled natural rubber. Natural rubber was selected as a model material as both unfilled and filled variants are widely used in engineering applications. Its rubbery – through to glassy – response provides an interesting challenge for the experimental characterisation under dynamic loading.

In this chapter, experimental technique developments are also presented, including: the enhancement of capability to the SHPB allowing low temperature, high rate experiments to be conducted; and an update to the methodology of conducting DMA experiments on soft polymers, to obtain high quality data for use in TTS.

By using different grades of particulate composites, the effect of filler volume fraction and mean particle diameter to the mechanical response is investigated. Further observations are based on: rate-temperature equivalence; enhancement of mechanical properties due to filler enhancement; strain activated damage; and *post-mortem* retrieved samples. The experimental insights give confidence that a TTS based modelling approach can be used to predict the high rate response of unfilled and filled

natural rubber.

Finally, **Chapter 6** presents the development of TTS based modelling frameworks that allow the ambient high strain rate response of unfilled and filled natural rubber to be predicted. This presents a significant achievement, as to the author's knowledge, the prediction of the full stress-strain response under these conditions using a model wholly calibrated with quasi-static data has not previously been presented. The sub-ambient high rate response of the particulate composites can also be captured, with suitable model adaptations, to include the brittle failure present under these conditions. However, due to the current damage definitions used, it was not possible to predict their high rate responses, and is therefore a proposed area for future research.

In summary, this body of research provides contributions made in better understanding the high rate properties of amorphous polymers and their particulate composites, and developments of novel modelling frameworks that enable the user to predict the high strain rate behaviour of these materials by using experimental insights obtained, and models calibrated, at low strain rates.

3 Preliminary experiments and proposed modelling framework

Before the high rate mechanical behaviour of particulate composites is predicted, it is important to characterise and predict the behaviour of the constituent matrix material — a soft, often rubbery polymer.

Rubbery polymers are widely used in engineering applications, such as vibration isolators and seals, in which they may be subjected to impact loading leading to high strain rate deformation. This resulting deformation may occur at a variety of temperatures, notwithstanding the self-heating of the material. For this reason, it is necessary to study the mechanical behaviour of these materials over a range of loading conditions. The strong rate and temperature dependence of their properties provides a further motivation for this understanding.

In this chapter, the relationships between the response of a neoprene rubber at various strain rates and temperatures are investigated, and a simple model making use of the time-temperature superposition (TTS) principle proposed to describe the material behaviour. As it is challenging to obtain high rate data on rubbery materials using conventional apparatus, such as the split-Hopkinson pressure bar (SHPB), the simple two parameter hyperelastic model, combined with a viscoelastic model, proposed here provides a useful complementary tool to interrogate the response.

3.1 Introduction

Many polymers, including neoprene rubber, exhibit strong temperature and rate dependence in their mechanical responses, including modulus and yield strength [186, 187]. Inhibitions in various molecular motions increase this sensitivity with decreasing temperature and increasing rate [188], i.e. as the material passes through the glass transition. However, experimental characterisation at high strain rates (above c. 500 s^{-1}) can be challenging.

In the past, time-temperature superposition has been used as an alternative method to validate high rate data [1]. The mechanical response at high rates was shown to be the same as that at low temperatures. Therefore, inhibitions to micromolecular movement were inferred to be analogous. Much of the constitutive modelling based on these observations has tended to focus on predicting single values such as the yield stress [189, 190], or made use of a large number of parameters [191, 192]. The research presented in this chapter provides the reader with a simple model, with minimal parameters, that can capture the mechanical response of neoprene rubber under compression at a variety of strain rates and temperatures.

3.2 Material

Since being invented by DuPont scientists in the early 1930s [193], neoprene (or polychloroprene) has been widely used in many applications. Although this study focusses on the energy absorbing capabilities of polymers and their composites, neoprene can also be found in applications as diverse as aquatics, consumer goods, sealants, coatings, and even fashion. High rate applications include padding for personal protective equipment, protective flooring and vibration isolators. The reason for its broad use is its range of favourable properties. It resists degradation more than natural rubber, so is more durable and long-lasting. It also resists fire better than pure hydrocarbon

rubbers. It is very pliable, highly insulating, and can be made into foams, which, depending on whether closed-cell or open-cell, can be made to be either waterproof or breathable.

The material used in this investigation was a commercial black neoprene rubber supplied by Brammer, UK in the form of a 5 mm thick sheet. There is no specific reason for the selection of neoprene rubber over other rubbers for this preliminary investigation other than its availability at the time of the investigation. The molecular structure of neoprene is depicted in Figure 3.1.

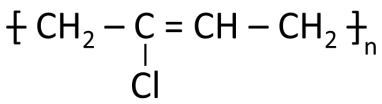

FIGURE 3.1: Molecular structure of neoprene rubber.

3.3 Compression experiments

The stress-strain relationship of many polymers (including neoprene rubber) is dependent on the applied strain rate and temperature. For this reason, in order to experimentally characterise the neoprene rubber in this study, compression experiments at various strain rates and temperatures are conducted using apparatus and techniques that will be described in more detail in this section.

3.3.1 Specimen geometry

For the series of compression experiments, right circular cylindrical samples with diameter and length of 5 mm were carefully machined from the sheet. This is done by using a bespoke cutter with a 5 mm diameter hole and 0.05 mm tapered cutting edge, which is inserted into a milling chuck and operated at a speed of c.200 RPM. This size was chosen based on geometry constraints in the high rate experiments. A soap/water mix was used for cooling and lubricating to ensure there was not a substantial increase in temperature during machining affecting the polymer microstructure, which can be

verified using DSC experiments. A common alternative is to punch out samples using a suitable die; however, stresses during the punching process result in specimens resembling conical frustums, and as such, this method was avoided. The difference between the two geometries is shown in Figure 3.2.

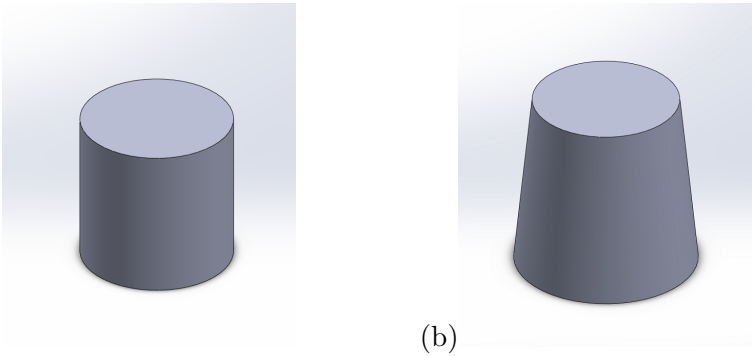

(a) (b)

FIGURE 3.2: (a) Specimen that can be produced by careful machining, and (b) deformed specimen that results from the punching process.

3.3.2 Low rate experiments

For the low strain rate characterisation of the neoprene rubber, three experiments were performed at each of the following strain rates: 10^{-3} s^{-1}/10^{-2} s^{-1}/10^{-1} s^{-1}. The maximum deformation for these experiments was 4 mm, leading to an engineering strain of 80%. These were conducted on a commercially available Instron 5980 Series electromechanical static testing machine with 2580 Series load cells and custom-built supports and loading anvils.

This apparatus has an axial stiffness of 275 kN mm^{-1} and testing speed range of $0.0001 - 1016$ mm/ min. Its force measurement accuracy with the load cell is $\pm 0.5\%$ of the reading down to 1/1000 of the load cell capacity, displacement measurement accuracy the greater of ± 0.01 mm or 0.5% of the displacement and the testing speed accuracy $\pm 0.1\%$ of the set speed [194].

For room temperature quasi-static experiments at the three strain rates, the load did not exceed 1.5 kN. For this reason, a 5 kN load cell was sufficient to record the force. At these low loads, compliance corrections are not necessary: preliminary experiments showed rig compliance to be negligible. However, in any case, an extensometer was

attached to the anvils, close to the specimen and used to provide strain measurements and closed loop control. As the uniaxial test progresses and the upper section of the rig moves downwards compressing the specimen, the speed of the crosshead decreases to maintain a constant true strain rate. In this study, an Instron 2620 Series dynamic strain gauge extensometer with a 12.5 mm gauge length and ±5 mm travel was used. The gauge requires an operating force of 1.5 N, and as it is mounted to the loading anvils, the stiffness contribution by these gauges is insignificant under these loading conditions. An image of the set-up, albeit within an environmental chamber, is shown in Figure 3.3.

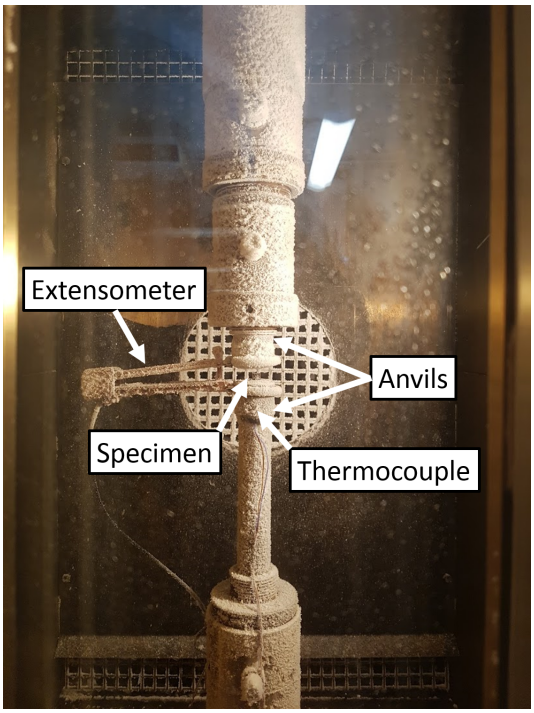

FIGURE 3.3: Environmental chamber set-up on the Instron apparatus for low strain rate, varying temperature experiments.

3.3.2.1 Varying temperature experiments

Varying temperature compression experiments were conducted at a constant true strain rate of 10^{-2} s^{-1} and temperatures from −100 °C to 80 °C in 20 °C increments using an Instron 3119-600 Series environmental chamber. This chamber features a Eurotherm

3208 temperature controller with closed loop control provided by a Type N thermocouple inside the chamber to monitor the temperature. It has a nominal temperature range of −80 °C to 350 °C.

For experiments at sub-ambient temperatures, the chamber was connected to a liquid nitrogen dewar. The cold nitrogen gas is fed into the chamber and convected to cool the interior (Figure 3.4). For super-ambient temperatures, the chamber's in-built forced convection heater was used.

(a)  (b) 

FIGURE 3.4: (a) Liquid nitrogen dewar used for the Instron environmental chamber, and (b) gaseous nitrogen fed into the chamber.

The temperature accuracy of the chamber is quite poor at ±3.5 °C [195]. Furthermore, its thermocouple is situated towards the back of the chamber and not near the specimen, so it does not give an accurate value of the specimen temperature. In order to measure the temperature close to the sample, with a ±1 °C accuracy, a second thermocouple was integrated into the loading platen. Each sample was held at temperature for a minimum of 30 minutes to ensure thermal stability. The holding time is significantly longer than the time scale for diffusion based on the thermal diffusivity of neoprene rubber at room temperature [196], and is therefore at equilibrium. The experiment

was started only once the two thermocouple readings were within 0.5 °C of each other, ensuring that the temperature is stable inside the chamber. For experiments below the glass transition (T_g) of neoprene, the force required to deform the material increases significantly, so a 50 kN load cell was used.

3.3.2.2 Results and analysis

The results of the quasi-static experiments on neoprene rubber are shown in Figure 3.5a and the results of the varying temperature experiments are shown in Figure 3.5b. In these graphs, the stress-strain relationship for each experiment is shown to better visualise the experimental variation.

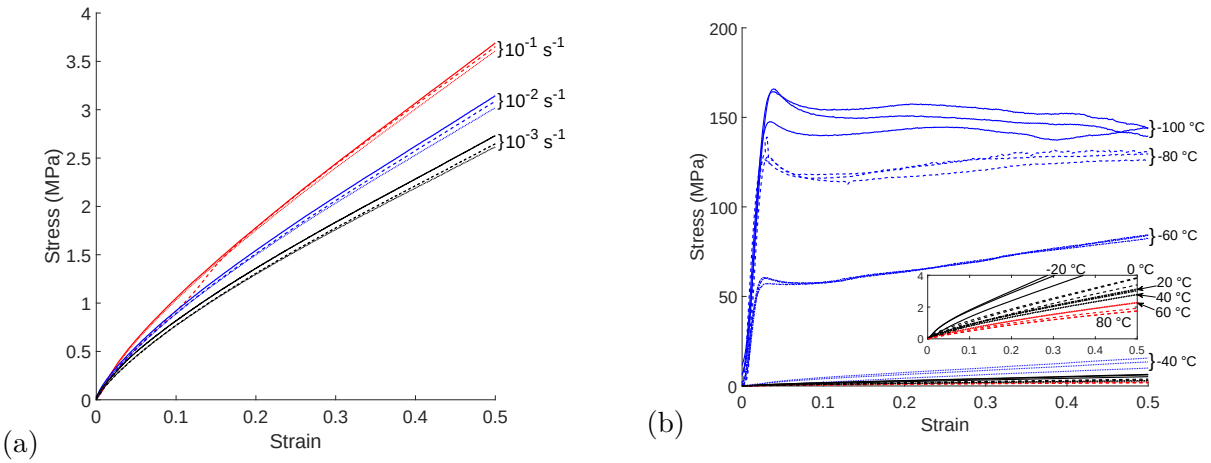

FIGURE 3.5: (a) Results from three varying rate quasi-static experiments, with three repeats, conducted on neoprene rubber at a constant temperature (20 °C), and (b) results from varying temperature experiments conducted at a constant strain rate (10^{-2} s^{-1}).

These graphs provide confidence on the repeatability of the quasi-static experiments as there is little variation between experiments. Thermal expansion is taken into account by firstly holding the specimen in the chamber until in equilibrium, and secondly by applying a small (c.10 N) pre-load prior to commencing the test. However, there is a slight spread at the lowest temperatures. This is as the properties are more temperature dependent, so small changes in temperature give larger changes in response. As the temperature decreases and the neoprene is tested below its T_g, any small defects induced by the specimen machining process or intrinsic material variation has a more noticeable

effect on the strength. This would be even more obvious at higher strains, but up to the moderate levels in this study, the variations are low.

Strain-time plots for the constant temperature, varying rate experiments are shown in Figure 3.6. The strain rate for each experiment was obtained based on the calculated slope for the section of the $\varepsilon - t$ curve from $0.2\varepsilon_{max} - 0.8\varepsilon_{max}$, where ε_{max} is the maximum true strain of the experiment. The rates for repeat experiments were averaged to obtain the mean true strain rate. As can be seen, and as expected, the Instron 5980 with its true strain controller is able to closely match the desired true strain rate for quasi-static experiments.

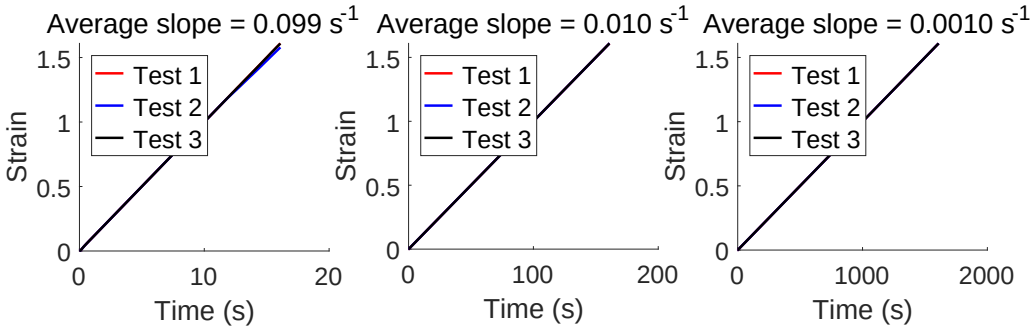

FIGURE 3.6: True strain versus time profiles for constant temperature, varying rate experiments, identifying the average true strain rate.

Strain-time plots for the varying temperature, constant rate experiments are shown in Figure 3.7. These experiments were performed at a strain rate of 10^{-2} s^{-1} and despite being conducted at various temperatures, the true strain control was still able to maintain the desired rate. Only in the -100 °C case did the average strain rate deviate from the desired 10^{-2} s^{-1} to 9.6×10^{-3} s^{-1}. This was an insignificant change in true strain rate, as the mechanical properties investigated typically change with $\log \dot{\varepsilon}$.

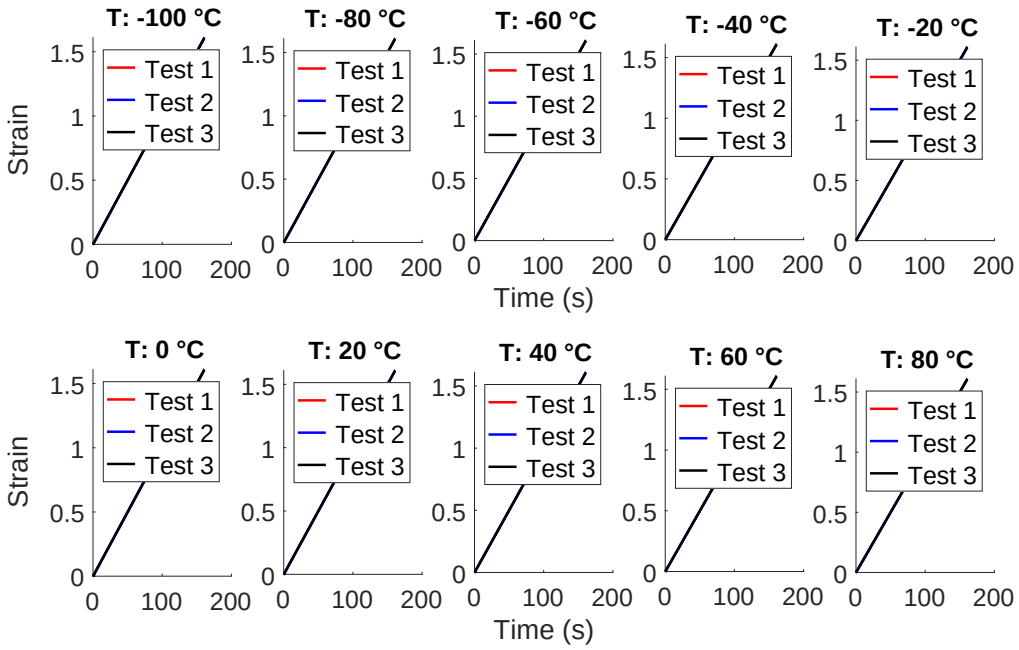

FIGURE 3.7: True strain versus time profiles for varying temperature, constant rate experiments.

3.3.3 Medium rate experiments

The speed limitations with the Instron static testing machine meant that the maximum speed of 1016 mm/ min was only sufficient to give an average engineering strain rate of around 4 s^{-1} with a maximum deformation of 4 mm. Although it is conceivable to investigate the compressive behaviour at a strain rate of 1 s^{-1} using the Instron machine, in order to characterise the compressive behaviour at intermediate strain rates (1 s^{-1} – 100 s^{-1}), a custom-built hydraulic loading frame was used. Details of this loading frame are given in the previous chapter.

3.3.3.1 Results and analysis

The results of all three of the medium rate experiments at each of the rates are shown in Figure 3.8. The intention was to conduct three experiments, each at: 1 s^{-1}, 10 s^{-1}, and 100 s^{-1}.

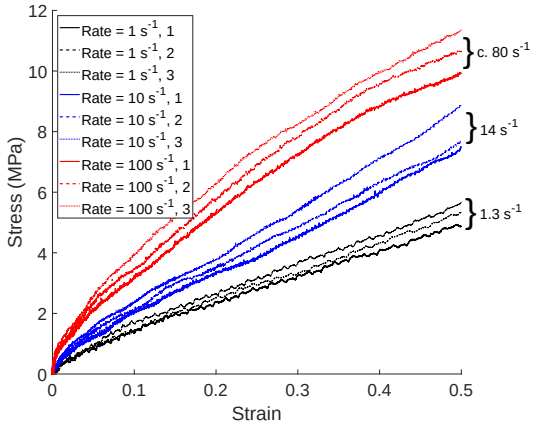

FIGURE 3.8: Results from varying rate hydraulic experiments conducted at a constant temperature (20 °C), highlighting the difference between intended and achieved strain rates.

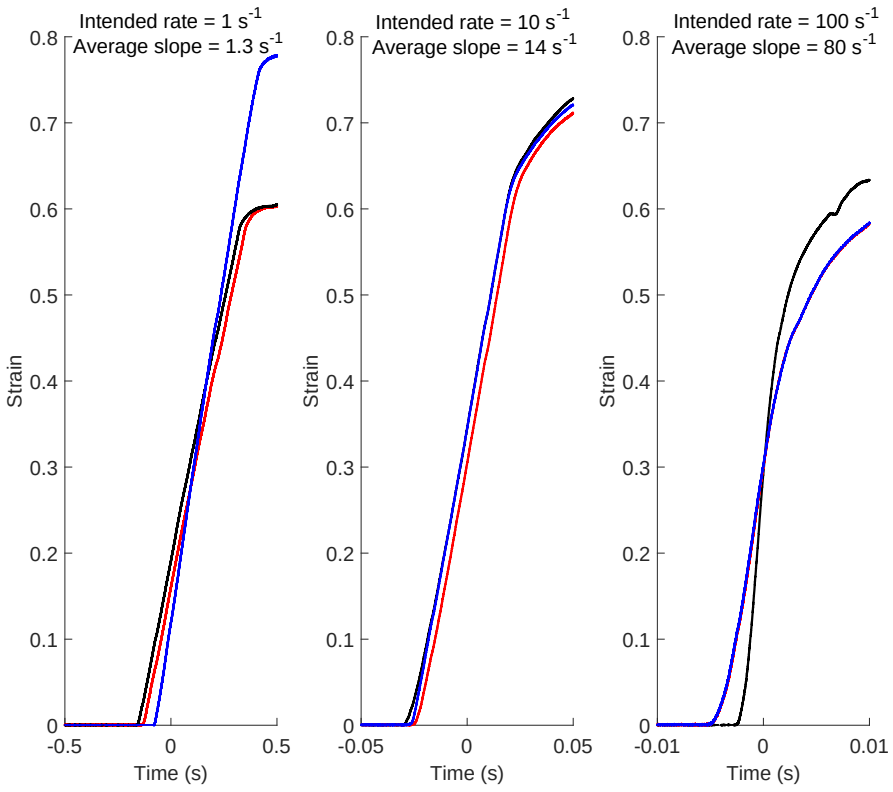

FIGURE 3.9: Comparison of the intended and measured strain rates.

Because this system does not have a closed loop control system, it is important to check the strain-time profiles for the experiments (Figure 3.9). At the lower end, the hydraulic press was able to achieve the desired strain rates, but it was not able to produce a strain rate of 100 s^{-1} accurately. Furthermore, there is more variation between repeated

experiments at medium rates compared to low rates. As with low rate experiments, the true strain rate for each experiment was calculated from $0.2\varepsilon_{max} - 0.8\varepsilon_{max}$ of the $\varepsilon - t$ curve. Although 100 s^{-1} was not achieved, data at 80 s^{-1} are still valuable as the material properties vary as $\log \dot{\varepsilon}$.

3.3.4 High rate experiments

For compression experiments at strain rates of the order 10^3 s^{-1}, an in-house split-Hopkinson pressure bar (SHPB) was used. This is a well established method to perform dynamic compression experiments at high strain rates and full details of the analysis procedure for SHPB testing of soft materials can be found in Gray and Blumenthal [197].

In these experiments, Ti-6Al-4V alloy bars with a diameter of 12.7 mm were used. The striker bar was 400 mm long, the input bar was 1000 mm long and the output bar was 500 mm long. The striker bar was able to reach speeds up to 20 $m\,s^{-1}$, corresponding to an average strain rate of around 4×10^3 s^{-1}. The input and output bars were instrumented with both strain gauges and piezoelectric gauges. Where the signal from the strain gauge is weak, the piezoelectric gauge signal can be used instead. Its voltage signal is amplified and converted into a force in a similar manner to the strain gauge.

In order to reduce inertial effects, right circular cylindrical specimens were used as described in §3.3.1. Each specimen was sandwiched between the input and output bars with a thin layer of petroleum jelly applied at the interfaces to reduce friction. No barrelling was observed upon immediate inspection after the experiment. In future, a high speed video camera can be used to validate this during the experiment, but previous studies have shown petroleum jelly to be an adequate lubricant [198].

3.3.4.1 Results and analysis

Results of three SHPB experiments conducted at a starting temperature of 20 °C are shown in Figure 3.10.

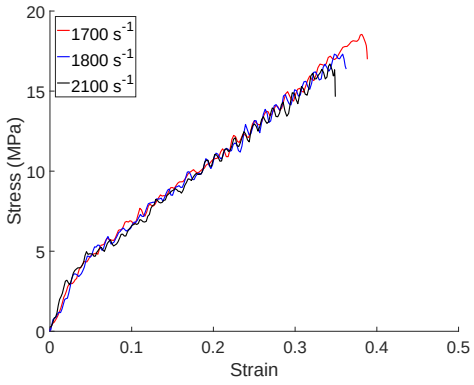

FIGURE 3.10: Results from the SHPB experiments on neoprene rubber at 20 °C.

As seen in the stress-strain profiles, there is considerable noise in the measurements from Pochhammer-Chree vibrations leading to the oscillatory results. In future experiments, a pulse shaper will be used between the striker and input bars. This reduces the high frequency components in the loading pulse and increases the rise time of the incident wave, thereby reducing the initial acceleration of the specimen and effectively *cushioning* the impact. The overall effect would be to produce smoother stress-strain curves.

Strain-time plots for the high rate experiments are shown in Figure 3.11. It is evident that even at these high strain rates, a fairly constant true strain rate has been achieved. This rate has been calculated from $0.2\varepsilon_{max} - 0.8\varepsilon_{max}$ of the $\varepsilon - t$ curve as before.

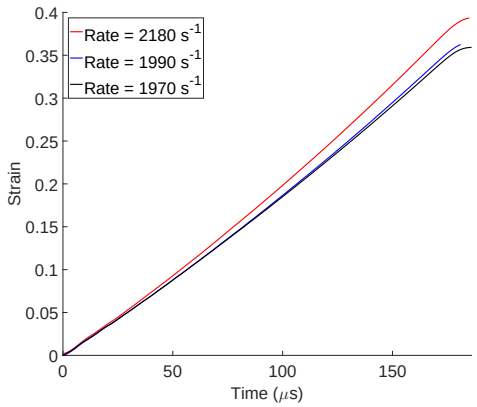

FIGURE 3.11: True strain versus time profiles for high rate experiments, identifying the true strain rate.

3.4 Dynamic Mechanical Analysis

Dynamic Mechanical Analysis (DMA) experiments were performed in order to quantify the response of the material in terms of its temperature and frequency dependent storage and loss moduli. The storage modulus relates the component of stress that is in phase with the applied oscillatory strain; the loss modulus, that which is out of phase.

3.4.1 Experimental method

For these experiments, rectangular samples were cut from the rubber sheet with dimensions 50 × 10 × 5 mm. These experiments were conducted on a TA Instruments Q800 apparatus, and all were in the dual cantilever configuration. Full calibration of the apparatus and clamp were performed in accordance with the manufacturer's protocol prior to data acquisition. An oscillatory amplitude of 0.1% strain was implemented with an isothermal frequency sweep in 2 °C temperature increments from −50 °C to 80 °C. The following frequencies were used with the intention they would be reasonably well spread out in the log domain: 0.5, 2, 5 and 10 Hz. This broadly corresponds to strain rates from 3.2×10^{-3} s^{-1} to 6.4×10^{-2} s^{-1}.[1]

3.4.2 Results and analysis

Storage and loss moduli curves at the four frequencies in the temperature range stated above are presented in Figure 3.12a.

From these results, it can be observed that there is a glass (α) transition centred just under −35 °C, where the storage modulus drops by two orders of magnitude. The loss modulus also approaches a peak at this temperature. This transition relates to restricted molecular motions of larger segments of the polymer backbone.

[1] The frequency can be approximated into a strain rate by considering a quarter cycle of a sinusoidal DMA loading profile. The time duration of a quarter cycle is simply $1/4f$ and the peak strain, ε_0, is prescribed in the experimental set up. By assuming a linear rise in strain over this quarter cycle, $\dot{\varepsilon} = 4f\varepsilon_0$.

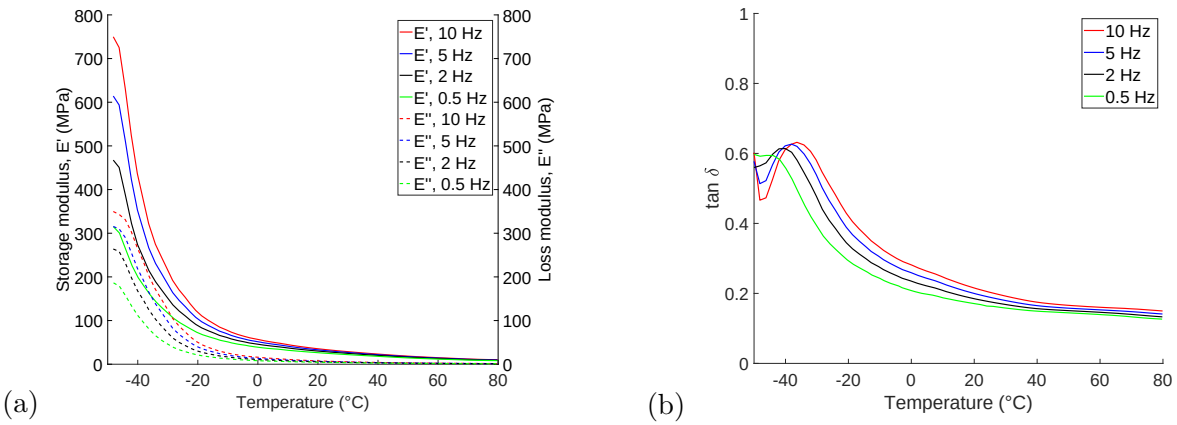

FIGURE 3.12: (a) Results from the DMA experiments conducted for neoprene rubber at 0.5, 2, 5 and 10 Hz for a temperature range from -50 °C to 80 °C, and (b) loss tangent ($\tan\delta$) as a function of temperature and frequency.

By observing the shift of the loss tangent peak to higher temperatures with increasing frequency, a shift factor can be assigned. Data in Figure 3.12b at -50 °C are not accurate and are experimental artefacts. Based on the results shown in Figure 3.12b, the observed shift factor based on this simplistic method is around 9 °C per decade of frequency/strain rate or 0.1 decades per °C. Alternative measures of the shift factor will be discussed later.

3.5 Discussion of rate and temperature dependence

3.5.1 Varying rate experiments

Three experiments were performed at each strain rate for the Instron and hydraulic press apparatus, and three experiments in total for the SHPB at impact speeds of approximately 10 $\mathrm{m\,s^{-1}}$. The results of these repeated experiments are plotted as shown in Figure 3.13. Since neither a constant true strain rate nor closed loop control was possible on the hydraulic press, as it was on the Instron machine, it should be noted that the actual strain rates as documented in Figure 3.13 varied from the intended ones.

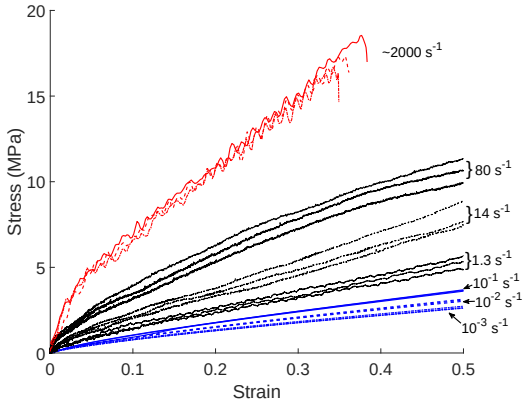

FIGURE 3.13: Results from compression experiments for varying strain rates at a constant temperature (20 °C).

It is clear that as the strain rate increases, the stress at a given value of strain is higher. However, the variation in stress is less prominent at the lowest strain rates, than at intermediate rates. In quantifying this, we consider the percentage difference in the characteristic stress (σ_c, the value of stress where $\varepsilon = 0.1$). At the lowest strain rates (10^{-3} $\mathrm{s^{-1}} - 10^{-1}$ $\mathrm{s^{-1}}$), σ_c increases from 0.79 MPa to 1.00 MPa representing a 27% rise. At intermediate strain rates (1.3 $\mathrm{s^{-1}}$ – 80 $\mathrm{s^{-1}}$), there is a 120% rise from 1.54 MPa to 3.43 MPa. This shows a greater sensitivity to rate in the intermediate range.

An explanation of this can be provided if we consider a flexible molecular chain model for polymers [199]. The increase in stress with strain rate is due to the time-scale for sub-molecular chain motions, like rotations, decreasing as the rate increases. The low strain rate limit stress is that of viscous flow and the high strain rate limit

stress arises from the maximum instantaneous stress, when there has been no time for any viscous effects.

The characteristic time-scale for these conformational motions at 20 °C can be inferred from the master curve shown later in Figure 3.17a. It is essentially found by inverting the frequency at which the storage modulus starts to significantly increase.

3.5.2 Varying temperature experiments

For the varying temperature experiments, the strain rate was kept constant at 10^{-2} s^{-1}; three tests were performed at each temperature. These results are shown again in Figure 3.14.

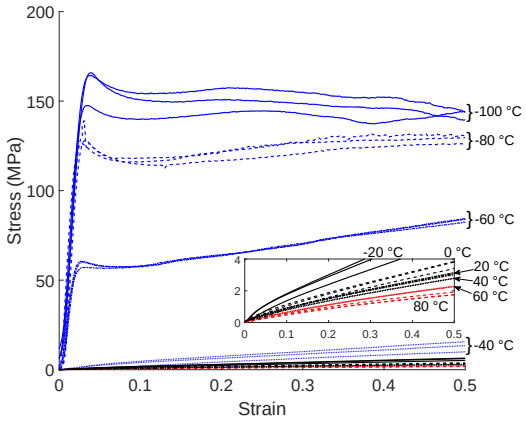

FIGURE 3.14: Results from varying temperature experiments conducted at a constant strain rate (10^{-2} s^{-1}).

The mechanical response of the neoprene rubber down to temperatures of −40 °C is largely similar to the super-ambient cases, despite showing a small increase in stress with decreasing temperature. However, the response undergoes a drastic change as the temperature decreases below −40 °C. The behaviour transitions from rubbery above this temperature to glassy below this temperature: the differing responses indicate the approximate value and effect of the T_g for neoprene rubber.

Considering the same flexible molecular chain model as in the previous section, the stress increase is due to the decreased temperature inhibiting cooperative segmental

motion. This inhibition means a higher force is required for deformation. During deformation, the strain is accommodated through the slipping and unravelling of polymer chains. At higher temperatures, the material has considerable flexibility and can conform to many configurations minimising free energy and thus a lower deforming force is required.

3.5.3 Rate-temperature equivalence

It is clear that stress increases with increasing strain rate, Figure 3.13, and with decreasing temperature, Figure 3.14. For the response at a particular high strain rate, is there a corresponding temperature where the low strain rate response is the same? In answering this question, we construct a graph plotting a characteristic stress, σ_c, against the logarithm of the strain rate and the inverse of the temperature (Figure 3.15). By inverting the temperature axis, the similarities between the two dependences are clearer.

This figure allows the reader to qualitatively appreciate that there exists a certain temperature at which the low strain rate compression response corresponds to the high strain rate response at an ambient temperature. For example, in principle, if the characteristic stress, σ_c, was desired at a strain rate of 10^3 s^{-1}, no further high rate experiments are required, as the value can simply be predicted by conducting a low strain rate (10^{-2} s^{-1}) experiment at a temperature of around -30 °C. This equivalence forms the basis of the time-temperature superposition (TTS) technique.

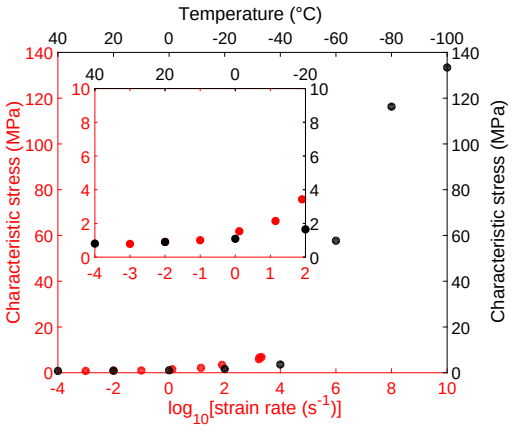

FIGURE 3.15: Equivalence between ambient, high strain rate and sub-ambient, low strain rate experiments.

3.5.4 Time-temperature superposition

As discussed in the previous chapter, the modulus at a lower temperature is analogous to that at a higher frequency. Therefore, it is possible to construct a single graph at a reference temperature to show the full array of analogous responses. Here the reference temperature is selected to match that of the varying rate compression experiments, 20 °C. In order to construct this *master curve*, isotherms from Figure 3.16a are shifted to the left if they are higher than the reference temperature (results analogous to lower frequencies) and shifted to the right is lower than the reference temperature (results analogous to higher frequencies). Therefore, at each temperature other than the reference, a certain *shift factor* is required to move the isotherm such that it overlaps other (shifted) isotherms to create one continuous curve of the response — the master curve. The shift factors required are shown in Figure 3.16b and the resulting master curve is shown in Figure 3.17a.

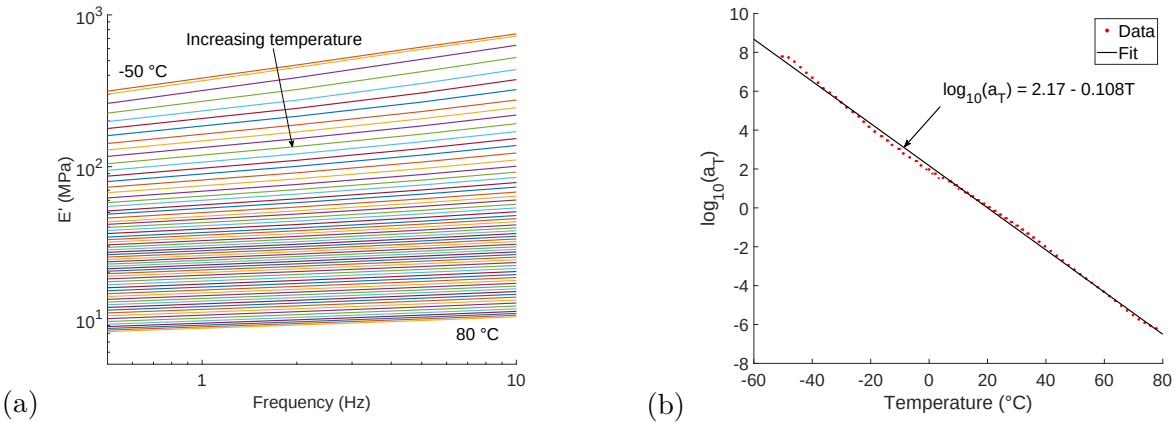

FIGURE 3.16: (a) Isotherms showing the frequency and temperature dependence of storage modulus and (b) shift factors required to move these to construct a master curve for neoprene rubber.

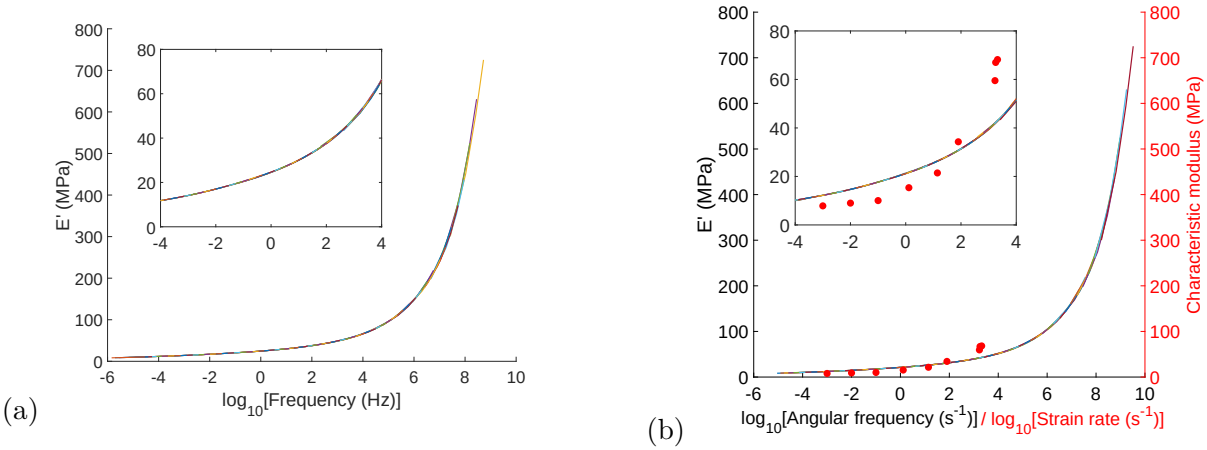

FIGURE 3.17: (a) Master curve for neoprene rubber at a reference temperature of 20 °C, and, inset, highlighting experimentally relevant frequencies; and (b) comparing the rate-temperature equivalence for the modulus with the characteristic stresses in Figure 3.15.

The characteristic moduli shown in Figure 3.17b, is approximated as $E_c = \sigma_c/\varepsilon_c$, where σ_c is the characteristic stress, and $\varepsilon_c = 0.1$, the value of the strain. This linear assumption gives a facile method to compare the rate-temperature equivalences inferred from the characteristic stresses in Figure 3.15 with those of the moduli, expressed with the master curve, in Figure 3.17a. The Cox-Merz rule [118] is used to directly compare strain rate data with frequency data.

The excellent agreement, despite using a simplistic approximation, gives confidence in using a methodology taking DMA results and deriving the stress-strain response.

3.6 Modelling framework

3.6.1 Requirements

One noticeable characteristic in the mechanical response of rubbers such as the neoprene in this study is that they undergo large reversible deformation. Although the behaviour is initially Hookean, it soon changes to non-linear elasticity: an increasing amount of force is required for each incremental deformation. As the chain straightens, its entropy tends towards zero, and the force required tends to infinity. This type of behaviour is deemed hyperelastic. In the stress-strain curve, this is typically observed in the large strain convexity. Models for this behaviour were initially developed by Mooney and Rivlin [136, 137], but for this study an Ogden model is used [141, 144]:

$$\sigma_1 = \frac{2\mu}{\alpha}\left(\mathrm{e}^{\alpha\varepsilon_1} - \mathrm{e}^{-\frac{1}{2}\alpha\varepsilon_1}\right) \tag{3.1}$$

where μ relates to the shear modulus, and α is the strain hardening exponent. Further details on this model are provided in Chapter 2, §2.5.1. Adiabatic self-heating at high strain rates was neglected in order to comply with the isothermal assumption in the Ogden model. The temperature rise can be calculated as:

$$\Delta T \approx \frac{1}{\rho C_p}\int_0^{\varepsilon} \sigma(\varepsilon)d\varepsilon \tag{3.2}$$

where ρ is the density and C_p is the heat capacity of the rubber. In this scenario, even if all of the high strain rate mechanical work were converted to heat in the sample, there was only a 2 °C rise in temperature — a negligible amount. This calculation was performed using the compression results at 2100 s^{-1}, where the maximum stress and strain were 16 MPa and 0.35 respectively. The heat capacity and density used in the calculation were 1.12 $\mathrm{J\,g^{-1}\,°C^{-1}}$ and 1.5 $\mathrm{g\,cm^{-3}}$ respectively [200].

3.6.2 Modelling results

Equation 3.1 was fit to the stress-strain profiles from the varying rate and varying temperature experiments. The results of the fitting are shown in Figure 3.18. The one-term Ogden model shows a good ability to fit to experimental data for both fixed temperature, varying strain rate (a) and varying temperature, fixed strain rate (b) cases. Since there is no separate viscoelastic definition in the model, there is a slight discrepancy between the experimental data and modelled results at the lowest strains. However, this difference is not significant to warrant a change to the model.

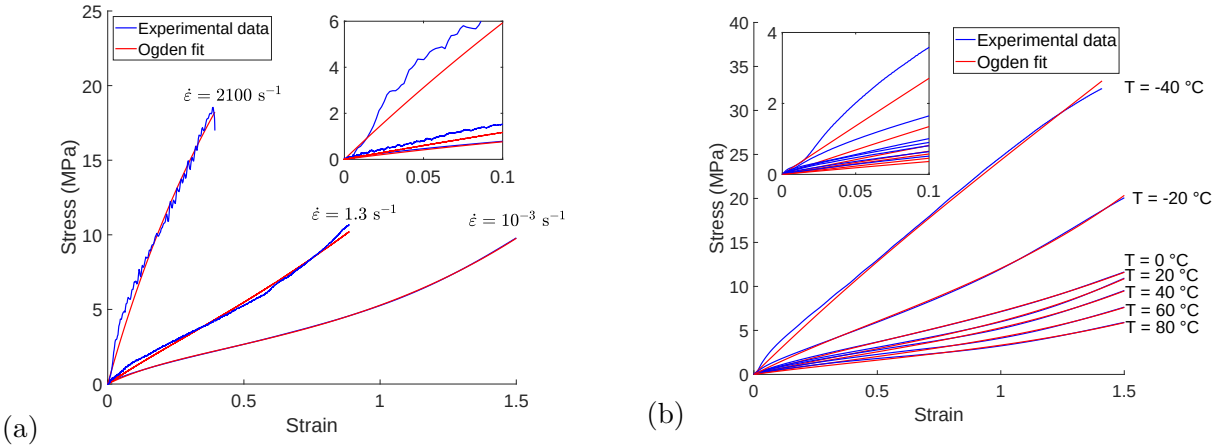

FIGURE 3.18: (a) Ogden model fits to the full response of varying strain rate experiments conducted at 20 ± 1 °C, and (b) to fit varying temperature experiments at 10^{-2} s^{-1}.

TABLE 3.1: Ogden parameters required for fitting.

$\dot{\boldsymbol{\varepsilon}}$ (s^{-1})	$\boldsymbol{\mu}$ (MPa)	$\boldsymbol{\alpha}$	$\boldsymbol{T}$ (°C)	$\boldsymbol{\mu}$ (MPa)	$\boldsymbol{\alpha}$
10^{-3}	2.00	2.32	80	1.27	2.15
10^{-2}	2.29	2.23	60	1.60	2.24
10^{-1}	2.73	2.18	40	2.02	2.21
1.3	4.23	3.24	20	2.29	2.23
14	6.44	2.95	0	2.83	1.69
80	7.59	1.30	-20	4.69	1.92
1700	18.6	3.05	-40	9.17	0.65
1800	19.6	3.19			
2100	19.2	2.90			

In this case, both of the Ogden parameters (μ and α) were allowed to vary to best fit the experimental data in a least squares sense. The parameters resulting from this fitting are provided in Table 3.1.

In order to perform the fit, the *lsqcurvefit* function on Matlab was used. The function minimised was the squared Euclidean distance between the vectors of experimental and modelled values.

$$\min_x \|F(x, xdata) - ydata\|_2^2 = \min_x \sum_i \left(F\left(x, xdata_i\right) - ydata_i\right)^2 \tag{3.3}$$

In this equation, $F(x, xdata)$ is the model to be calibrated using the parameters x and input vector $xdata$. Here, F is the Ogden model, x includes μ and α and $xdata$ is the vector of strain values for which the stresses are to be found. The Trust-Region-Reflective algorithm was used for this optimisation [201].

3.6.3 Rate and temperature dependence

From the obtained Ogden parameters, it is possible to infer a shift factor for μ that can be used to take the varying temperature results at a fixed strain rate of 10^{-2} s^{-1} and map them to an effective strain rate as shown in Figure 3.19 by noting that the shift factor is defined as $\log_{10} a_T = -k(T - T_{ref})$. The shifting gradient was $k = 0.07$ decades °C^{-1}. Note the similarity between this value, and that obtained for the modulus in DMA experiments (Figure 3.16b), which gave $k = 0.11$ (i.e. the gradient of the $\log_{10}(a_T)$ vs Temperature curve).

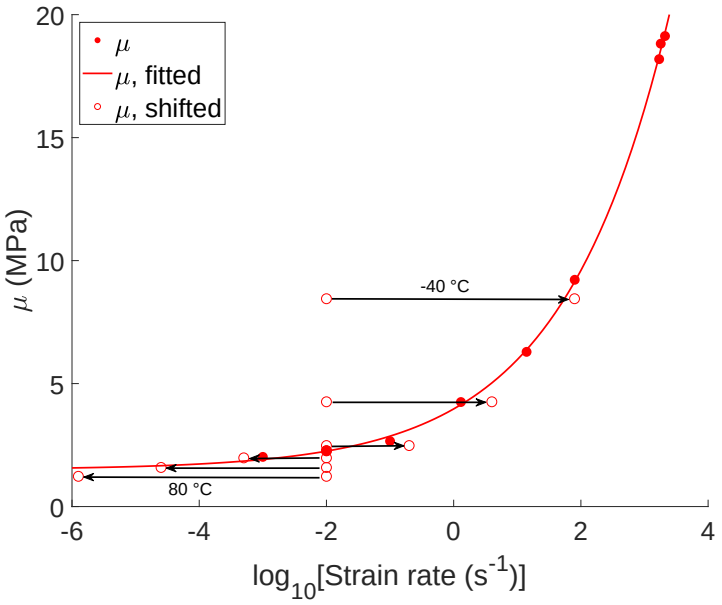

FIGURE 3.19: Implied shift factor relationship for μ.

The parameters for each set of experiments can be better visualised in Figure 3.20. In this figure, the two Ogden parameter for each individual fit are plotted against the strain rate or temperature, depending on the type of experiment the fit was conducted for.

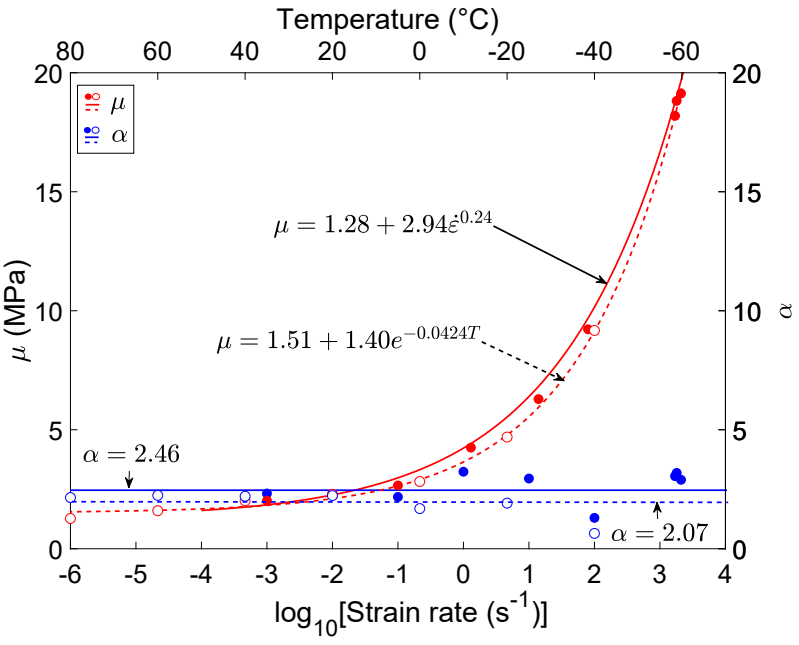

FIGURE 3.20: The rate and temperature dependence of Ogden parameters, with fits describing the dependences.

It is possible to fit power law and exponential curves to describe the rate and temperature dependence of μ. Additionally, there is apparently no systematic rate or temperature dependence for α. Since μ relates to the shear modulus of the material, it makes sense for it to depend on the strain rate. However, the strain hardening exponent refers to the large strain limiting response, which, rather than being rate or temperature dependent, depends on the macromolecular geometry. As such, it makes sense physically, the α parameter be considered as constant.

The fits were then repeated, this time using the mean value of α from the previous fits. The fits obtained are shown in Figure 3.21a for the varying rate experiments and Figure 3.21b for the varying temperature experiments. The parameters used in these updated fits are provided in Table 3.2.

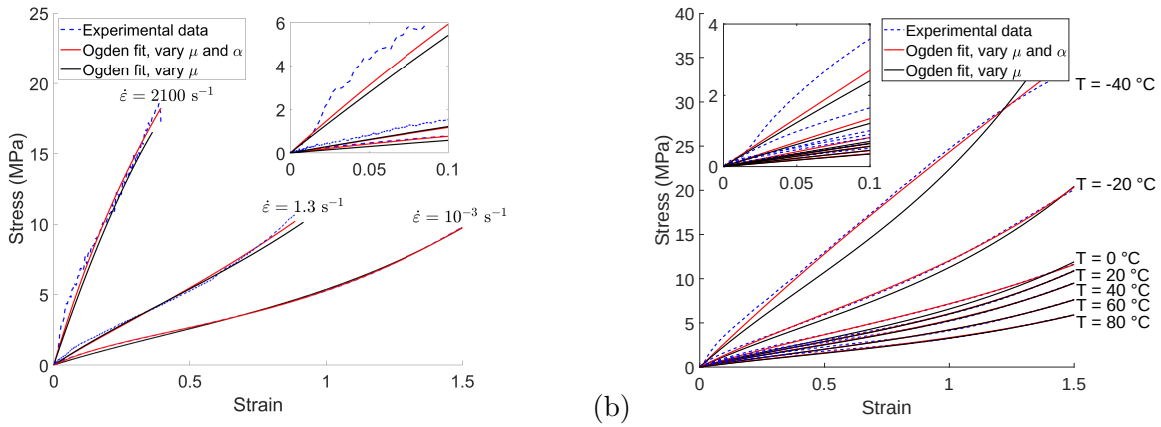

FIGURE 3.21: (a) Updated Ogden model fits to varying strain rate experiments conducted at 20 °C using a fixed α and (b) updated fits to the varying temperature experiments at 10^{-2} s^{-1}.

TABLE 3.2: Updated Ogden parameters for fits in Figure 3.21.

$\dot{\boldsymbol{\varepsilon}}$ (s^{-1})	$\boldsymbol{\mu}$ (MPa)	$\boldsymbol{T}$ (°C)	$\boldsymbol{\mu}$ (MPa)
10^{-3}	2.02	80	1.23
10^{-2}	2.27	60	1.59
10^{-1}	2.66	40	1.98
1.3	4.25	20	2.27
14	6.29	0	2.48
80	9.22	-20	4.26
1700	18.2	-40	8.45
1800	18.8		
2100	19.1		

Although the fixed α fits are well able to capture the overall trends for both varying rate and varying temperature experiments, they struggle to capture the high strain response at the lowest temperature featured, -40 °C. This is because the temperature approaches T_g: molecular mobility starts to become more restricted, and the mechanical response tends to shift from hyperelastic rubbery to glassy behaviour. Since the length of the striker bar in the SHPB restricts the maximum strain in the high rate

experiments, it is difficult to make similar comparisons with the high strain response at the highest strain rates.

In the same manner as Figure 3.20, it is possible to fit power law and exponential expressions to the rate and temperature dependence curves for the fixed α fits (Figure 3.22).

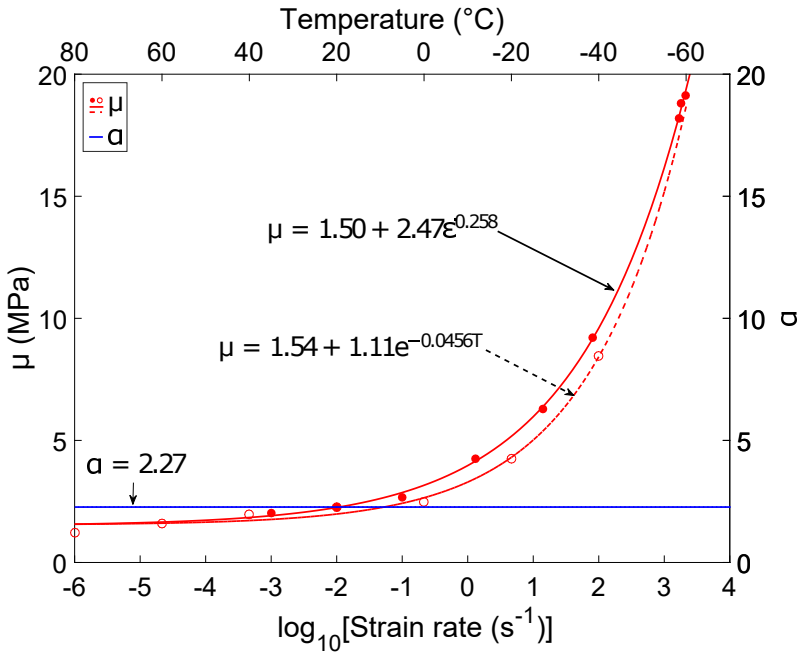

FIGURE 3.22: The rate and temperature dependence of the fixed α Ogden parameters, with fits describing the dependences.

The fact that the rate and temperature dependences are so similar for the parameters gives confidence in the ability to use TTS for this material. In fact, by equating the μ values for the rate and temperature dependences, it is possible to derive an expression for the shift factor. In this expression, the μ values for the lowest strain rate and the highest temperature are deemed to be the same. This assumption is valid based on the closeness of the values in the obtained fits, and by consideration of the physical equivalence at those two extremes.

By invoking the rate-temperature equivalence of μ and using the model fits to the data in Figure 3.22, we can say that:

$$\begin{aligned} \mu_{\dot{\varepsilon}} &= \mu_T \\ 1.50 + 2.47\dot{\varepsilon}^{0.258} &= 1.54 + 1.11\mathrm{e}^{-0.0456T} \\ 2.47\dot{\varepsilon}^{0.258} &\approx 1.11\mathrm{e}^{-0.0456T} \\ \log 2.47 + 0.258 \log \dot{\varepsilon} &\approx \log 1.11 - 0.0456T \log \mathrm{e} \end{aligned} \tag{3.4}$$

The μ values for the lowest strain rate and the highest temperature are deemed to be the same. This assumption is valid based on the closeness of the values in the obtained fits, and by consideration of the physical equivalence at those two extremes. Similarly:

$$\log 2.47 + 0.258 \log \dot{\varepsilon_0} \approx \log 1.11 - 0.0456T_{ref} \log \mathrm{e} \tag{3.5}$$

where $\dot{\varepsilon_0}$ is the strain rate at which varying temperature experiments were conducted (10^{-2} s^{-1}) and T_{ref} is the reference temperature (20 °C). By noting that the shift factor, $\log a_T = \log \dot{\varepsilon} - \log \dot{\varepsilon_0}$, and subtracting Equation 3.5 from Equation 3.4:

$$\begin{aligned} \log_{10} a_T &= -\frac{0.0456 \log \mathrm{e}}{0.258} \\ &= -0.077(T - T_{ref}) \end{aligned} \tag{3.6}$$

The shifting gradient of $k = 0.08$ obtained here with Equation 3.6 is very close to that obtained through manual shifting as shown in Figure 3.19 ($k = 0.07$) and that of the storage modulus in the DMA experiments as shown in Figure 3.16b ($k = 0.11$).

Based on this equivalence, a more accurate value for the equivalent temperature can be obtained than that which can be inferred from Figure 3.15 in Section 3.5.3 describing the rate temperature equivalence:

$$\begin{aligned} \mu_{T_{eq}} &= \mu_{\dot{\varepsilon}} \\ 1.11\mathrm{e}^{-0.0456T_{eq}} &\approx 2.47\dot{\varepsilon}^{0.258} \\ T_{eq} &\approx -\frac{1}{0.0456 \log \mathrm{e}} \log\left(\frac{2.47}{1.11}\right) + 0.258 \log \dot{\varepsilon} \\ &\approx A + 0.258 \log \dot{\varepsilon} \end{aligned} \tag{3.7}$$

These equivalent temperature values are those at which compression experiments at 10^{-2} s^{-1} must be conducted to obtain mechanical responses analogous to a desired

strain rate at 20 °C. By substituting these equivalent temperature values back into the μ_T expression in Equation 3.7, the μ values for the equivalent temperatures can be found using Equation 3.8. For reference, these values are provided in Table 3.3

$$\begin{aligned} \mu_{T_{eq}} &= 1.54 + 1.11\mathrm{e}^{-0.0456T_{eq}} \\ &= 1.54 + 1.11\exp[-0.0456(A + 0.258\log\dot{\varepsilon})] \end{aligned} \tag{3.8}$$

TABLE 3.3: Equivalent temperatures and associated parameters for analogue fits as shown in Figure 3.23.

Desired $\dot{\varepsilon}$ (s^{-1})	$\boldsymbol{T_{eq}}$ (°C)	$\boldsymbol{\mu}$ (MPa)	$\boldsymbol{\alpha}$
10^{-3}	22	1.94	2.27
10^{-2}	N/A	N/A	N/A
10^{-1}	-4.5	2.88	2.27
1.3	-19	4.16	2.27
14	-32	6.40	2.27
80	-42	9.17	2.27
1700	-60	18.4	2.27
1800	-60	18.6	2.27
2100	-61	19.3	2.27

By using these calculated values for μ alongside the fixed α value, the mechanical responses at a variety of strain rates can be predicted by substituting these values into Equation 3.1. These analogue responses are shown in Figure 3.23 highlighting the value of using the TTS technique alongside a simple phenomenological model to enable the predictions of high strain rate responses.

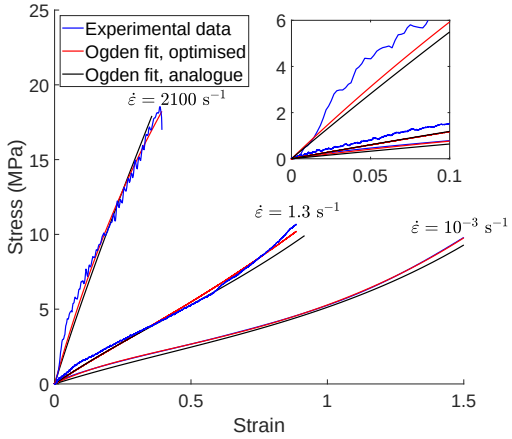

FIGURE 3.23: Comparing optimised Ogden fits as in Figure 3.18a and their analogues obtained by considering the response at 10^{-2} s^{-1} and an equivalent lower temperature.

3.6.4 Enhancing predictability with DMA results

It is evident that the form of curves representing the rate and temperature dependence of the Ogden μ parameter is very similar to that of the DMA master curve seen in Figure 3.17a. To compare how similar, the rate dependent Ogden shear modulus, $\mu_{\dot{\varepsilon}}$, obtained in Figure 3.20 is expressed as an equivalent Young's modulus using $E = 2\mu(1+\nu)$, where $\nu = 0.5$, the Poisson's ratio for an incompressible material. This comparison is shown in Figure 3.24a.

It is clear that the obtained rate dependent μ parameters from the Ogden model fits to varying rate data can be used to relate back to the modulus dependence on rate. If the rate dependent μ can be related to the master curve to this extent, it should be possible to use the master curve to obtain the rate dependent μ. This would be highly advantageous as it means that this relationship can be obtained without conducting any high strain rate experiments. Thereby, the predictive capability of this model could be enhanced. In Figure 3.24b it is clearly evident that the calculated μ values from the master curve are very similar to those obtained from Ogden model fits to the varying rate experiments.

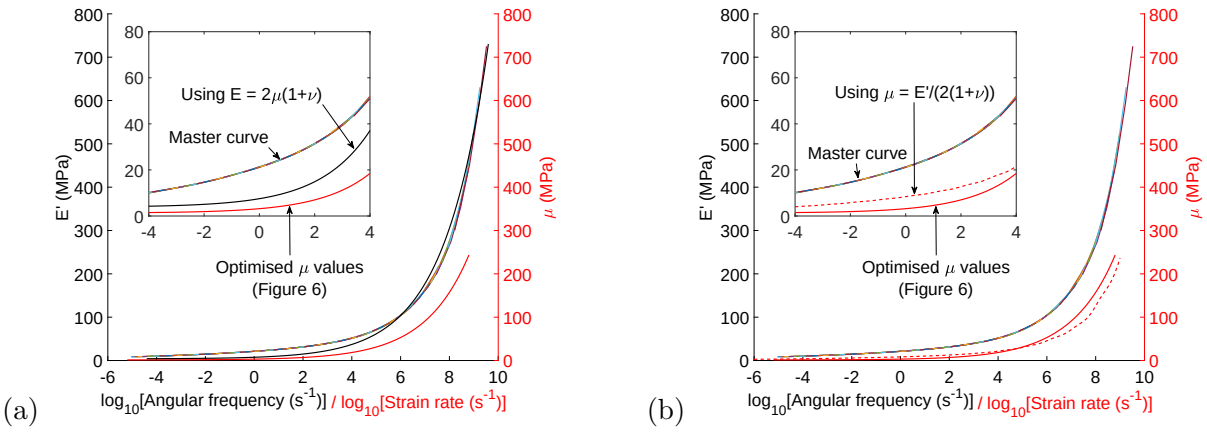

FIGURE 3.24: (a) Highlighting the similarity between E' and the equivalent Young's modulus, E, (b) Comparison of $\mu_{\dot{\varepsilon}}$ as obtained from the master curve with that from varying rate fits (Figure 3.20).

Once these *predicted* μ values are known, based on the TTS results, it is possible to use them to predict the stress-strain responses for varying rate experiments by substituting them along with the fixed α value into Equation 3.1. These predictions are shown in Figure 3.25.

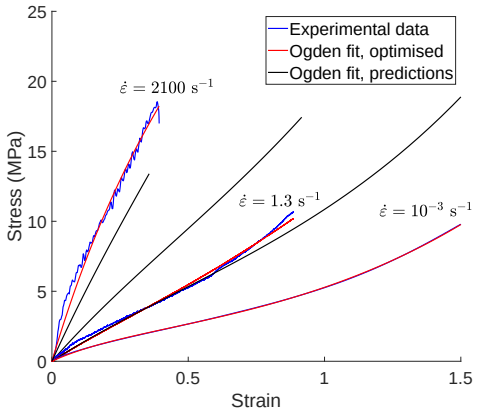

FIGURE 3.25: Predictions of the response using these μ values and the α obtained in varying temperature fits (also Figure 3.20).

Figure 3.25 shows that the similarity between the DMA based master curve and the rate dependent μ parameters does not necessarily translate to accurate predictions of the high strain rate response as did the previous method. Although the prediction of the response for a strain rate of 2100 s^{-1} comes close to matching the experiment, those at strain rates of 1.3 s^{-1} and 10^{-3} s^{-1} are overestimated considerably. This is

likely due to the greater discrepancy between the two μ values at the lower strain rates compared to that around 1000 s^{-1} as can be seen in the inset in Figure 3.24b. To explore this further, a sensitivity analysis was performed.

3.6.5 Sensitivity analysis

The sensitivity of the Ogden model to changes in the two parameters that govern its response were investigated. For this analysis, the model is applied to three strain rate experiments (2100, 1.3 and 10^{-3} s^{-1}) as before to cover the broad spectrum of responses. The fits to the experiments are those from Figure 3.23. The results for the sensitivity analysis in the two parameters for this simple hyperelastic model are presented in Figure 3.26. Although the sensitivity would depend on the relative magnitude of the values, this analysis based on perturbations helps to provide a visual impression of the effect of errors on these specific parameter values.

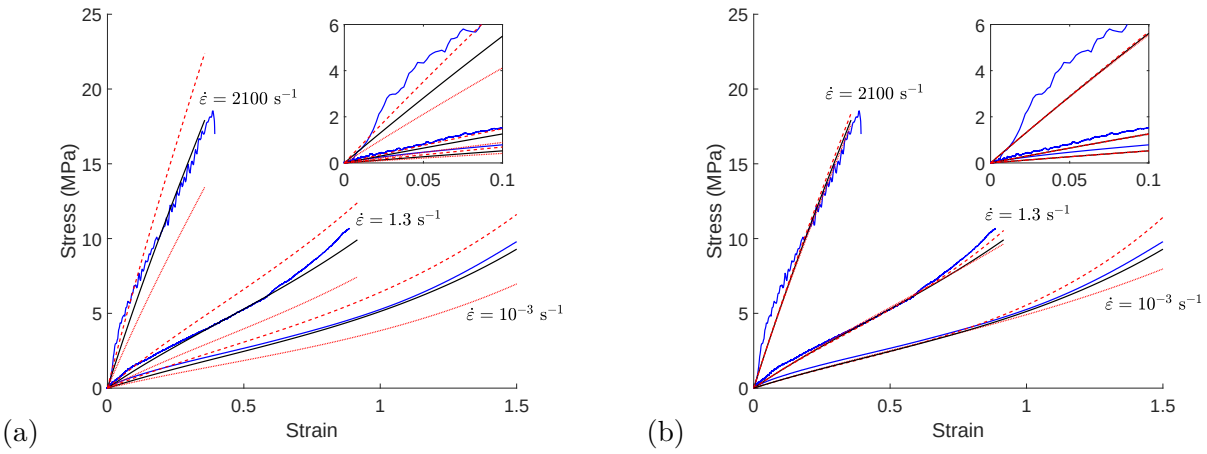

FIGURE 3.26: Sensitivity analysis for the fits to varying rate experiments where the model parameters are varied: (a) $\mu \pm 25\%$ and (b) $\alpha \pm 25\%$. Solid blue lines are experimental, solid black are the analogue fits using μ values based on T_{eq}, red dashed lines are the simulations with $+25\%$ values and red dotted lines are simulations with -25% values.

For this sensitivity analysis, it is clear that overall there is much greater sensitivity to variations in μ rather than α. One reason for this is that since the μ parameter relates to the shear modulus, any initial deviation from the true value would affect the entire mechanical response. On the other hand, since the α parameter only corresponds to

large strain convexity in the response, its effect is insignificant at low strains. It does however become increasingly important at larger strains as can be seen in Figure 3.26b for the lowest strain rate case. This sensitivity analysis can help us understand the discrepancies in the DMA based predictions in Figure 3.25.

In the predictions, the α value was kept constant as the averaged value found from fits to varying temperature experiments as in Figure 3.20, and the μ value was obtained based on the results of the DMA experiment. In this case the α value was only 8.6% lower than the average of the optimised values and since its impact is mostly at higher strains, it cannot be the reason for the discrepancies in the predicted stress-strain responses. Qualitatively, this is supported by the observation that at larger strains, the predicted responses show similar convexity to both experimental and optimised fits.

However, the difference in the μ values between the DMA based case and the optimised case for each of the predictions varied considerably. The value was 25% lower for the 2100 s^{-1} case, 75% higher for the 1.3 s^{-1} case and 110% higher for the 10^{-3} s^{-1} case. This explains why the prediction for the 2100 s^{-1} response looked better, as it was almost in line with the discrepancies noticed in this sensitivity analysis. However, the significant difference in μ value for the 1.3 s^{-1} and 10^{-3} s^{-1} cases led to their poor prediction.

3.7 Conclusions

In this chapter, a simple rate and temperature dependent two parameter hyperelastic model was presented and shown to accurately represent high strain rate experimental results for the commercial neoprene rubber. The low strain viscoelastic modulus was captured well by relation to a rate dependent μ parameter and the large strain non-linear rubber elasticity was captured by a fixed α parameter.

The model has its foundations on the one-term, two-parameter Ogden model, which is subsequently adapted to take rate and temperature dependence into account. This was possible due to the TTS technique based on DMA experiments. By observing the similarity in the dependence of the μ fitting parameter to both rate and temperature, an equivalent temperature can be found. This is the temperature at which fixed strain rate experiments could be conducted at to produce high rate analogues.

There are some limitations with this modelling strategy. As it stands, the rate and temperature dependence of the model parameters need to be characterised with a multitude of experiments. This is not as challenging for the varying temperature experiments, which are conducted on one instrument. For the varying rate experiments, three different instruments are required adding time, cost and potential errors and artefacts associated with making comparisons between very different types of apparatus.

Moreover, the fact that high rate experiments must be performed prior to the modelling means the predictive capability of this model is lacking. Although this was attempted to be mitigated by using the results of the DMA to provide the rate dependence, the small differences in modulus values from the DMA experiments for the neoprene in its rubbery state translate to a large difference in the predicted mechanical response.

In future, DMA shift factors could be used alongside the results of varying temperature quasi-static experiments to derive the rate-temperature equivalence, which would then allow the high rate stress-strain response to be calculated. In this manner, only the relative moduli would be used from the DMA experiments, and not the absolute

moduli, which have been shown to be inaccurate due to experimental variation and dependence on loading configuration.

This model also only works when the mechanical response is solely elastic. There were also assumptions made invoking the materials' isotropy and incompressibility, along with the requirement for the experiment to be performed isothermally. Therefore, there are many opportunities to extend this model to include heterogeneity, compressibility, effects from adiabatic self-heating, (rate dependent) plasticity and even evolving damage for materials where this is relevant.

Overall, this model provides the user with a simple method to represent the high strain rate behaviour of neoprene rubber. By characterising only two parameters with varying temperature and varying strain rate experiments, it is possible to interpolate the mechanical response at any temperature or strain rate within the range used in the characterisation process. In the next chapter, developments to this modelling strategy are presented that incorporate effects of adiabatic self-heating and rate dependent plasticity.

Modelling framework overview

In this section, the modelling framework used in this chapter is detailed with step-by-step information to guide the user and also presented as a simple flowchart (Figure 3.27).

Ogden fits to varying rate experiments

Varying rate experiments are performed at a constant temperature using an electromechanical static testing machine, hydraulic press and SHPB. Subsequently, the stress-strain response at each strain rate is individually fit to with a one-term Ogden model.

Ogden fits to varying temperature experiments

Varying temperature quasi-static compression experiments are performed at a constant strain rate using the same electromechanical static testing machine fitted with an environmental chamber. Similarly, the stress-strain response at each temperature is fit with a one-term Ogden model.

Refitting based on a constant strain hardening exponent

Upon averaging the α values obtained from the fits to the varying rate experiments and the varying temperature experiments, there will be a minor discrepancy between them. The average of these averages is taken and then fixed. The fitting process described in the previous two paragraphs is run again with this fixed α value and updated μ values are obtained.

Invoke rate-temperature equivalence

By plotting the μ values against the strain rate and the temperature, it is possible to draw curves representing their dependence on these variables. Exponential expressions can be fit to each curve.

Rate-temperature equivalence is then invoked by noticing the similarity between the rate and the temperature dependence of the μ values as obtained in the fitting process. In this manner, the shift factor can be obtained as well as an expression for the equivalent temperature.

Find equivalent temperatures for analogues

By equating the rate dependent μ to the temperature dependent μ, the resulting expression can be solved for the temperature. This is the equivalent temperature that the quasi-static experiments must be conducted at to produce stress-strain responses which act as analogues to the measured high rate responses.

Furthermore, since the expression for the temperature dependent μ is already known, these equivalent temperature values can be fed back to obtain μ values for analogues. These values, alongside the fixed α are used to interpolate the stress-strain response at any temperature or strain rate within the initial characterisation range.

Enhance predictability with DMA results

In order to *predict* the stress-strain responses and not simply interpolate them, it is possible to use the results of DMA experiments. Using the TTS principle, a master curve at the temperature of the compression experiments can be constructed. Assuming incompressibility (Poisson's ratio, $\nu = 0.5$), $\mu = E/3$. These rate dependent μ values at the temperature of interest are obtained independently of varying rate compression experiments. This means that they can be used instead as a means to *predict* the high strain rate response of the neoprene rubber.

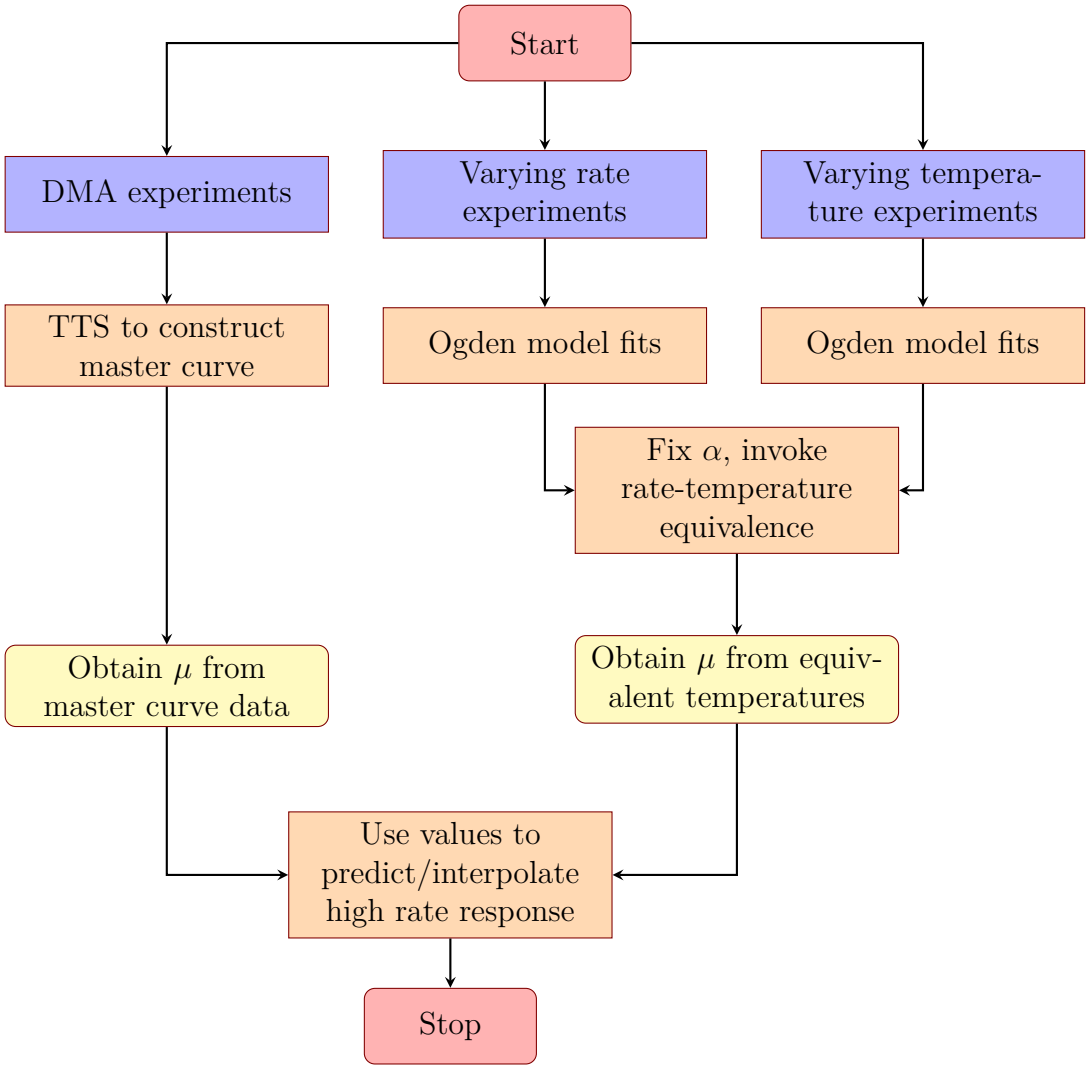

FIGURE 3.27: Flowchart to describe the preliminary modelling framework.

4 Modelling framework for (plasticised) poly(vinyl chloride)

In the previous chapter, preliminary experiments were detailed to aid material characterisation at varying strain rates and temperatures, including a holistic thermomechanical investigation integrating data from DMA experiments. A simple hyper-viscoelastic modelling framework was also proposed: a combination of the viscoelasticity and hyperelasticity, which was characterised by only two parameters. This was fitted to the varying rate and temperature experiments. This modelling strategy enabled the interpolation of the mechanical response at any temperature or strain rate within the range used in the characterisation process.

However, there were limitations to the strategy detailed in the previous chapter. Multiple apparatus needed to be used to characterise the response at various rates, high rate data were used to calibrate the model, reducing its predictive capabilities, the model only captured the elastic response and (for materials where this is relevant) it would not take into account the effects of adiabatic self-heating due to plastic work. Furthermore, the temporal relaxation of the modulus was not integrated into the calculation of the stress-strain curves.

Plasticised (PPVC) and unplasticised poly(vinyl chloride) (PVC) are used as engineering materials, for example in the aerospace and automotive sectors, where they may be subjected to impact loading leading to high strain rate deformation at a variety of temperatures, both ambient and from self-heating due to plastic work. It is therefore necessary to study the mechanical responses of these materials over a range of loading conditions.

In this chapter, a suitable modelling strategy overcoming the limitations of the previous model are presented. Details are given for the modelling of PVC and a PPVC

with 20 *wt*% plasticiser. The model was applied over a wide range of strain rates and strains and shown to have excellent agreement with experiments conducted in a previous study [3].

As it is challenging to obtain high rate data on low-impedance, rubbery materials using conventional apparatus, such as the split-Hopkinson pressure bar (SHPB), an alternative approach is presented based on a novel modelling framework, which uses the time-temperature superposition principle and is fully calibrated using quasi-static experiments at different temperatures, thus enabling the *prediction* of high rate responses.

4.1 Introduction

Plasticised PVC (PPVC) is another polymer which exhibits strong temperature and rate dependence in its mechanical response, including modulus, yield strength and post-yield behaviour. The sensitivity increases with increasing rate and decreasing temperature due to inhibitions in motions associated with the secondary (β) transitions [127, 202]. As with neoprene rubber in the previous chapter, the experimental characterisation for PPVC at high strain rates (above c. 500 s^{-1}) is also challenging.

Until a more robust experimental technique for characterising the high strain rate properties of soft polymers is developed, one must also explore other alternatives. Time-temperature superposition has been used in the past, as one such alternative, to validate high rate data [1]. However, the techniques used are limited in that they only map a single stress state, usually the initial yield stress. Furthermore, one of the key differences between high and low strain rate loading is that the former is adiabatic, and the specimen temperature increases because of the conversion of plastic work into heat. Previous work has focused on experimentally simulating a high rate test by either increasing the temperature during a low temperature isothermal test [61, 70] or through a series of strain rate jump tests [69], neither of which is wholly satisfying as it does not predict the continuous stress-strain curve at high strain rates. For this reason,

this chapter looks to a novel modelling framework that is able to *predict* the full high rate response of the PVC and PPVC via constitutive models calibrated entirely with data obtained accurately at low strain rates, and a range of temperatures.

4.2 Material

PVC is an amorphous polymer that represents 20% of all manufactured polymers [203]. Its production is expected to grow to around 50.6 million tonnes by 2021 [204]. Where rigid PVC is mostly used in construction, its plasticised variant is widely used in many engineering applications to increase ductility and energy absorption. This is as plasticisers add free volume, lowering the T_g, making the material more rubbery. These materials can be found in fields as diverse as aerospace, automotive, biomedical, cabling, clothing, sports and industrial vibration damping. A plasticiser is usually based on a phthalate ester compound [205]; in this case diisononyl phthalate (DINP). Molecular structures for both PVC and DINP and shown in Figure 4.1.

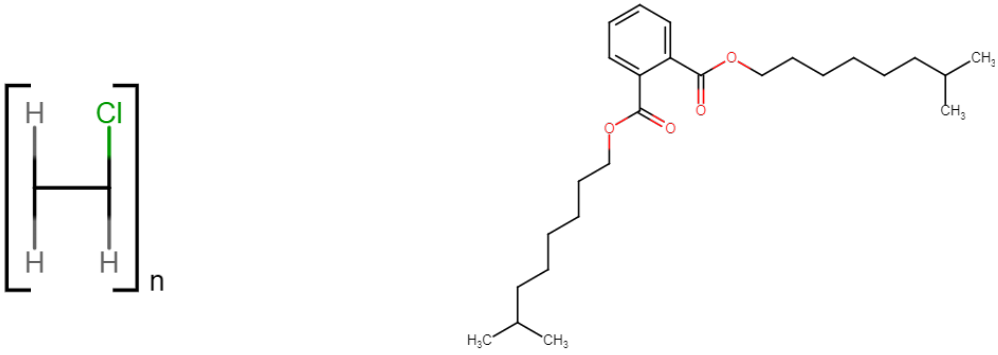

(a) (b)

FIGURE 4.1: (a) Molecular structure for PVC and (b) for DINP.

In order to be able to validate the predictive capabilities of the modelling framework presented in this paper, the materials selected were from the same batch as that in the previous study [3]. They were manufactured by Solvay under the trade name SolVin 264PC with and without DINP plasticiser. In the original study by Kendall, four

materials were investigated; the PVC and three plasticised PPVC variants: 20 $wt\%$, 40 $wt\%$ and 60 $wt\%$ DINP.

The existence of these materials allow validation of the model against an existing dataset and furthermore, relatively soft, plasticised PVC is challenging to test at high strain rates and obtain reliable, reproducible data. Another benefit of using this material is that the mechanical response is varied: featuring small strain viscoelasticity, glassy yield stress and softening at high strain rates or low temperatures, and large strain hyperelasticity at low strain rates or elevated temperatures. This allows a modelling framework with different capabilities to be developed.

For the purpose of detailing the modelling approach in this chapter, only the PVC and the 20 $wt\%$ DINP PPVC are focused on. The PVC has been selected due to the fact there appear to be fewer complex interactions between the primary, glass (α) transition and the secondary (β) transition at the temperatures, and rates, of interest. It will be shown that the total mechanical behaviour can be considered to be the additive sum of the α and β responses. The 20% plasticised variant provides an interesting trial of the modelling framework as there is a more complex interaction between the two transitions and the post-yield softening behaviour is different to that of the PVC.

4.3 Compression experiments

New uniaxial compression experiments were not performed as a full regime of testing was conducted in a previous study [3]. Right circular cylindrical specimens of 5 mm diameter and 2.5 mm length were used. The length to diameter aspect ratio of 1:2 has been shown to minimise inertial effects in high strain rate compression experiments [73], and as such, the ratio was used in lower rate uniaxial experiments too for consistency.

As in the previous chapter, the low rate experiments had been carried out on an Instron 5980 electromechanical static testing machine, intermediate rate experiments on a hydraulic press, and high rate experiments on a SHPB. These experiments were all performed at a temperature of 25 °C. Varying temperature experiments were also conducted at a lower rate of 10^{-2} s^{-1} using the Instron coupled with a temperature controlled environmental chamber.

4.3.1 Results and analysis

The results of the uniaxial compression experiments for both PVC and PPVC can be seen in Figure 4.2.

At high strain rates, both PVC (Figure 4.2a) and PPVC (Figure 4.2b) reach a similar yield stress, but at low to intermediate strain rates, PVC has the higher yield stress. The addition of DINP has softened the PVC as expected: the apparent modulus is generally lower at each rate and there is greater post yield softening. This softening in both materials is particularly significant at higher strain rates as a result of self-heating and thermal softening. At lower strain rates, strain hardening is observed instead at large strains as the deformation is isothermal.

Strain hardening is also seen in the isothermal quasi-static varying temperature experiments for both PVC (Figure 4.2c) and PPVC (Figure 4.2d). In PVC, the yielding is broader than in PPVC and the post-yield softening is less pronounced than in the PPVC. The gradient of strain hardening also increases with decreasing temperature for the PPVC but this is more subtle for the PVC.

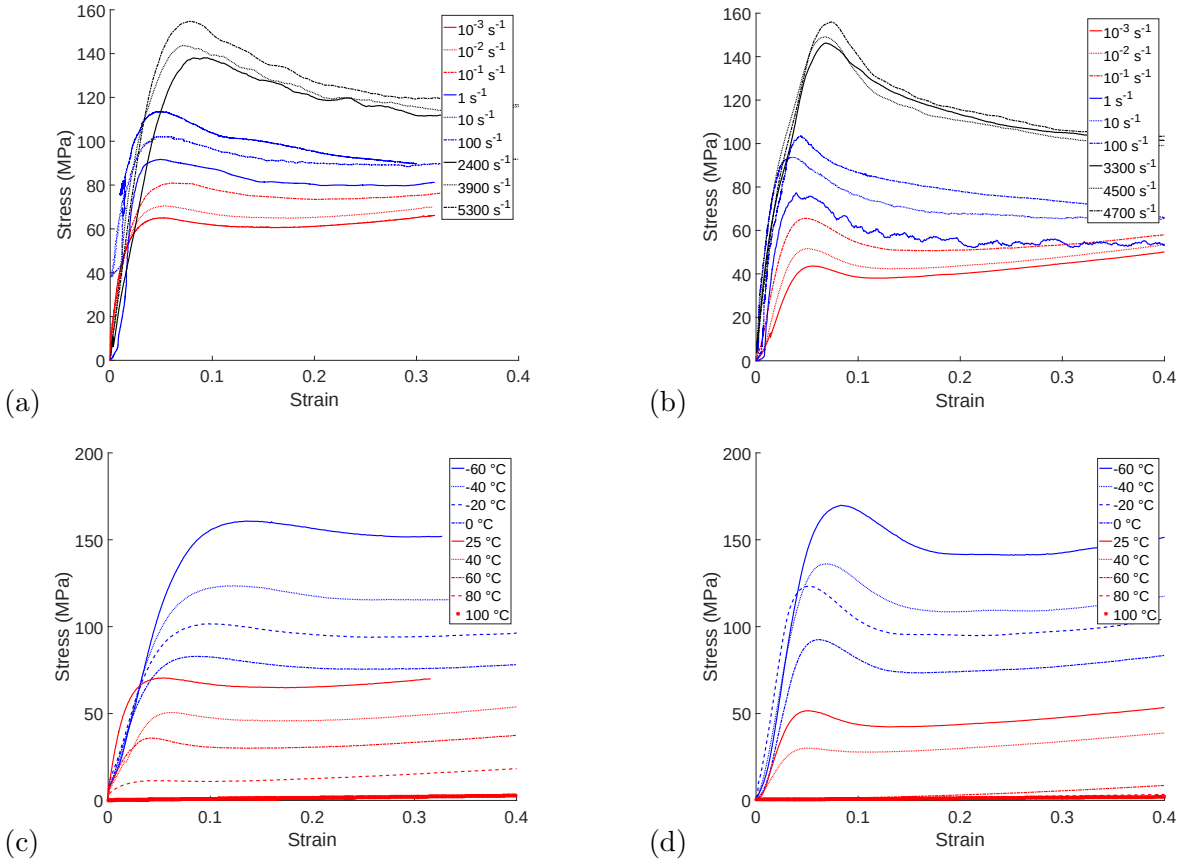

FIGURE 4.2: (a) True stress-strain curves from the uniaxial compression experiments at varying strain rates for PVC, (b) for PPVC, and (c) varying temperature experiments at a rate of 10^{-2} s^{-1} for PVC, and (d) for PPVC: from [3].

4.4 Dynamic Mechanical Analysis

4.4.1 Experimental method

As in the previous chapter, DMA experiments were performed on a TA Instruments Q800 in order to quantify the frequency and temperature dependence of the PVC and PPVC. The results presented here were obtained by Kendall and taken from [3]. Isothermal frequency sweeps were performed over two decades of frequency and a temperature range spanning the two material transitions. Rectangular specimens of dimension 5 $\times$ 10 $\times$ 60 mm were tested in dual cantilever configuration with a fixed strain amplitude of 0.1%, temperature range of -100 °C to 120 °C, and frequencies of 1, 10 and 100 Hz. As the temperature increases, the frequency sweep obtains the temperature dependence of the storage and loss moduli for each of the three frequencies.

4.4.2 Results and analysis

The results of these DMA experiments can be seen in Figure 4.3. For PVC (a), both transitions are well resolved: the glass (α) transition is centred around 82 °C and the secondary (β) transition is centred around -44 °C. For PPVC (b), only the α transition is easily resolved, being centred around 40 °C. Kendall found the β transition to be centred around -150 °C for this batch of PPVC [3].

The addition of 20 $wt\%$ DINP moves the α transition 42 °C lower and broadens it by around 40 °C: the plasticiser creates free volume in the PVC so that the large segment molecular motions are less restricted and require less energy to take place.

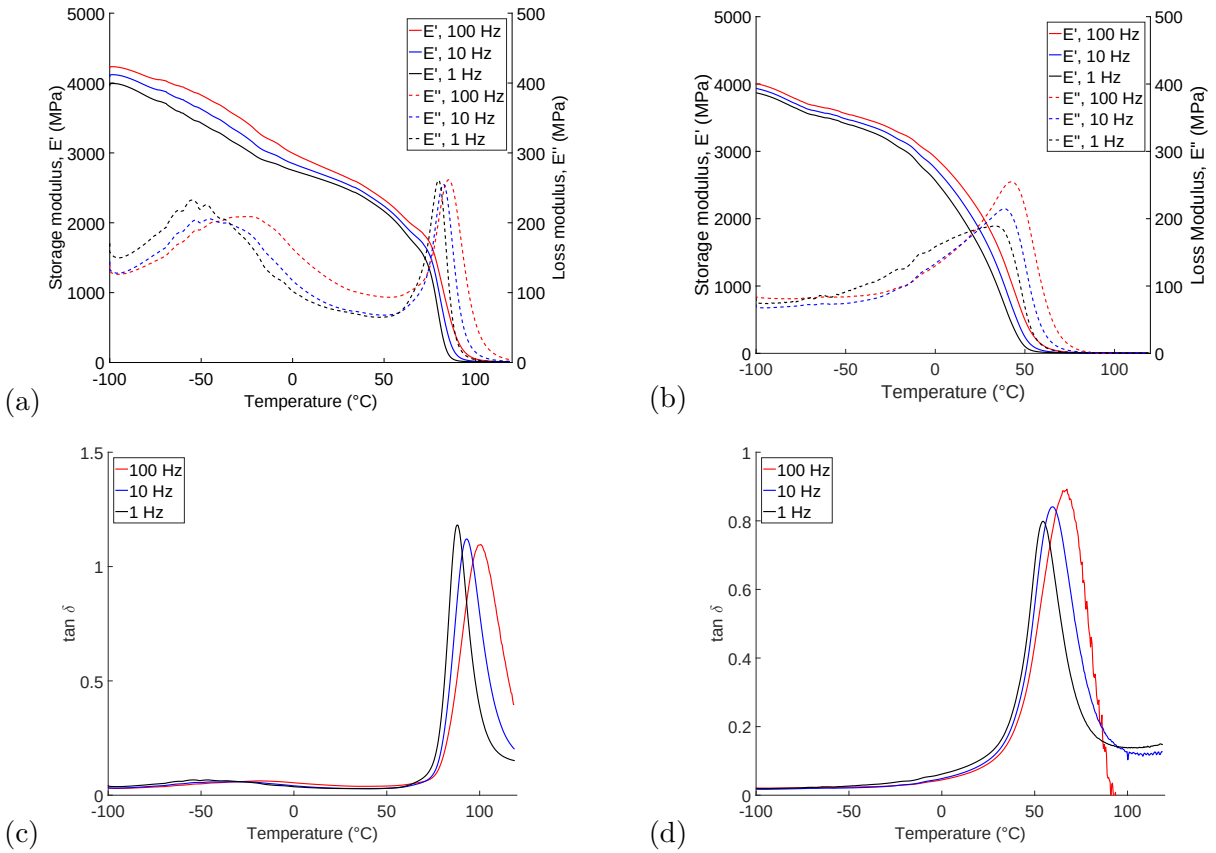

FIGURE 4.3: (a) Storage and loss moduli DMA results for PVC and (b) for PPVC. (c) Loss tangent ($\tan\delta$) as a function of temperature and frequency for PVC and (d) for PPVC: from [3].

By looking at the $\tan\delta$ peaks and how they shift to higher temperature with increasing frequency, it is possible to get an initial idea of the shift factor. For PVC (Figure 4.3c), the α peak shifts by an average of 6.4 °C per decade of frequency corresponding to a shift factor of 0.16 decades per °C. Similarly, the β peak shifts by 18 °C per decade of frequency, which is 0.055 decades per °C. For PPVC (Figure 4.3d), the α peaks shift by an average of 6.4 °C per decade of frequency corresponding to a shift factor of 0.16 decades per °C.

Based on this preliminary analysis of the loss tangent shifts, the addition of 20 $wt\%$ DINP as a plasticiser seems to have no impact on the α shifts. This means the rate dependence of the α transition does not change with this amount of plasticiser. The rate dependence of the α transition is based on main chain segmental motion, but the addition of plasticiser adds free volume, so does not affect the kinetics of the main

chain. Although it is not possible to make this comparison for the β transition, it can be noted that β transition shifts to higher temperatures more than the α transition for each decade of frequency. Relating this to the molecular dynamics, it means that the β transition is associated with those motions that require less energy to overcome compared to the motions associated with the α transition. This is indeed also obvious from the fact that the β transition occurs at lower temperatures.

4.4.2.1 Activation energies

Data from the DMA experiments (the loss tangent curves in particular) can be used to estimate the activation energy for each transition. This is done by considering the frequency dependence of the transition temperature, assuming it can be modelled by an Arrhenius equation:

$$f = f_0 \exp\left(-\frac{Q}{RT}\right) \tag{4.1}$$

where f is the experimental frequency, f_0 is the pre-exponential factor, Q is the activation energy, R is the universal gas constant and T is the absolute temperature.

By considering the shift required to move the loss tangent curve at one frequency (f_1) to be superimposed onto that at another frequency (f_2), the following equation can be written, where T_{p1} and T_{p2} are the temperatures associated with the loss tangent peaks at each frequency.

$$\frac{f_1}{f_2} = \frac{\exp(-Q/RT_{p1})}{\exp(-Q/RT_{p2})} \tag{4.2}$$

The shift factor ($\log a_T$) is defined as the logarithm of the frequency ratio in Equation 4.2:

$$\begin{aligned} \log a_T &= \log\left(\frac{f_1}{f_2}\right) \\ &= \frac{Q}{R}\left(\frac{1}{T_{p2}} - \frac{1}{T_{p1}}\right) \end{aligned} \tag{4.3}$$

Rearranging Equation 4.3, the activation energy can be obtained:

$$Q = -R\left[\frac{\mathrm{d}(\log f)}{\mathrm{d}(1/T_p)}\right] \tag{4.4}$$

Therefore, by plotting the logarithm of the experimental frequencies against the reciprocal of the absolute temperatures of the loss tangent peaks for each transition, the gradient of the curves obtained can be used to find the activation energies for the transitions. These plots are shown in Figure 4.4.

Based on these curves and Equation 4.4, the activation energy for the α transition in PVC is 400 kJ mol^{-1} and 58 kJ mol^{-1} for the β transition. Similarly, the activation energy for the α transition in PPVC is 330 kJ mol^{-1}. Literature shows the α transition activation energy can vary from around 330 kJ mol^{-1} to 540 kJ mol^{-1} [206]. As the β transition is based on the segmental motion of side chains, it requires less energy and so it makes sense that its activation energy is lower. The activation energies for the α transition should be similar as the segmental motion governing the transition are independent of the type and amount of plasticiser [207].

The value for the β transition in PPVC cannot be calculated since the loss tangent peaks for that transition cannot be found from the DMA experiments conducted.

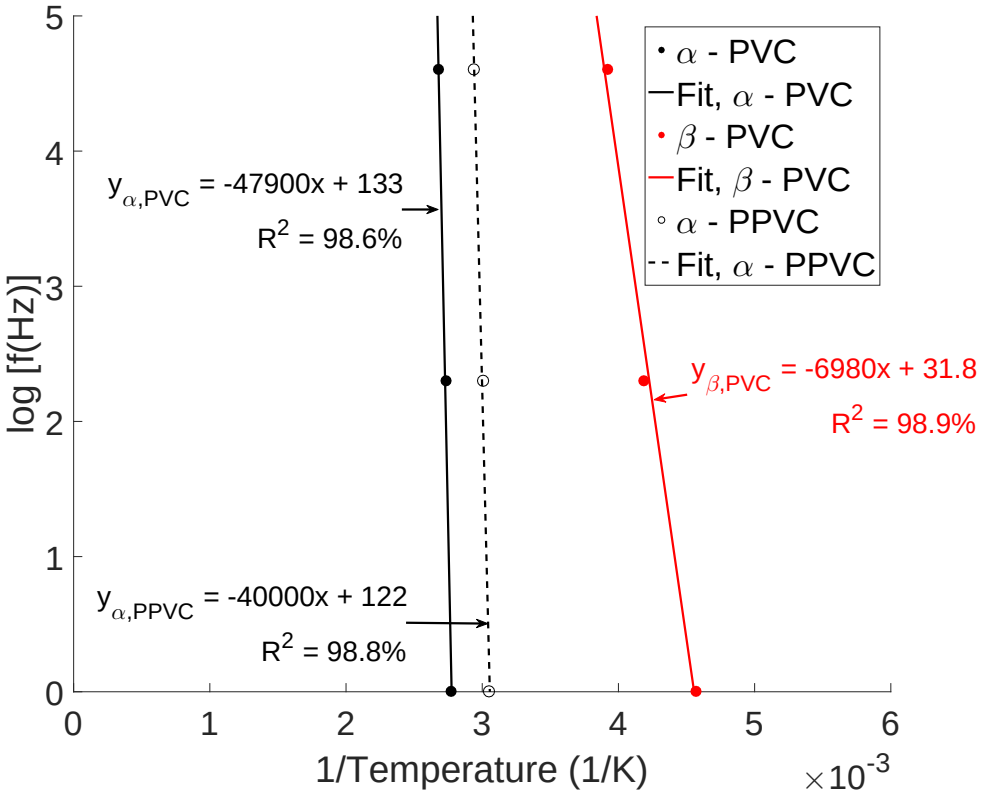

FIGURE 4.4: Plotting the temperature dependence of the shift factor for each transition process in order to find their activation energies.

4.4.3 Time-temperature superposition

In this section, the details of the TTS methodology are provided for the PVC. TTS for the PPVC is conducted in the same manner. The storage moduli results of the DMA experiments are plotted against the frequency on a log scale, where each of these isotherms is linear as shown in Figure 4.5b. Once all of the individual isotherms (532 in this study) are shifted using the shifting algorithm (similar to that presented in Chapter 2, §2.4), a master curve is produced at the desired reference temperature of 25 °C as seen in Figure 4.5c.

The error in constructing a master curve with isotherms characterised by only three data points per temperature is discussed in §4.8. In any case, the smooth master curve produced here provides confidence in the method employed.

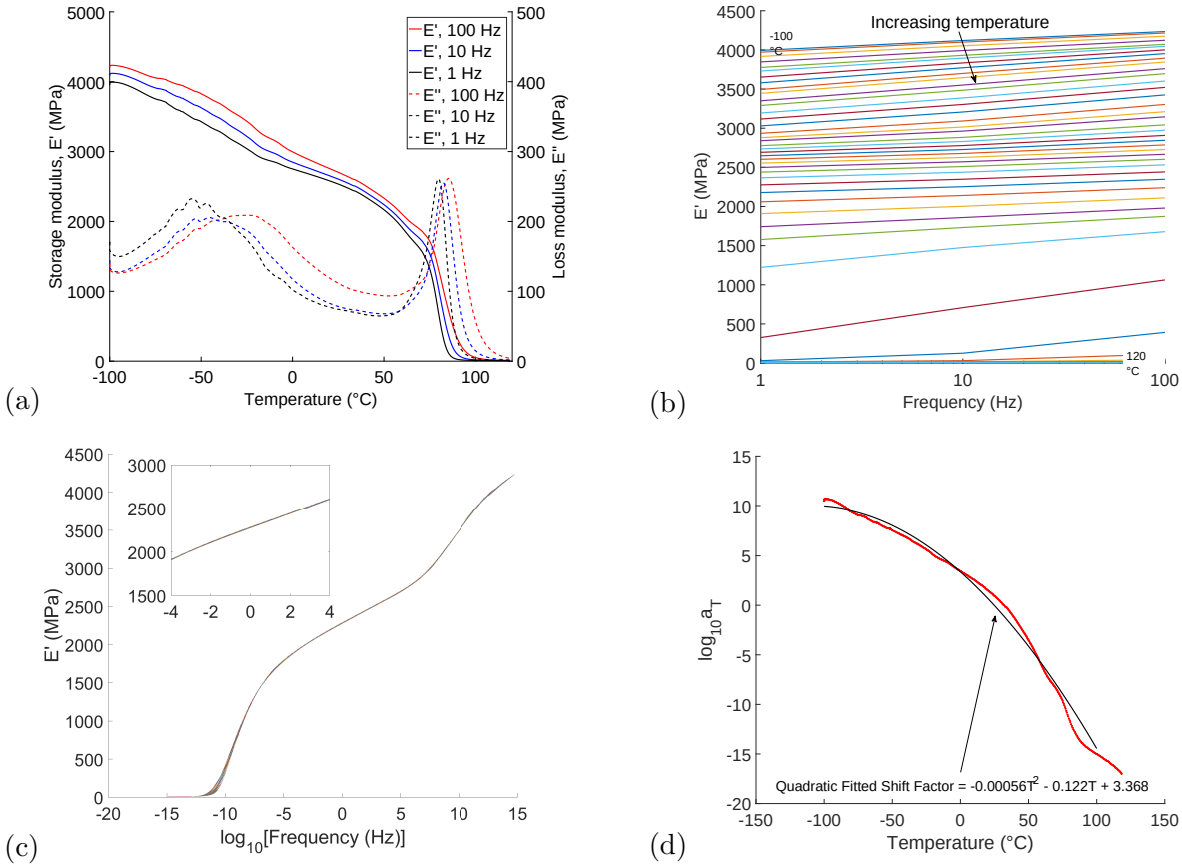

FIGURE 4.5: (a) Results of the DMA experiments, (b) isotherms showing the rate and temperature dependence of the modulus, (c) which are shifted laterally to construct a master curve at a reference temperature of 25 °C, (d) using the shift factors as described.

4.5 Differential Scanning Calorimetry

During high strain rate compression, self-heating of the specimen occurs due to the adiabatic conditions. In order to find the effect on the mechanical response, the resulting temperature rise must be quantified. In the previous chapter, it was shown that the temperature rise can be calculated, using Equation 3.2, as a function of the density, heat capacity and mechanical work done on the specimen. Density remains constant for these incompressible materials, and the mechanical work can be easily calculated experimentally or from the modelling process. What is yet to be determined is the heat capacity. The heat capacity is not constant with temperature, and as a result a Differential Scanning Calorimetry (DSC) experiment was performed to obtain this temperature dependence.

4.5.1 Method

A modulated DSC (MDSC) experiment was performed on a TA Instruments Q2000 DSC to better separate the desired thermodynamic transition behaviour from the kinetics. Calibration for the heat flow, temperature and baseline was conducted using standard manufacturer's procedures. A sapphire sample is used as a calibration standard. For each experiment, less than 10 µg of the sample material was cut into small slivers and crimped into a sealed aluminium pan.

For the MDSC experiments on PVC and PPVC, an underlying ramp of 3 °C min^{-1} was used over the temperature range from −90 °C to 200 °C. This ramp is typical for polymers as it is sufficiently slow to allow four or more modulation cycles over the temperature range of the transitions [208]. The temperature range is selected to cover all transitions in the range of interest for compression experiments. The modulation applied was ±0.5 °C min^{-1}, and was chosen as such for two reasons: the low amplitude provides good resolution, and the slow period compensates for the low thermal diffusivity of (P)PVC. Although 45 seconds is sufficient to analyse transitions in samples up to 15 µg in sealed aluminium pans, the longer duration allows a more

accurate measurement of C_p. A further increase in period would lead to diminishing gains in accuracy but a much larger experimental duration [208]. The modulation amplitude was selected as a trade-off between high resolution at low amplitudes and high sensitivity at large amplitudes.

4.5.2 Results

The results of the MDSC experiment for PVC are shown in Figure 4.6, which match well with literature values [209]. The results are split into reversing and non-reversing heat flow for the contribution from the instantaneous heating rate and the contribution that does not follow the modulation respectively.

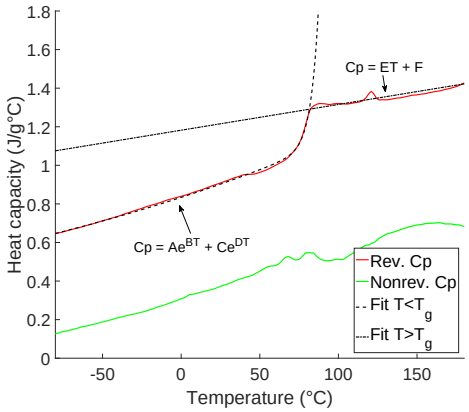

FIGURE 4.6: MDSC results for the PVC with descriptions of the heat capacity either side of the α transition.

Sub-T_g coefficients:

- $A = 7.788 \times 10^{-9}$ J g^{-1} °C^{-1}
- $B = 0.2100$ °C^{-1}
- $C = 0.8337$ J g^{-1} °C^{-1}
- $D = 3.172 \times 10^{-3}$ °C^{-1}

Super-T_g coefficients:

- $E = 1.335 \times 10^{-3}$ J g^{-1} °C^{-2}
- $F = 1.182$ J g^{-1} °C^{-1}

To find the heat capacity, the reversing heat flow as shown by Equation 2.7 is of interest. Two fits to heat capacity are provided, one each side of the glass (α) transition (T_g), to describe its temperature dependence. The coefficients used in the fits are shown to the right of the Figure 4.6.

The heat capacity of a solid at constant pressure can be thought of as the slope of the plot of internal energy versus temperature. Internal energy in a polymeric material corresponds primarily to rotations, translations and vibrations. As the temperature increases, so does the internal energy. There will come a point when there is enough energy to overcome the barrier associated with certain molecular motions. The glass (α)

transition (T_g) represents one such point of significant change in the internal energy. As the temperature increases through the glass transition, the internal energy drastically increases. This increase in the heat capacity is seen for the PVC (Figure 4.6) at 82 °C corresponding to the glass transition of PVC.

Once the glass transition has passed, an additional increase in temperature leads to a smaller increase in internal energy. The rate of increase of internal energy decreases, and as such, the slope of the heat capacity versus temperature curve decreases. At the highest temperatures, the solid has no more energy barriers to overcome and the heat capacity will reach a constant value, that is until melting starts to occur. These high temperatures are not reached in this study.

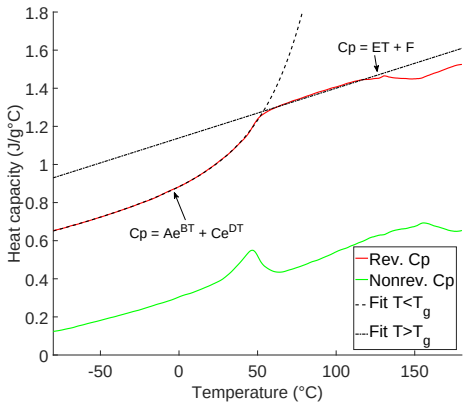

FIGURE 4.7: MDSC results for the PPVC with descriptions of the heat capacity either side of the α transition.

Sub-T_g coefficients:

- $A = 3.015 \times 10^{-2}$ J g^{-1} °C^{-1}
- $B = 3.977 \times 10^{-2}$ °C^{-1}
- $C = 0.8533$ J g^{-1} °C^{-1}
- $D = 3.410 \times 10^{-3}$ °C^{-1}

Super-T_g coefficients:

- $E = 2.613 \times 10^{-3}$ J g^{-1} °C^{-2}
- $F = 1.139$ J g^{-1} °C^{-1}

In a similar manner to the results of the PVC, those for the PPVC are shown in Figure 4.7. For the sub-T_g, and super-T_g fits, the coefficient values are shown to the right of the figure. The dependence of the heat capacity on temperature is very similar to that of the PVC. However, the glass transition for the PPVC is around 52 °C and the increase in heat capacity through the transition is not as sharp. These findings complement those of the DMA experiments (Section 4.4), where it was also observed that the addition of 20 $wt\%$ DINP moves the transition to a lower temperature and broadens it. The dip in the heat capacity at around 130 °C is likely due to volatile loss during the DSC experiment, as opposed to a material transition. Though the boiling

point of DINP is around 400 °C [210], this could represent the boiling of another sub-compound in the commercial formulation of PPVC.

The exact T_g differs, but is in the correct range. The reason for this difference is the varying definitions for T_g in each experiment. For the DMA experiments, T_g was defined as the peak of the loss modulus curve. For the DSC experiments, T_g was defined as the point at which the heat capacity versus temperature slope changes from increasing to constant. Typically, the T_g from DMA experiments is more accurate due to the inherent sensitivity in measurements of dynamic properties to the glass transition, whereas the DSC measurements are on a static sample.

4.5.3 Characterisation of self-heating

Let us consider again the results of the uniaxial compression experiments for the two materials as shown in Figure 4.2a-b. Upon observation of the stress-strain profiles, it appears that at strain rates higher than 10^{-1} s^{-1}, there is less strain hardening at higher strains, which is assumed to be a result of thermal softening. This is to say that the heat produced from the conversion of work during plastic deformation does not conduct out of the specimen on the time-scale of the experiment, and instead causes the temperature to rise, so-called adiabatic heating.

An analytical approximation to the rate above which the experiment may be regarded as adiabatic can be found using Equations 4.5a-c. Initially, the thermal diffusivity is obtained from the conductivity (k), density (ρ) and the heat capacity (C_p). Combining this with the characteristic length of the specimen (here 1.25 mm, half the specimen length), it is possible to find the characteristic time scale for diffusion out of the specimen. An approximate strain rate at which this time-scale becomes significant is thus given by the reciprocal of the characteristic time scale.

$$\alpha = \frac{k}{\rho C_p} \tag{4.5a}$$

$$l_t = 2\sqrt{\alpha t} \Longrightarrow t = \frac{1}{\alpha}\left(\frac{l_t}{2}\right)^2 \tag{4.5b}$$

$$\dot{\varepsilon} \approx \frac{1}{t} \tag{4.5c}$$

Using the conductivity, density and heat capacity values for PVC from Matthews [205], the lower and upper bounds of the diffusivity are 0.088 to 0.150 $\mathrm{mm^2\,s^{-1}}$. Using the characteristic length of the specimen, this gives the strain rate at which adiabatic effects start becoming significant to be approximately 0.5 $\mathrm{s^{-1}}$.

Note that despite being calculated for PVC and not PPVC, the result is broadly the same as the 10^{-1} $\mathrm{s^{-1}}$ observed experimentally for both materials. In any case, the exact value is not of importance as much as the order of magnitude, since the rate dependent material properties depend on the logarithm of the strain rate.

Once the temperature dependent heat capacity is known, the temperature rise due to this adiabatic self heating can be calculated using:

$$\Delta T \approx \frac{\beta}{\rho C_p(T)} \int_0^{\varepsilon} \sigma(\varepsilon) d\varepsilon \tag{4.6}$$

where β is the Taylor-Quinney coefficient dictating the amount of mechanical work that is transferred to heating the specimen. Unless stated otherwise, it is assumed that $\beta = 1$ and all mechanical work is converted to heat. As the deformation is typically associated with a reduction in entropy with no change in internal energy, it is fair to assume that all external work gets converted to heat in the sample. Figure 4.8 shows the approximate expected temperature rises for the adiabatic compression experiments in PVC (a) and PPVC (b) when the effect of the evolving heat capacity is included. This information can now be included in the modelling framework.

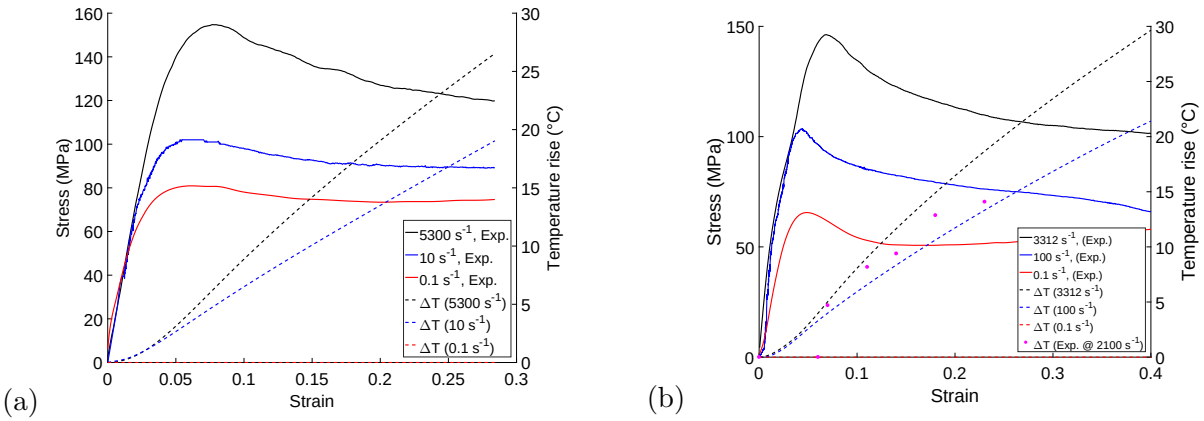

FIGURE 4.8: (a) Calculated temperature rise due to self heating for PVC and (b) for PPVC.

For PPVC, the experimental temperature measurements from Kendall's research [70] are also included for comparison. It can be observed that the calculated expected temperature rises are in line with his measurements. There are limitations with the experimental measurements that may have caused the small discrepancies: finite time is taken for heat to diffuse to the thermocouple, coupled with the poor time resolution, could mean that the measured values are for earlier times. Furthermore, a poor contact between the thermocouple and specimen could also lead to errors. Another difference is that the calculated rises presented here are better defined than those in [70], as more accurate temperature dependent heat capacity values are used for this specific formulation of P/PVC.

4.6 Modelling framework

In the previous chapter, a rate dependent hyperelastic model was introduced. Although it fared well at capturing the high rate rubbery behaviour of neoprene with only two parameters, it had a few limitations. The modelling framework required a multitude of experiments conducted at various strain rates for parameterisation, the predictive capability was therefore lacking since high rate experiments were conducted prior to the modelling, and post-yield thermal softening and rate dependent plasticity was not taken into account. In this section, a novel modelling framework will be presented that overcomes such limitations.

4.6.1 Requirements

Looking back at the varying strain rate experimental results in Figure 4.2a-b, the glassy mechanical response for both PVC and PPVC is governed by the following behaviour: low strain viscoelasticity, non-linear shift to yield, post-yield strain softening and large strain hyperelasticity. These observations will require different modelling components in order to accurately describe the behaviour, which are outlined below.

4.6.1.1 Hyperelasticity

In order to describe the large elasticity that many polymers exhibit, a linear elastic model like Hooke's law is often inadequate. To capture this type of non-linear elasticity, a hyperelastic model is needed. Many models have been proposed for this behaviour: the early invariant based continuum Mooney-Rivlin model [136, 137]; the continuum stretch based Ogden model [141]; and the macromolecular Langevin chain statistic based Arruda-Boyce model [143, 211]. In this research, the Langevin model is used.

Although these models are popular for capturing large stretch dominated elasticity, by themselves, their use is limited as they cannot describe plasticity or rate dependence. Suitable adaptations, such as the inclusion of rate dependence and thermal effects must be made in order to incorporate these features into the overall model.

4.6.1.2 Viscoelasticty

Despite the fact that the rate dependence of many materials has been known for some time [126, 128], the modelling of this behaviour can still be quite challenging. A common method to describe viscoelasticity has been to make use of linear combinations of springs and dashpots, which can be generalised with numerous such elements forming a Prony series [147, 212]. However, this approach has many disadvantages, one of which is the fact that each decade of frequency typically requires an element in the Prony series to describe the viscoelastic behaviour appropriately, thereby adding numerous parameters requiring characterisation.

A more satisfactory approach is shown below in which a more generalised fractional derivative model (FDM) [161, 162, 213] will be fitted to the results of the DMA experiment in order to describe the non linear viscoelastic behaviour.

4.6.1.3 Viscoplasticity

For large strain, glassy behaviour, viscoplasticity must be included in the model. Rate dependent plasticity has been implemented previously with the Mulliken-Boyce (MB) model [183, 184], and this is the model that forms the basis of this study. The model includes the effects of thermal softening through adiabatic heating by explicitly increasing the temperature based on the theoretical increases as calculated above [185]. However, the seamless integration of the effects of adiabatic heating into a model with predictive capabilities at high strain rates, entirely calibrated at low strain rates, has not been fully explored and is therefore the focus of this study.

4.6.2 Modifications to the Mulliken-Boyce model

The Mulliken-Boyce model is enhanced to capture some of the phenomenological nuances observed. These primarily relate to the description of the modulus used, and the thermal relaxation of the modulus due to adiabatic self-heating.

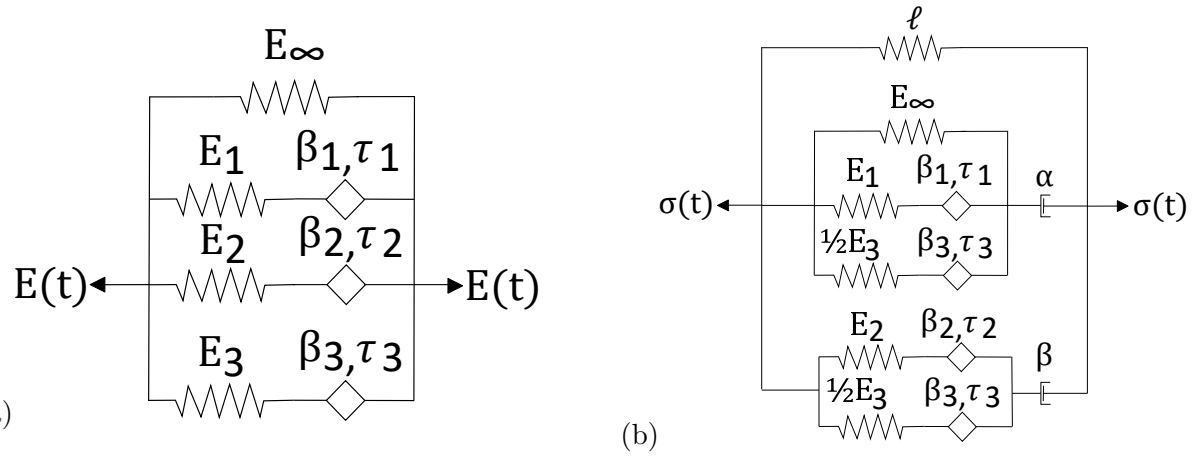

FIGURE 4.9: (a) The relaxation modulus with an FDM fit to the DMA results and (b) of the combined model as used in this research.

4.6.2.1 Fractional derivative model

The Mulliken-Boyce model is based on the premise that since the molecular motions of the α and β processes are rate and temperature controlled, by using the results of a DMA experiment, and in particular information about the rate dependence of α and β transitions, each transition is shifted independently to room temperature and then reconstructed to obtain the high rate behaviour at the temperature.

At this point, they assume the modulus is constant and there is no relaxation at all during the experiment. Since this is not true, the temporal relaxation of the modulus must be included in the modelling process. In order to define the modulus in Equation 2.26 over a wide range of rates, conventionally a Prony series as described in Equation 4.7 would be used, where E_∞ is the long term modulus, E_i is the modulus for an individual element, and t_i is the relaxation time for that element.

$$E^* = E' + iE'' = E_\infty + \sum_{i=1}^{N} \left[E_i \frac{if}{if + t_i^{-1}} \right] \tag{4.7}$$

The disadvantage with using this definition is that in order to get an accurate depiction of the modulus, a very large number of elements is needed. In this application, over the frequency ranges described in the master curve in Figure 4.5c, at least 25 elements would be required, each with an unknown requiring parameterisation. Meanwhile, with a FDM as decribed in Equation 4.8 (and Figure 4.9a), the number of parameters can be reduced to a minimum of seven for the same frequency range (namely the long term modulus, and three parameters for each transition present).

$$E^* = E' + iE'' = E_\infty + \sum_{i=1}^{M} \left[E_i \frac{(if)^{\beta_i}}{(if)^{\beta_i} + t_i^{-\beta_i}} \right] \tag{4.8}$$

Hence, the FDM is a preferable choice for representing the modulus over a wide frequency range. The new parameter β lies between zero and one, and dictates the slope of the transition in modulus with frequency, which is not therefore necessarily a rapid change, as is the case with a single Maxwell element. Note the similar forms of Equation 4.7 and Equation 4.8. The physical representation is that when all of the β terms are one, the model represents a Newtonian fluid and the FDM reduces to the Prony series, and when they are zero, the model represents a linear elastic body. Most materials exhibit a mixture of these behaviours, hence the FDM offers a more meaningful model to fit to this type of non-linear viscoelastic behaviour.

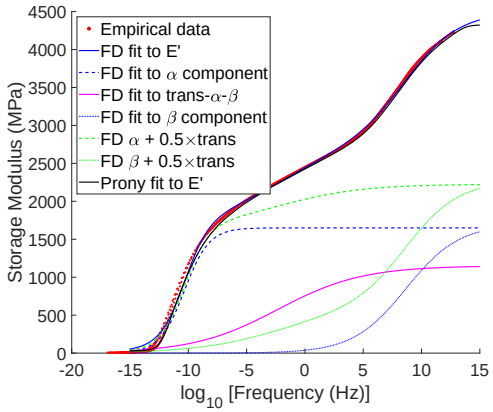

FIGURE 4.10: Fitting traditional Prony series and FDM to the DMA master curve.

In this application, both Prony series and FDM representations are applied to the DMA results, for comparison; the parameters are shown in Table 4.1, and the fits in

Figure 4.10. Using the three element version of the FDM as in Figure 4.9a, the additive sum of three elements along with the long-term modulus gives the full response. The three elements used explicitly represent the alpha and beta transitions, and also a third transition representing the change in modulus between the first two.

The biggest advantage of the FDM representation is that it complements the Mulliken-Boyce modelling framework, because it explicitly captures the modulus changes through the two transitions. It is for this reason that it is preferred to the conventional Prony series. A two component fractional derivative model would map directly to the two terms (α and β) used for viscoplasticity, making each FDM component physically meaningful. In order to maintain this advantage when the model was implemented in this study, the FDM branch associated with the third transition was split into two and allocated equally to the α and β components, which is shown schematically in Figure 4.9b.

TABLE 4.1: Parameters used for the Prony and Fractional fits to the DMA data.

Prony series (MPa)	E_∞	E_1	E_2	E_3	E_4	E_5	E_6	E_7	E_8	E_9
	30.39	113.9	114.9	127.7	160.7	207.3	210.8	209.1	191.1	138.2
	E_{10}	E_{11}	E_{12}	E_{13}	E_{14}	E_{15}	E_{16}	E_{17}	E_{18}	E_{19}
	107.9	90.19	82.97	81.04	81.8	80.81	86.94	72.88	110.2	82.12
	E_{20}	E_{21}	E_{22}	E_{23}	E_{24}	E_{25}				
	127.0	178.0	219.3	347.9	362.5	598.6				

Fractional model	E_∞ (MPa)	E_1 (MPa)	β_1	t_1 (s)	E_2 (MPa)	β_2	t_2 (s)	E_3 (MPa)	β_3	t_3 (s)
	3	1650	0.41	4×10^7	1150	0.12	4×10^{-1}	1700	0.19	4×10^{-12}

4.6.2.2 Thermal relaxation of the modulus

The evolution of the modulus during loading is considered as follows. The storage modulus from the DMA experiments describes the dependence on frequency. The frequency is approximately equal to the reciprocal of the time. For a given constant strain rate, $\dot{\varepsilon}$ and a maximum strain ε_{max}, the test is conducted over a time $t_{max} = \varepsilon_{max}/\dot{\varepsilon}$. The storage modulus, expressed in terms of angular frequency, can then be related to the relaxation modulus using an interconversion approximation [214]:

$$E(t) \approx E'(f)|_{f=1/t} \tag{4.9}$$

where t goes from zero to t_{max}. However, since the modulus at $t = 0$ is undefined, its value is taken to be the same as that for the second time-step in this approximation.

In characterising the self-heating phenomenon, the temperature rise for each simulation was obtained using Equation 4.10, where only plastic strain gives a temperature rise since stored elastic strain energy is recovered:

$$\begin{aligned} \dot{\theta} &= \frac{\beta}{\rho C_p(\theta)} \frac{d}{dt} \int_0^{\varepsilon} \sigma d\varepsilon^p \\ &= \frac{\beta}{\rho C_p(\theta)} \frac{d\varepsilon^p}{dt} \frac{d}{d\varepsilon^p} \int_0^{\varepsilon} \sigma d\varepsilon^p \\ &= \frac{\beta}{\rho C_p(\theta)} \dot{\varepsilon^p} \sigma \end{aligned} \tag{4.10}$$

Although the MB model includes the change in θ explicitly, its effect on the evolution of modulus is not captured. In this modelling framework, the thermal evolution of the relaxation modulus is incorporated: the master curve describing viscoelasticity is shifted according to the temperature resulting from the adiabatic heating.

In order to obtain the modulus at a given temperature above the reference temperature, $E'(\log f, T_0 + \Delta T)$, there are two possible approaches as seen in Figure 4.11a. One is to fully reconstruct the master curve at the new temperature and read off the value of the modulus at the frequency of interest. This however is cumbersome when

the modulus is required at each incremental temperature increase due to the adiabatic self-heating effect. The alternative method is to use the same master curve for the reference temperature, but read off the value at a frequency lower than that of interest, $E'(\log f - \log a_{\Delta T}, T_0)$, where $\log a_{\Delta T}$ is also a function of temperature.

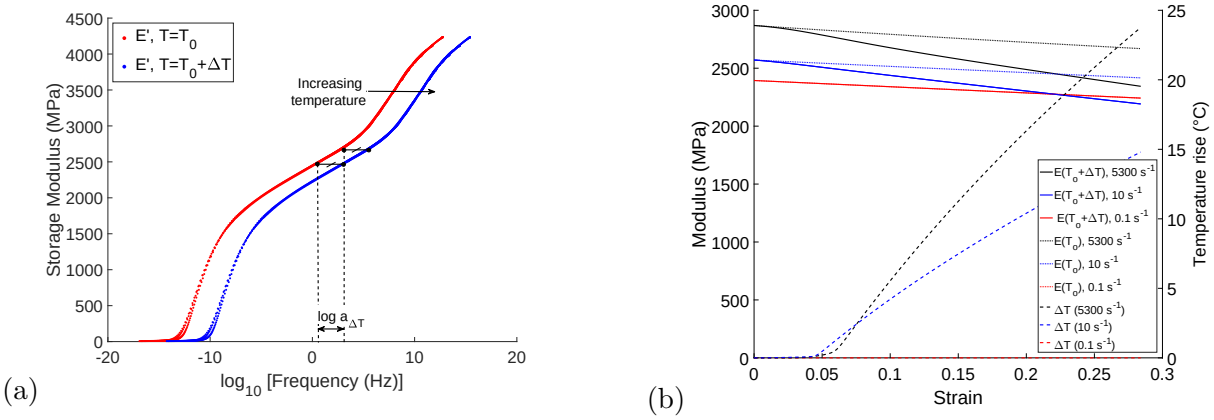

FIGURE 4.11: (a) Graphical representation of shifting the master curve for an increasing temperature and (b) highlighting the additional relaxation of the modulus due to temperature rise.

Since the temperature dependence of the shift factors is known (Figure 4.5d), the additional shift required to compensate for the higher temperature and take the master curve from the reference temperature (which is the same as that of the uniaxial experiments for the room temperature experiments, $T_0 = 25$ °C) to the increased temperature is simply obtained by substituting $T - \Delta T$ for T. At each timestep, this calculation is performed to obtain the temporally and thermally relaxed modulus to be used in the modelling framework as shown in Figure 4.11b. From this figure, it is clear to observe that the temperature rise causes the modulus to relax more than just the relaxation with time, and is therefore important to include in the modelling process.

4.6.3 Enhanced Fractional Thermo-Visco-Hyperelasto-Plastic (FTVHEP) model

In this section, the procedure will be described for applying the modelling framework to PVC in order to obtain the relevant parameters for the model. The process is conducted in the same way for the PPVC.

4.6.3.1 Langevin component

For the hyperelastic Langevin stress component, there is only one parameter that needs identifying - the limiting chain extensibility, $\sqrt{N}$. This can be obtained by applying Equation 4.11 to fit to the lowest rate quasistatic compression experiment. This is as the large strain response is dominated by the hyperelastic component.

$$\sigma = \frac{E_\infty}{3}\frac{\sqrt{N}}{\lambda_{chain}}\beta_{chain}\left(\mathrm{e}^{2\varepsilon} - \mathrm{e}^{-\varepsilon}\right) \tag{4.11}$$

Further details on the derivation of this equation are given in Chapter 2, §2.5.1.2.

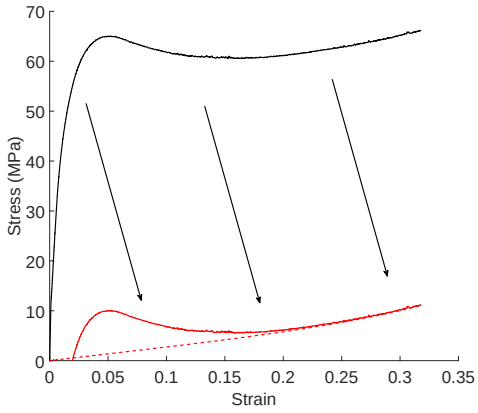

FIGURE 4.12: Obtaining the Langevin limiting chain extensibility, $\sqrt{N}$ parameter.

As seen in Figure 4.12, the experimental results for the uniaxial compression conducted at 10^{-3} s^{-1} is shifted downwards to isolate the large strain hyperelastic component. In this way, the Langevin model can be fit to obtain the value of $\sqrt{N}$.

4.6.3.2 α component

The α component, relating to the glass transition, dominates at lower strain rates. For this reason, the parameters associated with the α component were obtained by fitting the σ_α expression (as described in Chapter 2, §2.5.4.1) to the low rate experiments conducted from 10^{-3} s^{-1} to 10^{-1} s^{-1}.

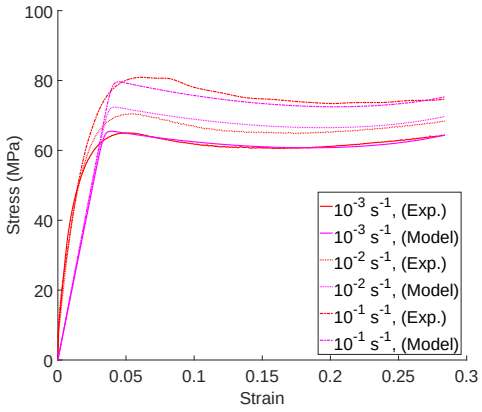

FIGURE 4.13: Obtaining the α parameters from the low strain rate experiments.

The results of the fitting can be seen in Figure 4.13. Both the yield stress and the large strain response are captured extremely well. There is however some discrepancy between the initial modulus as obtained from the experiments and that obtained from the FDM. The non-linear pre-yield behaviour is hard to capture with the MB model since for the α element, there is only one activation energy. In polymers however, there is a spectrum of energies associated with the varying length chains in the microstructure. This feature of the experimental response can be captured in a future model iteration by considering a distribution of activation energies, as is done in the Hasan-Boyce model, for example [215].

The parameters that are fitted in this step are the pre-exponential coefficient related to the attempt frequency ($\dot{\gamma}^p_{0,\alpha}$), the activation energy (Q_α), the steady state athermal shear strengh ($s_{ss,\alpha}$), the softening slope (h_α) and the pressure coefficient ($\alpha_{p,\alpha}$) for the α transition.

4.6.3.3 β component

Once the α component parameters are found and fixed, they can be used whilst allowing the β component parameters to vary and best fit to the low rate compression experiments at varying temperatures. These experiments are chosen for the fits since the β component to the mechanical response is only active at either low temperatures or high rates. The experiments required for parameterisation were those conducted at strain rates of 10^{-2} s^{-1} and temperatures from -60 °C to 0 °C. The experimental and modelling results for 25 °C are presented for completion.

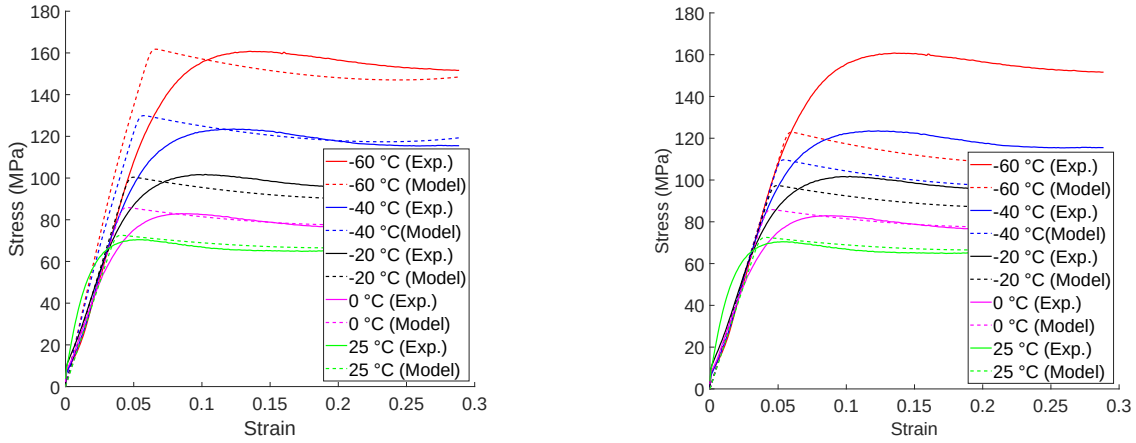

FIGURE 4.14: (a) Obtaining the β parameters from the low rate varying temperature experiments, and (b) illustrating what the modelled curves would look like without the β component.

The results of the fitting are seen in Figure 4.14. Once again, the yield stress is captured very well. The initial modulus varies for the different temperatures. Broadly speaking, the large strain response is well captured for all of the experiments, however they could be better for the -60 °C and the -20 °C experimental fits. Further experiments at these temperatures could help to understand how much of this discrepancy is due to experimental variation.

The parameters that are fitted in this step are the pre-exponential coefficient related to the attempt frequency ($\dot{\gamma}^{p}_{0,\beta}$), the activation energy (Q_{β}), and the pressure coefficient ($\alpha_{p,\beta}$) for the β transition. Since the β component is not expected to soften, the steady

TABLE 4.2: Parameters for the enhanced FTVHEP modelling framework and how they were obtained.

Parameters for the Mulliken-Boyce based FTVHEP modelling framework: PVC			
Parameter	α	β	**How the parameter is obtained**
Shear modulus, μ	551 MPa	567 MPa	Calculated based on ν and E_i
Athermal shear strength, S_0	84.9 MPa	87.3 MPa	Calculated based on μ_i
Pressure coefficient, α_p	0.999	0.0349	Curve fits, low rate data in [3]
Pre-exponential factor, $\dot{\gamma}_0$	6.33×10^{19} s^{-1}	9.64×10^{16} s^{-1}	Curve fits, low rate data in [3]
Activation energy, Q	3.28×10^{-19} J	1.53×10^{-19} J	Curve fits, low rate data in [3]
Softening slope, h	75.3 MPa	N/A	Curve fits, low rate data in [3]
Steady state athermal shear strength, S_{ss}	41.0 MPa	N/A	Curve fits, low rate data in [3]

Parameters for the Mulliken-Boyce based FTVHEP modelling framework: PPVC			
Parameter	α	β	**How the parameter is obtained**
Shear modulus, μ	554 MPa	567 MPa	Calculated based on ν and E_i
Athermal shear strength, S_0	85.3 MPa	87.3 MPa	Calculated based on μ_i
Pressure coefficient, α_p	0.999	0.0087	Curve fits, low rate data in [3]
Pre-exponential factor, $\dot{\gamma}_0$	2.18×10^{20} s^{-1}	1.64×10^{17} s^{-1}	Curve fits, low rate data in [3]
Activation energy, Q	2.97×10^{-19} J	1.81×10^{-19} J	Curve fits, low rate data in [3]
Softening slope, h	308 MPa	N/A	Curve fits, low rate data in [3]
Steady state athermal shear strength, S_{ss}	48.7 MPa	N/A	Curve fits, low rate data in [3]

state athermal shear strengh ($s_{ss,\beta}$) and the softening slope (h_β) do not exist in this model. The parameters required are shown in Table 4.2.

The fitted activation energy parameters for the glass transition (Q_α) and the secondary transition (Q_β) can be compared to the values obtained from DMA experiments in §4.4.2.1, Figure 4.4. By dividing the molar values from the experiment by the Avogadro constant, $Q_{\alpha,\mathrm{DMA}} = 6.61 \times 10^{-19}$ J and $Q_{\beta,\mathrm{DMA}} = 0.97 \times 10^{-19}$ J. From Table 4.2, the energy parameters are $Q_\alpha = 3.28 \times 10^{-19}$ J and $Q_\beta = 1.53 \times 10^{-19}$ J. Although different, the experimental measurements are the correct order of magnitude, and the value for the secondary transition is lower than the alpha transition. In future, the modelling process could be performed using the activation energies found through the DMA experiments.

Altogether there are nine parameters to characterise from fits to quasi-static compression experiments: one for Langevin hyperelasticity, five for the α transition and three for the β transition. These parameters can now be fixed and used alongside the parameters obtained from the FDM fit to the master curve in order to predict the mechanical response at high strain rates.

4.7 Modelling results

The purpose of this modelling framework is to be able to *predict* the mechanical response of the PVC and PPVC at high strain rates. None of the parameters in the modelling framework have been obtained from high rate experiments. Due to this, true predictions for the high strain rate behaviour can be made.

4.7.1 High rate predictions

The predictions for the mechanical response of PVC at various strain rates up to c. 10^3 s^{-1} and their comparisons to compression experiments are presented in Figure 4.15a. Similarly, Figure 4.15b shows the same for the PPVC obtained by following the same modelling procedure as outlined above.

For the PVC, the predicted high rate mechanical response matches the experimental results exceptionally well. This fact gives more confidence in the predictions for the intermediate strain rates, since those experiments are challenging to perform with a constant true strain rate. The incorporation of the adiabatic effects can also be seen where the large strain response is not dominated by hyperelasticity as it is for the lower strain rates.

On the whole, the predictions for the PPVC are also very good and closely match experimental results from the previous study. There is some discrepancy at the intermediate strain rates, however this could also be due to the challenge with performing experiments at these rates. Careful experiments can be done at these rates in the future – for example, with the use of a longer SHPB – to interrogate this further.

To the author's knowledge, the ability to predict the full mechanical response of PVC and PPVC at these strain rates is something that has not previously been achieved and represents a significant contribution to research on the dynamic behaviour of materials.

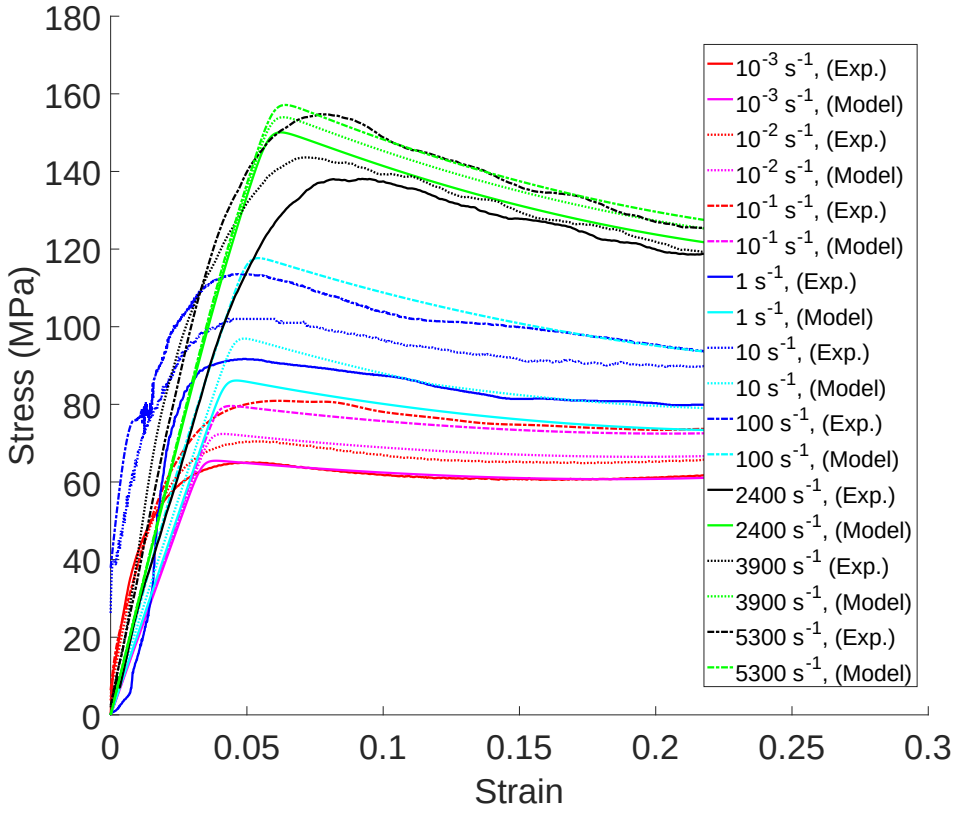

(a)

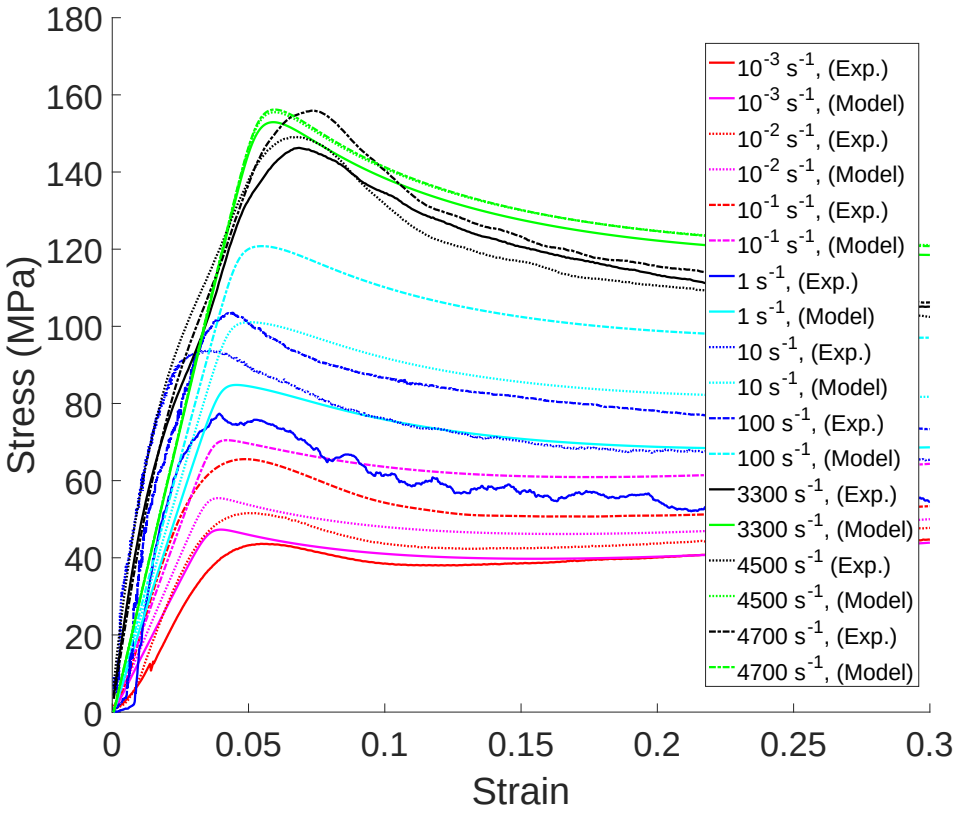

(b)

FIGURE 4.15: (a) Predictions and comparisons with experimental results for the entire mechanical response for PVC and (b) for PPVC.

4.7.2 Peak stresses

In literature, it is common to plot the yield or peak stress variation with the logarithm of the strain rate. For this reason, Figure 4.16a shows the predicted peak stresses of PVC and the experimental comparisons, and Figure 4.16b shows the same for the PPVC.

For the PVC, the peak stress predictions match very closely to the experimental results, as is expected since the whole stress-strain profile matched well for the PVC. For the PPVC, there is a consistent over-prediction for the peak stresses, with the largest discrepancies being for the intermediate strain rates. Due to the challenge in characterising the behaviour at these strain rates, the discrepancy is exacerbated. However, for a predictive model, the peak stresses for this material are well captured too.

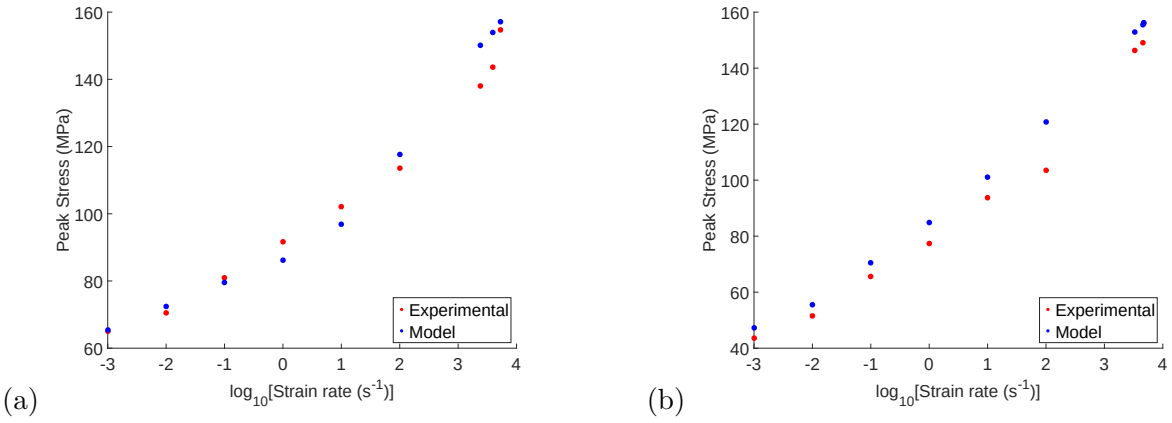

FIGURE 4.16: (a) Predictions and comparisons with experiments for the peak stresses for PVC and (b) for PPVC.

4.7.3 Effect of heating

In Section 4.5, the self heating at high strain rates was characterised and it was found that at rates above c. 10^{-1} s^{-1}, self heating of the specimen during the time-scale of the compression experiment must be considered. To highlight the effect of self heating, Figure 4.17 shows the difference in predictions for PVC with a model incorporating self heating through adiabatic effects, and one that is purely isothermal.

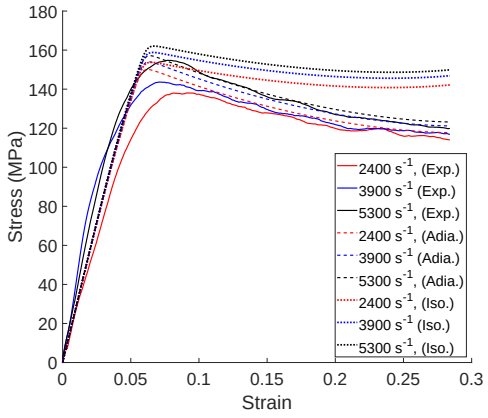

FIGURE 4.17: Comparing adiabatic and isothermal model predictions for PVC at high rate.

4.7.4 Simulating adiabatic experiments

In a previous study involving the PPVC [70], an experimental method was proposed that would effectively simulate high rate experiments with ones performed at lower rates and lower temperatures, but with a gradually increasing temperature during the experiment. The selection of the low temperature was based on the temperature at which the initial modulus and yield stress behaved similarly to that of the high rate experiment. Application of this technique is also possible within the modelling framework presented in this chapter.

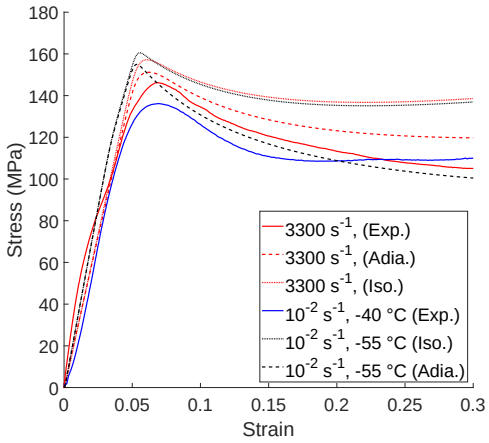

FIGURE 4.18: Using the model to simulate adiabatic conditions for PPVC with low rate low temperature experiments using an increasing temperature profile.

Figure 4.18 shows the experimental results for specimen compressed at 3300 s^{-1} (red solid) and the modelled high rate prediction (red dashed). In order to experimentally simulate this high rate result, a quasistatic experiment conducted at 10^{-2} s^{-1} and -40 °C (blue solid) is selected as it shows the most similar modulus and yield response to the high rate one. However, the differences are that the yield is slightly lower and that the larger strain response shows an upturn in stress, which is characteristic of isothermal conditions where there is no thermal stress softening.

Therefore, to better simulate the high rate experiment, the modelling framework described in this chapter is used. Firstly, the temperature is reduced for a simulation at 10^{-2} s^{-1}, in this case, from -40 °C to -55 °C (black dotted). The decreased temperature increases the yield strength and better matches the isothermal modelled result at 3300 s^{-1} (red dotted). The self heating is subsequently 'switched on' to better replicate the high rate experiment (black dashed). This method enables the adiabatic experiments to be simulated using this modelling framework, where in [70], this was done experimentally.

It may seem as if the simulated adiabatic response is better at capturing the high rate response of the PPVC, but it should be noted that the adiabatic simulation run at low temperature does not take into account the fact that the modulus for a model run at 3300 s^{-1} would be larger at all strain values considered than that for the 10^{-2} s^{-1}

simulation at −55 °C leading to higher calculated stresses. Furthermore, the viscoplastic effect would also influence the predicted stress for the high rate model prediction, leading to a higher response than the adiabatic simulation of the response despite the isothermal curves for both looking similar. Further research is needed to link the temperature-frequency dependence of the modulus and the yield stress.

The key benefit in using this modelling framework for adiabatic simulations is that no further experiments need to be conducted other than those required to parameterise the model in the first instance, and the one needed for comparison at high rate. Additionally, by comparing the modelling results with experimental findings, new insights could be generated.

4.8 Conclusions

In this chapter, it was shown that it is possible to use a combination of modelling techniques to *predict* the full stress-strain response of high rate compression experiments for both PVC and PPVC.

Starting with the MB model as a base, enhancements were made to allow this predictive capability. A relaxation modulus that not only shows its temporal decay via an approximation, but the drop associated with self heating of the specimen is included by considering the appropriate shifting of the master curve based on the TTS technique. By using a FDM representation for the modulus, not only was the number of parameters required greatly reduced when compared to the conventional Prony series representation, but the α and β elements in the FDM mapped directly onto the α and β elements in the MB model.

After incorporating these changes, the enhanced model was calibrated using solely quasi-static experiments at varying low rates and varying temperatures. Predictions for the high rate mechanical response were then made using the model and validated against carefully conducted experiments from a previous study [3] and shown to match very closely. In this chapter, the pressure dependence is obtained through compression experiments solely, which is not ideal since the yield stress in compression is more than that in tension and so at the very least both sets of experiments should be used. These incremental improvements can be made in the future.

The effect of self heating in the model was also investigated to show that the temperature increase during the higher rate experiments cannot be neglected in the modelling process and must be included. Furthermore, it was shown how this modelling framework can assist in the simulation of adiabatic experiments. Upon calibrating the model at varying low strain rates at room temperature, and varying low temperatures at a constant low strain rate, this model is able to provide insight into various isothermal and adiabatic experiments.

In future, this novel modelling framework will be able to form the basis of predicting

the high strain rate compression response for numerous materials where the behaviour is strongly rate and temperature dependent. The predictive capabilities of this modelling framework will therefore reduce the number of high rate experiments needing to be conducted as they would only be required for validation purposes and to interrogate particular rates of interest.

The next two chapters will focus on the application of the TTS-based modelling frameworks presented thus far to unfilled and filled natural rubber.

Modelling framework overview

In this section, the modelling framework used in this chapter is presented as a flowchart (Figure 4.20) and detailed with step-by-step information to guide the user.

Quasi-static and thermomechanical experiments

The first step is to conduct the various quasi-static and thermomechanical experiments required in the modelling framework. DMA experiments are conducted over a range of temperatures covering the transitions of interest, and at discrete frequencies. This combination allows the temperature and frequency (or rate) dependent properties of the material to be obtained. Quasi-static compression experiments are also performed both at an ambient temperature and a variety of low strain rates, and at sub-ambient temperatures at a fixed low strain rate. DSC experiments allow for the temperature dependent heat capacity to be deduced, alongside a corroboration of the transition temperatures for the material.

Obtaining E(t)

Starting with the results of the DMA experiments, one constructs a master curve to obtain the frequency dependence of the storage modulus, $E'(f)$, for a fixed reference temperature (usually set to room temperature). Once the master curve has been constructed, a function can be fit to it in order to describe its form. Traditionally, a Prony series of Maxwell elements has been used as a fitting function. This requires an additional element per decade of frequency covered by the master curve. By using a FDM representation, the number of fitting parameters is drastically reduced from two per element per decade of frequency for the Prony series (plus one to describe the long-term modulus) to three per element (plus one). The key difference is that with the FDM, one element can accurately describe the transition behaviour across many decades of frequency. In PVC and PPVC, there are two transitions and so a minimum of two elements of the FDM are required. Since there is a complex interaction

between the two transitions, an extra element is introduced to describe the behaviour in between the two distinct transitions. A big advantage of using a two component FDM over the Prony series is that the components map directly to the two terms used for viscoplasticity in this modelling framework. In order to maintain this advantage when the model was implemented in this study, this third element's contribution to the modulus is split evenly between the two elements describing the α and β transitions.

The task now is to convert from $E'(f)$ to the relaxation modulus, $E(t)$. When using the FDM, analytical conversions only exist for special cases of the fractional power, and so for arbitrary fractional derivatives, numerical interconversion methods may be used [166, 167]. A further approximation to this numerical conversion can simply state $E(t) \approx E'(f)$, where $f = 1/t$, this was deemed sufficient for obtaining the temporally relaxing modulus for the purposes of this modelling framework.

Error mitigation in master curve construction

In attempting to understand the extent to which isotherms characterised by only three data points per temperature (PPT) can be used to accurately construct the master curve, the following modelling based investigation is undertaken.

Start with the DMA based experimental master curve modelled with the Prony series (Equation 4.7, Table 4.1). By making use of the temperature dependent shift factors (Figure 4.5d), a series of smooth isotherms can be defined. Each isotherm shows the dependence of the storage modulus on the frequency. By multiplying the frequencies of interest with the shift factor, a_T at a particular temperature from Figure 4.5d, reduced frequencies are obtained. Substituting these reduced frequencies into Equation 4.7 give the values of the storage moduli as required for the reconstructed isotherm at that temperature. The temperature range was kept the same as the original DMA experiment; from -100 °C to 120 °C in 2.5 °C steps. For the isotherms characterised by three PPT, the same frequencies as the DMA experiments were chosen; 1, 10 and 100 Hz. For the series of smoother isotherms, the frequencies described in the ISO

standard [216] were used; 0.1, 0.2, 0.3, 0.5, 1, 2, 3, 5, 10 and 20 Hz. These smooth isotherms are each characterised by ten PPT as opposed to the experimental isotherms, which were only three PPT.

The shifting algorithm as defined above is then employed to construct the master curve. For the sake of completeness, reconstructed isotherms characterised by only three PPT are also used to produce a master curve, in order to compare directly with the original master curve presented in this paper.

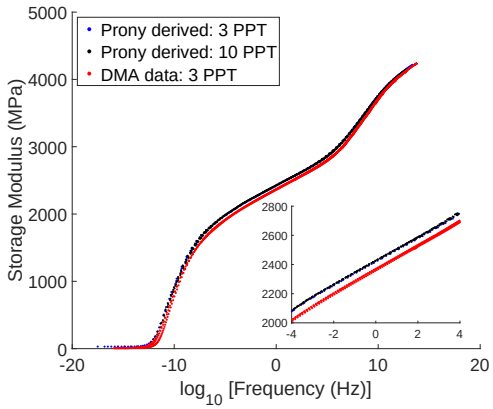

FIGURE 4.19: Comparison of master curves constructed with either three PPT or ten PPT. For completeness, the original master curve is also provided.

By comparing the master curves produced with isotherms characterised by either three or ten PPT, it is possible to determine whether a master curve can be produced with short segments. In Figure 4.19, these master curves are shown for comparison. As is evident, there is no significant inaccuracy resulting from using only three points to characterise each isotherm as the master curves effectively overlap each other perfectly. There is some discrepancy between the master curves produced using the Prony series and temperature dependent shift factors versus the original master curve using empirical shift factors. This is due to slight inaccuracies in using the quadratic shift factor definition to model the empirical shift factors measured, especially at 25 °C, as can be seen in Figure 4.5d. This results in a 0.8 decade mismatch between the empirical master curve and the two Prony derived reconstructions.

In order to mitigate the additive nature of the error in constructing the master curve, an additional shift factor has been introduced. The purpose of this 'zero-shift' factor is to take the whole master curve once it has been constructed and translate it such that the value of the shift factor at the reference temperature is zero. Further confidence in the accuracy of the constructed master curve is provided by the fact that they can be used in the modelling strategy presented in this chapter to accurately predict the mechanical response of (P)PVC. If there were significant errors, then the viscoelastic definition at a given strain rate would not be accurate and the model would not have been able to predict the behaviour with such fidelity. Of course, the overall modelling approach proposed can be used with any suitable TTS methodology.

Obtaining E(t,T)

From the DSC experiments, functions can be fit to the results of the heat capacity versus temperature graphs to describe this dependence and enable its implementation into the modelling framework. Here two fits were required, one to describe the dependence before the transition temperature, and one to describe the dependence post-transition.

For high strain rate simulations, since the temperature rise due to adiabatic effects and its effect on the modulus must be considered, information from the DMA and DSC experiments have to be combined to obtain $E(t, T)$. Since the FDM expression can lead to $E(t)$, it forms the foundation. Initially, the modulus for the simulation is taken as the room temperature value, which is also what the FDM uses as the reference temperature. Until the plastic strain is non-zero, this remains true. Once the plastic strain increases, Equation 4.10 can be used calculate the incremental temperature rise at each integration step. By using the same master curve for the reference temperature, one can read off the value at a frequency lower than that of interest, $E'(\log f - \log a_{\Delta T}, T_0)$, where $\log a_{\Delta T}$ is also a function of the temperature. Since the temperature dependence of the shift factors is known, the additional shift required to compensate for the higher temperature and take the master curve from the reference temperature to the increased

temperature is simply obtained by substituting $T - \Delta T$ for T. At each timestep, this calculation is performed to obtain the temporally and thermally relaxed modulus to be used in the modelling framework.

Obtaining Langevin parameters

In order to obtain the Langevin ($\mathcal{L}$) parameters, the results to the lowest strain rate uniaxial compression experiments are required. Since the mechanical response of the lowest strain rate ambient compression is dominated by the large-strain hyperelastic response, by fitting to it with the Langevin stress expression, it is possible to obtain the two parameters: E_0, the long-term rubbery modulus and $\sqrt{N}$, the limiting chain extensibility based on random walk statistics.

Obtaining α parameters

The α component dominates the response at low strain rates, and for this reason its parameters are obtained by fitting to ambient uniaxial compression experiments at a variety of low strain rates. The modulus used in these fittings are obtained directly from the FDM α element, which is supplemented by half of the transitory third element. Since these experiments are at low strain rates, there is no need to worry about the thermal softening of the modulus. Fits are made simultaneously to all relevant curves using a least squares minimisation scheme. Once obtained from these fits, the α parameters are fixed.

Obtaining β parameters

By noting the time-temperature equivalence in that the observed mechanical response at low temperatures is akin to the response at high strain rates and an ambient temperature, the remaining model parameters of the β viscoplastic element are fitted to low rate uniaxial compression experiments conducted at low temperatures. This is possible since the molecular motions associated with the β transition are inhibited by

a low temperature, and also by the lack of time duration for molecular motions during a high strain rate experiment.

Here, the modulus includes the full FDM description including contributions from all of the elements. For implementation into this modelling framework, the modulus is split into the α component (FDM α element and half of the transitory element) and the β component (FDM β element and the other half of the transitory element). As with the α parameters, fits are made simultaneously to all relevant curves and once obtained from these fits, the β parameters are also fixed.

Predicting and validating high strain rate response

The combination of the previously obtained α, β, $\mathcal{L}$ parameters and temporally and thermally relaxed modulus, $E(t, T)$ can be used in combination in this modelling framework to predict the high strain rate response of the PVC and PPVC. Until now, the thermal relaxation of the modulus has not been required, but in predicting the high strain rate response, this cannot be neglected. In the simulation process, at each integration step, the temperature increase is calculated and used to obtain the new modulus value to be used in the next integration step.

The model is run with the strain rate now set to the value for which the response is desired to be predicted, whilst retaining the fixed model parameters as obtained above. These simulations can then be validated against carefully conducted high strain rate experiments at the same strain rates.

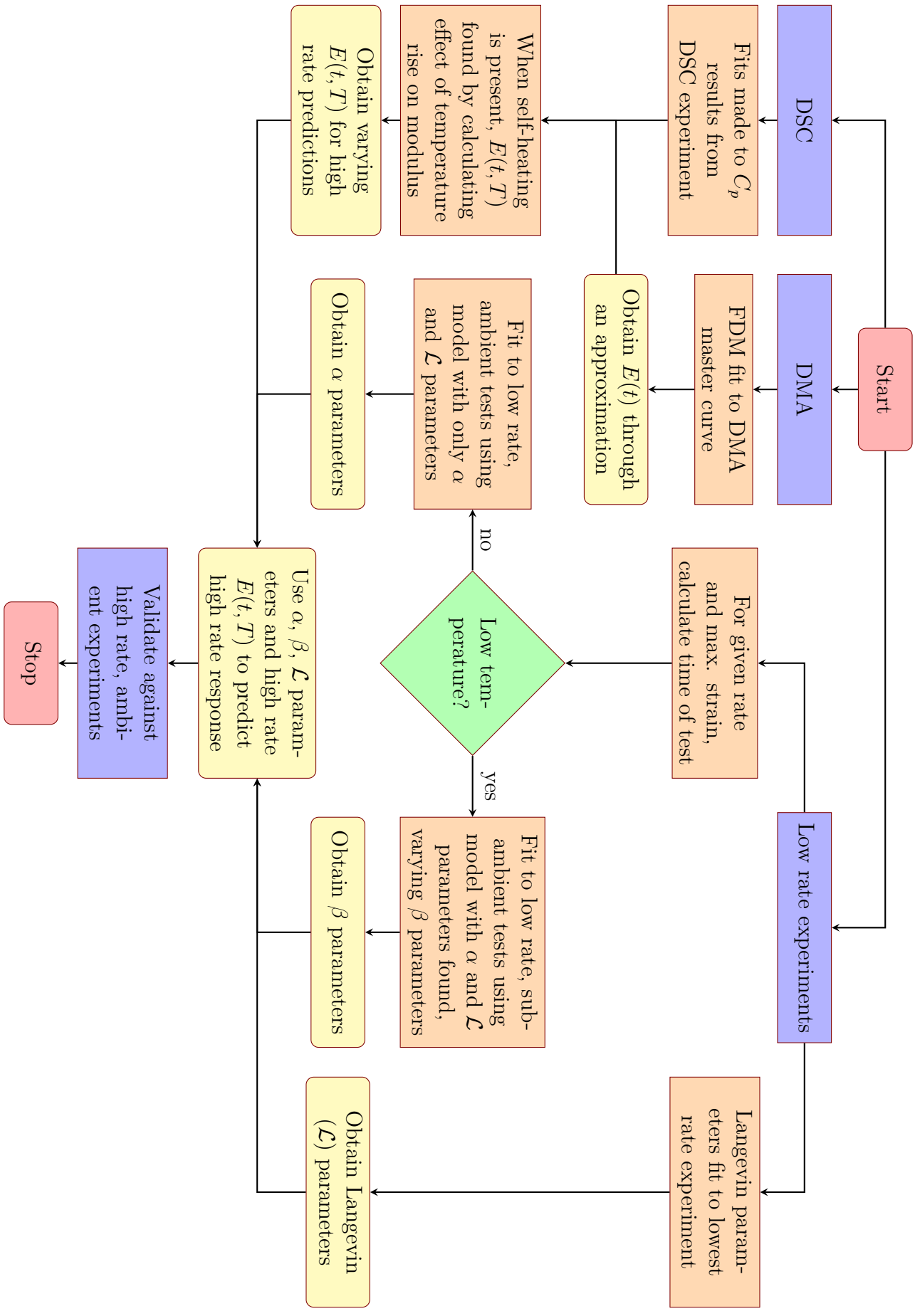

FIGURE 4.20: Flowchart to describe the modelling framework.

5 Experimental characterisation of unfilled and filled natural rubber

In the previous chapter, it was shown that it is possible to *predict* the full stress-strain response measured in high strain rate compression experiments using results of quasi-static experiments, basic thermomechanical characterisation and the time-temperature superposition technique. The modelling framework was developed and applied to PVC and PPVC, which exhibits viscoplasticity, but no strain induced damage. In order to further develop the model in the previous chapter to include damage, attention was shifted to focus on unfilled and filled natural rubber.

Rubbers are widely used in engineering applications where they are subjected to impact loading leading to high strain rate deformation. The strong rate and temperature dependence that is exhibited by rubbers and their composites provides further motivation for a deeper understanding of this complex behaviour including the interaction between the matrix and filler materials.

In this chapter, both unfilled and glass microsphere filled natural rubber are characterised experimentally over a range of strain rates and temperatures. The effect of filler volume fraction and mean particle size on the rate and temperature dependence of the overall mechanical response is studied. By using the novel modelling frameworks presented in the previous chapters, and by incorporating a suitable damage component, it will be possible to make predictions of the high strain rate behaviour of these natural rubber particulate composites. This chapter will present the experimental data and insights that will lead to the model development of the next chapter.

5.1 Introduction

Filled and unfilled natural rubber (F/U-NR) are widely used in the automotive sector, in industrial applications such as seals, energy absorbers and vibration dampers, and even novel technologies in medicine [217]. The addition of fillers is for improving mechanical properties, or functional purposes. In many of these applications, the material is subjected to impact loading leading to high strain rate deformation at a variety of temperatures. It is therefore necessary to study the time-dependent mechanical responses of these types of materials over a range of loading conditions. As the strain rate of deformation increases or temperature decreases, molecular motions in the polymeric network of U-NR become inhibited, leading to the strong rate and temperature sensitivity [188]. This consequently influences the mechanical response of the F-NR particulate composite.

In the previous chapter, predictions of the mechanical response of PVC and PPVC were made based on a novel modelling framework fully calibrated using quasi-static experiments, incoporating the TTS principle and a deeper understanding about the effects of adiabatic self-heating. These predictions were shown to have excellent agreement with carefully conducted experiments from a previous study [3]. In this chapter, progress is presented on extending this research to F/U-NR; a softer material that proves even more challenging than PVC to characterise experimentally at high strain rates.

5.2 Materials

Natural rubber latex extracted from the rubber tree, *Hevea brasiliensis*, is mainly formed of cis-1,4-polyisoprene. Its molecular structure can be seen in Figure 5.1.

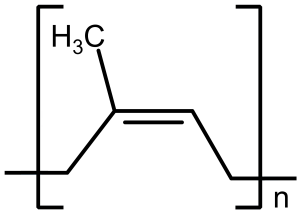

FIGURE 5.1: Molecular structure for cis-1,4-polyisoprene.

This latex forms the basis of the natural rubber (NR) used in this study. Our collaborators at the Tun Abdul Razak Research Centre (TARRC) in Hertfordshire manufactured plates of EDS 19 grade NR, for which the formulation can be found in [218]. This was a conventional accelerated-sulphur vulcanizate containing no filler.

In order to produce particulate composites, glass microspheres were mixed into the EDS 19 gum prior to curing. This filler was selected due to the big difference in modulus between the two constituents, it allows a model particulate composite to be created, and it provides a filler-rubber blend that TARRC has previous experience in. Two grades of spheres were used with an order of magnitude difference in the mean particle size between the grades. Basic material properties for these are shown in Table 5.1.

TABLE 5.1: Material properties for U-NR and glass microsphere fillers.

Material	**Density** ($kg\,m^{-3}$)	**Modulus** (MPa)	**Mean particle size** (µm)	**Particle range** (µm)
EDS 19/U-NR	966	0.52 (23 °C, 2% strain, 0.1 Hz)	N/A	N/A
Spheriglass 2429	1460 (bulk, untapped) 1570 (bulk, tapped)	69,000	70-100	53-106
Spheriglass 5000	1280 (bulk, untapped) 1620 (bulk, tapped)	69,000	7-10	N/A

With each grade of spheres, two sets of particulate composites were produced, with a 5% and 50% volume filler fraction. By assuming a perfect mixture, the expected

densities of the particulate composites can be calculated by using the rule of mixtures (Equation 5.1). These densities are shown for the various composites in Table 5.2. The various F-NR grades are also depicted diagrammatically in Figure 5.2.

$$\begin{aligned} m = \rho V &= m_f + m_m \\ &= \rho_f V_f + \rho_m V_m \\ &= \rho_f \phi_f V + \rho_m (1 - \phi_f) V \\ \rho &= \rho_f \phi_f + \rho_m (1 - \phi_f) \end{aligned} \tag{5.1}$$

TABLE 5.2: Theoretical densities of the F-NR based on a simple rule of mixtures.

Material	**Volume fraction (%)**	**Approx. particle size** (µm)	**Density** ($\mathrm{kg\,m^{-3}}$)
F-NR2	5	~100	1070
F-NR3	5	~10	1070
F-NR4	50	~100	1750
F-NR5	50	~10	1750

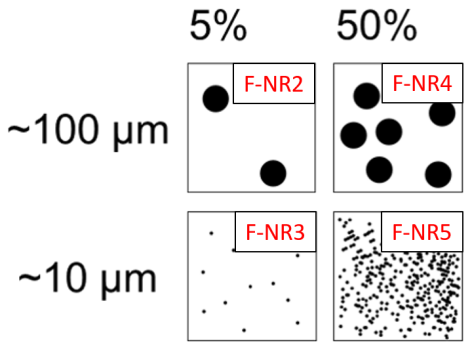

FIGURE 5.2: Highlighting the different grades of F-NR composites for easy identification (not to scale).

5.3 Compression experiments

A full regime of compression experiments were performed at a variety of strain rates on the Instron 5980, in-house hydraulic press and the SHPB (in standard, and Direct Impact configurations).

For the SHPB experiments, paper or copper pulse shapers were used to minimise the high frequency oscillations as observed in the results of neoprene rubber (§3.3.4.1). Up to strain rates of c.1500 s^{-1}, paper shapers were used. Above this rate, thin copper foil was preferred. A c.15 mm square piece of material was held in place on the impact side of the input bar with a thin layer of petroleum jelly. The shaper effectively dampens the high frequencies in the loading pulse. Piezoelectric gauges were also used for these SHPB experiments.

These experiments were conducted on right circular cylindrical specimens of 5 mm length and diameter, which were machined out of the moulded sheets using a bespoke cutter with a 5 mm diameter hole and 0.05 mm tapered cutting edge, which is inserted into a milling chuck and operated at a speed of c.200 RPM.

5.3.1 Varying temperature experiments

Low temperature experiments at a low strain rate of 10^{-2} s^{-1} were performed on the Instron using the temperature controlled environmental chamber. The temperature range varied from -80 °C to -40 °C in order to cover the transition region. Further experiments either below or above these temperatures would not contain any additional information of the temperature dependent mechanical behaviour in compression. Three runs were carried out at each temperature of interest.

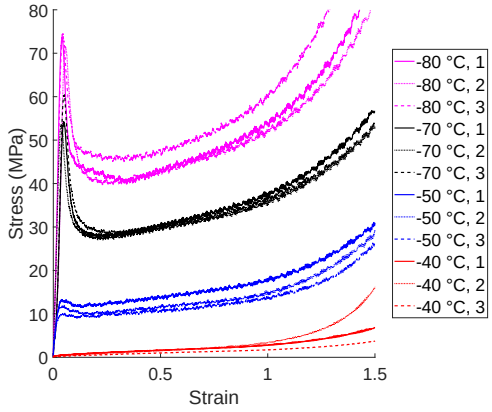

FIGURE 5.3: Low rate, varying temperature results for U-NR.

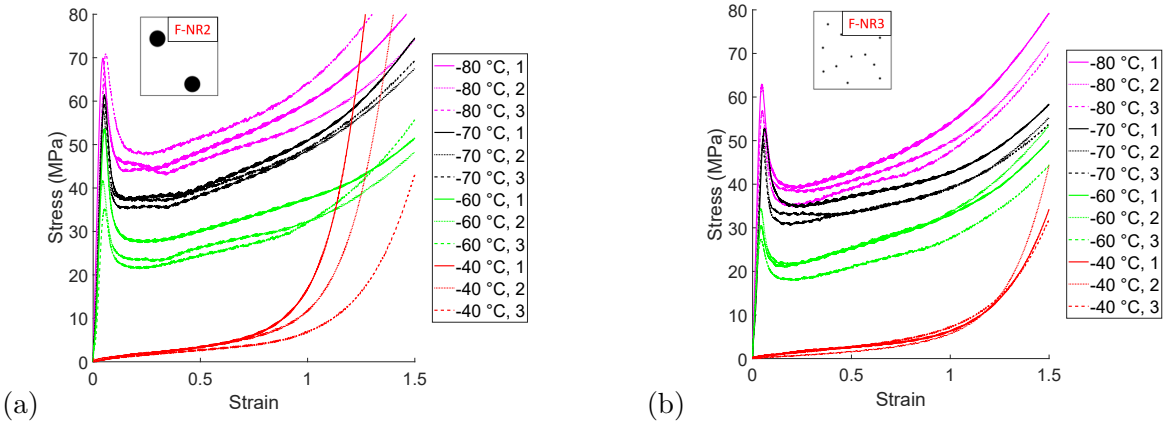

(a) (b)

FIGURE 5.4: Low rate, varying temperature results for (a) F-NR2 and (b) F-NR3.

In comparing the results of the U-NR (Figure 5.3) to the results of the 5% filled F-NRs (Figure 5.4), it is evident that the mechanical response is qualitatively similar. The dominant influence on the behaviour is the glass transition of the rubber. When the temperature is below -50 °C, the strength and modulus are significantly higher than above this temperature. In fact, in Figure 5.3, the results at -50 °C show the onset of the glass transition's influence.

There is considerable spread in the large strain response for the F-NR2 at -40 °C. This was as small variations in the starting position of the loading anvils caused a large effect at larger strains. A small amount of pre-strain at the start is hard to notice, but becomes more obvious at larger strains. The material's non-linear elasticity drives this behaviour, but is enhanced by strain hardening and apparatus friction at the highest

strains. In future, these experiments would be repeated, ensuring the same starting displacement between the loading anvils for all three tests at −40 °C.

Qualitatively, the lower the temperature, the higher the peak stress. There does appear to be a slight decrease in strength for the F-NR3 compared to the F-NR2 suggesting there may be an influence of the mean particle size, however this needs to be more carefully studied: the experiments below −50 °C show notable scatter such that nuanced comparisons of the peak stress between the grades of rubber are difficult to make. There are two expected reasons for this scatter: firstly, the addition of fillers with a given topology leads to stress variations across the cross-section and between samples; and secondly, the influence of the glass transition makes the response very sensitive to small changes in the temperature. This is particularly observed in the results at −60 °C in Figure 5.4; DMA data (§5.4) will show that this is within the transition region for this natural rubber.

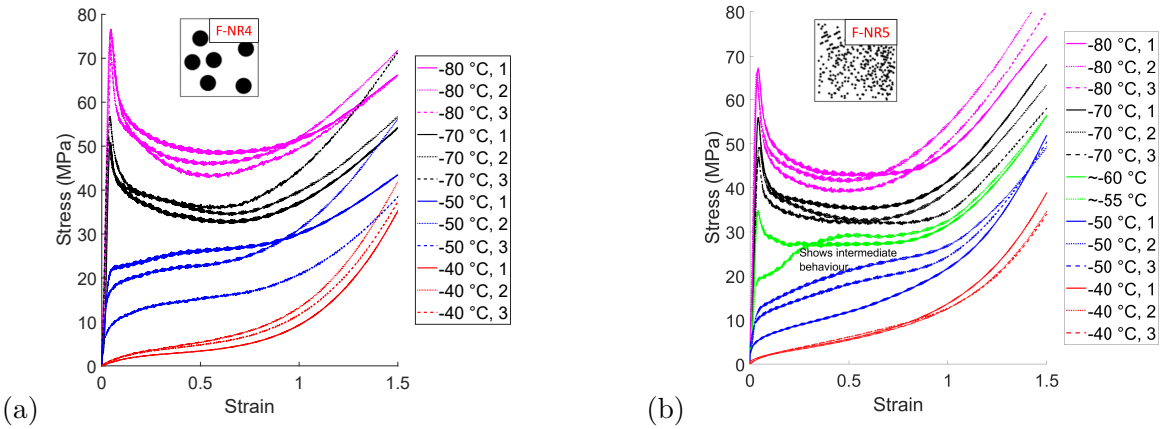

FIGURE 5.5: Low rate, varying temperature results for (a) F-NR4 and (b) F-NR5.

The results for the 50% filled particulate composites can be seen in Figure 5.5. Similar observations can be made as with the less filled composites. Most interestingly, for the more filled composite with smaller particles (F-RN5, Figure 5.5b), intermediate behaviour can be seen in the response at $T \approx -55$ °C. This is believed to be due to an insufficient hold time between closing the environmental chamber door after placing this specimen, and starting the experiment. This has led to a unique condition where the temperature is slightly higher at the start compared to the end. This issue is

resolved by ensuring thermal stability using the two thermocouples (in the chamber and on the loading anvils), but these data are kept as they provide more evidence for the high temperature sensitivity around the T_g for the rubber. Since it is the rubber that governs this intermediate behaviour, it would be expected with any of the rubber grades.

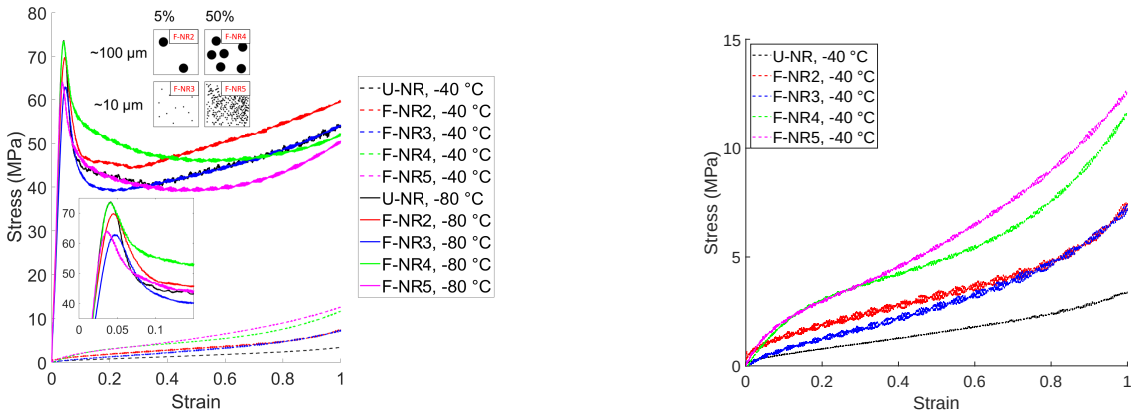

FIGURE 5.6: (a) Highlighting selected low rate, varying temperature experiments for all NR grades, and (b) better illustrating the higher temperature behaviour.

In order to better compare the low temperature quasi-static experiments for all grades of rubber, selected data are plotted in Figure 5.6 at −80 °C and −40 °C. At −40 °C, filler fraction has more of an influence on the response than the mean particle size. The 5% filled composites show a smaller increase in modulus compared to the 50% filled composites.

At −80 °C, the mean particle size appears to affect the peak stress: the samples with larger particles retain the strength seen with the U-NR. Those with smaller particles have a lower peak stress, although, as explained before, these findings need further scrutiny owing to scatter. The filler fraction influences the post-yield response, with the 5% filled composites both showing a sharp drop after the peak stress and a rubbery strain-hardening response, similar to that of U-NR. The 50% filled composites show a gradual reduction in stress followed by a shallower strain-hardening gradient.

5.3.2 Varying rate experiments

For the varying strain rate experiments, four different apparatus were used:

1. Instron: Low strain rate experiments at 10^{-3}, 10^{-2}, and 10^{-1} s^{-1}
2. Hydraulic press: Intermediate strain rate experiments at 1, 10, and 100 s^{-1}
3. SHPB experiments: High strain rate experiments to low strains at c. 1000 s^{-1}
4. Direct impact experiments: High strain rate experiments to higher strains at c. 1000 s^{-1}

The results of these experiments for the U-NR and the four grades of particulate composites are presented below.

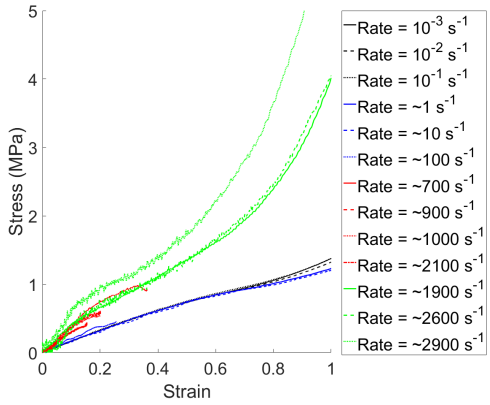

FIGURE 5.7: Varying strain rate data at 25 °C for U-NR.

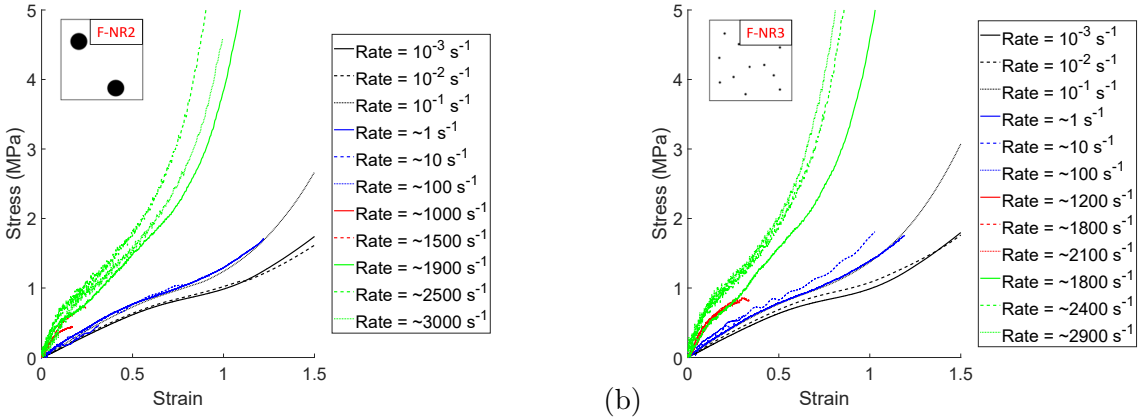

(a) (b)

FIGURE 5.8: Varying strain rate data at 25 °C for (a) F-NR2 and (b) F-NR3.

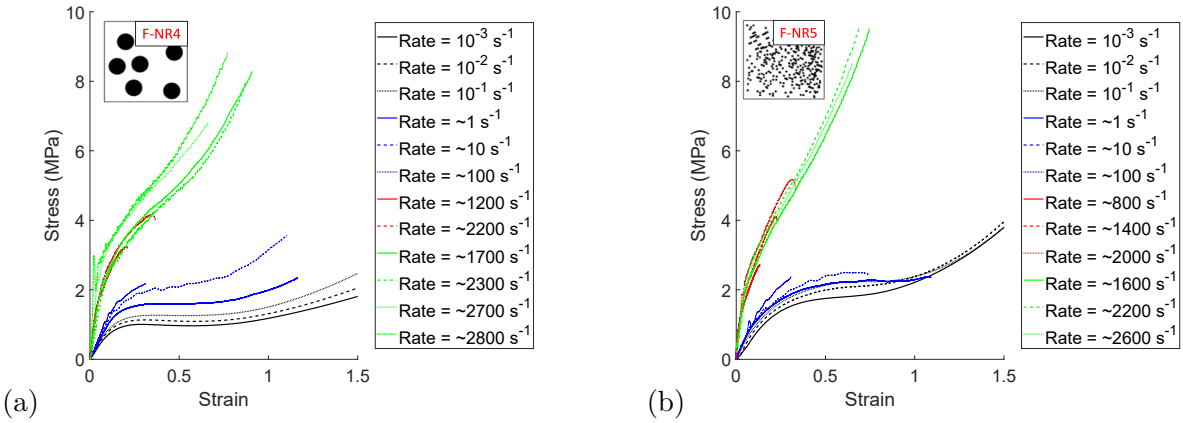

FIGURE 5.9: Varying strain rate data at 25 °C for (a) F-NR4 and (b) F-NR5.

From these experiments, the rate dependence in compression for the various grades of rubber can be obtained. As expected, the higher the rate, the greater the strength of the material. The addition of glass microspheres to a 5% volume fraction does not seem to affect the mechanical response, which is more clearly observed in Figure 5.10. However, further addition to 50% volume fraction suppresses the rubber hyperelasticity. This is since there is less rubber, but also as the filler creates a local concentration of the polymer network surrounding the filler, which is stiffer than the bulk elastomer — so-called hydrodynamic and interphasial effects [219]. This is further explored in §5.3.6.2 as contributors to the enhancement of modulus.

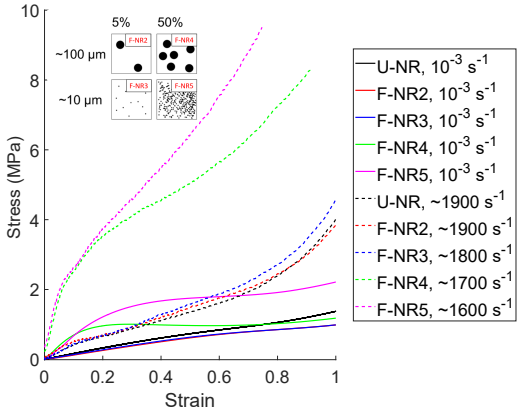

FIGURE 5.10: Highlighting selected varying strain rate data for all grades of NR.

Selected data showing the rate-dependent response for all grades of NR is shown in Figure 5.10. This enables comparisons to be made more easily. At 10^{-3} s^{-1}, the 5%

filled composites both show a slight decrease in large strain stress compared to the U-NR. This could be due to a small amount of filler causing degradation in the bulk polymer network, however the difference is not too significant and is likely simply experimental variation. This could be checked by reloading the samples to observe their residual strengths, or through the use of X-ray visualisations before and after loading. At c. 2000 s^{-1}, the mechanical response for the 5% F-NRs is very similar to that of the U-NR.

The apparent modulus can be calculated from the experimental data, taking into account results up to 10% true strain. The modulus is apparently 15-20% larger than the U-NR for the 5% F-NRs at c. 2000 s^{-1}. For the 50% F-NRs, at 10^{-3} s^{-1}, the apparent modulus is 5 times larger in the F-NR4/5 compared to the F-NR2/3 and U-NR. At c. 2000 s^{-1}, the apparent modulus is 9 times larger.

A further observation relates to the difference in response for the 50% F-NRs with differing particle size distributions. At 10^{-3} s^{-1} and c. 2000 s^{-1}, the response for both grades of F-NR is the same up to 10% true strain. However, beyond this, the strength of the F-NR5 exceeds that of the F-NR4. This indicates the possibility of strain activated damage, which affects F-NR4 more than F-NR5. In the future, tested specimens can be reloaded to check their residual strengths to better understand damage. This is expected as cavitation is more likely to take place with the larger fillers due to their smaller specific surface area. A consequence of this strain induced damage is that at low strain rates, F-NR4 is only stronger than the U-NR up to a strain of 75%. After this point, the performance is actually worse for the reinforced rubber compared to the unfilled rubber.

5.3.3 Rate-temperature equivalence

The rate-temperature equivalence observed in the U-NR along with all grades of F-NR is shown in the following figures.

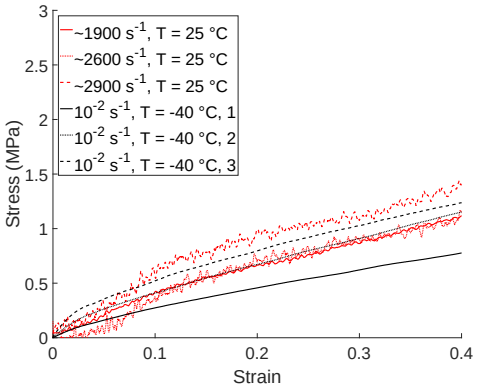

FIGURE 5.11: Highlighting the rate-temperature equivalence between high strain rate experiments at 25 °C and low rate experiments at −40 °C for U-NR.

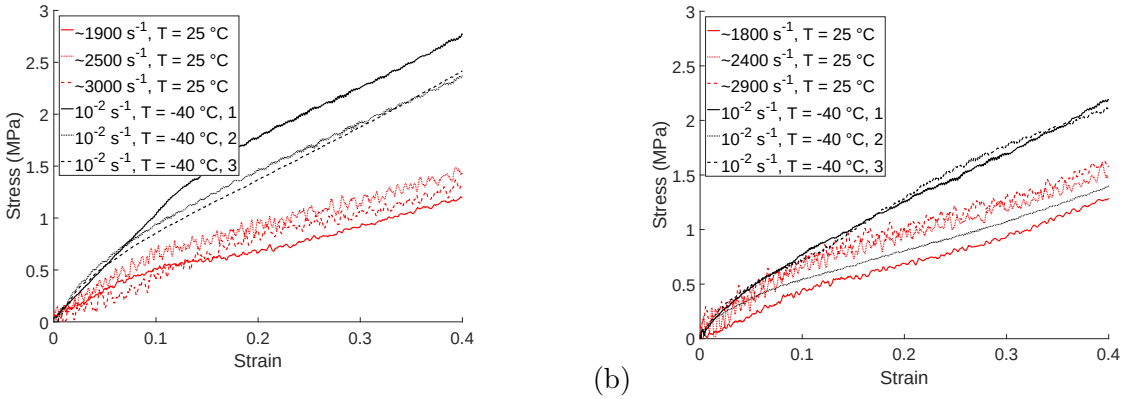

(a) (b)

FIGURE 5.12: Highlighting the rate-temperature equivalence between high strain rate experiments at 25 °C and low rate experiments at −40 °C for (a) F-NR2 and (b) F-NR3.

For U-NR and F-NR3, the mechanical responses of quasi-static compression experiments conducted at −40 °C correlate well with the high strain rate experiments performed on the SHPB at 25 °C (Figure 5.12). For F-NR2, there a greater variation that seems to suggest a slightly higher temperature would be more suitable. There is some noise in the high rate data and some variation in the low temperature experiments that make it difficult to identify the exact value of temperature required to simulate perfectly the high rate response. Further confidence will be provided from the results of the DMA experiments.

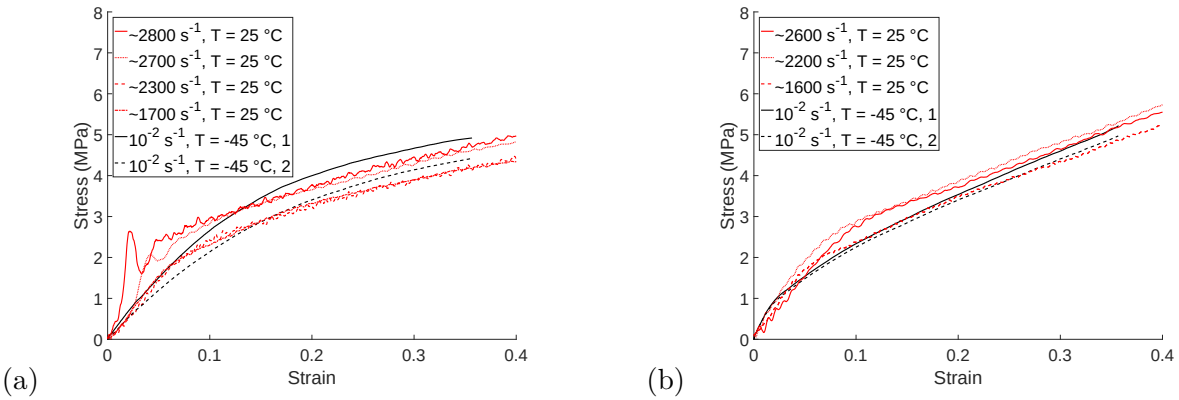

FIGURE 5.13: Highlighting the rate-temperature equivalence between high strain rate experiments at 25 °C and low rate experiments at −45 °C for (a) F-NR4 and (b) F-NR5.

For the 50% F-NRs, the results of the rate-temperature equivalence is excellent (Figure 5.13). This equivalence can be seen as low rate experiments *simulating* the high rate response. Here, the temperature of the quasi-static experiments was lower at −45 °C to take into account the enhancement with a higher filler volume fraction.

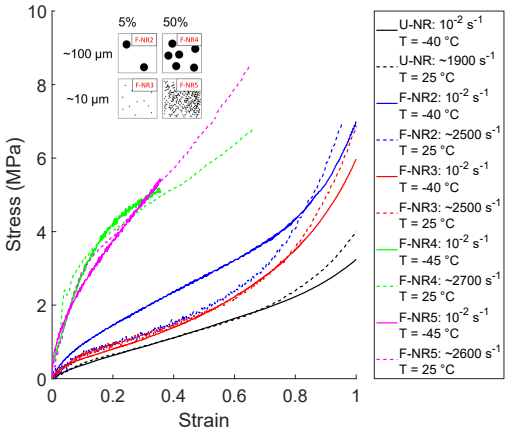

FIGURE 5.14: Showing that experimentally simulating the high rate response of all grades of NR is possible with the use of low temperature quasi-static analogue experiments.

A comparison of the experimental simulations to large strains is provided in Figure 5.14. Except for the simulation of F-NR2, there is excellent agreement for all grades of materials. This implies that not only is there a rate-temperature equivalence for the modulus, but the same equivalence likely exists for the damage mechanism too. This equivalent rate-temperature behaviour is as the response is dominated by the matrix.

This insight provides confidence in being able to use low rate, low temperature data to develop a predictive model for high rates.

5.3.4 Varying strain experiments

Literature suggests that the main form of damage in these materials is strain activated debonding [220, 221]. In order to experimentally characterise the strain activated debonding damage, quasi-static experiments were performed at a strain rate of 10^{-2} s^{-1} and 25 °C. Nine experiments were conducted for each grade of rubber, three repeats for each value of maximum strain. Maximum nominal strains of $e = 0.1/0.2/0.3$ were selected to see how the damage evolves on previously untested specimens with strain for each grade of rubber.

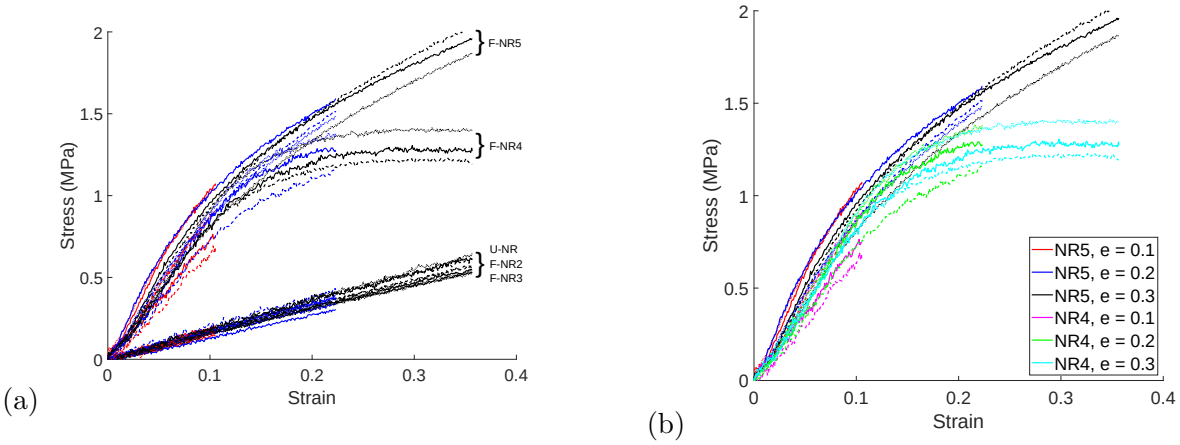

FIGURE 5.15: Results of varying strain quasi-static compression experiments at 10^{-2} s^{-1} and 25 °C for (a) all grades of rubber and (b) only 50% F-NRs to focus on strain activated damage.

From Figure 5.15a, it can be observed that for the 5% F-NRs, there is unlikely to be a significant amount of strain activated damage. This is as all the experiments show a linear increase in stress up to a nominal strain of 0.3. However, for the 50% F-NRs, even from nominal strains as low as 0.1, greater damage is observed for F-NR4 than F-NR5. Figure 5.15b focuses on the behaviour of F-NR4/5 since they are the grades experiencing any notable damage. This figure makes it clearer to identify the damage evolution with strain.

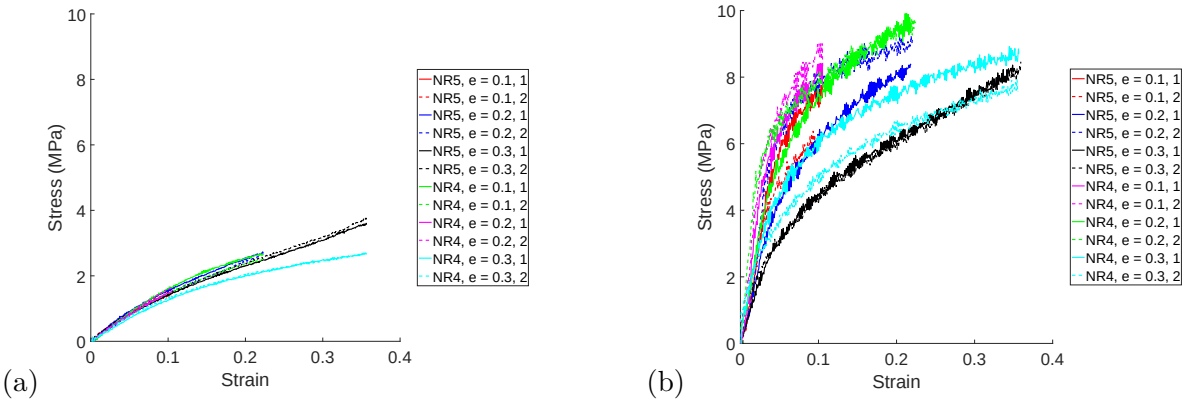

FIGURE 5.16: Results of varying strain quasi-static compression experiments at 10^{-2} s^{-1} for 50% F-NRs at (a) -40 °C and (b) -50 °C.

In the previous section, it was shown that there exists a rate-temperature equivalence for damage as well as modulus. To investigate the strain dependence of this, quasi-static compression experiments at a strain rate of 10^{-2} s^{-1} were performed at -40 °C and -50 °C. These temperatures were selected such that they would be similar to that in observations from the previous section. These results are shown in Figure 5.16.

In these low temperature varying strain experiments, it is less clear to make similar observations about strain activated damage. In Figure 5.16a, at -40 °C, it appears as though there is greater damage for F-NR4 than F-NR5 at the largest strains, but this trend is not seen at lower strains. In Figure 5.16b, at -50 °C, F-NR4 is stronger than F-NR5 as it broadly shows a higher value of stress for a given value of strain. At the largest strains though, the strain hardening rate is lower for F-NR4 compared to F-NR5 as evidenced by the shallower slope. This points to a greater amount of strain activated damage for F-NR4.

Varying strain experiments have also been conducted at high strain rates using the SHPB, and in future, the intention is to compare the extent of strain activated damage at high rates and low temperatures to interrogate the rate-temperature equivalence of damage further. Quasi-static experiments at room temperature will be conducted for recovered specimens from both sets of experiments and the residual strength measured in an attempt to quantify extent of damage. Further experiments using Computerised

Tomography (CT) scanning may be performed to visualise the internal damage. X-ray diffraction experiments with *in-situ* loading would also be useful to obtain a time resolved understanding of the damage mechanism that is not influenced by stress relaxation.

5.3.5 Low temperature, high rate experiments

5.3.5.1 Development of new experimental capability

To interrogate further the relationship between rate and temperature, a novel capability for the laboratory was developed. An ancillary device for the SHPB comprising of a liquid nitrogen immersion chiller for nitrogen gas (Figure 5.17a) and a bespoke fixture (Figure 5.17b) was created to conduct low temperature, high rate experiments.

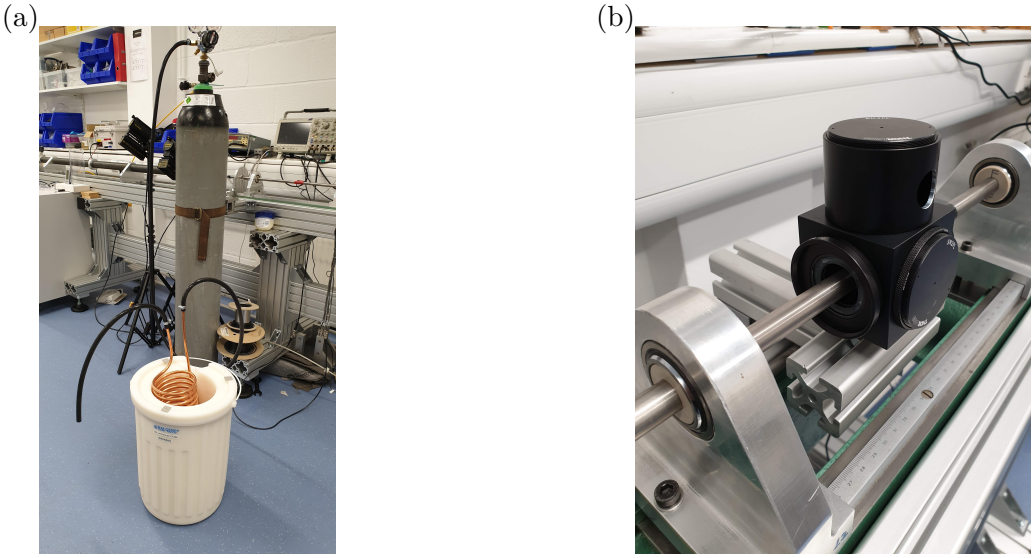

FIGURE 5.17: (a) Liquid nitrogen immersion chiller for nitrogen gas and (b) a bespoke fixture for the SHPB to conduct low temperature, high rate experiments.

Using the device, oxygen-free nitrogen gas was fed through silicone hosing into a copper coil. This copper coil was submerged in liquid nitrogen, all contained within a thermally insulating Nalgene® dewar. The cooled down nitrogen gas is then directed through the opening on the top of the fixture. The cold nitrogen gas subsequently cools the specimen that is contained within the fixture down to a minimum of -100 °C.

Oxygen-free nitrogen was used so that there is no chance of forming extremely flammable liquid oxygen inside the copper coil. For this reason, the nitrogen flow must be started before submerging the coil into the liquid nitrogen, in order to purge the air out of the system. Also the flow should not be turned off whilst the coil is submerged.

The fixture was built using commercial-off-the-shelf optical components from Thorlabs, Inc. such that it could be mounted to the pre-existing railing of the SHPB. The core of the fixture is based on a lens cube. The upper chamber is formed of a lens tube and cover. This chamber is for the nitrogen intake to mitigate any temperature fluctuations arising if the flow was directed at the specimen itself. Lens irises are used either side along the firing axis to allow varying diameter SHPB bars to be used. Lens covers are placed over all other cube openings. This set-up allows the potential to remove the front cover and record the experiment using a camera, as is the intention for future studies since in-situ visualisation is not included in this present research.

5.3.5.2 Results and analysis

Results of high strain rate experiments conducted at -40 °C for all grades of rubber are shown in Figure 5.18. The difference between a strain rate of c. 1000 s^{-1} and c. 2000 s^{-1} does not seem to affect the apparent stiffness. This is since the rubbers are already in their glassy state and so the influence of a further increase in rate is insignificant. Evidence for this will be provided with the results of DMA experiments shown in §5.4.

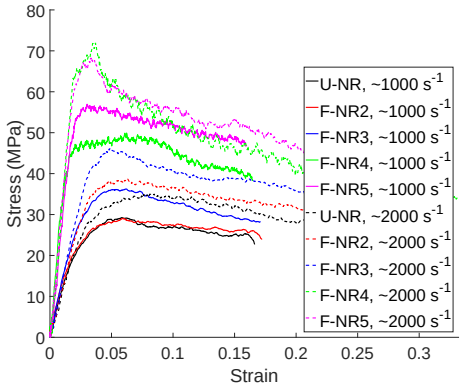

FIGURE 5.18: Comparison of high strain rate data from SHPB experiments at −40 °C for all grades of NR.

Filler volume fraction has more of an effect on the apparent stiffness. Upon calculating the initial moduli for all grades of rubber (at 1% true strain), it is observed that the values for the 5% F-NRs are on average 20% higher, and those for the 50% F-NRs are 3 times higher than that for the U-NR. At −40 °C, the stiffness enhancement due to filler volume fraction is not as significant as the change at 25 °C. This is because the decrease in temperature has already contributed to stiffness enhancement, and as the rubber becomes glassy, there is a limit to how much the stiffness can be enhanced. This limiting glassy stiffness can be seen in the results of the varying temperature experiments (Figure 5.6) and later, in the DMA results.

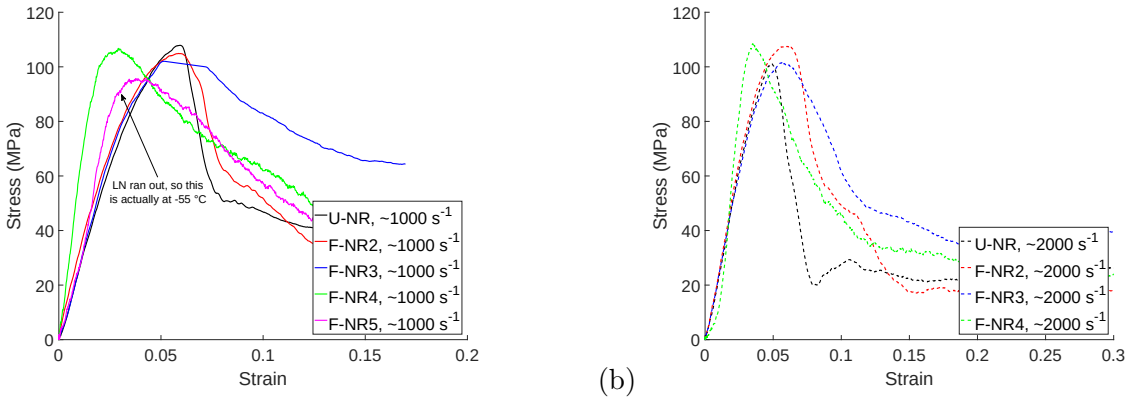

FIGURE 5.19: Preliminary high strain rate data from SHPB experiments at −60 °C and at (a) c. 1000 s^{-1} and (b) c. 2000 s^{-1} for all grades of NR.

Preliminary data for high strain rate experiments conducted using the SHPB at −60 °C are shown in Figure 5.19. The results of each rate are separated for clarity. There

seems to be very little difference in the yield stress for the different composites. This is as the behaviour is dominated by the natural rubber matrix. In terms of stiffness enhancement, there is very little difference for the 5% F-NRs. For F-NR4, the stiffness is 2 times higher than for the U-NR. This is lower than the 3 times increase observed at −40 °C and supports the hypothesis that as the temperature decreases through the T_g, the influence of the filler volume fraction on stiffness enhancement decreases.

To investigate the inhomogeneity and non-uniform strain rate during these low temperature, high rate experiments, the strain-time curves for a selection of high rate experiments are plotted in Figures 5.20–5.22.

For experiments at 25 °C, for all grades of rubber, the strain rate shows a slight, uniform increase over the duration of the experiment. For U-NR, both sub-ambient experiments show non-uniform strain rates (Figure 5.20). For the 5% F-NRs (Figure 5.21), both experiments at −60 °C show significant variations in the strain rate, however, at −40 °C, only F-NR3 shows this. The strain rate evolution for F-NR2 is similarly uniform to the experiment conducted at 25 °C. For the 50% F-NRs, there is a slight difference in the strain rate evolution as observed in Figure 5.22. For F-NR4, both sub-ambient experiments show a non-uniform evolution of strain rate, whereas for F-NR5, the evolution is more uniform and similar to that at 25 °C.

Inhomogeneity and non-uniform strain rates can indicate strain localisation and potential damage, the significance of which can be observed in the next section.

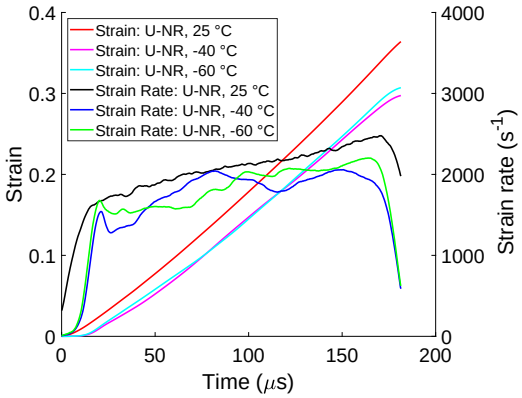

FIGURE 5.20: Evolution of strain and strain rate for U-NR.

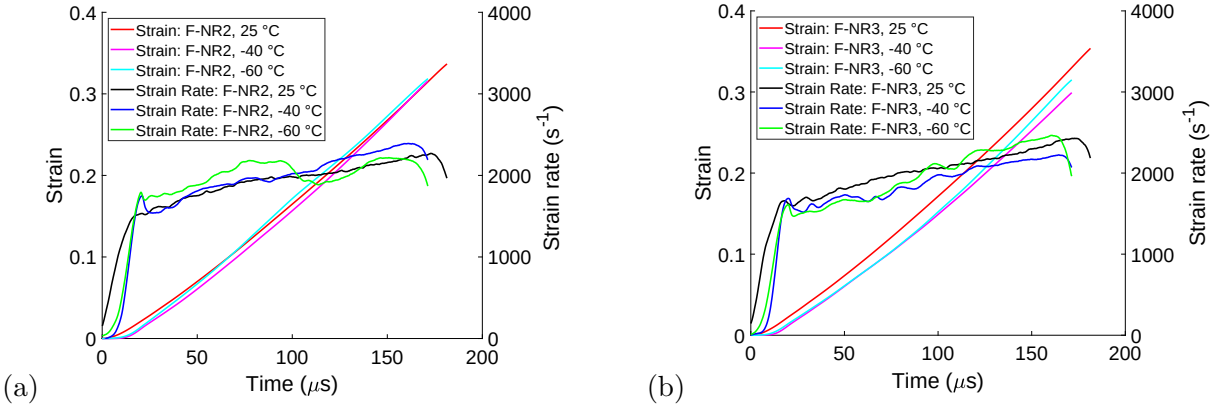

FIGURE 5.21: Evolution of strain and strain rate for (a) F-NR2 and (b) F-NR3.

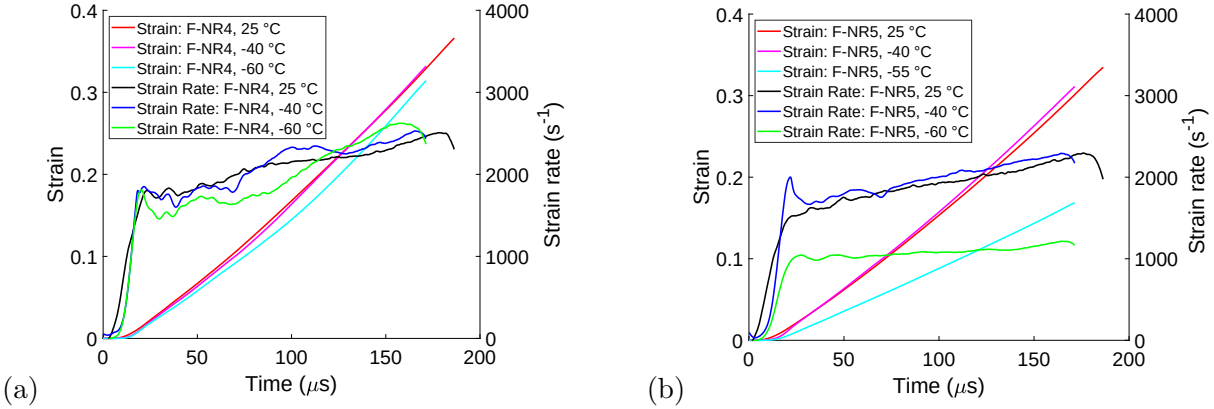

FIGURE 5.22: Evolution of strain and strain rate for (a) F-NR4 and (b) F-NR5.

5.3.5.3 *Post-mortem* damage analysis

At −40 °C, it was observed (Figure 5.18) that the samples with larger particles (F-NR2/4) showed a greater decrease in strength post-yield than those with smaller particles (F-NR3/5). In the case of F-NR2, there seems to be no advantage at large strains in adding the filler as the response (taking into account any experimental variations) is the same as that for the U-NR.

At −60 °C, the elastic behaviour is similar at both rates and the post-yield behaviour is affected by the increase to c. 2000 s^{-1} (Figure 5.19). For the more filled F-NRs, damage begins at a lower strain. All grades of F-NR seem to show the same extent of damage at larger strains other than F-NR3. The F-NR3 sample at c. 1000 s^{-1} appears not to damage as much as the other samples.

The lower performance of F-NRs with larger mean particle size is expected to be due to strain induced debonding. Since the surface to volume ratio is ten times higher for F-NR3/5 compared to F-NR2/4, the interfacial bond strength is greater in F-NR3/5 than F-NR2/4. Hence, strain induced debonding is hypothesised to cause the decreased performance for F-NRs with larger particles. It is debonding, rather than filler fracture, that is expected to be the dominant failure mechanism. Previous literature [220] has shown that deformations in the filler are minimal when fillers are significantly stiffer than the binder as in this case (69 GPa vs 0.52 MPa), and that the fillers realign by rotating and sliding to accommodate the larger deformations in the matrix. Here, due to a lower fill fraction and spherical nature of the fillers, it is expected that cavitation is a likely damage mechanism. This can lead to debonding between the rubber and the filler material.

Post-mortem examinations can be conducted for each experiment to visualise simply the extent of damage. Despite the non-uniform strain rates and inhomogeneity observed in Figures 5.20–5.22 at −40 °C, there was no visibly observable damage upon inspection in any of the material grades. In the future, it would therefore be useful to conduct *in-situ* X-ray experiments such that the damage evolution in these experiments can be studied at a sub-surface level. At −60 °C, extensive damage was evident from visual observations and photographs are shown in Figures 5.23 through 5.27.

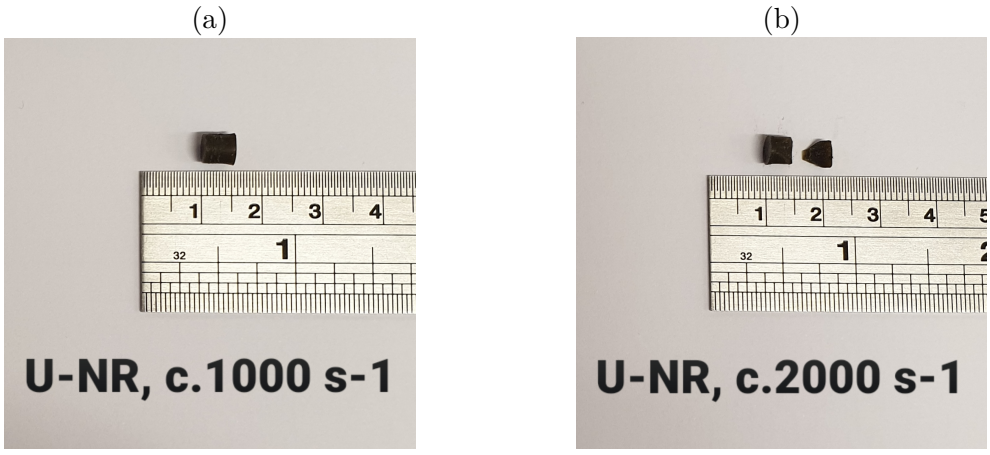

FIGURE 5.23: *Post-mortem* examination for high strain rate experiments at −60 °C for U-NR at (a) c. 1000 s^{-1} and (b) c. 2000 s^{-1}.

For the U-NR, catastrophic damage is only seen at the higher strain rate (Figure 5.23b). This is also evident from the stress-strain data in Figure 5.19, which shows a sharp drop in strength for the sample compressed at c. 2000 s^{-1}.

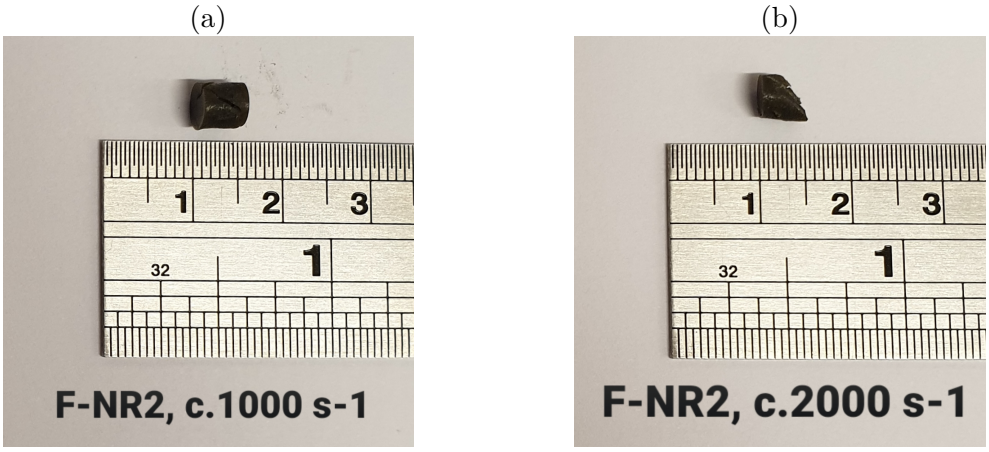

FIGURE 5.24: *Post-mortem* examination for high strain rate experiments at −60 °C for F-NR2 at (a) c. 1000 s^{-1} and (b) c. 2000 s^{-1}.

For F-NR2, samples at both strain rates showed similar damage. At c. 1000 s^{-1}, though there was a fracture running across the sample, it was held together by some of the rubber, whereas at c. 2000 s^{-1}, the rubber was unable to hold the pieces of the sample together.

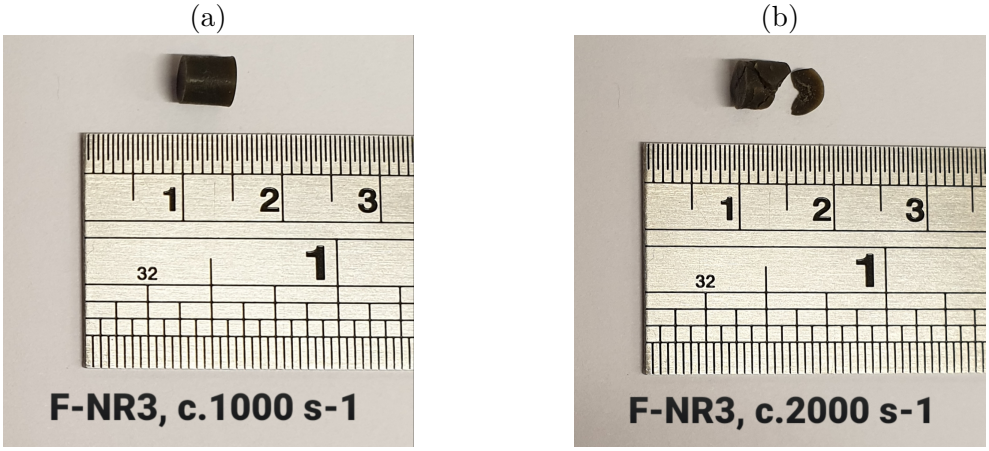

FIGURE 5.25: *Post-mortem* examination for high strain rate experiments at −60 °C for F-NR3 at (a) c. 1000 s^{-1} and (b) c. 2000 s^{-1}.

For F-NR3, the sample compressed at c. 1000 s^{-1} did not show any damage at all. This explains the relatively higher strength observed in the stress-strain profile in

Figure 5.19. However at c. 2000 s^{-1}, catastrophic failure occurred and the sample split into two pieces, showing a similar diagonal fracture to other failures.

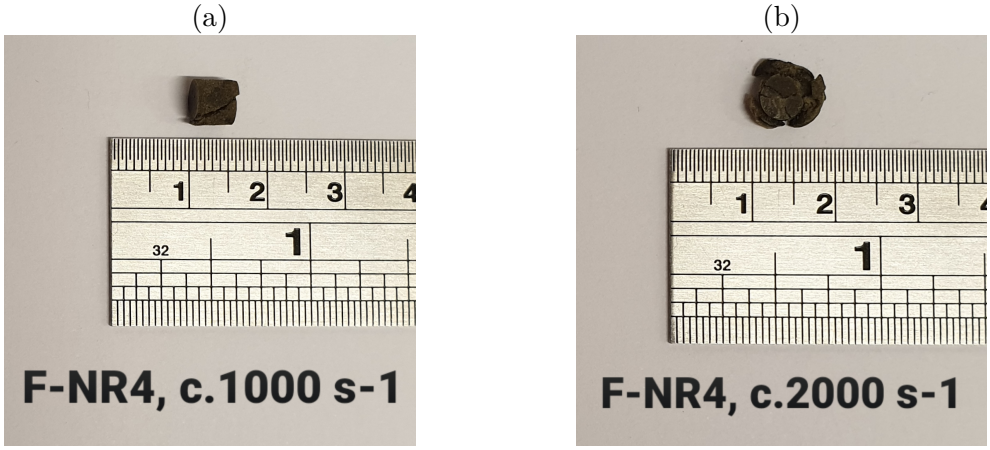

FIGURE 5.26: *Post-mortem* examination for high strain rate experiments at −60 °C for F-NR4 at (a) c. 1000 s^{-1} and (b) c. 2000 s^{-1}.

For F-NR4, both samples showed extensive damage. At c. 1000 s^{-1}, a diagonal fracture split the sample into two pieces held together by a small amount of rubber spanning the fracture plane. At c. 2000 s^{-1}, catastrophic failure was observed where the sample has been completely destroyed into many small pieces, albeit still held together by the rubber matrix.



FIGURE 5.27: *Post-mortem* examination for high strain rate experiments at $T \approx -55$ °C for F-NR5 at c. 1000 s^{-1}.

Although only one experiment with F-NR5 was conducted, it showed a similar type of failure as the other samples that failed. A diagonal fracture plane was observed at

approximately 45° to the axis of compression. It is odd however, that Figure 5.22b does not show any signs on inhomogeneity in the strain rate.

The presence of diagonally oriented fracture planes points to failure induced by adiabatic shear instability — a form of localised shear failure in polymers at high strain rates. Due to the low thermal diffusivity of natural rubber ($\kappa \approx 10^{-7}$ m^2 s^{-1} [222]), adiabatic conditions are present at relatively low strain rates. Given a sample with a 2.5 mm length-scale (half of the diameter/length), adiabatic conditions would exist at strain rates over c. 10^{-2} s^{-1}. This means that in high strain rate experiments, the sample heats up due to internal plastic dissipation and the inability for the heat to diffuse out of the sample during the time-scale of the experiment.

This may subsequently lead to thermal softening and unstable growth of localised shear bands [223]. To estimate the bulk temperature rise, the mechanical work done on the U-NR sample for a compression experiment at c. 2000 s^{-1} is calculated (to a stress of 100 MPa and strain of 0.05), and divided by the density (966 kg m^{-3}) and heat capacity (shown in §5.5 to be 925 J kg^{-1} °C^{-1} at −60 °C), to give a temperature rise just under 3 °C. Due to strain localisation, the internal temperature rise near these areas may be much higher. Though this seems small, it has been shown earlier with the results of varying temperature compression experiments (e.g. Figure 5.5b), that small changes in temperature around the T_g significantly affect the mechanical response. Furthermore, it is shown later in §5.4 that the modulus for U-NR can drop by as much as 60% by increasing the temperature by 3 °C from −60 °C.

By employing the perturbation analysis of Bai [224], it is deduced that adiabatic shear instability occurs when the thermal softening rate exceeds the strain hardening rate. Since thermal softening rapidly occurs through the T_g, by starting the high rate compression experiments just below the T_g of U-NR, it is possible to induce this instability and observe the shear based failures as shown above.

This shear localisation instability can also occur at lower temperatures due to a negative strain hardening rate from microcrack and craze formation [72] due to the particulate nature of the material. In future, experiments at temperatures below T_g

could be conducted and more thorough *post-mortem* examination of the fracture surface conducted to determine whether localised melting or brittle fracture is observed.

5.3.6 Discussion of results

5.3.6.1 Variation of peak stress

It is common in literature to quote the values of peak stress, yield stress or a characteristic stress against the temperature or logarithm of the strain rate [1, 225, 226]. For this reason, to facilitate comparisons and discussion, the figures below show the peak stresses against these two variables for all grades of NR. Where the data did not show the sample yielding, a characteristic stress (value at $\varepsilon = 0.1$) is shown instead.

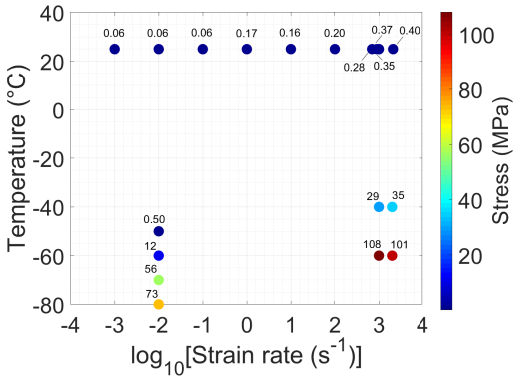

FIGURE 5.28: Strain rate and temperature dependence on the peak stress for U-NR.

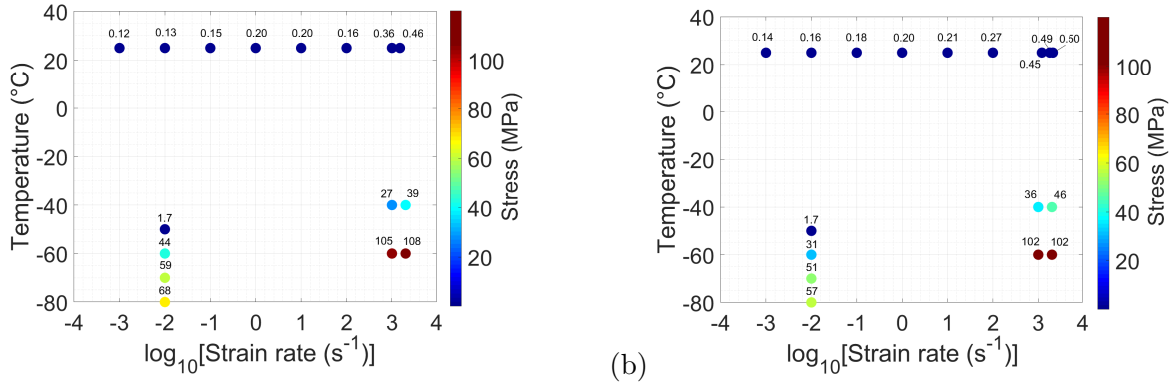

FIGURE 5.29: Strain rate and temperature dependence on the peak stress for (a) F-NR2 and (b) F-NR3.

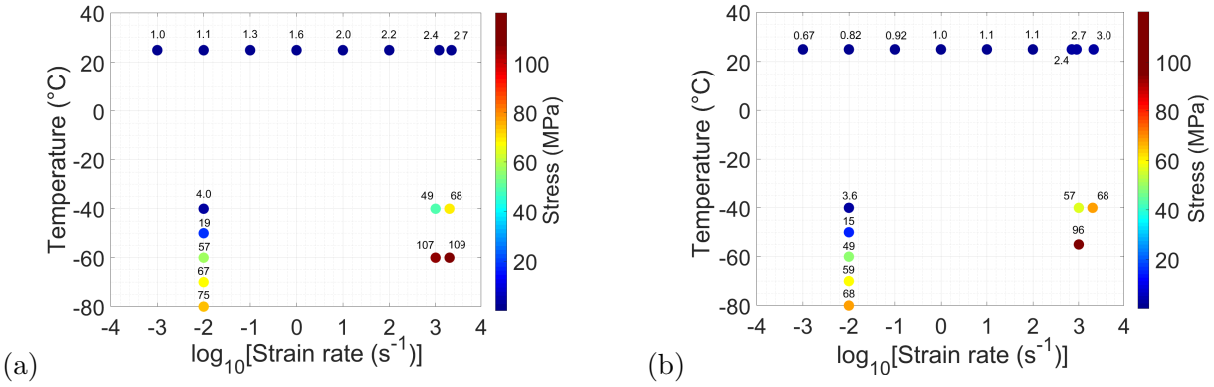

FIGURE 5.30: Strain rate and temperature dependence on the peak stress for (a) F-NR4 and (b) F-NR5.

As expected, peak stress increases with increasing strain rate and decreasing temperature. In future, further experiments can be conducted to explore intermediate regions and a modelled surface could be generated to describe the dependence of peak stress on both the temperature and rate.

5.3.6.2 Enhancement of the apparent modulus

The general behaviour of filler modulus enhancement has been extensively studied in past research [227–230], albeit with a focus on linearly elastic fillers and binders.

The modulus enhancement observed in the varying strain rate experiments can be compared to the result of the Guth modified Einstein-Smallwood relation as shown in Equation 5.2, where E_m is the modulus of the natural rubber matrix and ϕ_f is the filler volume fraction [231, 232]. Where the Einstein-Smallwood relation predicted the modulus of particle filled solids at low volume fractions, the Guth modification extends its application to higher volume fractions. Einstein initially derived the increase in viscosity caused by rigid spherical particles in a viscous liquid. Further modifications to the relation followed in order to incorporate interactions with neighbouring particles.

$$E = E_m(1 + 2.5\phi_f + 14.1\phi_f^2) \tag{5.2}$$

At 10^{-3} s^{-1} and 5% volume fraction, this relation gives the modulus enhancement to be 16%. Whereas at 50% volume fraction, the enhancement is 5.8 times the matrix

modulus. For the 5% F-NRs, this prediction is similar to the experimentally observed apparent modulus enhancement of 20%. At the lower strain rate, the modulus enhancement observed experimentally ($4.9E_m$) in the 50% F-NRs is similar to that predicted by the Guth relation. However, at the larger strain rate, the apparent modulus enhancement observed ($9.1E_m$) exceeds the prediction from the Guth relation. This may be analogous to the particle aggregation phenomenon described by Guth. They described the clustering of particles leading to an even greater stiffness enhancement than expected with perfectly distributed spheres. At high strain rates, the immobility of the polymer network may be giving rise to pseudo-clusters leading to this further enhancement. Furthermore, localised strain crystallisation may further stiffen the region around fillers. The Guth model for rod-like shapes (Equation 5.3) can be used to characterise these clusters formed by the spheres.

$$E = E_m[1 + 0.67f\phi_f + 1.62(f\phi_f)^2] \tag{5.3}$$

Bergstrom estimates the shape factor (=length/breadth), f, to vary between 4 and 10 [233]. When 4 is used as the factor, the modulus enhancement using Equation 5.3 yields a 20% rise for the 5% F-NRs and a 9 times increase for the 50% F-NRs. It is conceivable that a 3D network is formed by stiffer regions at the filler-matrix interface and localised strain induced crystallisation. These prediction match the experimental observations exactly. In future, X-ray diffraction and/or scattering techniques can be conducted to validate the existence of these proposed structures.

Due to the rate-temperature equivalence, modulus is dependent on both the rate and the temperature. For this reason, the above analysis becomes less feasible for experiments conducted at lower temperatures without making appropriate modifications. For example, for low strain rate, varying temperature experiments as shown in Figure 5.6, at -80 °C, there appears to be no filler influenced modulus enhancement. However, at -40 °C, the apparent modulus is on average 2 times larger for F-NR2/3 and 5 times larger for F-NR4/5. When high strain rate experiments are conducted at

the same temperature, the apparent modulus is only 20% larger for the 5% F-NRs and 3 times larger for the 50% F-NRs. This means that the sensitivity of the modulus enhancement mechanism drops as temperature is reduced and as strain rate is increased. This is as there is a plateau for the instantaneous modulus corresponding to the immobility of the rubber. This immobility is governed by both decreasing temperature (lack of energy to overcome activation barrier for motion) and increasing strain rate (motions cannot occur on the time-scale of the experiment). DMA experiments are conducted in the next section to better quantify the modulus dependencies on rate and temperature.

5.4 Dynamic Mechanical Analysis

In order to use the TTS principle, themo-mechanical characterisation of each material was performed, similar to the experiments detailed in the previous chapters, using the TA Instruments Q800. The soft natural rubber proved more challenging to characterise using the existing experimental procedure, as such, a discussion of the improvements in methodology will be presented along with the improved results.

5.4.1 Initial method

The DMA experiments described in previous chapters were conducted in a dual cantilever configuration, with an oscillatory strain amplitude of 0.1% and isothermal frequency sweeps at 2 °C - 2.5 °C increments. For neoprene, for example, the specimen size was 5 mm $\times$ 10 mm $\times$ 60 mm and the frequencies were 0.5, 2, 5 and 10 Hz. These conditions formed the basis for the DMA experiments on the natural rubber.

5.4.2 Initial results and analysis

Figure 5.31 shows the results of the DMA experiment performed under the same set of experimental conditions as previous experiments, as described above. These data are very poor and do not represent the underlying behaviour of the U-NR.

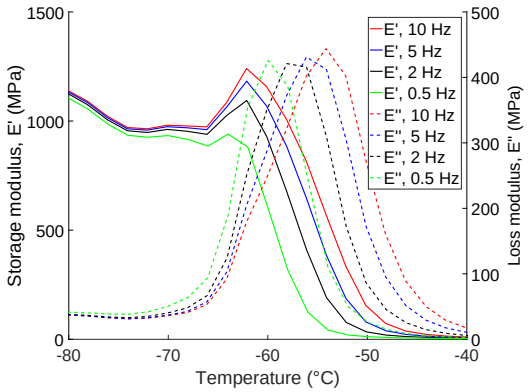

FIGURE 5.31: DMA results for U-NR with major clamping artefacts.

As the temperature increases and approaches T_g, there is a sharp rise in measured modulus. These local maxima in the storage moduli are not real properties, as the modulus is expected to decrease monotonically with increasing temperature. The increase is hypothesised to be due to a significant increase in specimen volume as the U-NR goes through its T_g. Since the dual cantilever configuration clamps the sample either side of the drive shaft, a considerable rise in axial strain occurs leading to a greater drive force required to maintain the desired oscillatory profile, causing errors in the measured storage modulus. In order to mitigate this, the samples were reduced in length to dimensions of 5 mm $\times$ 10 mm $\times$ 40 mm so that DMA experiments using the single cantilever configuration could be conducted.

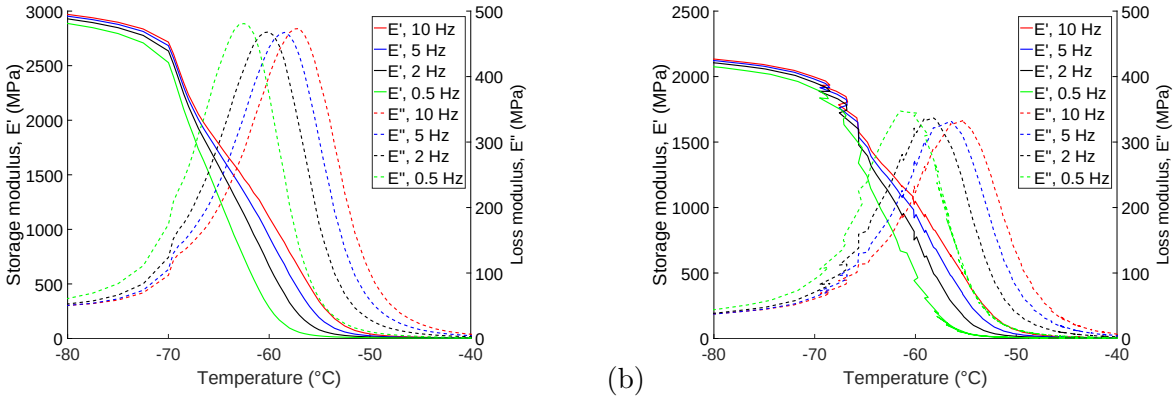

FIGURE 5.32: DMA results for F-NR2 with (a) substantial clamping artefacts and (b) poor temperature control.

In Figure 5.32, results of the single cantilever experiment on F-NR2 are shown. Despite changing to single cantilever configuration, there are still substantial clamping artefacts remaining. This is due the length to thickness ratio still being too small. To ameliorate this, the thickness would have to be further reduced for these single cantilever samples. In order to do this, a Universal Laser Systems VLS4.60 laser cutter was used to trim the samples so that the new dimensions were 2 mm $\times$ 5 mm $\times$ 40 mm. The platform has a 10.6 µm CO_2 laser source ranging in power from 10 to 60 W. The default setting for a low-odour rubber was used and adjusted to reduce the power by 30%. This was done in order to reduce the risk of fire. Higher power settings visibly damaged the top 2 mm of the rubber.

A further difficulty that also emerged was that of poor temperature control, as seen in Figure 5.32b. It was determined that a new clamp screen, which had a solid metallic baffle around the centre of the screen's mesh (Figure 5.33), was causing eddy currents leading to significant temperature fluctuations. The old clamp screen performed better, as it did not have this metallic baffle and therefore provided a more even delivery of coolant to the measuring system. The difference in temperature control between the old screen (a) and the new screen (b) can be seen by comparing the two sets of results in Figure 5.32. To further aid with temperature control, an additional change was introduced. The isothermal step size in the glass transition region was reduced from 2.5 °C to 0.5 °C.



FIGURE 5.33: Comparison of old (left) and new (right) clamp screens for the DMA.

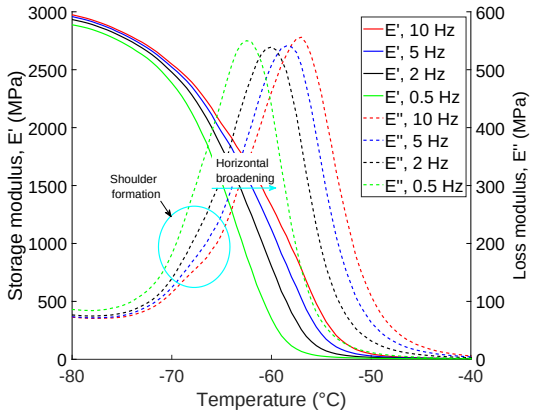

FIGURE 5.34: DMA results for F-NR3 with mild clamping artefacts.

It is clear that improving the aspect ratio of the sample has improved the data considerably (Figure 5.34). However, there is still a horizontal broadening of the storage moduli curves, which is noticeable at temperatures around -60 °C. As this temperature is within the glass transition region, this artefact masks the underlying properties. This is also evident from the shoulders formed on the loss moduli data at around -70 to -65 °C.

This artefact is again associated with clamping, despite tightening the clamping screws at -90 °C when the rubber is in its shrunken glassy state. The rubber samples have small variations in shape due to the various cutting and trimming processes. This means that the contact area between the clamping and sample surfaces does not remain constant through the volume expanding process as the temperature passes T_g. The increase in contact area is perceived as an increase in modulus by the instrument. This effect is more prominent at higher frequencies and is also seen in the results of the DMA experiments for F-NR4 and F-NR5 (Figure 5.35). To maintain the contact area through T_g, additional pieces of the same rubber were placed in the clamp either side of the sample to level the clamping surface and also distribute the clamping pressure more evenly. This is shown schematically in Figure 5.36.

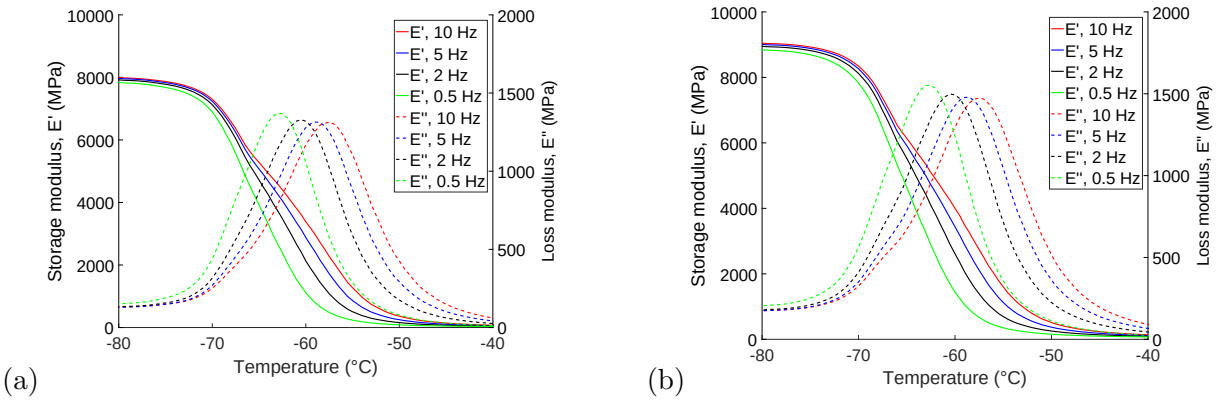

FIGURE 5.35: DMA results for (a) F-NR4 and (b) F-NR5 with significant clamping artefacts.

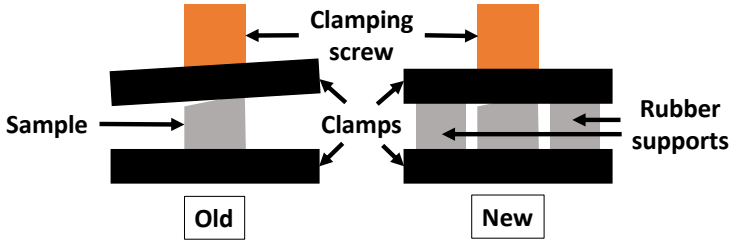

FIGURE 5.36: Diagram showing new clamping method, placing rubber supports either side of the sample, ensuring even distribution of the clamping pressure and an improved contact area through T_g.

5.4.3 Updated method

In order to mitigate the challenges in conducting DMA experiments for U-NR and the F-NRs using the existing methodology, the following changes were made.

1. Single cantilever DMA experiments were conducted instead, reducing the increase in axial strain effect due to volume expansion with the dual cantilever experiments.

2. A clamp screen without a solid baffle was used to ensure a more even delivery of coolant to the specimen.

3. Isothermal step size reduced in the transition region to 0.5 °C.

4. The specimen dimension was reduced to 2 mm × 5 mm × 40 mm to improve the aspect ratio.

5. Additional pieces of the rubber to be investigated added either side of the sample to ensure a good contact area between the sample and clamping surfaces and to also distribute pressure evenly.

6. Clamping torque reduced significantly

7. Reduce the frequencies interrogated to all be below 2 Hz

The last two points were not mentioned in the previous section. In order to reduce the clamping artefacts further, the default clamping torques were changed and the range of frequencies was reduced. By lowering the frequencies, the experimental duration is significantly increased. As a trade-off, the number of stabilisation and collection cycles for the DMA were reduced from 4 and 3 to 2 and 2 respectively.

Previously, for DMA experiments on elastomers, an initial room temperature clamping torque and low temperature shrinkage correction torque of around 3 to 5 lb in or 0.3 to 0.6 N m was used. In the updated experiments, the room temperature and low temperature correcting clamping torque were lowered significantly to 0.6 lb in (0.07 N m) and 1 lb in (0.1 N m) respectively.

5.4.4 Updated results and discussion

5.4.4.1 Complex moduli and loss tangents

Figure 5.37 shows the DMA results for U-NR with the updated methodology.

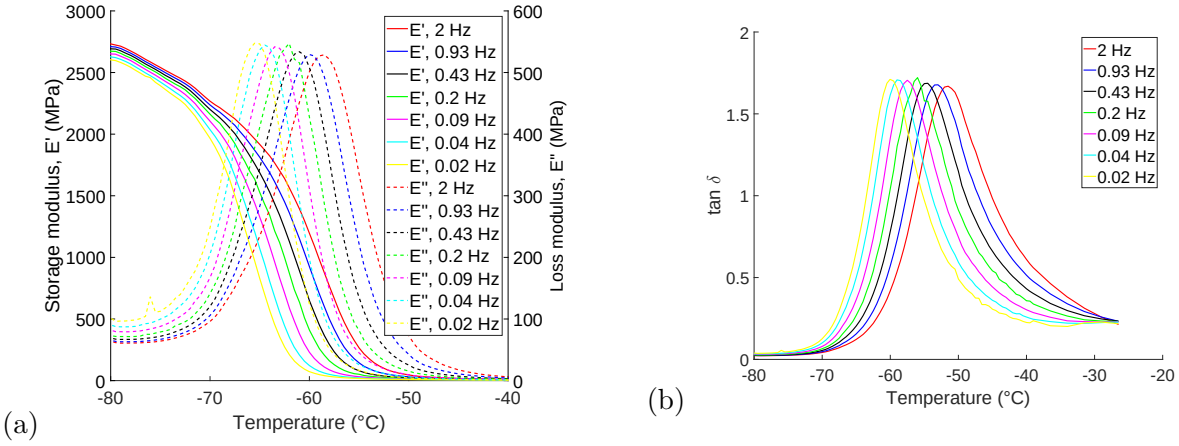

FIGURE 5.37: DMA results for U-NR highlighting (a) temperature dependent viscoelasticity and (b) loss tangents.

It is immediately clear that these data are significantly better than those collected previously. In order to obtain data that can be used to perform TTS to a higher standard, more frequencies were swept at each temperature step and more values per decade of frequency were included.

Results for the DMA experiments on F-NR2 and F-NR3 are found in Figures 5.38 and 5.39 respectively.

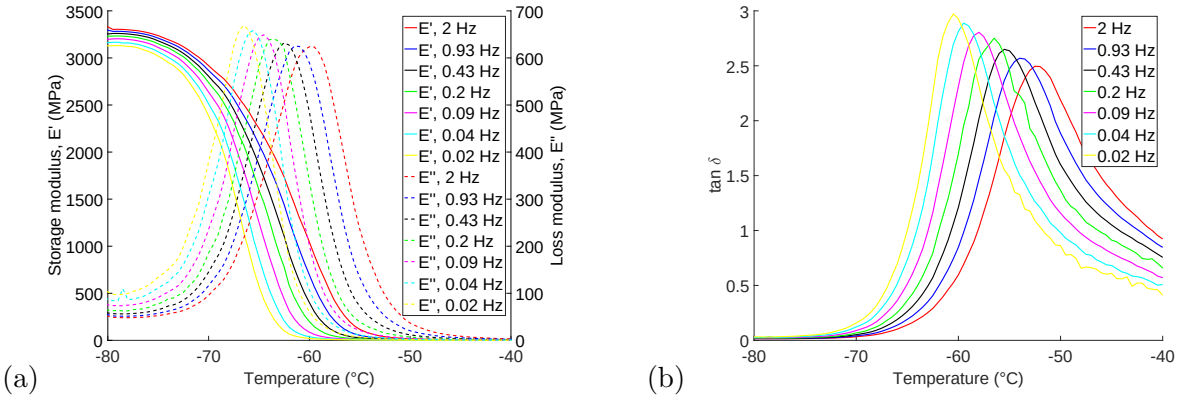

FIGURE 5.38: DMA results for F-NR2 highlighting (a) temperature dependent viscoelasticity and (b) loss tangents.

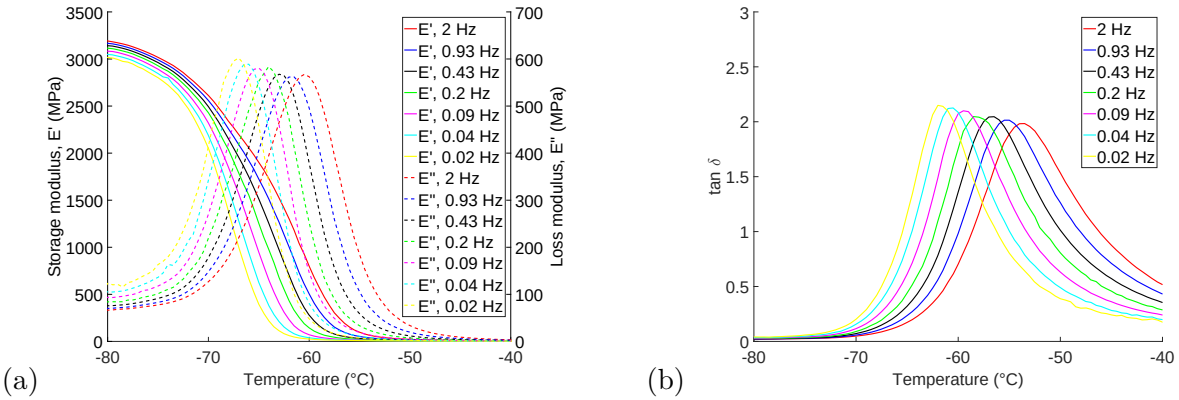

FIGURE 5.39: DMA results for F-NR3 highlighting (a) temperature dependent viscoelasticity and (b) loss tangents.

The storage and loss moduli for both 5% filled composites – F-NR2 and F-NR3 – are similar to those of U-NR, but the loss tangent peaks show a decreasing magnitude with increasing frequency. This is as the addition of particles immobilises some of the polymer surrounding the filler, restricting the damping response [234]. Furthermore, an increasing frequency decreases the intensity of the loss tangent.

The results for the DMA experiments on the 50% filled composites, F-NR4 and F-NR5, are shown in Figures 5.40 and 5.41 respectively[1].

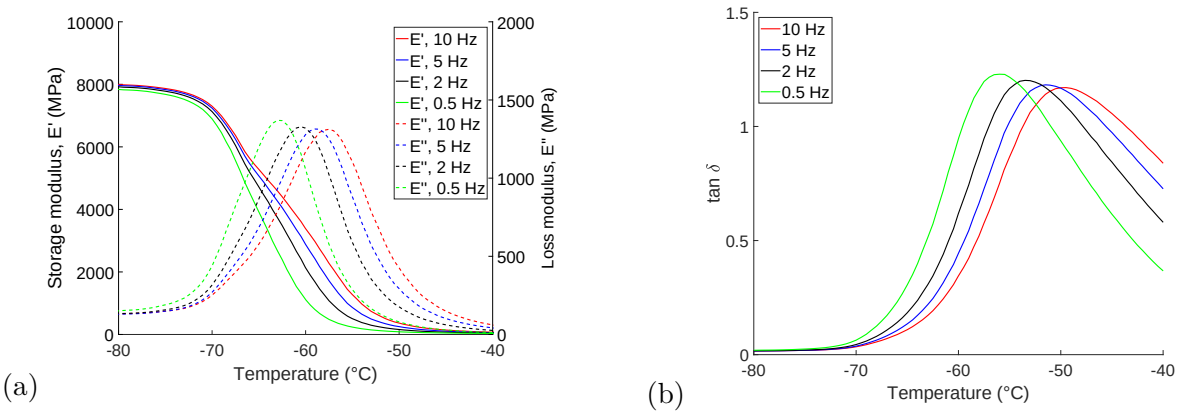

FIGURE 5.40: DMA results for F-NR4 highlighting (a) temperature dependent viscoelasticity and (b) loss tangents.

[1]These results are not based on the updated method, as there was insufficient time to perform these experiment, since I was unable to access the laboratory facilities due to the Covid-19 pandemic. If time permits, I will redo these experiments once the laboratory reopens, and these data will act only as place-holders. However, using these results does not detract from the core message of the thesis.

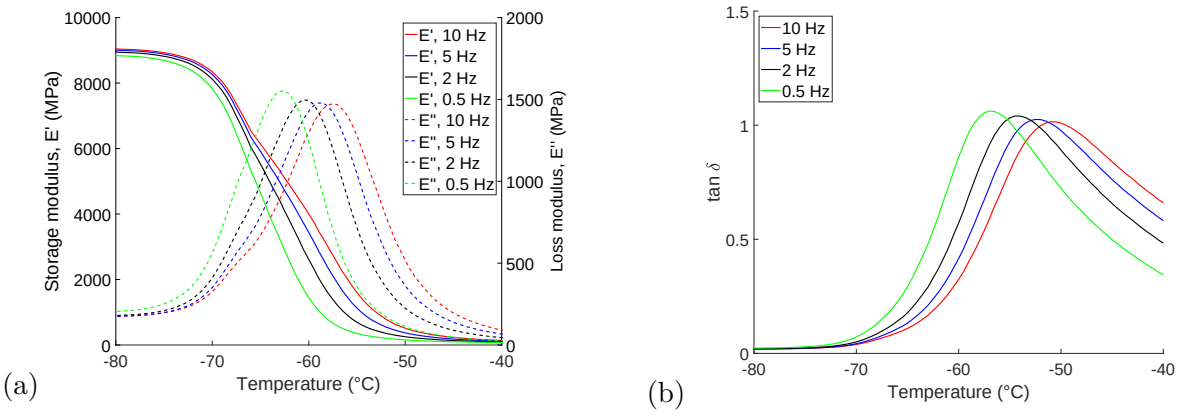

FIGURE 5.41: DMA results for F-NR5 highlighting (a) temperature dependent viscoelasticity and (b) loss tangents.

It is clear that these results are not similar to the unfilled or 5% filled natural rubbers. The glassy storage modulus plateau is at 8 GPa for F-NR4 and 9 GPa for F-NR5 — three times larger than that for U-NR, F-NR2 and F-NR3. The higher plateau for F-NR5 is observed because the modulus is inversely proportional to the particle radius and depends on the surface-to-volume ratio [235]. Although the Guth equations earlier (5.2 and 5.3) express the modulus variation with filler content, Alter [235] suggests the inverse dependence on the particle radius could simply be a shape factor correction as proposed by Guth. There is also considerably less damping through the glass transition for the 50% filled composites, as the loss tangent peaks are lower than the other three materials.

5.4.4.2 Master curves

Instead of plotting the modulus against temperature as in the previous section, it can be plotted against frequency, producing isotherms of the response. These are shown for U-NR in Figure 5.42a.

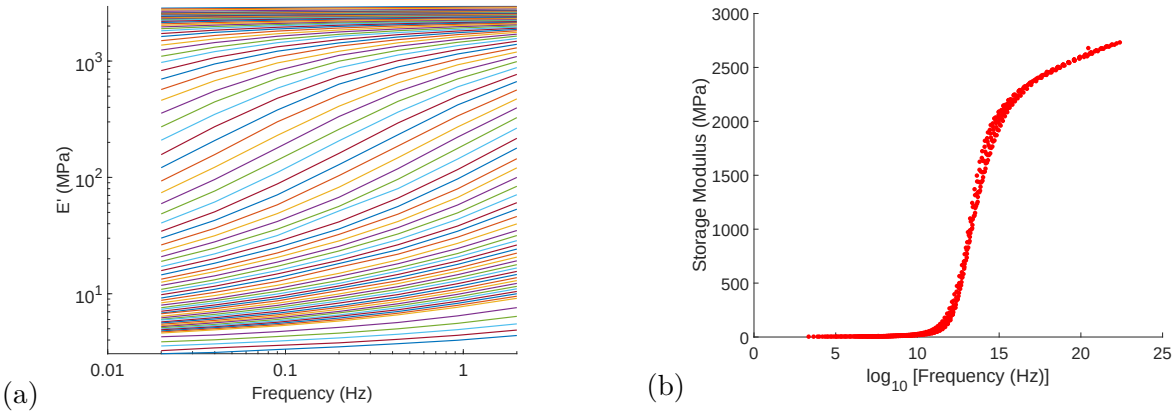

FIGURE 5.42: (a) Isotherms from the DMA results for U-NR and (b) the master curve generated by shifting these at a reference temperature of 25 °C.

By using a TTS shifting algorithm such as the one described in Chapter 2, §2.4, the isotherms for U-NR shown in Figure 5.42a can be shifted to construct the master curve as shown in Figure 5.42b at a reference temperature of 25 °C. This same process can be performed for the composites, leading to the master curves as shown in Figure 5.43. They are plotted on the same set of axes to facilitate comparison.

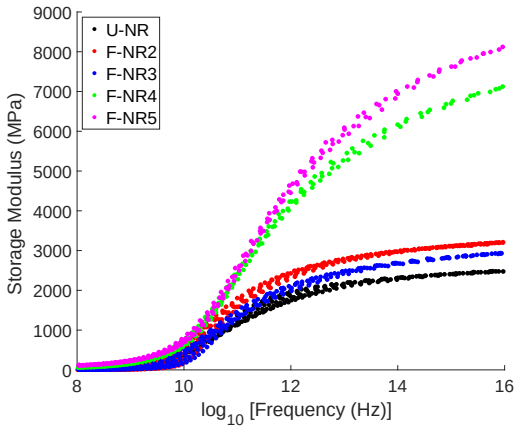

FIGURE 5.43: Master curve for each material generated at a reference temperature of 25 °C.

In these master curves, the low frequency plateau represents the long-term modulus, obtained from shifting the highest temperature isotherms. Conversely, the high frequency plateau represents the instantaneous modulus, obtained from shifting the lowest temperature isotherms. It is evident that the addition of fillers enhances the mechanical performance of natural rubber. However, a 5% volume fraction does not

significantly increase the instantaneous modulus: an average of 17%, which is consistent with the observed 20% increase in apparent modulus experimentally, and that calculated by the Guth equation earlier (16%). There is a threefold increase in the instantaneous modulus by increasing the filler volume fraction to 50%. As F-NR5 has smaller particles, and hence a higher surface area to volume ratio, its instantaneous modulus value is 14% higher than F-NR4, which has ten times larger particles.

5.4.4.3 Shift factor relationships

For each material, their isotherms were moved according to a temperature dependent shift factor, to construct the master curve at the reference temperature of 25 °C. These temperature dependent shift factors take an Arrhenius form below T_g (shown for U-NR in Figure 5.44a) and a WLF form above T_g (Figure 5.44b).

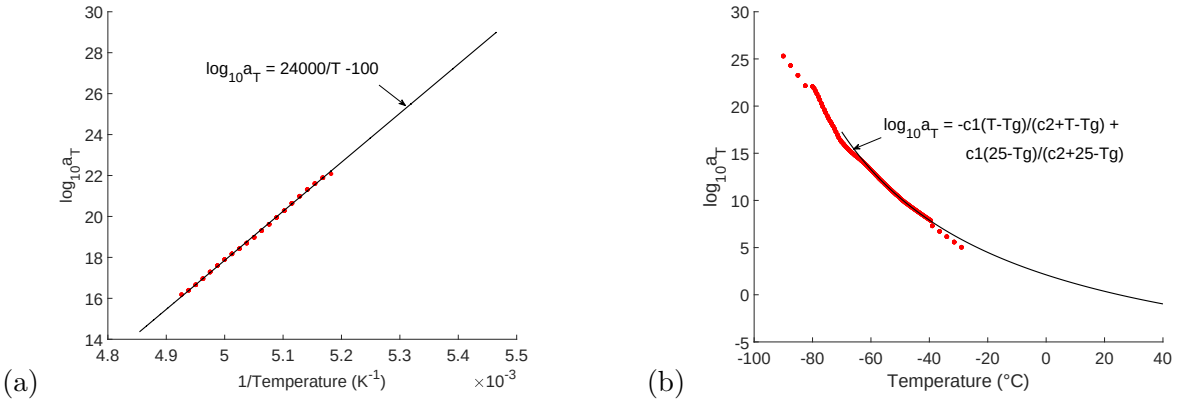

FIGURE 5.44: Shift factors used to construct the master curve follow an (a) Arrhenius form below T_g and (b) WLF form above T_g.

The duration of each DMA experiment was approximately three days, despite only ranging from −80 °C to −40 °C. This meant that it was not feasible to perform DMA experiments from below T_g through to the desired reference temperature of 25 °C, within a reasonable time-frame. Therefore, the WLF relation was extrapolated from its fit at T_g to enable the master curve to be constructed at 25 °C. The additional shift required to take the curve from T_g to 25 °C is represented by the second term in the $\log a_T$ equation in Figure 5.44b.

The shift factors for the filled rubbers have the same relationships as U-NR, below and above T_g, and are presented below: Figure 5.45 for F-NR2; 5.46 for F-NR3; 5.47 for F-NR4; and 5.48 for F-NR5. In all the WLF fits, the reference temperature is taken to be the glass transition temperature, $T_g = -60$ °C, which is the same for all materials. Not only is this evident from the DMA results in this section, but is shown more clearly in the next section (§5.5) with the results of the DSC experiments.

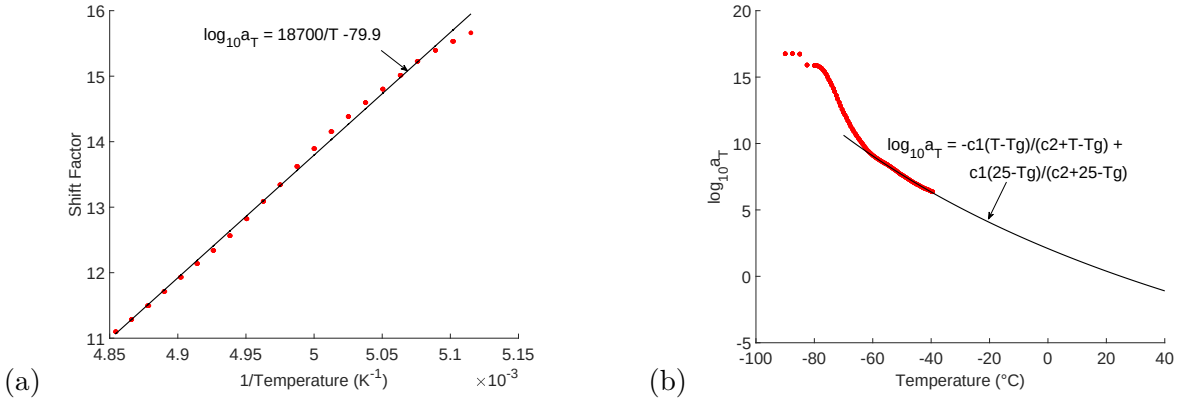

(a) (b)

FIGURE 5.45: Shift factors used to construct the master curve for F-NR2 follow an (a) Arrhenius form below T_g and (b) WLF form above T_g.

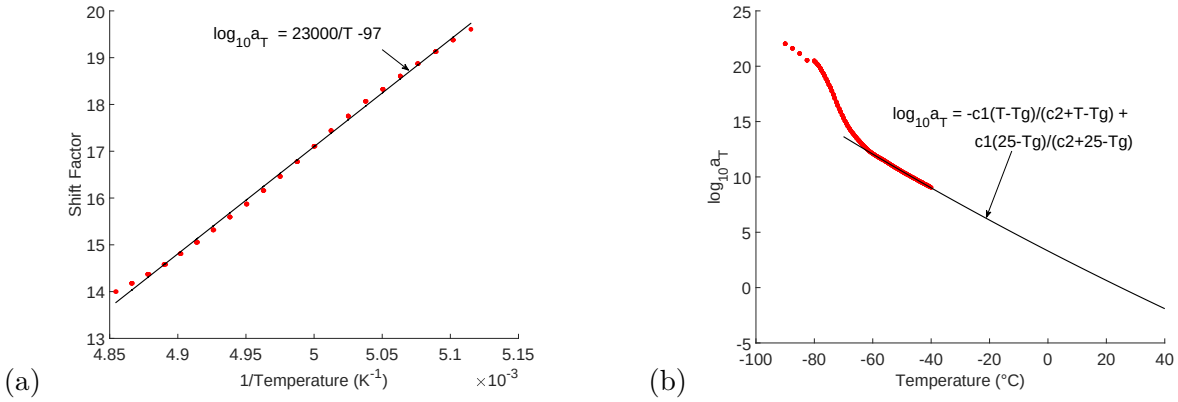

(a) (b)

FIGURE 5.46: Shift factors used to construct the master curve for F-NR3 follow an (a) Arrhenius form below T_g and (b) WLF form above T_g.

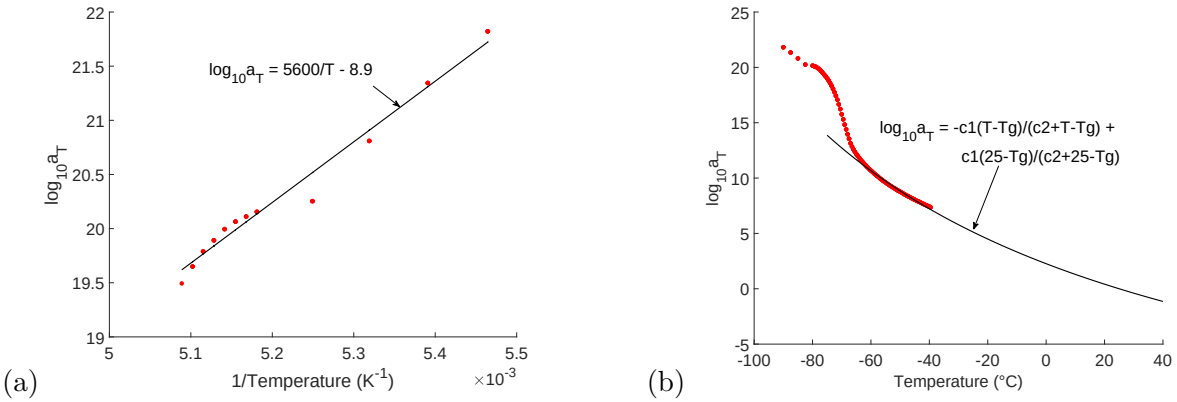

FIGURE 5.47: Shift factors used to construct the master curve for F-NR4 follow an (a) Arrhenius form below T_g and (b) WLF form above T_g.

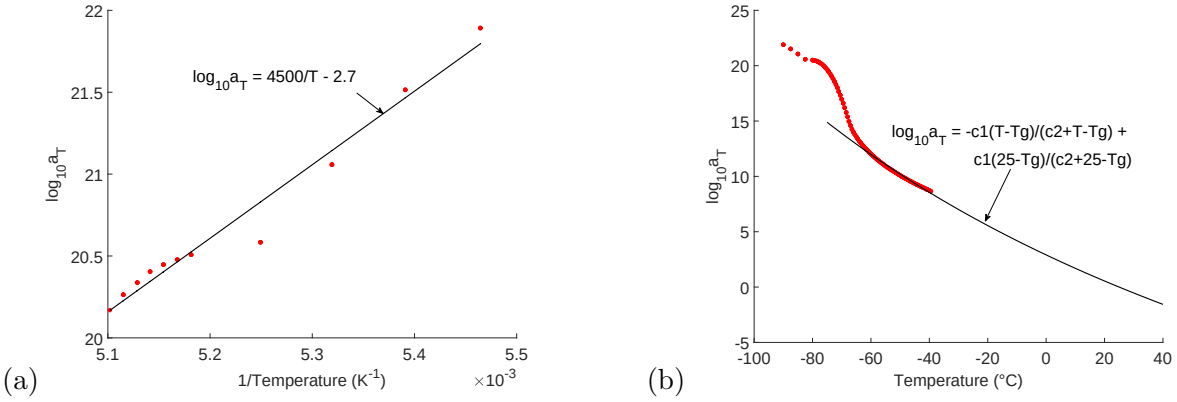

FIGURE 5.48: Shift factors used to construct the master curve for F-NR5 follow an (a) Arrhenius form below T_g and (b) WLF form above T_g.

Table 5.3 contains information on the range of temperatures the Arrhenius relationship is valid for based on the fits to the experimental data below T_g, and the constants used for the WLF fits to the data above T_g.

TABLE 5.3: Additional information for the shift factor relationships presented in Figures 5.44 through 5.48.

Material	**Arrhenius range**	**WLF constants**
U-NR	-70 °C to -80 °C	$c1 = 24$, $c2 = 71$
F-NR2	-66 °C to -77 °C	$c1 = 32$, $c2 = 220$
F-NR3	-66 °C to -77 °C	$c1 = 130$, $c2 = 850$
F-NR4	-77 °C to -91 °C	$c1 = 30$, $c2 = 160$
F-NR5	-69 °C to -81 °C	$c1 = 52$, $c2 = 280$

In §5.3.3, it was observed that experimentally simulating high rate experiments with quasistatic, low temperature experiments led to similar mechanical responses. This implies that the rate-temperature dependence for the damage mechanism is the same as that for the modulus. For this reason, the shift factors presented in this section enable the full mechanical response for these materials to be modelled, as will be seen in the next chapter.

5.4.4.4 Activation energies

It is possible to infer the value of the activation energy for the glass transition by considering the Arrhenius equation fitted to the shift factors below T_g. Furthermore, the activation energy can also be calculated by analysing the shifting of the loss tangents.

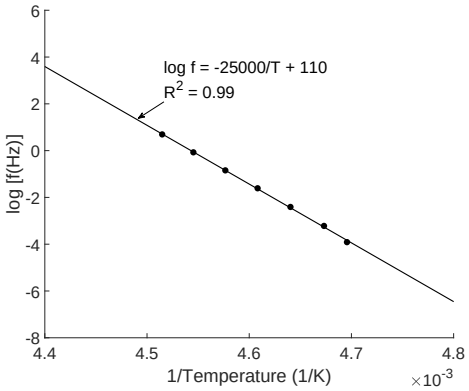

FIGURE 5.49: Using the loss tangent peaks to find the activation energy.

The Arrhenius equation takes the form $A\exp(-Q/RT)$. If log frequency is plotted against the reciprocal of the absolute temperature, the gradient of this curve gives $-Q/R$, where Q is the activation energy for the glass transition, and R is simply the gas constant.

This type of curve has already been plotted in terms of the shift factor relationship below T_g; obtained empirically by shifting storage modulus isotherms. A similar plot can be constructed by analysing the shifting of the loss tangent curves. For U-NR, consider the loss tangents shown in Figure 5.37b. The natural logarithm of the frequency

can be plotted against the reciprocal of the absolute temperature for each of the loss tangent peaks as shown in Figure 5.49.

This type of plot constructed using the loss tangent peaks has been provided in Figure 5.50 for the filled composites. A comparison of the activation energies resulting from these two methods is shown in Table 5.4.

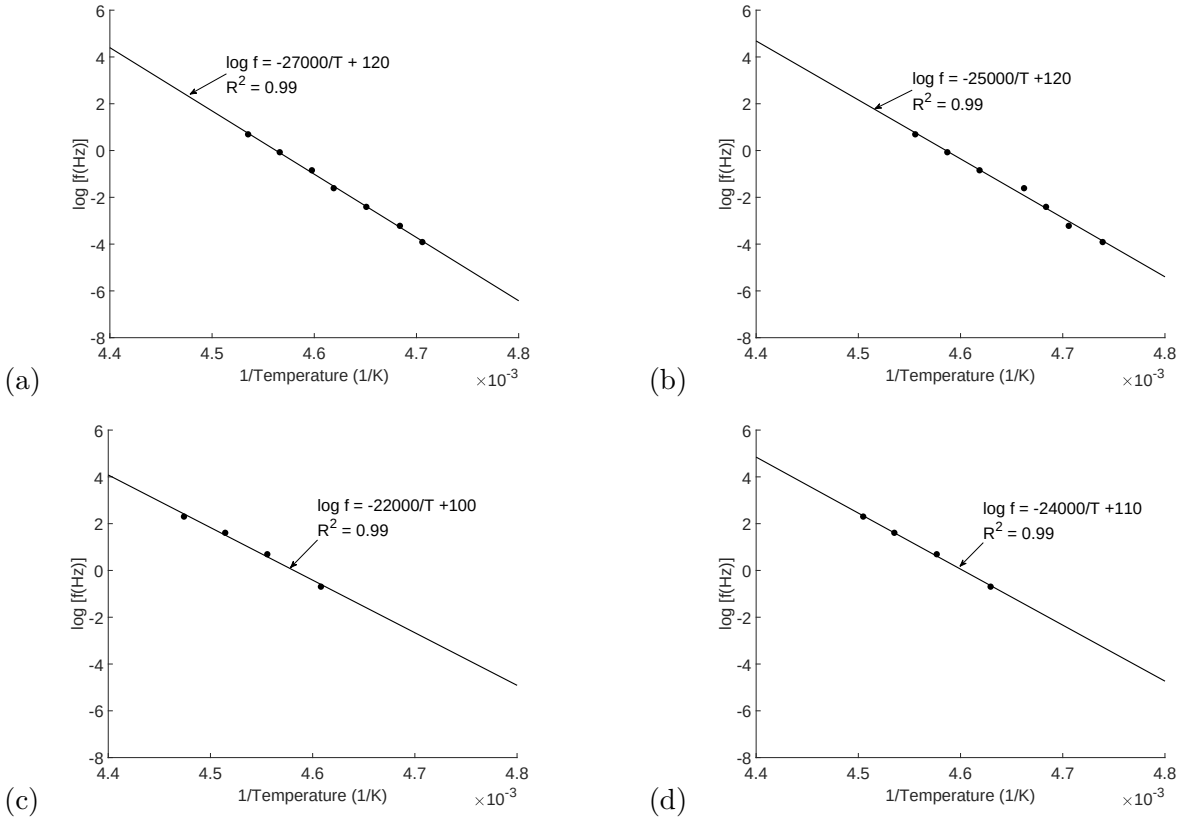

FIGURE 5.50: Using the loss tangent peaks to find the activation energy for (a) F-NR2, (b) F-NR3, (c) F-NR4, and (d) F-NR5.

TABLE 5.4: Comparison of the glass transition activation energies resulting from analysing the shifting of the loss tangent peaks (Method A), and from the empirical storage modulus shift factor relationship below T_g (Method B).

Material	**Method A** ($\mathrm{kJ\,mol^{-1}}$)	**Method B** ($\mathrm{kJ\,mol^{-1}}$)	**% difference**
U-NR	210	200	-4.8%
F-NR2	220	160	-27%
F-NR3	210	190	-9.5%
F-NR4	180	47	-74%
F-NR5	210	37	-82%

With an average of 206 kJ mol^{-1}, there appears to be a very good agreement between the activation energy values found for all of the materials using Method A: analysing the shifting of the loss tangent peaks. Excluding the values for the 50% filled composites, there is a decent agreement between the values using Method B: analysing the empirical storage modulus shift factor relationship below T_g. However, as the DMA experiments for F-NR4 and 5 were performed using the old method, the confidence in the TTS algorithm producing accurate shift factors is lower than that for those using the updated method. In future, the DMA experiments for F-NR4/5 will be repeated using the updated method, leading to more accurate TTS results.

5.5 Differential Scanning Calorimetry

As discussed earlier in the chapter, and earlier in this thesis, since the deformation at higher strain rates is adiabatic, the specimen increases in temperature as the heat cannot diffuse out on the time-scale of the experiment. This was illustrated with an example in §5.3.5.3, where there was a 3 °C temperature rise calculated for a high rate experiment (c. 2000 s^{-1}) conducted at −60 °C. The temperature rise, and its effect on modulus in particular, is an important effect, altering the overall mechanical response, and must be incorporated into modelling strategies. In order to find the temperature rise in the specimen due to this adiabatic self-heating, as in previous chapters, the density and a Taylor-Quinney coefficient of one for the conversion of mechanical work into heat is used.

$$\Delta T \approx \frac{\beta}{\rho C_p(T)} \int_0^{\varepsilon} \sigma(\varepsilon) d\varepsilon \tag{5.4}$$

In order to use this equation, the temperature dependent heat capacity must first be obtained for each rubber grade. These are measured using MDSC experiments. The results of the MDSC experiments on the different rubbers will also give more accurate values for the glass transition temperature than conventional DSC experiments.

5.5.1 Method

The methodology for conducting the MDSC experiments is the same as Chapter 4, §4.5.1. Three experiments on each material were performed with an underlying ramp of 3 °C min^{-1} and modulation of ±0.5 °C min^{-1} over the temperature range from −90 °C to 200 °C. This temperature range ensures that the glass transition is covered, but also allows the elucidation of other transitions that may be present at typical temperatures encountered in this current study. The reasons for selecting this particular ramp and modulation are given in Chapter 2, §2.3.4.

5.5.2 Results and analysis

The results of the MDSC experiments for U-NR are shown in Figure 5.51. Three experiments are performed and the average of the temperature dependent heat capacity is plotted. Models either side of the glass transition are fitted to the average data. Below T_g, an exponential description is fitted, and above T_g, a linear fit is used.

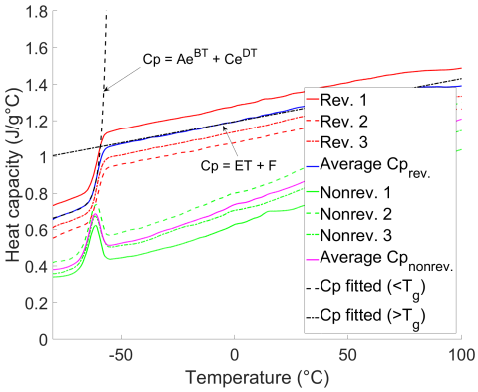

FIGURE 5.51: MDSC results for U-NR with model fits either side of the T_g.

The MDSC results for the F-NRs are shown in Figure 5.52. The form of the results for the MDSC experiments on the particulate composites is the same as that of the U-NR, so the same models can be fit either side of their T_g. Table 5.5 shows the parameters required for the model fits.

TABLE 5.5: Parameters for the model fits to the MDSC results.

Material	**A** ($J\,g^{-1}\,°C^{-1}$)	**B** ($°C^{-1}$)	**C** ($J\,g^{-1}\,°C^{-1}$)	**D** ($°C^{-1}$)	**E** ($J\,g^{-1}\,°C^{-2}$)	**F** ($J\,g^{-1}\,°C^{-1}$)
U-NR	1.5×10^{11}	0.46	1.1	5.8×10^{-3}	2.4×10^{-3}	1.2
F-NR2	1.7×10^{4}	0.19	0.93	1.8×10^{-3}	2.5×10^{-3}	1.3
F-NR3	1.3×10^{4}	0.19	0.94	1.7×10^{-3}	2.7×10^{-3}	1.3
F-NR4	1600	0.17	0.71	2.1×10^{-3}	1.9×10^{-3}	0.87
F-NR5	1800	0.17	0.88	2.3×10^{-3}	1.8×10^{-3}	1.0

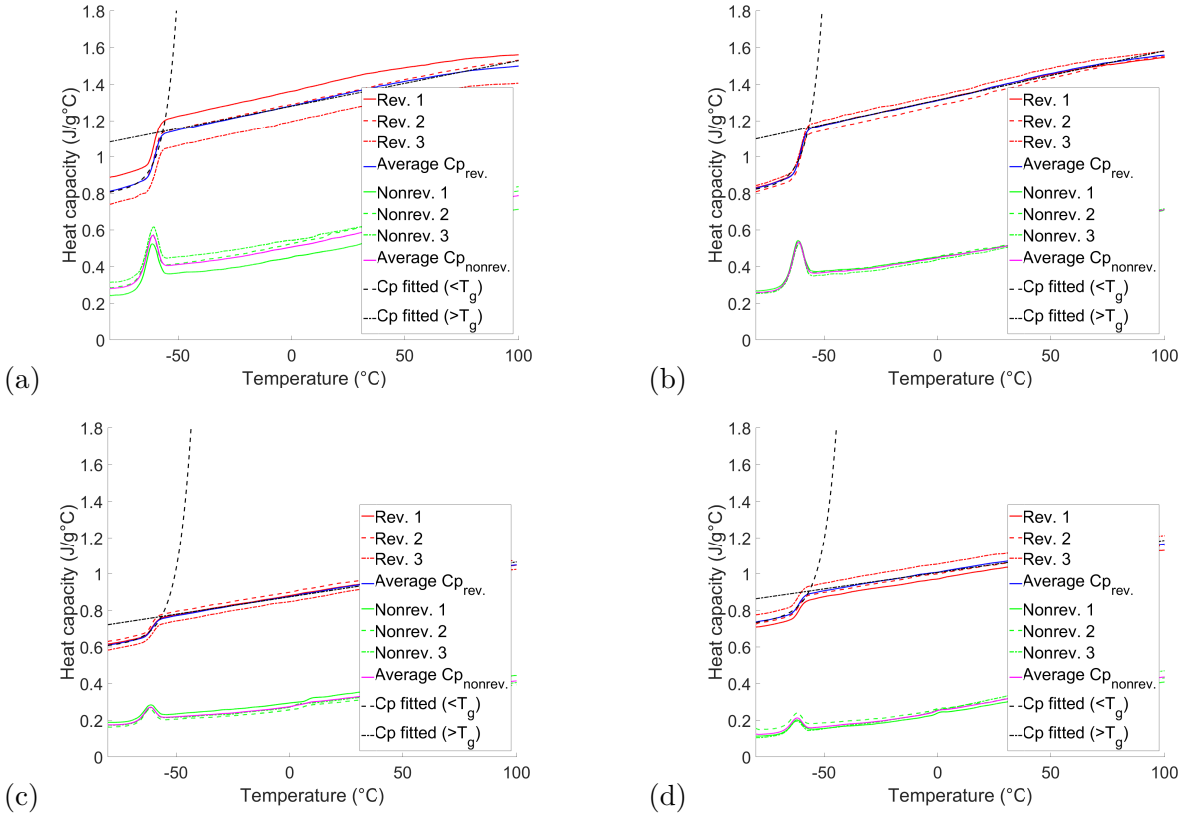

FIGURE 5.52: MDSC results for (a) F-NR2, (b) F-NR3, (c) F-NR4, and (d) F-NR5, with model fits either side of T_g.

The three main thermal behaviours that can be extracted from these results are the calorimetric T_g of the material (calculated as the mid-point of the transition), the increase in heat capacity and the temperature range of the transition.

To better aid comparison, the results of the reversing C_p for each material is re-plotted in Figure 5.53. The curves are shifted slightly along the y-axis such that the ordinate at the onset of the glass transition has the same value for each curve.

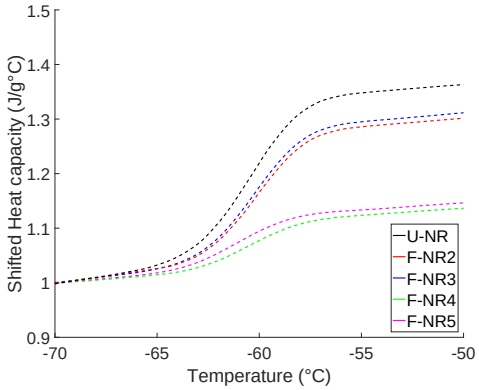

FIGURE 5.53: Shifted MDSC results for all grades of NR to compare T_g, heat capacity rise and breadth of transition.

From Figure 5.53, the addition of glass microspheres is observed to cause a decrease in the rise in heat capacity. For U-NR, the rise was $+0.30\ \mathrm{J\,g^{-1}\,°C^{-1}}$, whereas for F-NR2/3 this rise fell to $+0.26$ and $+0.24\ \mathrm{J\,g^{-1}\,°C^{-1}}$ respectively. The change was even more significant for the 50% F-NRs as the rise fell to $+0.10$ and $+0.09\ \mathrm{J\,g^{-1}\,°C^{-1}}$ for the F-NR4/5 respectively. This drop is primarily due to there being less rubber present for the transition process as the filler volume fraction is increased. Similar observations have been made with clay-polymer nanocomposites [234] and spherical silica-polymer nanocomposites [236].

The heat capacity results show a smaller dependence on the particle size distribution. For the samples with smaller particle sizes (F-NR3/5), the heat capacity is slightly higher than that for the samples with larger particle sizes at the same filler volume fraction. This may be since there is a greater temperature dependence of interfacial energy for the composites with smaller particles as the surface area to volume ratio is inversely proportional to the radius for spherical particles. This means for a given mass, more energy is required to raise the temperature of the composite with smaller fillers by a degree than the composite with the larger fillers, thereby increasing its heat capacity.

There is a very slight broadening of the transition with increasing filler volume fraction. Upon considering the temperature range either side of the T_g used to establish a linear dependence in the transition, the breadth of the transition can be calculated.

For U-NR, $\Delta T = 4.2$ °C and this increases to $\Delta T = 4.4$ °C for the 5% F-NRs and $\Delta T = 5.1$ °C for the 50% F-NRs. This phenomenon is due to segmental dynamics becoming more heterogeneous as the amount of particles increase and mobility of polymer chains is greatly reduced in the interfacial region between the filler and matrix [237].

Based on these MDSC experiments, it is clear that the addition of glass microspheres does not influence the T_g. This is as the available surface area from the fillers is too small for the segmental motion to be significantly reduced. There is no dependence on filler volume fraction or filler particle size at the values used in this study. In each set of experiments, $T_g = -60$ °C. This result correlates well with the findings from the DMA experiments in the previous section.

5.6 Conclusions

The experimental results in this chapter provide insights and confidence that a modelling framework based on the results of these experiments and the TTS principle will be able to predict the mechanical behaviour of the F-NR composites.

In order to model the behaviour of the composites, as described in previous chapters, the results of quasi-static compression experiments conducted at various temperatures will be used alongside results of the DMA and DSC experiments. The DMA results will allow the modulus enhancement from fillers and the mesophase at the interface between filler and matrix to be included. Strain activated damage behaviour will also be incorporated to take into account the observations in this chapter. The next chapter details the model developments required to apply the strategies covered in previous chapters with neoprene rubber and (P)PVC to the natural rubber particulate composites.

6 Modelling framework for natural rubber particulate composites

In the previous chapter, the experimental results for the unfilled and filled natural rubbers (U/F-NR) were presented. These not only helped to characterise the basic thermomechanical response of these materials, but provided insights and confidence towards using a TTS based modelling framework to capture their high rate response.

In this chapter, modelling strategies will be discussed for representing and predicting the high rate behaviour of the U-NR matrix and glass microsphere F-NR particulate composites. Depending on whether the focus is on ambient or sub-ambient high rate simulations, different considerations are made. The modelling encompasses viscoelasticity from DMA experiments, hyperelasticity from an Ogden strain energy density function or non-Gaussian Langevin chain statistics basis, viscoplasticity from the Mulliken-Boyce foundation, the enhancement obtained from filler addition, and strain activated damage. The effect of temperature rise during the experiment due to adiabatic self heating will also be included via the results of DSC experiments. In combining these modelling aspects, it will be possible to predict the high strain rate behaviour of particulate composites, one of the major aims of this research project.

6.1 Introduction

Rubber can crystallise at large strains, though this is typically in tension above 200% strain [238]. Although it can crystallise at low temperatures, it is typically when it is held at low temperatures on the order of weeks [239]. For the purpose of this study, given the loading conditions considered, the rubber is treated as amorphous.

Different models have been used in the past to describe the mechanical behaviour of amorphous polymers either side of the T_g. In terms of the glassy behaviour, one such model is the Eyring based Boyce model, which focusses on large strain viscoplasticity based on activation energy processes [119, 182, 211, 215]. This Boyce model has subsequently been extended to focus on the behaviour in the rubbery state [233, 240]. Some effort has been made to enhance this type of model to capture high strain rate behaviour [183, 184]. However, full use has not been made of the TTS principle in order to exploit the rate-temperature equivalence to develop predictive modelling frameworks. Furthermore, the integration of the effect of adiabatic self-heating on the thermal relaxation of the modulus has not been satisfactorily included. Though the temperature has been explicitly increased, the modulus has remained unchanged.

Another modelling strategy, focusing on the elastomeric behaviour above T_g primarily, uses a hyper-viscoelastic basis [153, 191]. The overall stress is calculated from the superposition of a hyperelastic stress (from an Ogden [141, 142] or Mooney-Rivlin [136, 137] model) and a viscoelastic stress (from an SLS [149] or K-BKZ [169, 170] model). However, in these models most, if not all, of the parameters must be calibrated using varying strain rate data. This diminishes the model's desired predictive capability.

This chapter builds on two modelling strategies developed earlier. Firstly, minimisation of parameter calibration experiments was shown to be possible by using the results of DMA experiments along with quasi-static compression experiments in order to capture the high rate mechanical response of neoprene rubber. Secondly, it was shown that a novel modelling framework fully calibrated using quasi-static experiments could predict the high rate response of (P)PVC. Here, they are combined with

the experimental data and insights of the previous chapter. This will allow development of models providing a greater understanding of the adiabatic self heating, filler enhancement and strain activated damage under a variety of loading conditions.

6.2 Model requirements

There are broadly three types of mechanical response for the U/F-NRs. These are better visualised by looking at the experimental data in Figure 6.1.

1. Hyper-viscoelastic response under ambient conditions, Figure 6.1a
2. Viscoplastic response under sub-ambient, low rate conditions, Figure 6.1b
3. Strain activated damage under sub-ambient, high rate conditions, Figure 6.1c

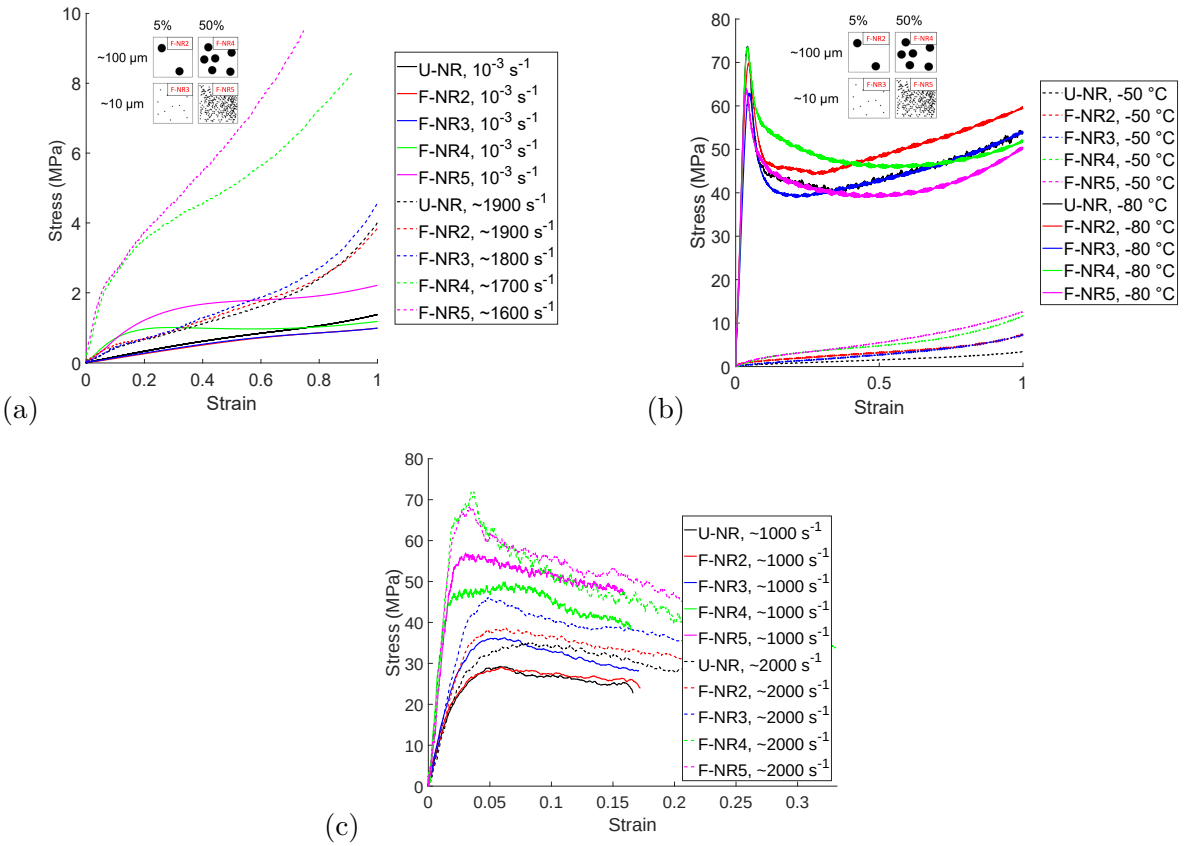

FIGURE 6.1: Experiments highlighting the three distinct responses: (a) Hyper-viscoelastic response under ambient, varying rate conditions, (b) viscoplastic response under sub-ambient conditions at a rate of 10^{-2} s^{-1} and (c) also featuring strain activated damage under sub-ambient, high rate conditions at -40 °C.

In (a), the ambient varying rate behaviour comprises of small strain viscoelasticity and large strain hyperelasticity. The response for the F-NRs also depends on filler enhancement and strain activated damage. In (b), the sub-ambient low rate glassy response is formed of small strain viscoelasticity, followed by viscoplastic strain softening and large strain hyperelasticity. There is similarly a contribution of filler enhancement and damage to the response of F-NRs. However, observing the recovered specimens from sub-ambient low rate experiments showed no readily visible signs of damage. In (c), when high rate and sub-ambient conditions are present simultaneously, strain activated damage does feature. This is most clearly evidenced from the fact that the *post-mortem* analysis of these specimens showed significant damage.

6.2.1 Models considered

In order to capture the behaviours seen above, two modelling foundations have been selected, informed by research discussed in previous chapters.

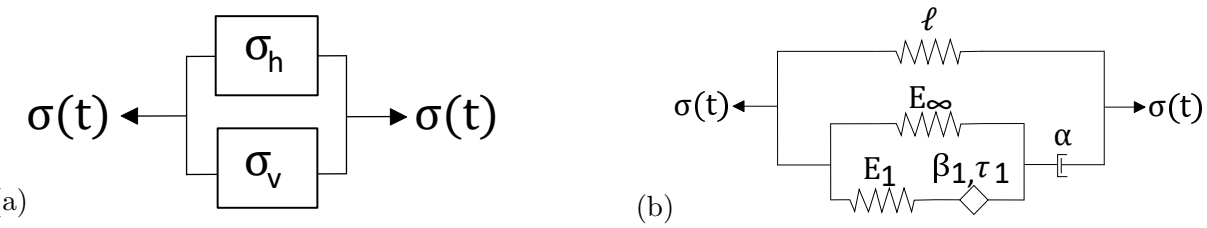

FIGURE 6.2: Diagrams of the (a) hyper-viscoelastic (HV) model and (b) modified Mulliken-Boyce (MB) model.

The models are depicted diagrammatically in Figure 6.2. In order to describe the response above T_g, a hyper-viscoelastic (HV) modelling basis as shown in Figure 6.2a is used. To describe the glassy behaviour below T_g, a Mulliken-Boyce (MB) [183, 185] inspired modelling basis is used. Both models are modified to take fillers into account to describe the composite behaviour. The following sections will describe features of these models and the modifications made in order to capture the dependence on particle filler volume fraction and size distribution.

6.2.2 Viscoelasticity

In order to characterise the linear viscoelasticity of the materials, DMA experiments were performed as described in the previous chapter. The data from these experiments were used to calibrate the viscoelastic definitions in each model.

6.2.2.1 Hyperviscoelastic (HV) model

To model the viscoelasticity in the HV model, a Prony series was used, as described in §4.6.2 with Equation 4.7 and shown diagrammatically in Figure 6.3a. This definition allowed the DMA master curve to be captured with high accuracy (Figure 6.3b) and an analytic solution to the relaxation modulus to be found. This solution was then easily integrated with the Boltzmann superposition principle to obtain the viscoelastic stress component (Equation 6.1).

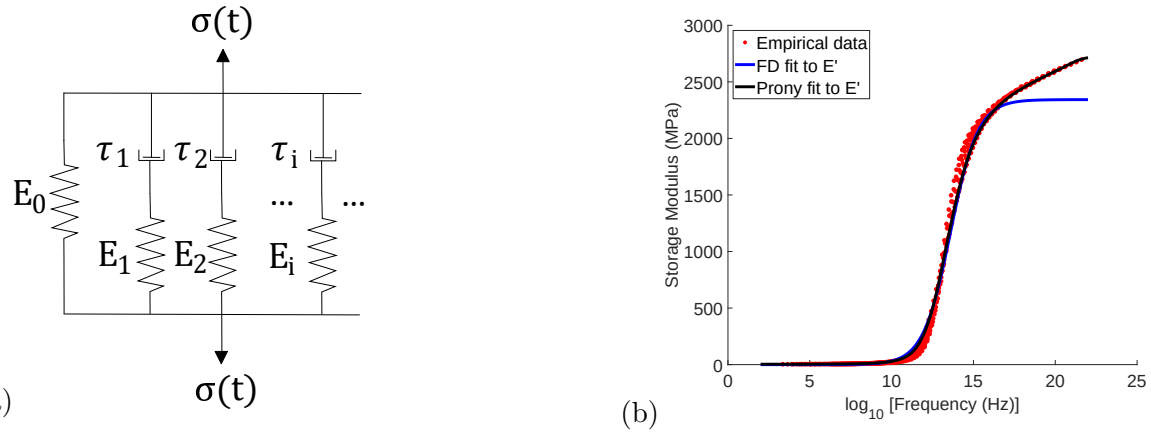

FIGURE 6.3: (a) Prony series representation of the viscoelasticity in the HV model and (b) using the Prony and Fractional Derivative (FD) models to fit the U-NR DMA data.

$$\sigma_v = \int_{-\infty}^{t} E(t-\xi)\dot{\varepsilon}(\xi)d\xi \tag{6.1}$$

In the Boltzmann superposition integral, although the integral is from $-\infty$, in practice the lower limit is zero as the samples are all strain rate and stress free at time $t = 0$. Also, since the true strain rate is constant, $\dot{\varepsilon}$ can be placed outside of the integral and $t = \varepsilon/\dot{\varepsilon}$. $E(t)$ is the analytic relaxation modulus as prescribed by the Prony series equation (Equation 4.7) with the parameters shown in Table 6.1.

6.2.2.2 Mulliken-Boyce (MB) model

To represent viscoelasticity in the MB model, the FD description was used instead of the Prony series. This is described in more detail in §4.6.2.1, with Equation 4.8. The reason for this was to retain the link by which each FD chain correlates directly to an MB chain, and maps onto a single transition. Additionally, this allows more direct comparisons between the modelling process used here for U/F-NRs and the (P)PVC in Chapter 4.

In Chapter 4, the MB model used had two chains representing the α (glass) transition and the β (secondary) transitions of the (P)PVC. Based on the DMA and DSC experiments on U-NR, only the α transition is present in this material over the temperatures and frequencies interrogated. This means that the FD model only had one chain, using the parameters in Table 6.1, to describe the master curve (Figure 6.3b).

At the highest frequencies, there is a mismatch between the FD and Prony series descriptions. However, these high frequency components will relax on a much smaller time-scale than those relevant to the experiments of interest. In this research, the highest strain rates investigated were of the order 10^3 s^{-1}. Using the Cox-Merz relation ($\dot{\varepsilon} \approx 2\pi f$), this represents frequencies of the order 10^2 to 10^3 Hz. Higher frequencies would be probed with sub-ambient, high rate experiments. At most, frequencies of c. 10^5 Hz would be expected in SHPB experiments, where relaxations on time-scales of 10^{-5} s would affect the data. However, these would still be well below the frequencies where there is this observed mismatch.

Table 6.1: Parameters used for the Prony and Fractional fits to the DMA data.

Prony series (MPa)	E_∞	E_1	E_2	E_3	E_4	E_5
	0.50	1.1	0.63	0.95	3.3	5.3
	E_6	E_7	E_8	E_9	E_{10}	E_{11}
	16	38	280	890	640	270
	E_{12}	E_{13}	E_{14}	E_{15}	E_{16}	E_{17}
	150	110	78	74	60	100

Fractional model	E_∞ (MPa)	E_1 (MPa)	β_1	t_1 (s)
	0.50	2300	0.52	2.7×10^{-14}

6.2.3 Hyperelasticity

To capture the large strain non-linear elastic behaviour of the response above T_g, hyperelasticity was incorporated using two different definitions.

6.2.3.1 Hyperviscoelastic (HV) model

In the HV model, the hyperelasticity was captured with the Ogden strain energy density function. This is described in more detail in §2.5.1 and §3.6. Equation 6.2 gives the hyperelastic contribution to the stress in the HV model depicted in Figure 6.2a.

$$\sigma_h = \frac{2\mu}{\alpha}\left(\mathrm{e}^{\alpha\varepsilon} - \mathrm{e}^{-\frac{1}{2}\alpha\varepsilon}\right) \tag{6.2}$$

In this research, the value of μ is fixed using $\mu = E_\infty/3$. Therefore, α is the only parameter to be calibrated from the lowest strain rate experimental data.

6.2.3.2 Mulliken-Boyce (MB) model

In the MB model, hyperelasticity is represented by a non-linear, non-Gaussian Langevin spring. This takes the entropic resistance to chain alignment into account in the fact that it requires extra stress to stretch by an incrementally larger amount. The MB model derives from the earlier Arruda-Boyce [143] model, where the Langevin hyperelasticity is represented by Equation 6.3. Further details can be found in §2.5.4.1.

$$\sigma_h = \frac{E_\infty}{3}\frac{\sqrt{N}}{\lambda_{chain}}\mathcal{L}^{-1}\left(\frac{\lambda_{chain}}{\sqrt{N}}\right)\left[(\exp\varepsilon)^2 - (\exp\varepsilon)^{-1}\right] \tag{6.3}$$

In the current research, the Langevin hyperelasticity parameter, N, is calibrated using the lowest strain rate experiment at ambient conditions.

6.2.4 Viscoplasticity

Viscoplasticity only features in the MB model, and details on how it is represented are given in §2.5.4.1. Whereas α and β chains required calibration in Chapter 4, only an α chain is required for U/F-NRs. This is as only the glass transition features. For strain compatibility, the strain in the Langevin spring is the same as that in the MB α chain. Therefore, the stress can be expressed as $\sigma_\alpha = E_\alpha(t)\varepsilon^e$, where ε^e $(= \varepsilon - \varepsilon^p)$ is the elastic strain. The plastic shear strain rate in the viscoplastic dashpots is given by:

$$\dot{\gamma}^p = \dot{\gamma}_0^p exp\left[- \frac{Q}{k\theta}\left(1 - \frac{\tau}{s + \alpha_p p}\right)\right] \tag{6.4}$$

This plastic shear strain rate can be used to infer the plastic normal strain rate with a factor of $\sqrt{3}$, which subsequently can be used to calculate the stress rate $\dot{\sigma}_\alpha = E_\alpha(t,T)(\dot{\varepsilon} - \dot{\varepsilon}^p)$. Integrating numerically with respect to time gives the stress in acting on the viscoplastic MB chain.

$$\sigma_\alpha = \int_0^t E_\alpha(t,T)\frac{(\dot{\gamma} - \dot{\gamma^p})}{\sqrt{3}}dt \tag{6.5}$$

The temporally and thermally relaxing modulus is obtained from the results of DMA experiments and understanding the effect of adiabatic self-heating on the thermal softening of the modulus. Details on how this is obtained are found in Chapter 4, §4.8.

6.2.5 Filler enhancement

The relaxation modulus for implementation in these modelling strategies has its foundation in the results of the DMA experiment for U-NR. However, in §5.3.6 of the previous chapter, theories concerning the enhancement of the modulus with fillers were presented. For implementation into the models, the modified Guth-Gold equation [231, 241] was used:

$$E_c = E_m[1 + 0.67f\phi_f + 1.62(f\phi_f)^2] \tag{6.6}$$

This representation allows the effect of the filler volume fraction to be taken into account. This is the primary driver for the enhancement in modulus due to the addition of fillers. Equation 6.6 also allows for aggregates, agglomerates and other shape effects to be taken into account by the use of a simple geometry factor, f. The intention of f in the Guth-Gold model was to modify the expression for non-spherical particles. In the first instance, these aggregates or agglomerates can be considered as larger non-spherical objects. Furthermore, this factor allows the mesophase region surrounding the particles to be taken into account. This mesophase region has been widely reported to change the mechanical behaviour of filled polymers [242–244], having a multiplier effect on the stiffness. Additionally, it has been suggested that this geometry factor can be used as a means to take into account the inverse dependence of the modulus on the particle radius [235]. Here, f is used as a fitting parameter when modelling particulate composites using the results of U-NR. Physically, it is hoped to take into account the stiff mesophase region, particle size effect, and the potential of localised strain induced crystallisation between particles. The particle size distribution, which mainly affects the debonding and damage sustained, is dealt with in the next section.

6.2.6 Strain activated damage

A strain activated continuum damage model was implemented for the F-NRs to describe the expected degradation in properties due to debonding and matrix rupture, which can be visibly observed. This model was chosen as it has been used successfully in previous research [2, 134, 221] to describe this type of damage in particulate composites.

6.2.6.1 Hyperviscoelastic (HV) model

In the HV model, the damage is represented by a degradation in modulus affecting the subsequent stress response. It is a function of the input mechanical energy and tracked

using an activation function:

$$E_d = (E_c - E_r)\Big[1 - \exp\Big(-\frac{w_0}{w}\Big)\Big] + E_r \tag{6.7}$$

where E_d is the damaged modulus, E_c is the relaxation modulus of the composite taking into account filler enhancement, E_r is the residual modulus of the damaged material, w_0 is the activation energy for damage and w is the input mechanical energy in the form of volumetric work done, which is simply the integral of the stress-strain curve. The moduli E_c and E_r can both be related back to the modulus of the unfilled rubber, E_m, and E_d may be re-written as:

$$E_d = E_m\left[(C - R)\Big[1 - \exp\Big(-\frac{w_0}{w}\Big)\Big] + R\right] \tag{6.8}$$

where C and R are constant parameters quantifying the filler enhancement and post-damage residual moduli respectively. Therefore, the two further unknowns requiring parameterisation to obtain E_d are R and w_0, since $C = 1 + 0.67f\phi_f + 1.62(f\phi_f)^2$ from Equation 6.6, where f is a fitting parameter.

In the undamaged HV model used for U-NR, the stress is given by:

$$\sigma = \sigma_v + \sigma_h = \dot{\varepsilon}\int_0^t E(t-\xi)d\xi + \frac{2\mu}{\alpha}\big(\mathrm{e}^{\alpha\varepsilon} - \mathrm{e}^{-\frac{1}{2}\alpha\varepsilon}\big) \tag{6.9}$$

The damaged stress expression is similar, and represents a continuum damage model, applying over both stress components. In this damage model, E is replaced by E_d for the damaged viscoelastic stress, σ_v^{dam}; and the damaged hyperelastic stress, σ_h^{dam}, takes the following form:

$$\sigma_h^{\mathrm{dam}} = \sigma_h\Big[C + (R - C)\exp\Big(-\frac{w_0}{w}\Big)\Big] \tag{6.10}$$

and is based on the same strain activated damage definition as in Equaton 6.8, where C, R and w_0 are as defined. Therefore, the total damaged stress may be written out as:

$$\begin{aligned}\sigma_d &= \sigma_v^{\text{dam}} + \sigma_h^{\text{dam}} \\ &= \dot{\varepsilon}\int_0^t E_d(t-\xi)d\xi + \sigma_h\Big[C + (R-C)\exp\Big(-\frac{w_0}{w}\Big)\Big] \\ &= \dot{\varepsilon}\int_0^t E_d(t-\xi)d\xi + \frac{2\mu}{\alpha}\big(\mathrm{e}^{\alpha\varepsilon} - \mathrm{e}^{-\frac{1}{2}\alpha\varepsilon}\big)\Big[C + (R-C)\exp\Big(-\frac{w_0}{w}\Big)\Big]\end{aligned} \tag{6.11}$$

6.2.6.2 Mulliken-Boyce (MB) model

In the MB model implementation, the stress rate is obtained prior to the stress using $\dot{\sigma_\alpha} = E_\alpha(\dot{\varepsilon} - \dot{\varepsilon}_\alpha^p)$ (see Chapter 2, §2.5.4.1 and also Equation 6.5). The activation based damage is incorporated by replacing E_α with E_d, where E_d is the damaged modulus. This is similar to Equation 6.8 in the previous section, and how damage was applied to the hyperelastic component.

$$E_d = E_\alpha\left[(C-R)\Big[1 - \exp\Big(-\frac{w_0}{w}\Big)\Big] + R\right] \tag{6.12}$$

where E_α is the modulus of the undamaged rubber in the MB model and the other terms are as previously described. Here, the two unknowns requiring parameterisation are C (or more specifically, f, the geometry factor in Equation 6.6), R and w_0.

6.3 Modelling results and analysis: Ambient, high rate

6.3.1 Unfilled natural rubber

In order to show that a HV model is appropriate for capturing the ambient, high rate response for U/F-NR, a simple Ogden and SLS model was fitted to the high rate data for U-NR simultaneously as a "proof-of-concept."

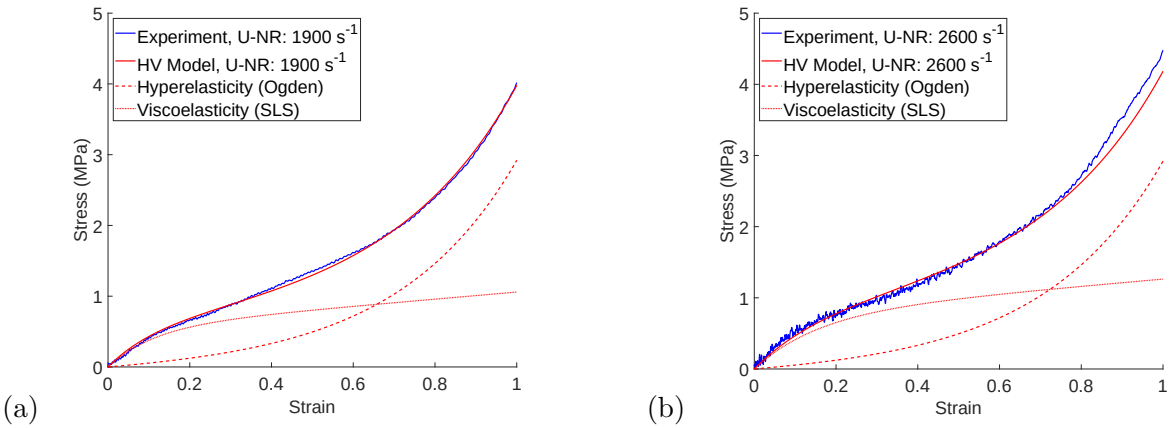

FIGURE 6.4: SLS + Ogden proof-of-concept for U-NR at (a) 1900 s^{-1} and (b) 2600 s^{-1}.

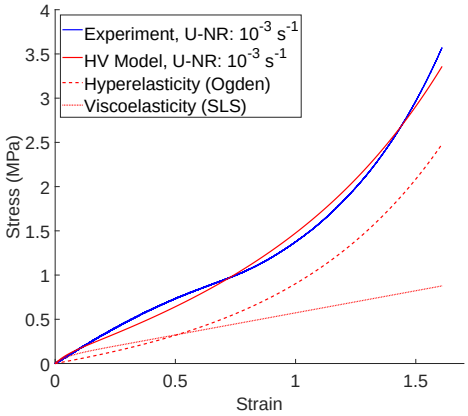

FIGURE 6.5: SLS + Ogden proof-of-concept for U-NR at the lowest strain rate: 10^{-3} s^{-1}.

Figure 6.4 shows that a simple HV model is able to capture the high rate response of U-NR to an excellent standard. For completeness, the fit to data at the lowest strain rate, 10^{-3} s^{-1}, is also shown in Figure 6.5. In these, the stress is given by:

$$\sigma = \sigma_v + \sigma_h = \varepsilon E_\infty + \varepsilon\tau E_1\left(1 - \mathrm{e}^{-\frac{\varepsilon}{\dot{\varepsilon}\tau}}\right) + \frac{2\mu}{\alpha}\left(\mathrm{e}^{\alpha\varepsilon} - \mathrm{e}^{-\frac{1}{2}\alpha\varepsilon}\right) \tag{6.13}$$

where E_∞, E_1 and τ are the SLS fitting parameters and μ and α are the Ogden fitting parameters. Two of these parameters were fixed based on information in the U-NR datasheet [218]: $E_\infty = 0.5$ MPa and therefore $\mu = 0.17$ MPa. The remaining three parameters were fitted, and found to be $E_1 = 4.9$ MPa, $\tau = 60$ µs and $\alpha = 3.4$. A summary of the parameters used for this proof-of-concept is shown in Table 6.2. Since the SLS model has a single relaxation time, it is not possible for one set of parameters to describe the stress-strain relationship across a very wide range of strain rates, and so the table shows two sets of parameters.

TABLE 6.2: Fitting parameters used in the SLS + Ogden HV model as a proof-of-concept.

$\dot{\varepsilon}$ (s^{-1})	$\mathbf{E_\infty}$ **(MPa)**	$\mathbf{E_1}$ **(MPa)**	τ	μ **(MPa)**	α
c.10^3	0.5	4.9	60 μs	0.17	3.4
10^{-3}	0.5	1.6	45 s	0.17	1.5

6.3.1.1 Quasi-static calibration: U-NR

Having shown that this type of model is able to capture the ambient, high rate behaviour of U-NR, its predictive capability was enhanced by using the DMA experimental results to calibrate the viscoelastic parameters. Furthermore, the hyperelastic convexity was calibrated to data at −50 °C and 10^{-2} s^{-1} (Figure 6.6). Data at −50 °C was selected for this calibration as it is just above T_g and so the effect of plasticity could be ignored, making calibration easier. Yet, it is not so far above T_g, where the hyperelastic convexity is suppressed leading to miscalibration of the parameter.

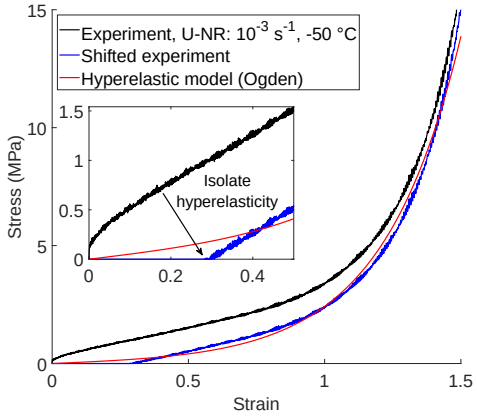

FIGURE 6.6: Calibrating the hyperelastic convexity, α using data at -50 °C and 10^{-2} s^{-1}.

In order to isolate the large strain hyperelasticity and obtain a more accurate value for α, the low strain response was discarded. This was done by shifting the stress-strain curve downwards on a trial-and-error basis such that a smooth hyperelastic response is obtained, removing the effect of low strain viscoelasticity at that strain rate. Based on this fitting, $\alpha = 4.4$.

6.3.1.2 Predictions of high rate response: U-NR

As the calibration of parameters was performed using the results of DMA experiments and the compression result of a low strain rate, low temperature experiment, no further fitting parameters are required to predict the high rate response for U-NR. These results are shown in Figure 6.7. The stress is given by Equation 6.9.

The modelled results are not as good as the complete fits described with the SLS based HV model in Figure 6.4, however, these are *predicted* responses based on model parameters solely calibrated using quasi-static data.

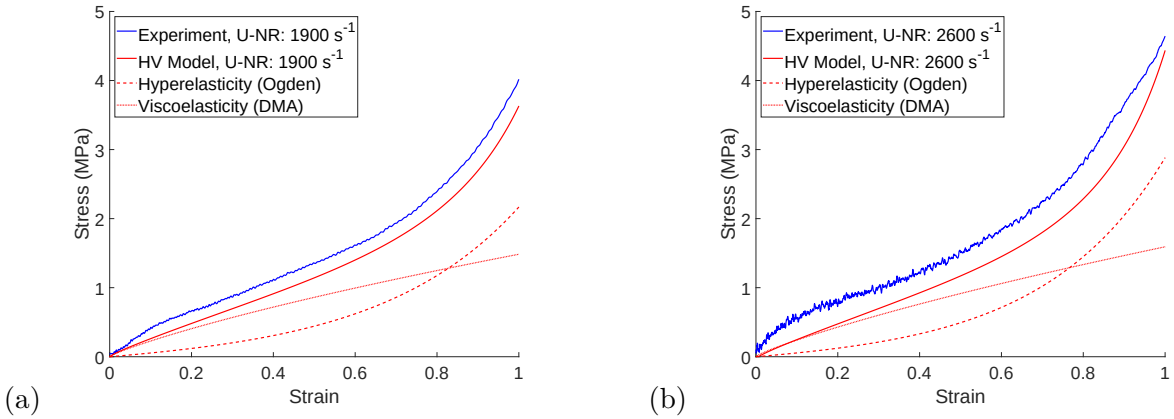

FIGURE 6.7: High rate HV model results for U-NR at (a) 1900 s^{-1} and (b) 2600 s^{-1}.

6.3.2 Filled natural rubber

The modified HV model presented in §6.2 was used to capture the ambient, high rate response of the particulate composites. In this case, there are four fitting parameters: the geometry factor, f; the strain hardening exponent, α, the residual modulus multiplier, R and the damage activation energy, w_0. The parameters used in the model are shown in Table 6.3.

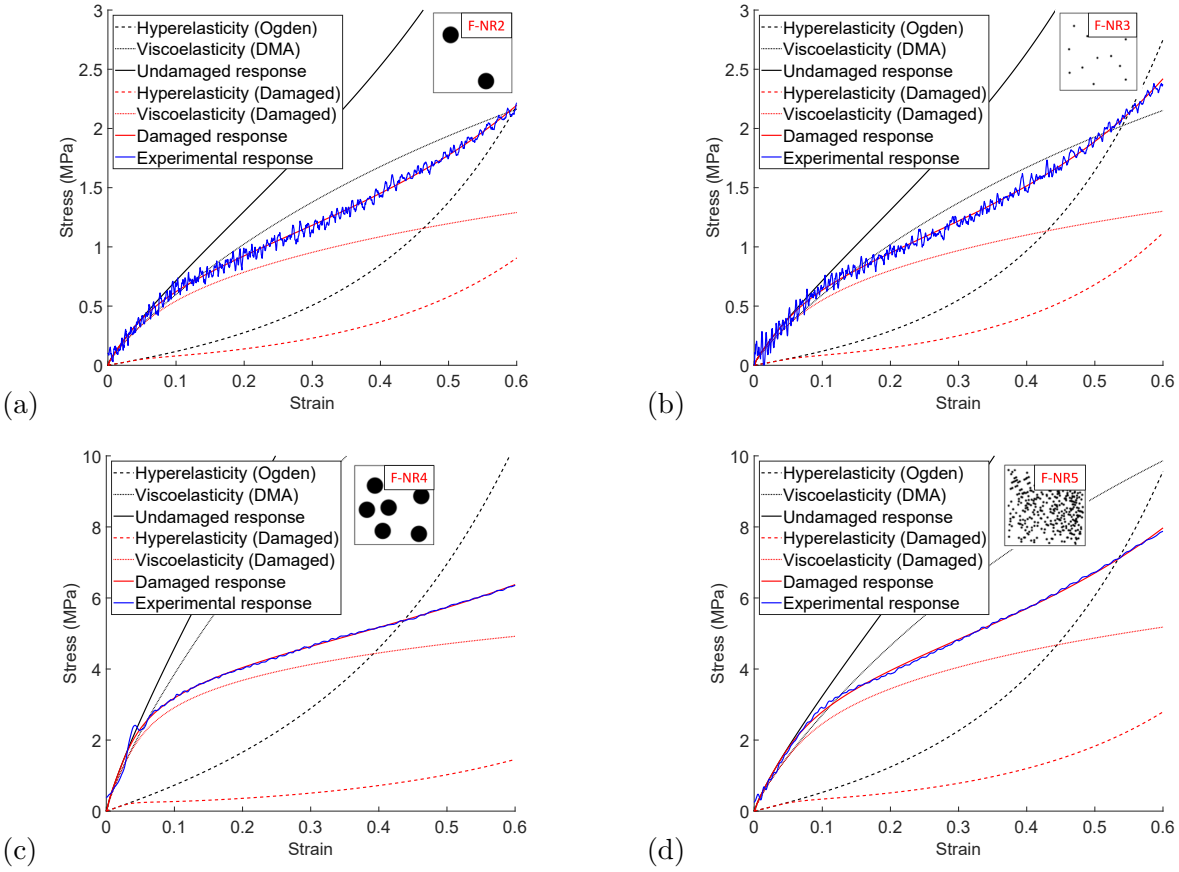

FIGURE 6.8: HV model results for (a) F-NR2 at 2500 s^{-1} and (b) F-NR3 at 2400 s^{-1}, (c) F-NR4 at 2700 s^{-1}, and (d) F-NR5 at 2600 s^{-1}.

From Figure 6.8, it is clear that the addition of a damage definition was essential in order to capture the high rate response of the F-NRs. In future iterations, the model could be decomposed into three constituents to also take into account the mesophase region between the fillers and matrix. However, the goal should still be to calibrate most, if not all, modelling parameters with the results of simple, low rate experiments.

TABLE 6.3: Fitting parameters used in the HV model for the particulate composites.

Particulate composite	**Strain rate,** $\dot{\varepsilon}$ (s^{-1})	**Geometry factor, f**	α	**Residual modulus multiplier, R**	**Damage activation energy,** $\mathbf{w_0}$ ($mJ\,mm^{-3}$)
F-NR2	2500	13	4.5	0.82	13
F-NR3	2400	13	5.0	0.81	16
F-NR4	2700	5.1	3.6	1.7	39
F-NR5	2600	4.1	4.4	2.54	67

6.3.3 Quasi-static calibration of model

In order to explore the predictive capability of the model, results from quasi-static experiments at ambient and low temperatures were used to calibrate the HV model. Ultimately, f and w_0 were calibrated using the results of quasi-static, ambient experiments, and R and α using quasi-static, sub-ambient experiments. The discussion below shows why this was the case.

6.3.3.1 Quasi-static, ambient calibration

Initially, all four of the model parameters were calibrated with the results of quasi-static, ambient experiments for the F-NRs conducted at 10^{-1} s^{-1} and 25 °C. The fastest quasi-static experiment ensured that the model parameters were sensitive to the observed leathery response of the material. The results of these calibration experiments are shown in Figure 6.9, and the resulting model parameters in Table 6.4.

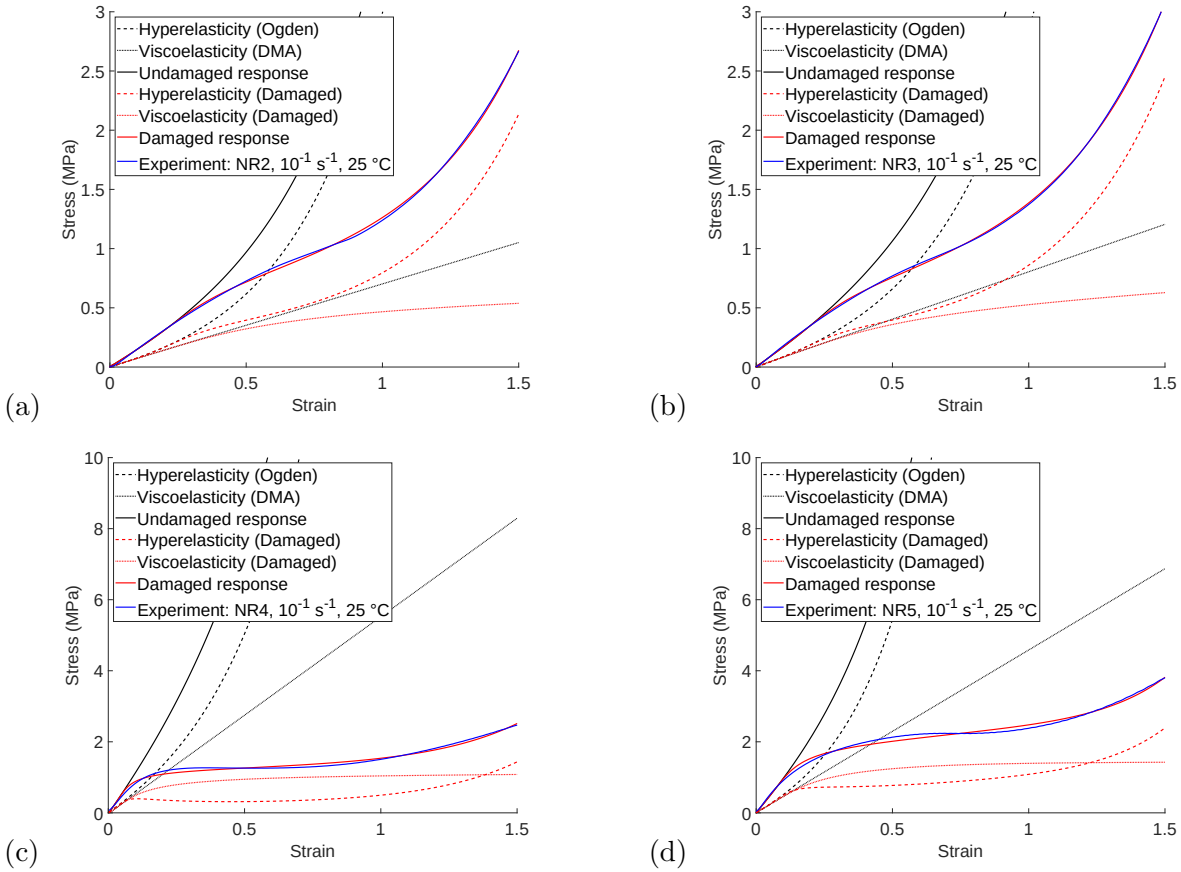

FIGURE 6.9: Results from the quasi-static (10^{-1} s^{-1}), ambient (25 °C) calibration of the model parameters for (a) F-NR2, (b) F-NR3, (c) F-NR4, and (d) F-NR5.

TABLE 6.4: Fitting parameters used in the quasi-static (10^{-1} s^{-1}), ambient (25 °C) calibration of the HV model for the particulate composites.

Particulate composite	**Geometry factor, f**	α	**Residual modulus multiplier, R**	**Damage activation energy, w_0** ($mJ\,mm^{-3}$)
F-NR2	6.7	2.9	0.17	140
F-NR3	8.8	2.7	0.30	120
F-NR4	4.6	3.1	0.11	42
F-NR5	4.1	4.0	0.040	130

The geometry factor shows a difference between the 5% and 50% F-NRs, indicating that the proposed structures may have varying shapes at the different fill fractions. This can be validated in the future with X-ray techniques. There appears to be an anomalous w_0 value for F-NR4, which will be discussed later.

These parameters were subsequently used to *predict* the high rate response of the F-NRs at the same strain rates as those in Figure 6.8 in the previous section. The results of these predictions are shown in Figure 6.10.

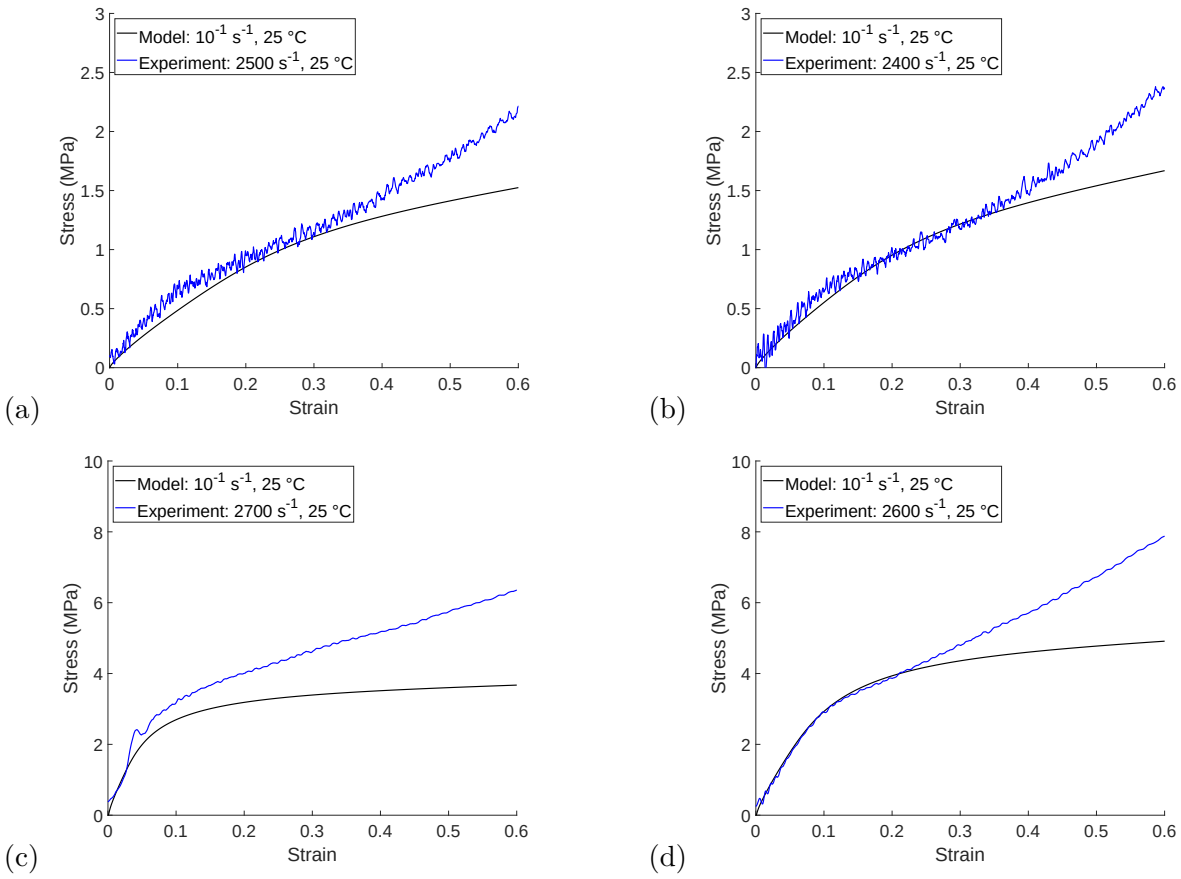

FIGURE 6.10: Predictions of the high rate response for (a) F-NR2, (b) F-NR3, (c) F-NR4, and (d) F-NR5 using the parameters calibrated under quasi-static, ambient conditions.

From the modelling results in Figure 6.10, it is clear that the the quasi-static, ambient experiments can be used to calibrate part of the model. The initial viscoelasticity and onset of damage is well predicted, as indicated by the close fit at low strains. However, the extent of damage and the large strain hyperelastic convexity is not. This leads to the conclusion that the ambient experiments can be used to calibrate f and w_0, but R and α must be calibrated differently. Therefore, only the f and w_0 values from this section are used in the final predictive HV model.

6.3.3.2 Quasi-static, low temperature calibration

It was shown in the previous chapter (§5.3.3), that the response at sub-ambient temperatures and quasi-static strain rates was qualitatively similar to the response at an ambient temperature and high strain rates. It is also known that at the highest strains, a decreased temperature leads to a greater strain hardening behaviour due to a decrease in the polymer chain mobility [245]. For this reason, the model was re-calibrated with the results of quasi-static, low temperature experiments for the F-NRs conducted at 10^{-2} s^{-1} and between -40 and -45 °C. The objective is to use these data to calibrate the R and α parameters. The results of these calibration experiments are shown in Figure 6.11, and the resulting model parameters in Table 6.5.

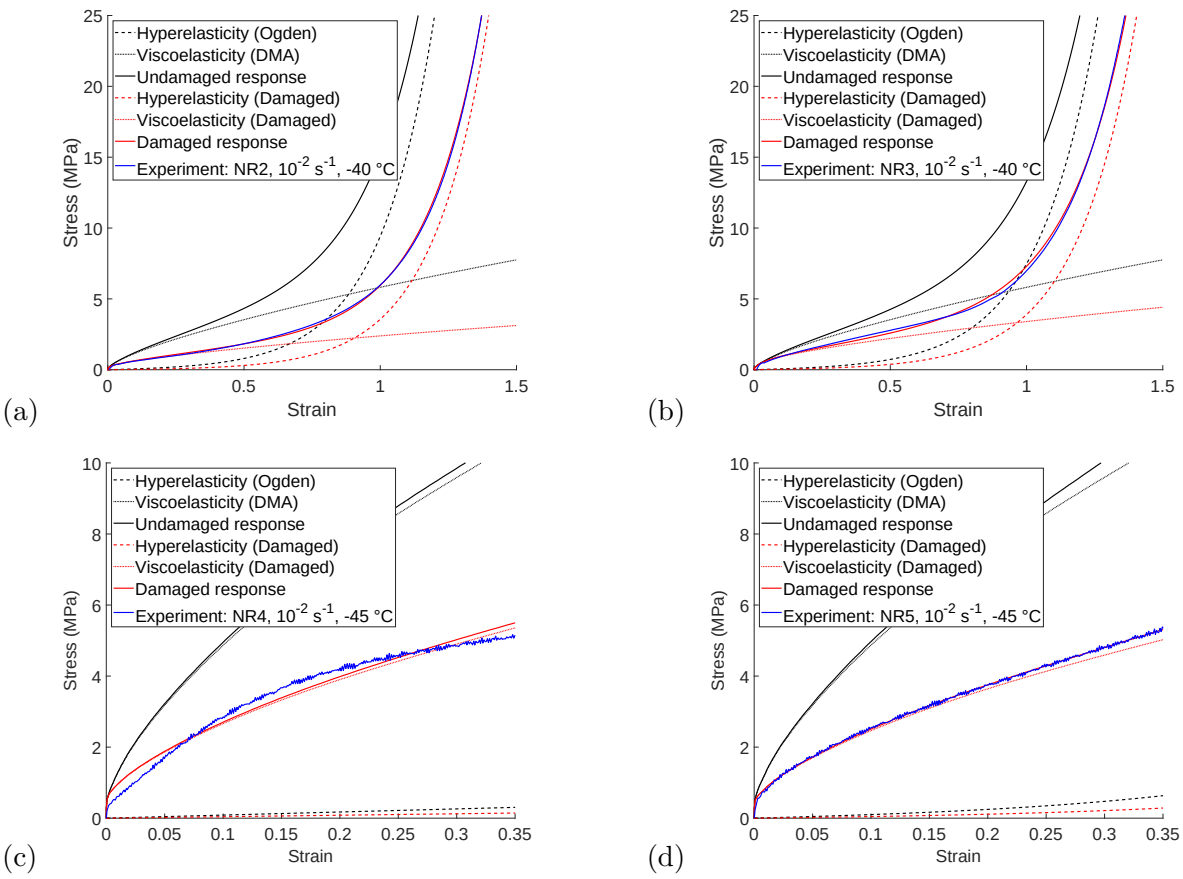

FIGURE 6.11: Results from the quasi-static (10^{-2} s^{-1}) calibration of the model parameters: (a) F-NR2 and (b) F-NR3 at -40 °C; (c) F-NR4 and (d) F-NR5 at -45 °C.

TABLE 6.5: Fitting parameters used in the quasi-static (10^{-2} s^{-1}), low temperature (-40 and -45 °C) calibration of the HV model for the particulate composites.

Particulate composite	**Geometry factor, f**	α	**Residual modulus multiplier, R**	**Damage activation energy, w_0** ($mJ\,mm^{-3}$)
F-NR2	1	4.9	0.39	0.38
F-NR3	1	4.6	0.54	4.9
F-NR4	1	0*	0.82	0.038
F-NR5	1	5.1	0.78	0.0049

From Table 6.5, it is clear that the geometry factor is not sensitive to the results of quasi-static, low temperature experiments despite being allowed to vary. The damage activation energy terms also appear to be related. As these parameters have already been calibrated with the results of quasi-static, ambient experiments, this is not a concern. However, there was an anomalous $\alpha = 0$ parameter obtained for F-NR4. For this reason, the value of $\alpha = 3.1$ from the ambient calibrations presented earlier was used. As α relates to the hyperelastic convexity, selecting this value will not significantly effect the stress-strain response for NR-4 up to $\varepsilon = 0.35$. This anomaly could be due to experimental variation or lack of sensitivity in the response to variations in α. In future, the calibration experiments at low temperature for F-NR4 and 5 should also be performed to large strains to ensure sensitivity to α.

For completeness, the predictions resulting from using the parameters in Table 6.5 for the high rate response of the F-NRs are shown in Figure 6.12. Although the predicted responses do not match the experimental results, the large strain response, including hyperelastic convexity, appears to be well captured as the slopes of the experimental and modelled curves are similar, thereby giving confidence in the values of R and α obtained. The slope is calculated using numerical differentiation, and has been smoothed using a Savitzky-Golay filter of order 3 and frame length of 201. There is a greater discrepancy for the 50% F-NRs, and contributes to the slightly poorer predictions seen later in Figure 6.13.

Overall, this calibration process shows that the large strain response, including hyperelastic convexity, is well captured. Therefore, the values of R and α from the calibration presented in this section are used in the final predictive HV model.

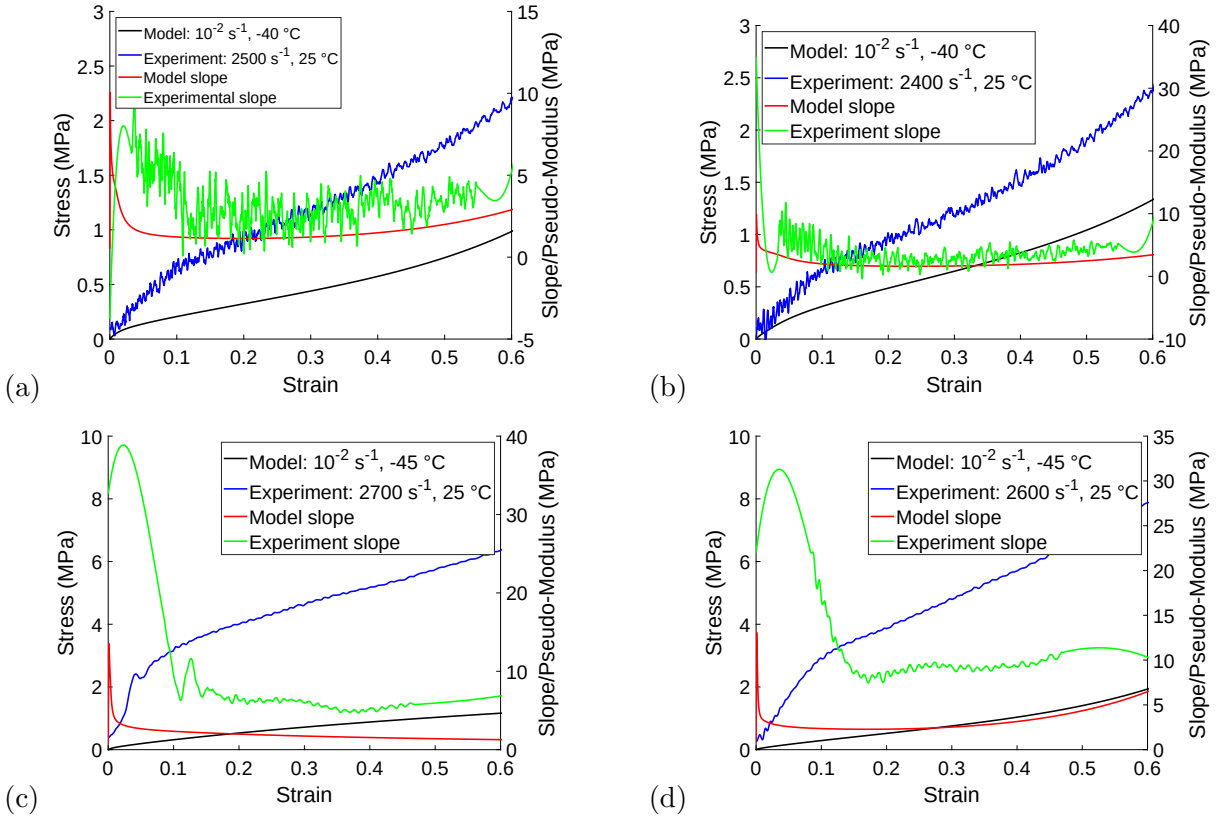

FIGURE 6.12: Predictions of the high rate response for (a) F-NR2, (b) F-NR3, (c) F-NR4, and (d) F-NR5 using the parameters calibrated under quasi-static, low temperature conditions.

6.3.4 Predictions of high rate response

The insights from the calibration conducted under ambient and low temperature conditions were applied to obtain the *predicted* high rate responses for the F-NRs. The f and w_0 parameters were calibrated under quasi-static, ambient conditions, whereas α and R were calibrated under quasi-static, low temperature conditions. The model parameters used in the combined, predictive HV model are shown in Table 6.6.

TABLE 6.6: Combined HV model parameters used in the predictive modelling of the high rate response for the particulate composites.

Particulate composite	**Geometry factor, f**	α	**Residual modulus multiplier, R**	**Damage activation energy, $\mathbf{w_0}$** ($\mathrm{mJ\,mm^{-3}}$)
F-NR2	6.7	4.9	0.39	140
F-NR3	8.8	4.6	0.54	120
F-NR4	4.6	3.1*	0.82	42
F-NR5	4.1	5.1	0.78	130

The results of the modelling using the parameters from quasi-static calibration are shown in Figure 6.13.

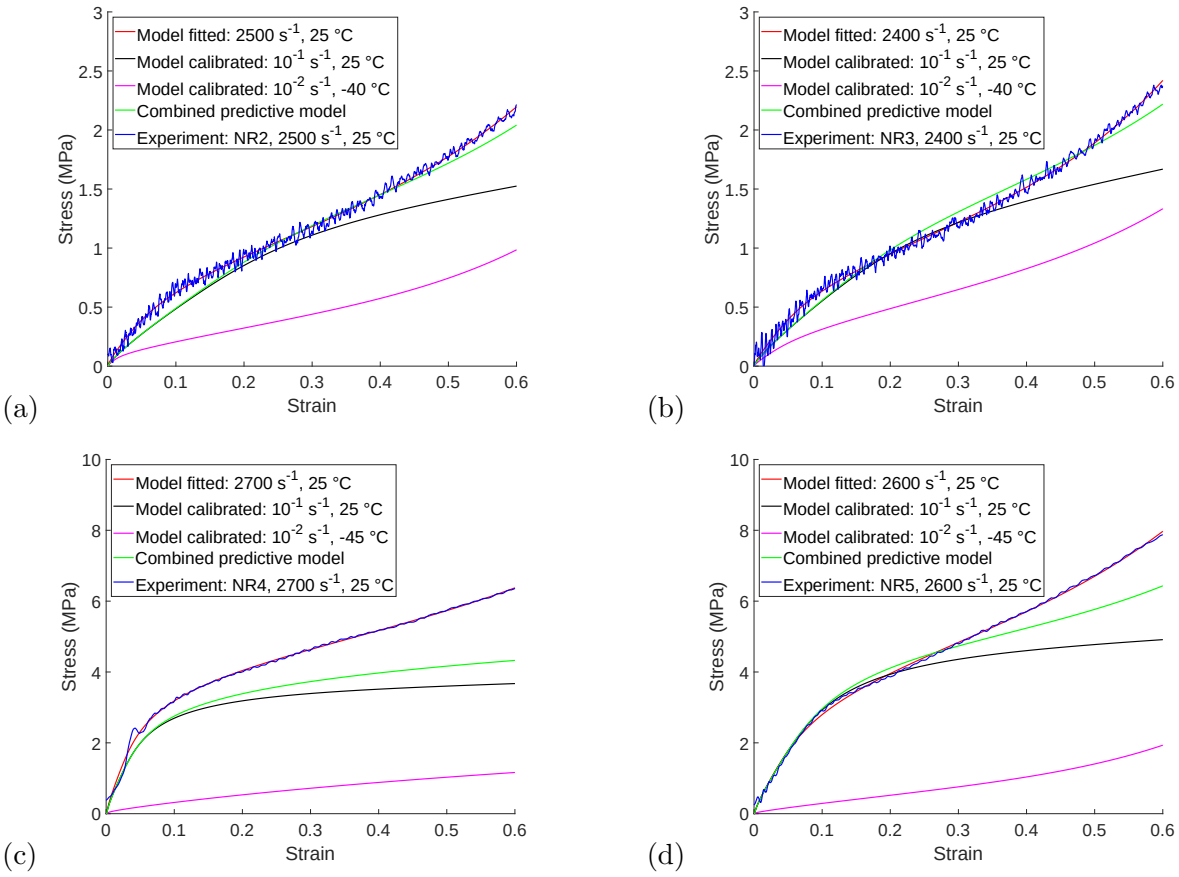

FIGURE 6.13: Predictions of the high rate response for (a) F-NR2, (b) F-NR3, (c) F-NR4, and (d) F-NR5: f and w_0 calibrated under quasi-static, ambient conditions; α and R calibrated under quasi-static, low temperature conditions.

The combined predictive HV model does an excellent job at predicting the high rate response for the 5% filled composites, almost as well as the model fitted directly to the high rate data. The combined model shows an improvement in predicted response for the 50% filled composites compared to calibrating against either ambient or low temperature experiments. The prediction for F-NR5 is very good, but that for F-NR4 is not as good at higher strains. This is most likely due to the fitting anomaly, leading to a suboptimal value for α being used. Furthermore, the damage activation energy for F-NR4 was significantly lower compared to the other composites. Although it is expected that the composite with the larger particles will show greater damage, this low value overestimates the damage.

It is worth noting that these predictions are based on the viscoelasticity obtained from DMA experiments on U-NR. In future iterations of the model, the DMA results

of the F-NRs would directly give the viscoelasticity of the composite, with no need to model the filler enhancement.

To improve calibration of the model, multiple quasi-static experiments at various temperatures can be performed. This would provide a better insight into the parameters and their sensitivity to rate and temperature. Furthermore, the model itself may help understand these sensitivities. In future, the residual strength of samples from interrupted compression experiments at high rates and those from low temperature, low rates can be compared to evaluate the extent to which the damage is the same. Further experiments using x-ray Computerised Tomography could also be used to validate the extent and similarity of the damage in samples from each case.

6.4 Modelling results and analysis: Sub-ambient, high rate

6.4.1 Unfilled natural rubber

In order to model the high rate response of the U/F-NRs under sub-ambient conditions, the MB model was used to allow the viscoplasticity and strain softening to be captured.

The one chain (α) MB model has five parameters: the pressure coefficient, α_p; the pre-exponential factor, $\dot{\gamma}_0^p$; the softening slope, h; the activation energy, Q; and the steady state athermal shear strength, S_{ss}. Two of these parameters can be fixed before the calibration process.

Based on previous investigations into the variation of tensile and compressive strengths for various polymers [76], and the analysis described in [120], the pressure coefficient for PVC, polycarbonate, polystyrene and poly(methyl methacrylate) was found to be 0.23 on average. Hence, $\alpha_p = 0.23$ is used. Tensile experiments were not performed in this study, but in future, by comparing the variation in tensile and compressive strengths for U-NR under the same temperature and loading rate conditions, a more accurate value for α_p can be found for this particular material. Equation 6.14 using [120] gives:

$$\alpha_p = 3\frac{\sigma_y^c - \sigma_y^t}{\sigma_y^c + \sigma_y^t} \tag{6.14}$$

The activation energy can also be fixed based on the analysis of the DMA results for U-NR. In Chapter 5 §5.4.4, Figure 5.49 plots the logarithm of the experimental frequency against the reciprocal of the absolute temperature for the peak of each loss tangent curve. The temperature dependence of the frequency based on the Arrhenius law is given by:

$$f = A\mathrm{e}^{-\frac{Q}{RT}} \tag{6.15}$$

where $-Q/R$ corresponds to the gradient in Figure 5.49. Hence, $Q = 3.45 \times 10^{-19}$ J.

6.4.1.1 Mulliken-Boyce (MB) model calibration

Before the other parameters for the α component to the model can be calibrated, the Langevin hyperelasticity parameters are calibrated. The hyperelastic stress is given by the expression in Equation 6.3, and since E_∞ is known, only the limiting chain extensibility, N, needs to be calibrated. This is found using the results of the lowest strain rate, ambient experiment on U-NR. This experiment was selected to calibrate N as the response is dominated by the large strain hyperelasticity. The result of this calibration is shown in Figure 6.14, where $N = 8.7$.

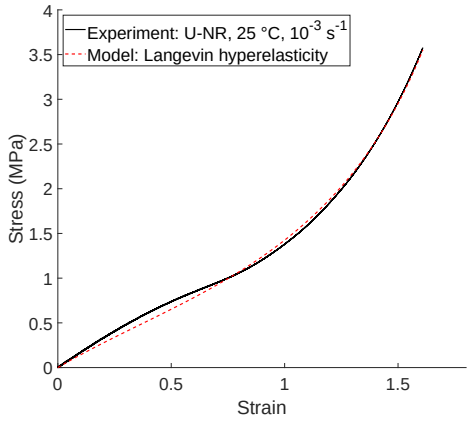

FIGURE 6.14: Calibration of the limiting chain extensibility, N, for U-NR with an experiment conducted at 25 °C and 10^{-3} s^{-1}.

The other model parameters were calibrated using the low temperature, low rate (10^{-2} s^{-1}) experimental results for U-NR (Figure 6.15a).

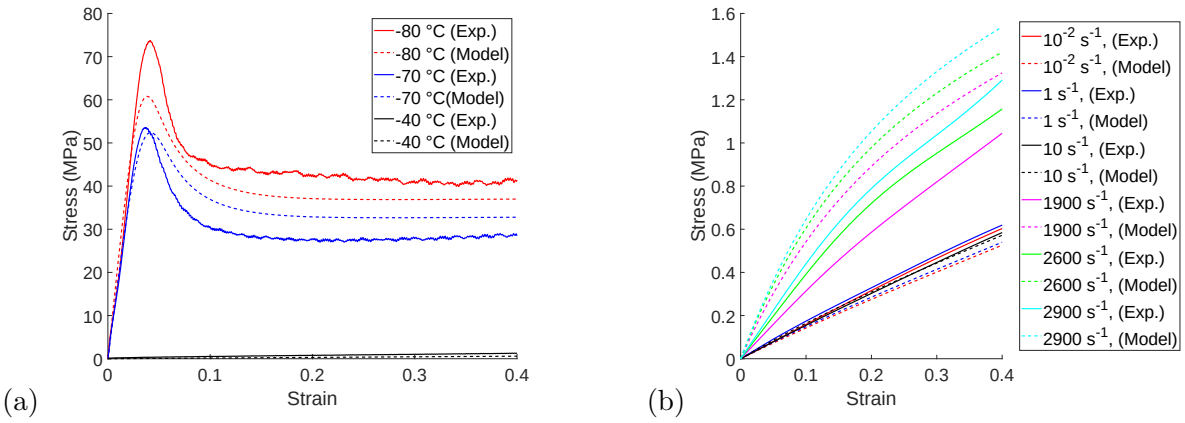

FIGURE 6.15: (a) Calibration of MB parameters for U-NR with sub-ambient experiments and (b) using the MB model to predict the ambient varying rate response for U-NR.

One of the challenges of calibrating the parameters accurately using the low temperature quasi-static data is that small changes in temperature significantly affect the response. This is more clearly observed in the perturbation analysis presented later in Figure 6.16. The parameters obtained for the MB model are shown in Table 6.7. The modelled results under ambient conditions using the MB model shown in Figure 6.15 are provided for completeness, as the HV model described previously was preferred for the modelling of experiments under ambient conditions. Since there was no observed viscoplasticity, it did not warrant the use of this more complex modelling strategy.

TABLE 6.7: Fitting parameters used in the MB model for U-NR.

Parameter	**N**	$\dot{\gamma}_0^p$ (s^{-1})	**h (kPa)**	S_{ss} **(kPa)**
Value	8.7	130	840	64

6.4.1.2 Results: U-NR

Once the MB model has been calibrated using the low temperature quasi-static data, it can be used to predict the response at high strain rates under sub-ambient conditions. The initial results of these predictions are shown in Figure 6.16. Using only four parameters calibrated under quasi-static conditions, alonside the DMA based viscoelasticity information, it is possible to get a relatively good agreement with the experimental results.

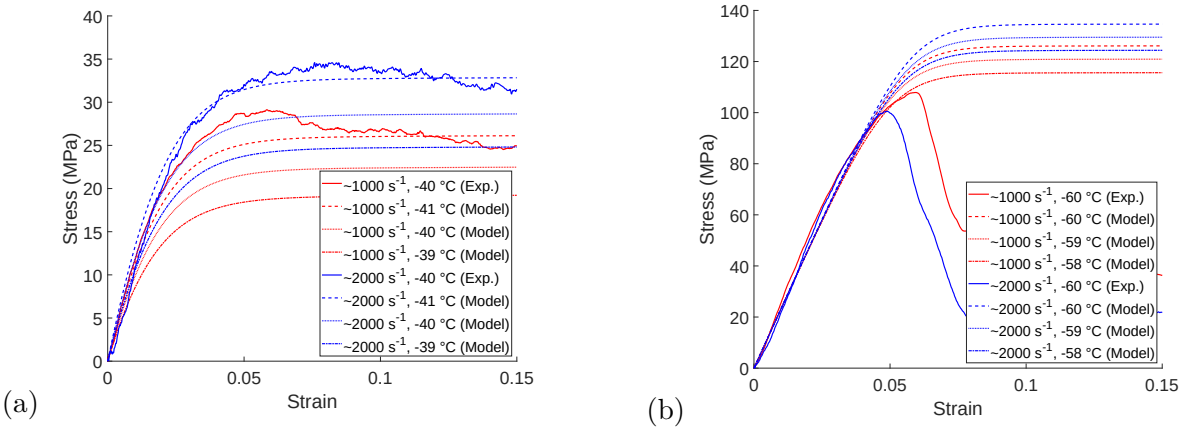

FIGURE 6.16: Using the MB model to predict the sub-ambient high rate response for U-NR and highlighting its temperature sensitivity at (a) −40 °C and (b) −60 °C.

From Figure 6.16a, it can be observed that the MB model fares quite well in predicting the high rate responses of U-NR at −40 °C. However, the model is highly sensitive to temperature change. The best modelling results were obtained using −41 °C, which may mean that the actual temperature of the experiment was also −41 °C, well within the precision of the temperature measurement in the experiment. However, due to the presence of both model sensitivity and experimental variation, it is difficult to be certain.

The results for U-NR at −60 °C in Figure 6.16b show that there is still a sensitivity to temperature; however, it is weaker and a small perturbation in the temperature represents a less significant relative change in the response. The one chain MB model by itself is not able to capture the full mechanical response for U-NR as it does not include a brittle damage or cavitation definition. Above strains of 0.05 and 0.06 for experiments at c.2000 s^{-1} and c.1000 s^{-1} respectively, the U-NR undergoes significant damage. This was observed and discussed in the previous chapter (Figure 5.23). The model therefore needs further refinement. Although the model captures the elastic loading well, a damage definition is added:

$$\sigma_d = \sigma_\alpha + (\sigma_r - \sigma_\alpha) \exp\Big(- \frac{w_0}{w} \Big), \ \varepsilon > \varepsilon_d \tag{6.16}$$

where ε_d is the damage onset strain, above which, there is damage for the U-NR. The

value is chosen to match the strain at which the stress significantly drops as can be seen for the −60 °C curves in Figure 6.17. This onset strain has been added as a modification to the strain activated damage models previously presented in [2, 134, 221]. Although this type of equation was used to describe the damage to an F-NR composite, a functional form of the definition can be used to describe the damage in a U-NR provided the filler enhancement effect is removed and σ_α is set as the stress in the undamaged U-NR, as opposed to the undamaged F-NR. Since damage is only visibly observed at −60 °C, the MB model with damage was only implemented in that case.

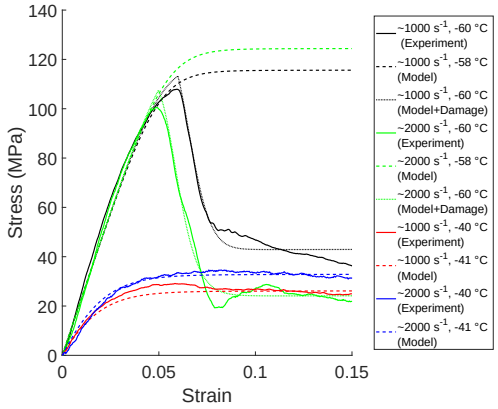

FIGURE 6.17: Using the MB model with an incorporated damage definition to capture the sub-ambient high rate response for U-NR.

From Figure 6.17, it is evident that this damage modification is essential for allowing the full mechanical response at these low temperatures to be captured and does so very well, although it should be noted that this is not predictive. The use of Equation 6.16 in representing the damage of U-NR, despite it being originally formulated for F-NRs, is justified by its observed effectiveness. Three additional fitting parameters are required to capture this response: the damage onset strain, ε_d; the damage activation energy, w_0; and the residual stress, σ_r. The parameters fitted are shown in Table 6.8. Though the residual stress term has no particular significance other than the final stress shown during the experiment, the damage activation energy appears to be linked to the onset strain. This is evident from the fact that the larger damage activation energy correlates with the sample that fails at a higher strain. In future, an alternative approach would

be required to enable the prediction of brittle failure in the high rate response of U-NR at the lowest temperatures. It may also be possible to link the value of w_0 to ε_d.

TABLE 6.8: Fitting parameters for the damage implementation in the MB model for U-NR.

$\dot{\varepsilon}$ (s^{-1})	$\varepsilon_{\mathbf{d}}$	$\mathbf{w_0}$ ($J\,mm^{-3}$)	$\sigma_{\mathbf{r}}$ **(MPa)**
1000	0.06	18	43
2000	0.05	12	24

6.4.2 Filled natural rubber

The modelling of the F-NRs under sub-ambient, high rate conditions requires an additional consideration and fitting parameter. Since the modelling results are based on the U-NR viscoelasticity with a modification allowing for the filler enhancement to the modulus, the geometry factor, f, as used in Equation 6.6 is required. With f, the filler enhanced modulus can be captured for the four F-NRs.

$$\begin{aligned} E_c &= E_\alpha[1 + 0.67f\phi_f + 1.62(f\phi_f)^2] \\ &= E_\alpha C \end{aligned} \tag{6.17}$$

In order to reflect the damage that afflicts the composite, the following damaging modulus definition is used:

$$E_d = E_\alpha \left[(C - R)\left[1 - \exp\left(- \frac{w_0}{w} \right)\right] + R \right] \tag{6.18}$$

which is subsequently used in the MB model stress rate definition to obtain the damaging stress rate: $\dot{\sigma_d} = E_d(\dot{\varepsilon} - \dot{\varepsilon}^p_\alpha)$. Integrating through each time increment gives the stress.

6.4.2.1 Results: F-NR, −40 °C

There are three parameters that are required to model the high rate response at −40 °C for each F-NR: the geometry factor, f; the residual modulus multiplier, R; and the damage activation energy, w_0. The modelling results for the F-NRs at −40 °C are shown in Figure 6.18, and the parameters in Table 6.9.

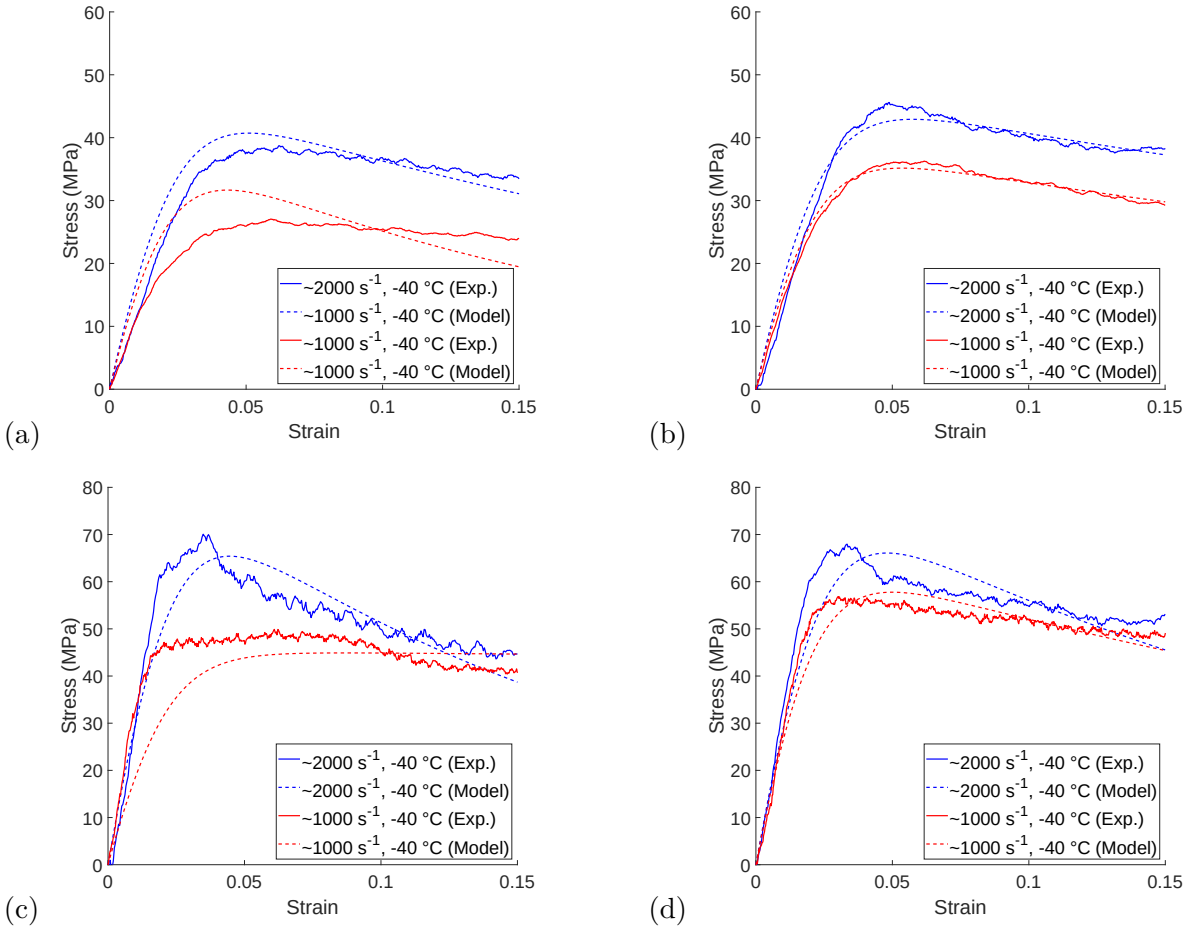

FIGURE 6.18: Using the MB model with an incorporated damage definition to capture the high rate response at −40 °C for (a) F-NR2, (b) F-NR3, (c) F-NR4 and (d) F-NR5.

In general, there is good agreement between the modelled results and the sub-ambient compression experiments conducted at high rates. The best results are for F-NR3, where the modelled modulus is within 9% of the experimental apparent modulus and the yield stress is within 4%. The worst results are for F-NR2 and 4 at c. 1000 s^{-1}. For F-NR2, the modelled modulus is 40% higher and the yield stress is 15% higher. For F-NR4, the modulus is 50% lower and the yield stress is 10% lower. The responses that were not satisfactorily captured tended to be those that were flatter post yield. It should be noted that these results are not predictive as they make use of a fitting parameter: f. The predictive capability of this model can be improved by using results from the DMA experiments on the specific composites[1], and by calibrating the MB model to the low temperature, quasi-static data separately for each composite.

[1]This was not possible to complete due to the Covid-19 lockdown.

TABLE 6.9: Fitting parameters for the damage implementation in the MB model for F-NRs at −40 °C.

Composite	$\dot{\varepsilon}$ (s^{-1})	**f**	**R**	$\mathbf{w_0}$ ($\mu J\,mm^{-3}$)
F-NR2	1000	0.50*	1.0	3.1×10^{-8}
F-NR2	2000	0.50*	1.0	2.4×10^{-8}
F-NR3	1000	0.50*	1.0	4.4×10^{-7}
F-NR3	2000	0.50*	1.0	3.3×10^{-6}
F-NR4	1000	3.9	1.0	7.7
F-NR4	2000	10	1.0	34
F-NR5	1000	9.8	1.0	17
F-NR5	2000	9.6	1.0	25

By considering the values of the parameters used in the modelling of the high rate response for the F-NRs at −40 °C, greater insights into the models limitations can be gleaned.

The geometry factor, f, locked at 0.5 for the 5% filled composites and the residual modulus locked at 1.0 for all F-NRs from the fitting. Despite capturing the mechanical response well, this seems to suggest that the model may not be using accurately calibrated parameters. In future iterations of this model, DMA results from the F-NRs will be used such that the filler enhancement will not need to be modelled. This would also remove any adverse interaction that this parameter is having on the others.

The geometry factor, f, is primarily dependent on the volume fraction of the composite. It seem that a multiplier of around 10 is suitable for modelling the 50% F-NRs. This is why the simulation at 1000 s^{-1} for F-NR4, where $f = 3.9$ fared particularly poorly in modelling the experiment.

The damage activation energies for the 50% filled composites shows a similar dependency as observed with the ambient, high rate results. There appears to be a rate dependence to the energy value for these composites too, where at a higher strain

rate, they have a higher damage activation energy. To understand this in more detail, microstructural analysis of the damage process would be necessary.

6.4.2.2 Results: F-NR, −60 °C

In Chapter 5 §5.3.5, it was discussed that during the high rate experiments on F-NRs at −60 °C, fracture was observed. For this reason, Equation 6.18 by itself was not used to represent the damage, but the definition described earlier for the U-NR in Equation 6.16 was used instead. This definition assumes there is no damage until a critical strain, ε_d. Deforming the material further results in a damage evolution governed by the input mechanical energy, and drops the stress down to a residual value, σ_r, which is actually just the value of stress at the end of the experiment. The results of this modelling are shown in Figure 6.19. It should be noted that these modelling results are not predictive, and the results present a simplified approach to model the stress-strain response based on existing modelling strategies. In future, due to the presence of brittle fracture, a more suitable definition should be included into the modelling strategy. This could be one where brittle failure is defined to occur when the formation of crazes reaches a critical size [246], or one using a diffuse phase-field crack definition [247]. The use of a better damage definition would help to enhance the predictive capability of the model.

From the results in Figure 6.19, it can be observed that the filler modified damaging MB model does an adequate job at capturing the sub-ambient, high rate response of F-NRs. The 5% filled composites in Figure 6.19a/b are better described than the 50% filled ones in Figure 6.19c/d. This is as the strength does not drop as significantly following the onset of damage for the more filled composites. The more filled composites show a gradual drop in the stress as opposed to a sharp drop seen in the less filled composites, as the fillers can act as a barrier to crack growth in these composites [243]. Furthermore, the fact that there are more fillers mean the effect of filler-filler interactions and the stiffer mesophase region surrounding fillers would be larger.

The parameters resulting from this modelling process are provided in Table 6.10.

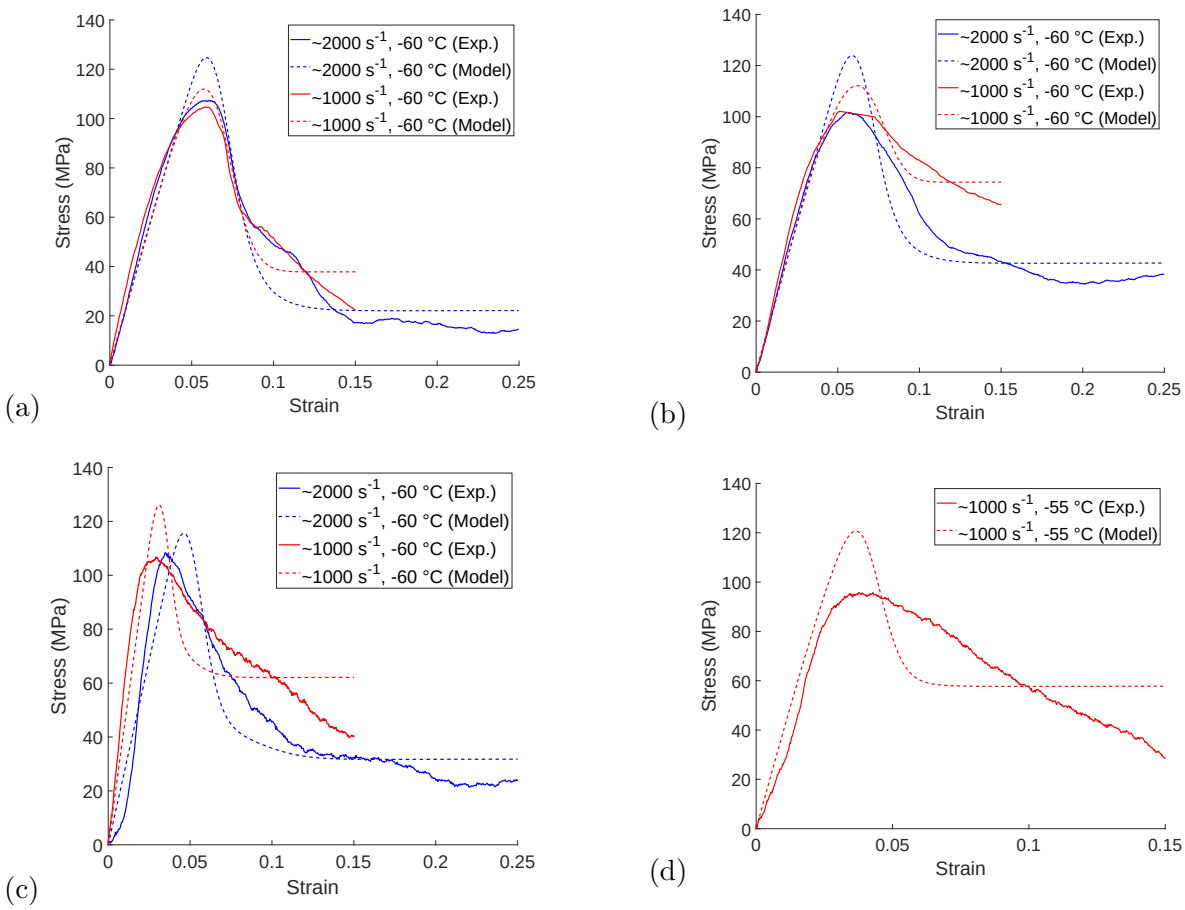

FIGURE 6.19: Using the MB model with an incorporated damage definition to capture the high rate response at −60 °C for (a) F-NR2, (b) F-NR3, (c) F-NR4 and (d) F-NR5 (−55 °C).

TABLE 6.10: Fitting parameters for the damage implementation in the MB model for F-NRs at −60 °C.

Composite	$\dot{\varepsilon}$ (s^{-1})	$\varepsilon_{\mathbf{d}}$	**f**	$\mathbf{w_0}$ ($mJ\,mm^{-3}$)	$\sigma_{\mathbf{r}}$ (MPa)
F-NR2	1000	0.050	1.3×10^{-7}	22	39
F-NR2	2000	0.050	3.2×10^{-8}	19	21
F-NR3	1000	0.050	2.3×10^{-14}	19	77
F-NR3	2000	0.050	1.8×10^{-13}	18	42
F-NR4	1000	0.025	1.1	9.0	62
F-NR4	2000	0.025	0.36	13	31
F-NR5*	1000	0.025	0.15	12	58

To implement the damage model at −60 °C, the value for the damage onset strain, ε_d, was initially selected based on the experimental observations. The other parameters were then calibrated against the experimental results. The failure strain for the 5% filled composites was twice that for the 50% filled composites. With fewer particles, there are fewer locations for internal cracks to initiate and propagate. There are also fewer stress raisers and regions for localised inhomogeneous stress distributions.

As with the results at −40 °C, there is little to no filler enhancement observed for the 5% filled composites. There was less enhancement required for the 50% filled composites too, compared to the results at −40 °C. This is likely due to a limiting value being reached for the modulus. Future iterations of this model will use the results of the DMA experiments on the F-NRs directly, so the filler enhancement will not have to be modelled.

For the 5% F-NRs, the damage activation energy is broadly the same. There is no apparent influence of the mean particle size at this volume fraction. The damage activation energy for the 50% F-NRs is lower than the 5% F-NRs, opposite to what was observed at ambient temperatures with the HV model. This implies that when the binder is glassy, the particles act as damage initiators, and the more filled the composite, the easier it is for damage to occur as less energy is required to fracture.

The residual stresses obtained in the modelling process are dependent on the final stress observed in the experiments, and as such do not have much physical meaning in themselves. By informing the model's damage definition based on *post-mortem* investigations into the residual strengths of samples, and observations of the fracture surface, a greater physical understanding into the damage mechanics can be obtained.

6.5 Conclusions

In this chapter, two modelling strategies have been presented that allow the high rate response of many unfilled and filled natural rubber to be predicted. These modelling strategies have not only been informed by previous frameworks (Chapters 3 and 4), but also the insights developed and the dataset produced from the experimental characterisation of U/F-NRs (Chapter 5).

When the focus is on ambient, high rate investigations – typically rubbery behaviour well above the T_g – a HV model was preferred. This modelling framework is similar in principle to that presented in Chapter 3. The HV model was modified with filler enhancement and strain activated damage definitions to enable it to capture the response of the particulate composites. Upon calibrating the HV model using quasi-static data, it was successful at *predicting* the high rate response of particulate composites at 25 °C.

When focusing on the sub-ambient, high rate response – typically closer to the material's T_g – a MB-inspired model was preferred, due to the viscoplasticity present. This modelling framework is similar to that presented in Chapter 4. To capture the response of the particulate composites, the MB model was similarly adapted with filler enhancement and damage definitions. Although the model was able to successfully predict the low temperature, high rate response of U-NR at −40 °C, due to brittle fracture occurring at lower temperatures, its behaviour at −60 °C could not be predicted. A stress-based damage expression was used to capture this fracturing behaviour in a simple manner. For the F-NRs, at −40 °C, the damaging MB model was able to capture the high rate behaviour well. However, this was not predictive. A similar stress-based damage expression as with the U-NR was required to model the fracturing behaviour at the lowest temperatures.

In future, the development of modelling strategies presented here will form a good foundation for further investigations of filled and unfilled polymers. Improvements include using DMA experiments for the F-NRs to represent their viscoelasticity directly,

calibrating the MB model for the F-NRs using low temperature, quasi-static data for F-NRs, and making use of in-situ diagnostic tools and *post-mortem* examination to improve the damage definitions used. The aim would be to enhance the predictive capability of the modelling strategies when focussing on the high rate response at lower temperatures, where brittle fracture is present.

The key modelling aspect here was the use of the TTS principle to enable the prediction of the high rate response for both U-NR and F-NRs at temperatures above T_g. By combining these different modelling approaches, it was shown that it is possible to *predict* the high strain rate behaviour of particulate composites at certain temperatures, a significant objective of this project.

7 Conclusions

7.1 Thesis objectives

The primary objective of this research was to predict the high strain rate behaviour of amorphous polymers and their particulate composites by using experimental insights obtained, and models calibrated, at low strain rates.

As the high rate behaviour of particulate composites is a result of the polymer binder's response, Chapters 3 and 4 focused on experimentally characterising the response of amorphous polymers under various conditions. Suitable modelling frameworks were developed for neoprene rubber and (plasticised) PVC, by using the insights from experimentation, facilitating the prediction of their high rate response.

Prior to extending and adapting these modelling frameworks to predict the high rate response of particulate composites, it was necessary to experimentally characterise them. In Chapter 5, unfilled natural rubber and four glass microsphere filled natural rubber composites were studied: two of different filler volume fractions and two of different mean particle diameters. Experimental insights were drawn from: rate-temperature equivalence; enhancement of mechanical properties due to filler enhancement; strain activated damage; and *post-mortem* retrieved samples. In general, increasing the volume fraction of fillers enhanced the modulus, increases the yield stress and decreases the heat capacity. Increasing the filler size increases the amount of damage observed, reduces the strain at which failure occurs, and decreases the heat capacity.

These insights led to the development of TTS based modelling frameworks, which were able to predict the high rate response of the unfilled polymer above T_g (provided there was no brittle fracture). The high rate behaviour for filled rubber composites at an ambient temperature was also predicted, however it was not possible at sub-ambient temperatures due to challenges including the presence of brittle fracture at

the lowest temperatures. In order to fulfil the objectives of this research, several novel contributions were made, broadly split into experimental and modelling categories.

7.2 Summary of accomplishments

In this section, details are presented on the discrete contributions that have been made to the fields of experimental mechanics, dynamic behaviour of materials, and constitutive modelling.

7.2.1 Experimental contributions

7.2.1.1 Technique development for Dynamic Mechanical Analysis experiments

As the rate and temperature dependence of the polymeric binder is what gives the particulate composite its rate and temperature sensitivity, it was essential to be able to characterise the thermomechanical behaviour of the polymer system at various frequencies (or loading rates). One method for such investigations involves the use of DMA.

The existing methodology for performing DMA experiments on soft polymers led to poor, inaccurate results, which could not be used meaningfully in TTS. This meant the data was not suitable for calibrating the proposed modelling frameworks. Several modifications to the methodology were proposed, including: changing the specimen dimensions; using specific and bespoke clamping configurations; reducing the isothermal step size in temperature ranges corresponding to important transitions; and reducing the values of frequencies interrogated. The numerous iterations following suggested changes has ultimately led to an enhanced methodology that will allow soft polymers like natural rubber to be better characterised in future.

7.2.1.2 Low temperature capability enhancement for the split-Hopkinson pressure bar

For some materials, like unfilled and filled natural rubber, high strain rate experiments on the SHPB under ambient temperatures show little to no rate dependence in the mechanical response. This is as the T_g is so low in these materials, that the strain rate required to shift the glass transition to an ambient temperature is beyond the scope of the SHPB.

In order to probe the high rate response of these materials, SHPB experiments would have to be performed at a reduced temperature. This capability did not exist in the laboratory, and so an ancillary device for the SHPB comprising of a liquid nitrogen immersion chiller and bespoke fixture was developed. Using the device, oxygen-free nitrogen gas was fed through silicone hosing into a copper coil. This copper coil was submerged in liquid nitrogen, all contained within a thermally insulating Nalgene® dewar. The cooled down nitrogen gas was then directed through the opening on the top of the fixture, where the baffle ensures the cold gas is distributed well around the chamber. The gas subsequently cools the specimen that is contained within the fixture down to a minimum of -100 °C, enabling low temperature SHPB experiments to be conducted.

7.2.1.3 Generation of new data for unfilled and filled natural rubbers

Through a varied and thorough experimental regime, a large dataset for the mechanical response of unfilled and filled natural rubber was generated. This dataset comprises uniaxial compression experiments performed under: an ambient temperature and varying strain rates; sub-ambient temperatures and varying strain rates; varying temperature at a fixed low strain rate; and an ambient temperature, varying strain rates, to varying levels of maximum strain. Furthermore, thermal experiments were performed with: a DMA characterising the thermomechanical behaviour over a wide temperature range and multitude of frequencies; and a DSC to characterise the temperature

dependent heat capacity.

The results of these experiments, and the insights they generated, were used to define, calibrate, and validate the models presented in this research. It is hoped that in future, these data may be used as a starting point for further investigations.

7.2.2 Modelling contributions

7.2.2.1 Development of a hyper-viscoelastic model to capture the high rate behaviour of neoprene rubber

A simple isotropic, incompressible and isothermal hyper-viscoelastic model was developed exploiting the rate-temperature equivalence observed in the compressive mechanical responses of neoprene rubber. Upon calibrating the model based on this equivalence, it was able to capture the mechanical response of neoprene rubber at varying temperatures and strain rates.

Only two parameters were used to model the behaviour, and it was shown that the TTS results of a DMA experiment on neoprene rubber could be used to enhance the model's predictive capability. This modelling framework provides the user with a simple method to interpolate, and ultimately predict, the high rate response of polymers in the rubbery to leathery states.

7.2.2.2 Time-Temperature Superposition based modified Mulliken-Boyce model to *predict* the high rate response of (plasticised) poly(vinyl chloride)

Some polymers, especially glassy amorphous polymers, show viscoplastic behaviour commonly observed by the post-yield stress softening. Both plasticised and unplasticised PVC show this mechanical response, and as such a modelling framework was developed using the Mulliken-Boyce model as its foundation.

By introducing a thermally relaxing modulus, based on a measured temperature dependent heat capacity and an assumed, full conversion of plastic work to heat, it

was shown that the high rate response of (plasticised) PVC could be well captured. The TTS principle, alongside insights from an observed rate-temperature equivalence, enabled the model parameters to be calibrated solely using the results of quasi-static experiments. This model was subsequently able to predict the full high strain rate stress-strain response of the materials.

In future, this modelling framework will be able to form the basis of predicting the high strain rate compression response for numerous materials where the behaviour is strongly rate and temperature dependent, especially glassy amorphous polymers. The predictive capabilities of this modelling framework will also reduce the number of high rate experiments needing to be conducted as they would only be required for validation purposes and to interrogate particular rates of interest.

Furthermore, this modelling framework was useful in simulating adiabatic experiments by introducing an artificial temperature rise to quasi-static, low temperature experiments. As the measurement of temperature rise on the time-scale of the high rate experiment is challenging, these modelling results, along with their experimental counterparts, can provide a complementary tool to allow the user to better interrogate the effect of adiabatic self-heating.

7.2.2.3 Development of hyper-viscoelastic model with strain activated damage to *predict* the high rate behaviour of natural rubber based particulate composites

By using the data generated from the experimental characterisation of unfilled and filled natural rubber, a hyper-viscoelastic model was developed to capture the mechanical response of these materials under an ambient temperature and varying strain rates. Incorporating suitable filler enhancement, and strain activated damage, enabled the accurate representation of the particulate composites' mechanical response.

It was shown that the model parameters could be calibrated using the results of quasi-static experiments conducted under ambient and sub-ambient temperatures,

upon which it was possible to predict the high strain rate response of both unfilled and filled natural rubber.

This modelling framework will provide the user with a complementary tool, alongside high rate experimental techniques, to better understand the mechanical behaviour of particulate composites at high strain rates.

7.3 Recommendations for future work

Although significant progress has been made towards better understanding the high strain rate properties of soft polymers and their particulate composites, investigations during this research project unveiled further open questions that can be explored.

The experimental characterisation in this project focused mainly on uniaxial, compression experiments conducted at a constant strain rate. When the materials in this study are used in engineering applications, loading can lead to a multi-axial stress state, where one part of the structure is subjected to a different strain rate to another.

By characterising the materials with multi-axial experiments, there is opportunity to enhance the modelling frameworks to cover more complex stress states. Furthermore, such modelling frameworks could be validated against impact experiments, which provide a multi-axial stress state and varying strain rates, comparable to real scenarios. If experiments are also conducted in tension, comparing the tensile and compressive yield strengths can allow the pressure coefficient in the modelling framework to be characterised.

In this research, the process of calculating the temperature rise due to adiabatic self-heating assumed the full conversion of irrecoverable mechanical work to heat. However, it has been shown previously that this does not hold true for all polymers. There may be structural changes, like strain induced crystallisation, which would change the energy balance. Further investigations, making use of adiabatic simulations and compression experiments to varying strains, could allow a deeper understanding to be gained on the amount of temperature rise required to model the high rate response to a certain strain.

Alongside DSC experiments interrogating the thermal evolution on virgin and tested samples, a more accurate value for the Taylor-Quinney coefficient can be obtained.

Another use of conducting experiments to various strains would be to compare the extent of damage in ambient, high rate experiments to sub-ambient, low rate experiments. This would allow the rate-temperature equivalence of the damage to be investigated further, providing more confidence in the ability to use the shift factors for the modulus to also shift the damage in the TTS based modelling frameworks. By comparing residual strengths in quasi-static compression experiments on tested samples to the strengths of virgin samples, the extent of damage can also be studied further. Computerised Tomography could then allow the damage to be visually validated. These experiments would also better define damage expressions.

Other diagnostic tools could also be used to make in-situ measurements on the time-scale of the experiments. X-ray imaging techniques would provide greater insights on damage progression and the extent of its propagation at various strains. This would allow the formation of various microstructures in the particulate composites, such as agglomerates or aggregates, to also be identified. For example, Small Angle X-ray Scattering (SAXS) experiments would be able to identify cavitation and other macromolecular structures. Thermography with a high temporal resolution could allow the temperature rise due to adiabatic self-heating to be directly measured. By accompanying this with an in-depth analysis of the fracture surface, and noting the presence of localised melting, crazing or brittle fracture, damage definitions can be further improved. These techniques will ultimately lead to an even better understanding of the high rate properties of particulate composites.

7.4 Closing remarks

The aim of this research has been to gain an improved understanding of the high rate behaviour of particulate composites. This has been achieved through the development of: experimental techniques, better characterising the rate and temperature dependence of the underlying binder; analytical techniques, better quantifying the observed rate-temperature equivalence in the materials; and constitutive modelling, better using experimental insights and calibrating parameters to quasi-static experimental results.

Through further investigations and similar research, it will one day be possible to predict the mechanical response of any polymer composite from knowledge of its formulation, and the basic characterisation of its constituents. Conversely, if a certain mechanical performance is required, the precise composition of the polymer system could be predicted. This will enable researchers to design polymer structures optimised to work efficiently under any loading condition.

Bibliography

[1] C. Siviour et al. “The high strain rate compressive behaviour of polycarbonate and polyvinylidene difluoride”. In: *Polymer* 46.26 (2005), pp. 12546–12555.

[2] C. Siviour et al. “High strain rate properties of a polymer-bonded sugar: their dependence on applied and internal constraints”. In: *Proceedings of the Royal Society A: Mathematical, Physical and Engineering Sciences* 464.2093 (2008), pp. 1229–1255.

[3] M. J. Kendall and C. R. Siviour. “Rate dependence of poly(vinyl chloride), the effects of plasticizer and time-temperature superposition”. In: *Proceedings of the Royal Society A: Mathematical, Physical and Engineering Sciences* 470.2167 (2014), pp. 20140012–20140012.

[4] D. M. Williamson et al. “Temperature-time response of a polymer bonded explosive in compression (EDC37)”. In: *Journal of Physics D: Applied Physics* 41.8 (2008), p. 085404.

[5] P. J. Rae and E. N. Brown. “The properties of poly(tetrafluoroethylene) (PTFE) in tension”. In: *Polymer* 46.19 (2005), pp. 8128–8140.

[6] E. N. Brown et al. “The influence of temperature and strain rate on the constitutive and damage responses of polychlorotrifluoroethylene (PCTFE, Kel-F 81)”. In: *Polymer* 47.21 (2006), pp. 7506–7518.

[7] P. J. Rae and D. M. Dattelbaum. “The properties of poly(tetrafluoroethylene) (PTFE) in compression”. In: *Polymer* 45.22 (2004), pp. 7615–7625.

[8] A. B. Anderson. “The composition and structure of wood”. In: *Journal of Chemical Education* 35.10 (1958), p. 487.

[9] J. Rodríguez-López et al. “Cultura de paso de la amada, creadora del juego de pelota’ mesoamericano / Culture of paso de la amada, creator of mesoamerican ballgame’”. In: *Revista Internacional de Medicina y Ciencias de la Actividad Física y del Deporte* 61.2016 (2016).

[10] C. Goodyear. *Gum-elastic and its Varieties: With a Detailed Account of its Applications and Uses, and of the Discovery of Vulcanization*. Vol. 2. Published for the author, 1853.

[11] “Celluloid”. In: *Journal of the Franklin Institute* 107.5 (1879), pp. 334–337.

[12] L. H. Baekeland. “Bakelite, a condensation product of phenols and formaldehyde, and its uses”. In: *Journal of the Franklin Institute* 169.1 (1910), pp. 55–60.

[13] S. Hermann and H. Werner. *Polymerized styrene*. 1937.

[14] W. L. Semon and G. A. Stahl. “History of Vinyl Chloride Polymers”. In: *Journal of Macromolecular Science: Part A - Chemistry* 15.6 (1981), pp. 1263–1278.

[15] C. W. Hume. *Diamine-dicarboxylic acid salts and process of preparing same*. 1938.

[16] O. G. Reginald et al. *Laminated product*. 1940.

[17] J. R. Whinfield and J. T. Dickson. “Improvements relating to the manufacture of highly polymeric substances”. In: *British Patent* 578 (1941), p. 79.

[18] J. W. Lstiburek. “Coil Springs , Rubber Bands , Spaghetti and Tinkertoys”. In: *ASHRAE Journal* 55.October (2013), pp. 54–59.

[19] *The Holy Bible: containing the Old and New Testaments: King James Version*. Conerstone Bible Publishers, 1998.

[20] P. T. Nicholson and I. Shaw. *Ancient Egyptian materials and technology*. Cambridge University Press, 2000.

[21] M. Vitruvius Pollio. *De architectura*. Ed. by J. V. Sulpitius. Vol. 1-10. 1487.

[22] J. Thornton. “The History, Technology, and Conservation of Architectural Papier Mâché”. In: *Journal of the American Institute for Conservation* 32.2 (1993), p. 165.
[23] C. A. Bergman and E. McEwen. “Sinew-Reinforced and Composite Bows”. In: *Projectile Technology* (1997), pp. 143–160.
[24] M. F. Ashby et al. “Technology of the 1990s: Advanced Materials and Predictive Design [and Discussion]”. In: *Philosophical Transactions of the Royal Society A: Mathematical, Physical and Engineering Sciences* 322.1567 (1987), pp. 393–407.
[25] Ralph L Tiede. *Glass composition*. 1959.
[26] V. Arthur and D. Ewald. *Artificial resins and process of making them*. 1936.
[27] M. B. Merlin. *Synthetic resin*. 1936.
[28] C. Pierre. *Process of preparing synthetic resins*. 1943.
[29] G. Marsh. “50 years of reinforced plastic boats”. In: *Reinforced plastics* 50.9 (2006), pp. 16–19.
[30] *Aerospace Composites Market Forecast 2015-2025*. Tech. rep. New York, 2015.
[31] S. Hasumi. “Composite Materials for Car Parts.” In: *Journal of the Surface Finishing Society of Japan* 42.10 (1991), pp. 991–996.
[32] *GFRP Composites Market by Resin Type - Global Forecast to 2026*. Tech. rep. MarketsandMarkets, 2016, p. 163.
[33] M. Natali et al. “Science and technology of polymeric ablative materials for thermal protection systems and propulsion devices: A review”. In: *Progress in Materials Science* 84 (2016), pp. 192–275.
[34] S. L. Kwolek and H. H. Yang. “History of aramid fibers”. In: *Manmade fibers: their origin and development*. Elsevier Applied Science Publishers Ltd., Barking, United Kingdom, 1993, pp. 315–336.
[35] H. Peng et al. “Fabrication of WCp/NiBSi metal matrix composite by electron beam melting”. In: *Materials Science and Engineering: A* 666 (2016), pp. 320–323.
[36] N. D. Cox et al. “Free-standing silver/carbon nanotube metal matrix composite thin films”. In: *Journal of Materials Science* 51.24 (2016), pp. 10935–10942.
[37] K. M. Rahman et al. “A High Strength Ti-SiC Metal Matrix Composite”. In: *Advanced Engineering Materials* 19.7 (2017), p. 1700027.
[38] F. Krumeich et al. “Microstructure of a Ce 0.1 Zr 0.9 O 2 -MgAl 2 O 4 Ceramic Matrix Composite for Use in Dentistry”. In: *Journal of the American Ceramic Society* 97.5 (2014). Ed. by I.-W. Chen, pp. 1602–1609.
[39] D. J. Bertrand et al. “Fatigue behavior of sylramic-iBN/BN/CVI SiC ceramic matrix composite in combustion environment”. In: *Journal of Materials Science* 50.22 (2015), pp. 7437–7447.
[40] J. M. Köhler et al. “Continuous-flow preparation of nanoporous metal/polymer composite particles by in situ synthesis of silver nanoparticles in photopolymerized acrylate/diethylene glycol droplets”. In: *Journal of Materials Science* 48.5 (2013), pp. 2158–2166.
[41] L. Önnby et al. “Polymer composite adsorbents using particles of molecularly imprinted polymers or aluminium oxide nanoparticles for treatment of arsenic contaminated waters”. In: *Water Research* 46.13 (2012), pp. 4111–4120.
[42] S. Yanagida et al. “Preparation of gold nanoparticle dispersed TiO2-polymer composite film by a combined layer-by-layer and photocatalytic deposition method”. In: *Colloids and Surfaces A: Physicochemical and Engineering Aspects* 456.1 (2014), pp. 55–61.
[43] C. Feng et al. “Nonlinear free vibration of functionally graded polymer composite beams reinforced with graphene nanoplatelets (GPLs)”. In: *Engineering Structures* 140 (2017), pp. 110–119.

[44] Z. Xu et al. "Bioinspired Multifunctional Ceramic Platelet-Reinforced Piezoelectric Polymer Composite". In: *Advanced Engineering Materials* 19.2 (2017), p. 1600570.
[45] C. M. Seubert et al. "The characterization and effects of microstructure on the appearance of platelet-polymer composite coatings". In: *Journal of Materials Science* 51.5 (2016), pp. 2259–2273.
[46] F. Xu et al. "Mineral nanofibre reinforced composite polymer electrolyte membranes with enhanced water retention capability in PEM fuel cells". In: *Journal of Membrane Science* 377.1-2 (2011), pp. 134–140.
[47] L. Meng-Meng et al. "Dielectric properties of electrospun titanium compound/polymer composite nanofibres". In: *Chinese Physics B* 19.2 (2010), p. 28102.
[48] M. Varga et al. "Diamond growth on copper rods from polymer composite nanofibres". In: *Applied Surface Science* 312 (2014), pp. 220–225.
[49] Y. Yang et al. "Porous Ag/polymer composite microspheres for adsorption and catalytic degradation of organic dyes in aqueous solutions". In: *Composites Science and Technology* 107 (2015), pp. 137–144.
[50] B. Liu et al. "Facile method for synthesis of hollow porous magnetic microspheres with controllable structure". In: *Journal of Colloid and Interface Science* 375.1 (2012), pp. 70–77.
[51] W Suthabanditpong et al. "Improved optical properties of silica/UV-cured polymer composite films made of hollow silica nanoparticles with a hierarchical structure for light diffuser film applications". In: *Phys. Chem. Chem. Phys.* 18.24 (2016), pp. 16293–16301.
[52] S. Peper et al. "Plasticizer-free microspheres for ionophore-based sensing and extraction based on a methyl methacrylate-decyl methacrylate copolymer matrix". In: *Analytica Chimica Acta*. Vol. 500. 1-2. 2003, pp. 127–136.
[53] P. Prasanthi et al. "Effectiveness of Buckminster Fullerene Reinforcement on Mechanical Properties of FRP Composites". In: *Procedia Materials Science* 6 (2014), pp. 1243–1252.
[54] N. Ballav. "Some experimental results on polyN-vinylcarbazolebuckminsterfullerene (C60) nanocomposite system". In: *Materials Letters* 59.27 (2005), pp. 3419–3422.
[55] P. Prasanthi et al. "Mechanical performance of Buckminster fullerene-reinforced composite with interface defects using finite element method through homogenization techniques". In: *Composite Interfaces* 22.4 (2015), pp. 299–314.
[56] W. Guo et al. "Aligned carbon nanotube/polymer composite fibers with improved mechanical strength and electrical conductivity". In: *J. Mater. Chem.* 22.3 (2012), pp. 903–908.
[57] X. Liu et al. "Superstretchability and stability of helical structures of carbon nanotube/polymer composite fibers: Coarse-grained molecular dynamics modeling and simulation". In: *Carbon* 115 (2017), pp. 220–228.
[58] R. Rahman and P. Servati. "Effects of inter-tube distance and alignment on tunnelling resistance and strain sensitivity of nanotube/polymer composite films". In: *Nanotechnology* 23.5 (2012), p. 55703.
[59] D. R. Drodge et al. "The mechanical response of a PBX and binder: combining results across the strain-rate and frequency domains". In: *Journal of Physics D: Applied Physics* 43.33 (2010), p. 335403.
[60] C. Siviour et al. "High strain rate properties of a polymer-bonded sugar: their dependence on applied and internal constraints". In: *Proceedings of the Royal Society A: Mathematical, Physical and Engineering Sciences* 464.2093 (2008), pp. 1229–1255.
[61] M. J. Kendall and C. R. Siviour. "Experimentally Simulating High Rate Composite Deformation in Tension and Compression: Polymer Bonded Explosive Simulant". In: *Journal of Dynamic Behavior of Materials* 1.2 (2015), pp. 114–123.

[62] F Bueche. “Segmental mobility of polymers near their glass temperature”. In: *The Journal of Chemical Physics* 21.10 (1953), pp. 1850–1855.
[63] J. A. Rinde and K. G. Hoge. “Time and temperature dependence of the mechanical properties of polystyrene bead foam”. In: *Journal of Applied Polymer Science* 15.6 (1971), pp. 1377–1395.
[64] C. Bauwens-Crowet. “The compression yield behaviour of polymethyl methacrylate over a wide range of temperatures and strain-rates”. In: *Journal of Materials Science* 8.7 (1973), pp. 968–979.
[65] J. L. Jordan et al. “Mechanics of particulate composites with glassy polymer binders in compression”. In: *Philosophical Transactions of the Royal Society A: Mathematical, Physical and Engineering Sciences*. Vol. 372. 2015. Royal Society of London, 2014, p. 20130215.
[66] J. L. Jordan et al. “High strain rate tensile and compressive effects in glassy polymers”. In: *EPJ Web of Conferences*. Vol. 26. EDP Sciences, 2012, p. 01001.
[67] S Hillmansen et al. “The effect of strain rate, temperature, and molecular mass on the tensile deformation of polyethylene”. In: *Polymer Engineering & Science* 40.2 (2000), pp. 481–489.
[68] S. Hillmansen and R. N. Haward. “Adiabatic failure in polyethylene”. In: *Polymer* 42.22 (2001), pp. 9301–9312.
[69] J. Furmanski et al. “Time-temperature equivalence and adiabatic heating at large strains in high density polyethylene and ultrahigh molecular weight polyethylene”. In: *Polymer* 54.1 (2013), pp. 381–390.
[70] M. J. Kendall and C. R. Siviour. “Experimentally simulating adiabatic conditions: Approximating high rate polymer behavior using low rate experiments with temperature profiles”. In: *Polymer* 54.18 (2013), pp. 5058–5063.
[71] M. J. Kendall and C. R. Siviour. “Experimentally simulating high-rate behaviour: rate and temperature effects in polycarbonate and PMMA.” In: *Philosophical transactions. Series A, Mathematical, physical, and engineering sciences* 372.2015 (2014), p. 20130202.
[72] N. A. Fleck et al. “High strain-rate shear response of polycarbonate and polymethyl methacrylate”. In: *Proceedings of the Royal Society of London. A. Mathematical and Physical Sciences* 429.1877 (1990), pp. 459–479.
[73] D. A. Gorham. “Specimen inertia in high strain-rate compression”. In: *Journal of Physics D: Applied Physics* 22.12 (1989), pp. 1888–1893.
[74] D. A. Gorham. “The effect of specimen dimensions on high strain rate compression measurements of copper”. In: *Journal of Physics D: Applied Physics* 24.8 (1991), pp. 1489–1492.
[75] S. K. Bhateja. “The Effects of Hydrostatic Pressure on the Mechanical Behavior of Polymers”. In: *Journal of Macromolecular Science, Part C* 13.1 (1975), pp. 1–75.
[76] R. Raghava et al. “The macroscopic yield behaviour of polymers”. In: *Journal of Materials Science* 8.2 (1973), pp. 225–232.
[77] J. Field et al. “Review of experimental techniques for high rate deformation and shock studies”. In: *International Journal of Impact Engineering* 30.7 (2004), pp. 725–775.
[78] P. Duhem. *Les Origines de la Statique*. fre. Paris: A. Hermann, 1909.
[79] R Hooke. *Lectures de potentia restitutiva*. 1678.
[80] M. D. Kirkaldy. “Results of an experimental inquiry into the comparative tensile strength and other properties of various kinds of wrought iron and steel”. In: *Journal of the Franklin Institute* 75.6 (1863), pp. 397–404.
[81] H. A. Kuhn. “Uniaxial Compression Testing”. In: *ASM Handbook Vol. 8 Mechanical Testing and Evaluation*. Ed. by H. A. Kuhn and D. Medlin. ASM International, 2007. Chap. Chapter 2, pp. 143 –151.
[82] J. E. Hockett and N. A. Lindsay. “Cam plastometer data acquisition system”. In: *Journal of Physics E: Scientific Instruments* 4.7 (1971), pp. 520–522.

[83] F Scarpa et al. "Dynamic crushing of auxetic open-cell polyurethane foam". In: *Proceedings of the Institution of Mechanical Engineers, Part C: Journal of Mechanical Engineering Science* 216.12 (2002), pp. 1153–1156.

[84] J. P. Parker and C. S. Kemic. "A flywheel impact test for measuring physical properties of tire cords". In: *Journal of Applied Polymer Science* 6.21 (1962), pp. 255–263.

[85] P. Viot et al. "Polymeric foam behavior under dynamic compressive loading". In: *Journal of Materials Science*. Vol. 40. 22. Springer, 2005, pp. 5829–5837.

[86] F. I. Niordson. "A unit for testing materials at high strain rates - By using ring specimens and electromagnetic loading, high strain rates are obtained in a tension test in a homogeneous, uniaxial strain field". In: *Experimental Mechanics* 5.1 (1965), pp. 29–32.

[87] H Zhang and K Ravi-Chandar. "Dynamic fragmentation of ductile materials". In: *Journal of Physics D: Applied Physics* 42.21 (2009), p. 16.

[88] B. Song et al. "A Long Split Hopkinson Pressure Bar (LSHPB) for intermediate-rate characterization of soft materials". In: *Experimental Mechanics* 48.6 (2008), pp. 809–815.

[89] F. De Cola et al. "Effect of Particle Morphology, Compaction, and Confinement on the High Strain Rate Behavior of Sand". In: *Experimental Mechanics* 58.2 (2018), pp. 223–242.

[90] G. J. Albertoni. "Impact Machine for Rubber Testing. Determining the Stress-Strain Diagram at High Speed". In: *Rubber Chemistry and Technology* 10.2 (1937), pp. 317–328.

[91] F. L. Roth and W. L. Holt. "Tensile Properties of Rubber Compounds at High Rates of Stretch". In: *Rubber Chemistry and Technology* 13.2 (1940), pp. 348–360.

[92] P. H. Mott et al. "High-speed tensile test instrument". In: *Review of Scientific Instruments* 78.4 (2007), p. 045105.

[93] G. I. Taylor. "The testing of materials at high rates of loading." In: *Journal of the Institution of Civil Engineers* 26.8 (1946), pp. 486–519.

[94] G. F. Raiser et al. "Plate impact response of ceramics and glasses". In: *Journal of Applied Physics* 75.8 (1994), pp. 3862–3869.

[95] K. J. Frutschy and R. J. Clifton. "High-temperature pressure-shear plate impact experiments using pure tungsten carbide impactors". In: *Experimental Mechanics* 38.2 (1998), pp. 116–125.

[96] J. C. Smith et al. "Stress-Strain Relationships in Yarns Subjected to Rapid Impact Loading". In: *Journal of Research of the National Bureau of Standards* 57.2 (1956), pp. 83–89.

[97] D. R. Drodge et al. "Ballistic impact to access the high-rate behaviour of individual silk fibres". In: *Journal of the Mechanics and Physics of Solids* 60.10 (2012), pp. 1710–1721.

[98] B. Hopkinson. "A Method of Measuring the Pressure Produced in the Detonation of High Explosives or by the Impact of Bullets". In: *Philosophical Transactions of the Royal Society A: Mathematical, Physical and Engineering Sciences* 213.497-508 (1914), pp. 437–456.

[99] H Kolsky. "An Investigation of the Mechanical Properties of Materials at very High Rates of Loading". In: *Proceedings of the Physical Society. Section B* 62.11 (1949), p. 676.

[100] K. T. Ramesh. "High Strain Rate and Impact Experiments". In: *Handbook of Experimental Solid Mechanics* (2008), p. 874.

[101] G. T. Gray III and W. R. Blumenthal. *Split-Hopkinson Pressure Bar Testing of Soft Materials*. 2000.

[102] W. Chen and B. Song. *Split Hopkinson (Kolsky) Bar*. Mechanical Engineering Series. Boston, MA: Springer US, 2011.

[103] B Karp and D Durban. *Saint-venant's principle in dynamics of structures*. 2011.

[104] L. Pochhammer. "About the propagation speeds of small vibrations in an unlimited isotropic circular cylinder." In: *Journal for pure and applied mathematics* 1876.81 (1876), pp. 324–336.
[105] C Chree. "Longitudinal vibrations of a circular bar". In: *Quart. J. Pure Appl. Math* 21 (1886), pp. 287–298.
[106] W Chen et al. "A Split Hopkinson Bar Technique for Low Impedance Materials". In: *Experimental Mechanics* 39.2 (1999), pp. 81–85.
[107] W. Chen et al. "Dynamic compression testing of soft materials". In: *Journal of Applied Mechanics, Transactions ASME* 69.3 (2002), pp. 214–223.
[108] M. J. Forrestal et al. "The effect of radial inertia on brittle samples during the split Hopkinson pressure bar test". In: *International Journal of Impact Engineering* 34.3 (2007), pp. 405–411.
[109] M. Sasso et al. "Experimental and numerical characterization of a polymeric Hopkinson bar by DTMA". In: *International Journal of Impact Engineering* 103 (2017), pp. 50–63.
[110] M. J. Kendall et al. "Stress gage system for measuring very soft materials under high rates of deformation". In: *Measurement Science and Technology* 25.7 (2014), p. 075603.
[111] D. J. Frew et al. "Pulse shaping techniques for testing brittle materials with a split hopkinson pressure bar". In: *Experimental Mechanics* 42.1 (2002), pp. 93–106.
[112] T. J. Cloete et al. "A tapered striker pulse shaping technique for uniform strain rate dynamic compression of bovine bone". In: *DYMAT - International Conference on the Mechanical and Physical Behaviour of Materials under Dynamic Loading*. Vol. 1. EDP Sciences, 2009, pp. 901–907.
[113] B. Song et al. "Radial inertia effects in kolsky bar testing of extra-soft specimens". In: *Experimental Mechanics* 47.5 (2007), pp. 659–670.
[114] K. J. Laidler. *The world of physical chemistry*. Oxford University Press, 1995, p. 476.
[115] *ASTM E473-18: Standard Terminology Relating to Thermal Analysis and Rheology*. Tech. rep. West Conshohocken, PA: ASTM International, 2018.
[116] J. H. Poynting. "On Pressure Perpendicular to the Shear Planes in Finite Pure Shears, and on the Lengthening of Loaded Wires When Twisted". In: *Proceedings of the Royal Society A: Mathematical, Physical and Engineering Sciences* 82.557 (1909), pp. 546–559.
[117] K te Nijenhuis. *Rheology Volume 1 Principles, edited by G. Astarita et al.* 1980.
[118] W. P. Cox and E. H. Merz. "Correlation of dynamic and steady flow viscosities". In: *Journal of Polymer Science* 28.118 (1958), pp. 619–622.
[119] H. Eyring. "Viscosity, plasticity, and diffusion as examples of absolute reaction rates". In: *The Journal of Chemical Physics* 4.4 (1936), pp. 283–291.
[120] J Richeton et al. "Influence of temperature and strain rate on the mechanical behavior of three amorphous polymers: Characterization and modeling of the compressive yield stress". In: *International Journal of Solids and Structures* 43.7-8 (2006), pp. 2318–2335.
[121] K. Wang et al. "Elastic and yield behaviors of recycled polypropylene-based composites: Experimental and modeling study". In: *Composites Part B: Engineering* 99 (2016), pp. 132–153.
[122] T. Murayama. *Dynamic mechanical analysis of polymeric material*. Elsevier Scientific Pub. Co., 1978.
[123] B. E. Read and G. D. Dean. *The determination of dynamic properties of polymers and composites*. Halsted Press, 1978.
[124] M. Sepe. *Dynamic mechanical analysis for plastics engineering*. William Andrew, 1998.
[125] K. P. Menard. *Dynamic mechanical analysis: a practical introduction*. CRC press, 2008.

[126] A. V. Tobolsky. "Elastoviscous Properties of Polyisobutylene. VI. Relation between Stress Relaxation Modulus and Dynamic Modulus". In: *Journal of the American Chemical Society* 74.15 (1952), pp. 3786–3788.
[127] C. Bauwens-Crowet et al. "Tensile yield-stress behavior of glassy polymers". In: *Journal of Polymer Science* 7.4 (1969), pp. 735–742.
[128] Ferry J.D. *Viscoelastic Properties of Polymers*. Wiley, 1980.
[129] K. S. Cho. "Time-Temperature Superposition". In: Springer, Dordrecht, 2016, pp. 437–457.
[130] C. Roland. "Viscoelastic Behaviour of Rubbery Materials". In: (2011), p. 332.
[131] M. L. Williams et al. "The Temperature Dependence of Relaxation Mechanisms in Amorphous Polymers and Other Glass-forming Liquids." In: *Journal of American Chemical Society* 77.12 (1955), pp. 3701–3707.
[132] N. Phan-Thien. "On the Time-Temperature Superposition Principle of Dilute Polymer Liquids". In: *Journal of Rheology* 23.4 (1979), pp. 451–456.
[133] D. Porter. *Group interaction modelling of polymer properties*. CRC Press, 1995.
[134] R Cornish et al. "Comparison of Porter-Gould constitutive model with compression test data for HTPB/SUGAR". In: *AIP Conference Proceedings*. Vol. 955. 777. 2007, pp. 777–780.
[135] D. Porter and P. J. Gould. "Predictive nonlinear constitutive relations in polymers through loss history". In: *International Journal of Solids and Structures* 46.9 (2009), pp. 1981–1993.
[136] M. Mooney. "A theory of large elastic deformation". In: *Journal of Applied Physics* 11.9 (1940), pp. 582–592.
[137] R. S. Rivlin. "Large Elastic Deformations of Isotropic Materials. IV. Further Developments of the General Theory". In: *Philosophical Transactions of the Royal Society A: Mathematical, Physical and Engineering Sciences* 241.835 (1948), pp. 379–397.
[138] G Heinrich and M Kaliske. "Theoretical and numerical formulation of a molecular based constitutive tube-model of rubber elasticity". In: *Computational and Theoretical Polymer Science* 7.3-4 (1997), pp. 227–241.
[139] M. C. Boyce and E. M. Arruda. "Constitutive Models of Rubber Elasticity: A Review". In: *Rubber Chemistry and Technology* 73.3 (2000), pp. 504–523.
[140] G. Marckmann et al. "Comparison of hyperelastic models for rubber-like materials". In: *Rubber Chemistry and Technology* 79.5 (2006), pp. 835–858.
[141] R. Ogden. "Large deformation isotropic elasticity - On the correlation of theory and experiment for incompressible rubber like solids." In: *Proceedings of the Royal Society A: Mathematical, Physical and Engineering Sciences* 326.1567 (1972), pp. 565–584.
[142] R. W. Ogden and E Sternberg. *Nonlinear Elastic Deformations*. 1985.
[143] E. M. Arruda and M. C. Boyce. "A three-dimensional constitutive model for the large stretch behavior of rubber elastic materials". In: *Journal of the Mechanics and Physics of Solids* 41.2 (1993), pp. 389–412.
[144] O. A. Shergold et al. "The uniaxial stress versus strain response of pig skin and silicone rubber at low and high strain rates". In: *International Journal of Impact Engineering* 32.9 (2006), pp. 1384–1402.
[145] W. Kuhn. "Beziehungen zwischen Molekülgröße, statistischer Molekülgestalt und elastischen Eigenschaften hochpolymerer Stoffe". In: *Kolloid-Zeitschrift* 76.3 (1936), pp. 258–271.
[146] L. R. G. Treloar. *The physics of rubber elasticity*. 3rd ed. Clarendon Press, 1975, p. 310.
[147] N. W. Tschoegl. *The Phenomenological Theory of Linear Viscoelastic Behavior: An Introduction*. Springer Berlin Heidelberg, 1989, p. 769.
[148] O. E. Meyer. "Zur Theorie der inneren Reibung." In: *Journal für die reine und angewandte Mathematik* 78 (1874), pp. 130–135.

[149] C. M. Zener and S. Siegel. “Elasticity and Anelasticity of Metals.” In: *The Journal of Physical and Colloid Chemistry* 53.9 (1949), pp. 1468–1468.
[150] C. Gamonpilas and R. McCuiston. “A non-linear viscoelastic material constitutive model for polyurea”. In: *Polymer (United Kingdom)* 53.17 (2012), pp. 3655–3658.
[151] K. Patra and R. K. Sahu. “A visco-hyperelastic approach to modelling rate-dependent large deformation of a dielectric acrylic elastomer”. In: *International Journal of Mechanics and Materials in Design* 11.1 (2015), pp. 79–90.
[152] K. Manda et al. “Linear viscoelasticity - bone volume fraction relationships of bovine trabecular bone”. In: *Biomechanics and Modeling in Mechanobiology* 15.6 (2016), pp. 1631–1640.
[153] Y. Bai et al. “A Hyper-Viscoelastic Constitutive Model for Polyurea under Uniaxial Compressive Loading”. In: *Polymers* 8.4 (2016), p. 133.
[154] P. Nutting. “A new general law of deformation”. In: *Journal of the Franklin Institute* 191.5 (1921), pp. 679–685.
[155] A. Gemant. “A Method of Analyzing Experimental Results Obtained from ElastoViscous Bodies”. In: *Physics* 7.8 (1936), pp. 311–317.
[156] A. Gemant. “Fractional Differentials”. In: *London, Edinburgh and Dublin Philosophical Magazine and Journal of Science* 25.168 (1938). Last updated - 2013-02-24, p. 540.
[157] M. Caputo. “Linear Models of Dissipation whose Q is almost Frequency Independent–II”. In: *Geophysical Journal International* 13.5 (1967), pp. 529–539.
[158] M. Caputo. “Elasticita e Dissipazione”. In: *Zanichelli, Bologna,* 1969.
[159] M. Caputo and F. Mainardi. “A new dissipation model based on memory mechanism”. In: *Pure and Applied Geophysics PAGEOPH* 91.1 (1971), pp. 134–147.
[160] F. Mainardi. *Fractional Calculus and Waves in Linear Viscoelasticity: An Introduction to Mathematical Models*. IMPERIAL COLLEGE PRESS, 2010, p. 368.
[161] R. L. Bagley and P. J. Torvik. “A Theoretical Basis for the Application of Fractional Calculus to Viscoelasticity”. In: *Journal of Rheology* 27.3 (1983), pp. 201–210.
[162] R. L. Bagley and P. J. Torvik. “On the Fractional Calculus Model of Viscoelastic Behavior”. In: *Journal of Rheology* 30.1 (1986), pp. 133–155.
[163] S. W. J. Welch et al. “Application of time-based fractional calculus methods to viscoelastic creep and stress relaxation of materials”. In: *Mechanics Time-Dependent Materials* 3.3 (1999), pp. 279–303.
[164] R. Garrappa. “Numerical Evaluation of Two and Three Parameter Mittag-Leffler Functions”. In: *SIAM Journal on Numerical Analysis* 53.3 (2015), pp. 1350–1369.
[165] R. C. Koeller. “Toward an equation of state for solid materials with memory by use of the half-order derivative”. In: *Acta Mechanica* 191.3-4 (2007), pp. 125–133.
[166] R. Schapery and S. Park. “Methods of interconversion between linear viscoelastic material functions. Part IIan approximate analytical method”. In: *International Journal of Solids and Structures* 36.11 (1999), pp. 1677–1699.
[167] S. W. Park. “Analytical modeling of viscoelastic dampers for structural and vibration control”. In: *International Journal of Solids and Structures* 38.44-45 (2001), pp. 8065–8092.
[168] G. Alotta et al. “On the behavior of a three-dimensional fractional viscoelastic constitutive model”. In: *Meccanica* (2016), pp. 1–16.
[169] A Kaye. *Non-Newtonian flow in incompressible fluids*. Tech. rep. College of Aeronautics Cranfield, 1962.
[170] B. Bernstein et al. “A Study of Stress Relaxation with Finite Strain”. In: *Transactions of the Society of Rheology* 7.1 (1963), pp. 391–410.
[171] C. Li and J. Lua. “A hyper-viscoelastic constitutive model for polyurea”. In: *Materials Letters* 63.11 (2009), pp. 877–880.

[172] M. A. P. Mohammed. "Visco-hyperelastic model for soft rubber-like materials". In: *Sains Malaysiana* 43.3 (2014).
[173] A. R. Johnson et al. "A viscohyperelastic finite element model for rubber". In: *Computer Methods in Applied Mechanics and Engineering* 127.1-4 (1995), pp. 163–180.
[174] L. Yang et al. "A visco-hyperelastic approach to modelling the constitutive behaviour of rubber". In: *International Journal of Impact Engineering* 24.6-7 (2000), pp. 545–560.
[175] Y. Anani and Y. Alizadeh. "Visco-hyperelastic constitutive law for modeling of foam's behavior". In: *Materials & Design* 32.5 (2011), pp. 2940–2948.
[176] L. Yang and V. Shim. "A visco-hyperelastic constitutive description of elastomeric foam". In: *International Journal of Impact Engineering* 30.8-9 (2004), pp. 1099–1110.
[177] M. L. Ju et al. "Visco-hyperelastic constitutive model for modeling the quasi-static behavior of polyurethane foam in large deformation". In: *Polymer Engineering & Science* 55.8 (2015), pp. 1795–1804.
[178] H. Arora et al. "Modelling the damage and deformation process in a plastic bonded explosive microstructure under tension using the finite element method". In: *Computational Materials Science* 110 (2015), pp. 91–101.
[179] K. S. Yeom et al. "New pseudo-elastic model for polymer-bonded explosive simulants considering the Mullins effect." In: *Journal of Composite Materials* 47.27 (2013), pp. 3401–3411.
[180] R. N. Haward and G. Thackray. "The Use of a Mathematical Model to Describe Isothermal Stress-Strain Curves in Glassy Thermoplastics". In: *Proceedings of the Royal Society A: Mathematical, Physical and Engineering Sciences* 302.1471 (1968), pp. 453–472.
[181] R. E. Robertson. "Theory for the Plasticity of Glassy Polymers". In: *The Journal of Chemical Physics* 44.10 (1966), pp. 3950–3956.
[182] A. S. Argon. "A theory for the low-temperature plastic deformation of glassy polymers". In: *Philosophical Magazine* 28.4 (1973), pp. 839–865.
[183] A. Mulliken and M. Boyce. "Mechanics of the rate-dependent elasticplastic deformation of glassy polymers from low to high strain rates". In: *International Journal of Solids and Structures* 43.5 (2006), pp. 1331–1356.
[184] J. L. Jordan et al. "Mechanical properties of Epon 826/DEA epoxy". In: *Mechanics of Time-Dependent Materials* 12.3 (2008), pp. 249–272.
[185] A. D. Mulliken et al. "High-rate thermomechanical behavior of poly(vinyl chloride) and plasticized poly(vinyl chloride)". In: *Journal de Physique IV (Proceedings)* 134 (2006), pp. 217–223.
[186] J. Richeton et al. "Influence of temperature and strain rate on the mechanical behavior of three amorphous polymers: Characterization and modeling of the compressive yield stress". In: *International Journal of Solids and Structures* 43.7-8 (2006), pp. 2318–2335.
[187] E. M. Arruda et al. "Effects of strain rate, temperature and thermomechanical coupling on the finite strain deformation of glassy polymers". In: *Mechanics of Materials* 19.2-3 (1995), pp. 193–212.
[188] F. S. Conant et al. "Equivalent effects of time and temperature in the shear creep and recovery of elastomers". In: *Journal of Applied Physics* 21.6 (1950), pp. 499–504.
[189] C. A. Bernard et al. "Multiscale description and prediction of the thermomechanical behavior of multilayered plasticized PVC under a wide range of strain rate". In: *Journal of Materials Science* 53.20 (2018), pp. 14834–14849.
[190] M. Kendall and C. Siviour. "Strain rate dependence in plasticized and unplasticized PVC". In: *EPJ Web of Conferences* 26 (2012), p. 02009.

[191] Z. Wang et al. “A thermovisco-hyperelastic constitutive model of HTPB propellant with damage at intermediate strain rates”. In: *Mechanics of Time-Dependent Materials* (2017), pp. 1–24.
[192] R. Österlöf et al. “Constitutive modelling of the amplitude and frequency dependency of filled elastomers utilizing a modified Boundary Surface Model”. In: *International Journal of Solids and Structures* 51.19-20 (2014), pp. 3431–3438.
[193] W. H. Carothers et al. “Acetylene polymers and their derivatives II. A new synthetic rubber: Chloroprene and its polymers”. In: *Journal of the American Chemical Society* 53.11 (1931), pp. 4203–4225.
[194] Instron. *5980 Series | Dual Column Floor Model*. Tech. rep. 2018.
[195] Instron. *3119 Series | Environmental Chambers*. Tech. rep. 2014.
[196] D. Doss. “Thermal diffusivity of vascular tissue and polymers: Effects of finite deformation and direction”. PhD thesis. 1999.
[197] G. T. Gray and W. R. Blumenthal. “Split-Hopkinson Pressure Bar Testing of Soft Materials”. In: *ASM Handbook: Mechanical Testing and Evaluation* (2000), pp. 488 –496.
[198] A. Trautmann et al. “Lubrication of polycarbonate at cryogenic temperatures in the split Hopkinson pressure bar”. In: *International Journal of Impact Engineering* 31.5 (2005), pp. 523–544.
[199] I. M. Ward and D. W. Hadley. *An introduction to the mechanical properties of solid polymers*. 1993.
[200] P. A. Ciullo and N. Hewitt. *The rubber formulary*. William Andrew, 1999.
[201] A. Conn et al. *Trust Region Methods*. MPS-SIAM Series on Optimization. Society for Industrial and Applied Mathematics, 2000.
[202] S. Walley and J. Field. “Strain rate sensitivity of polymers in compression from low to high rates”. In: *DYMAT j* 1.3 (1994), pp. 211–227.
[203] BPF. *British Plastics Federation*. `http://www.bpf.co.uk/plastipedia/polymers/PVC.aspx` [Accessed:19/10/18].
[204] Ceresana. *Global Growth Market PVC*. `https://www.ceresana.com/en/about-us/news/press-release-polyvinyl-chloride-pvc-ceresana.html` [Accessed:19/10/18].
[205] G. Matthews. *PVC: Production, Properties and Uses*. Vol. 587. The Institute of Materials, 1996.
[206] A. Nogales and B. B. Sauer. “Cooperative motions in PVC studied by thermally stimulated currents: Comparison with A.C. dielectric derivative analysis”. In: *Journal of Polymer Science, Part B: Polymer Physics* 36.5 (1998), pp. 913–918.
[207] K. L. Ngai and A. F. Yee. “Some connections between viscoelastic properties of PVC and plasticized PVC and molecular kinetics”. In: *Journal of Polymer Science Part B: Polymer Physics* 29.12 (1991), pp. 1493–1501.
[208] L. C. Thomas. *Modulated DSC Basics; Optimization of MDSC Experimental Conditions*. Tech. rep. 2011, pp. 1–10.
[209] S.-S. Chang. “Heat Capacity and Thermodynamic Properties of”. In: *Journal of Research of the National Bureau of Standards* (1977), p. 9.
[210] *European Union Risk Assessment Report: DINP*. Tech. rep. Institute for Health and Consumer Protection: European Chemicals Bureau, 2003, p. 302.
[211] E. M. Arruda et al. “Effects of strain rate, temperature and thermomechanical coupling on the finite strain deformation of glassy polymers”. In: *Mech. Mater.* 19 (1995), pp. 193–212.
[212] Y. Fung. *Foundations of solid mechanics*. Prentice Hall, 1965.
[213] R. C. Koeller. “Polynomial operators, stieltjes convolution, and fractional calculus in hereditary mechanics”. In: *Acta Mechanica* 58.3-4 (1986), pp. 251–264.
[214] R. Christensen. *Theory of Viscoelasticity*. Academic Press, New York, 1982.

[215] O. A. Hasan and M. C. Boyce. "A constitutive model for the nonlinear viscoelastic viscoplastic behavior of glassy polymers". In: *Polymer Engineering and Science* 35.4 (1995), pp. 331–344.
[216] ISO 18437. *Mechanical vibration and shock Characterization of the dynamic mechanical properties of viscoelastic materials*. 2012.
[217] A Rahimi and A Mashak. *Review on rubbers in medicine: Natural, silicone and polyurethane rubbers*. 2013.
[218] MRPRA. *Natural Rubber Engineering Data Sheet - EDS 19*. Tech. rep. Malaysian Rubber Producers' Research Association, 1980.
[219] T. Goudarzi et al. "Filled elastomers: A theory of filler reinforcement based on hydrodynamic and interphasial effects". In: *Journal of the Mechanics and Physics of Solids* 80 (2015), pp. 37–67.
[220] S. Ravindran et al. "Local Deformation and Failure Mechanisms of Polymer Bonded Energetic Materials Subjected to High Strain Rate Loading". In: *Journal of Dynamic Behavior of Materials* 2.1 (2016), pp. 146–156.
[221] D. R. Drodge and D. M. Williamson. "Understanding damage in polymer-bonded explosive composites". In: *Journal of Materials Science* 51.2 (2016), pp. 668–679.
[222] H. K. Frensdorff. *The thermal diffusivity of natural rubber*. 1962.
[223] N. Fleck. "Adiabatic Shear Instability: Theory". In: *Mechanical Properties and Testing of Polymers*. Springer, 1999, pp. 15–19.
[224] Y. L. Bai. "Thermo-plastic instability in simple shear". In: *Journal of the Mechanics and Physics of Solids* 30.4 (1982), pp. 195–207.
[225] J Richeton et al. "A formulation of the cooperative model for the yield stress of amorphous polymers for a wide range of strain rates and temperatures". In: *Polymer* 46.16 (2005), pp. 6035–6043.
[226] K. Cao et al. "Effects of strain rate and temperature on the tension behavior of polycarbonate". In: *Materials and Design* 38 (2012), pp. 53–58.
[227] J. Eshelby. "The determination of the elastic field of an ellipsoidal inclusion, and related problems". In: *Proceedings of the Royal Society of London. Series A. Mathematical and Physical Sciences* 241.1226 (1957), pp. 376–396.
[228] R. Hill. "Elastic properties of reinforced solids: Some theoretical principles". In: *Journal of the Mechanics and Physics of Solids* 11.5 (1963), pp. 357–372.
[229] T. B. Lewis and L. E. Nielsen. "Dynamic mechanical properties of particulate-filled composites". In: *Journal of Applied Polymer Science* 14.6 (1970), pp. 1449–1471.
[230] T. Mori and K. Tanaka. "Average stress in matrix and average elastic energy of materials with misfitting inclusions". In: *Acta Metallurgica* 21.5 (1973), pp. 571–574.
[231] E. Guth. "Theory of filler reinforcement". In: *Journal of Applied Physics* 16.1 (1945), pp. 20–25.
[232] H. M. Smallwood. "Limiting law of the reinforcement of rubber". In: *Journal of Applied Physics* 15.11 (1944), pp. 758–766.
[233] J. S. Bergström and M. C. Boyce. "Mechanical behavior of particle filled elastomers". In: *Rubber Chemistry and Technology* 72.4 (1999), pp. 633–656.
[234] C. A. Rezende et al. "Natural rubber-clay nanocomposites: Mechanical and structural properties". In: *Polymer* 51.16 (2010), pp. 3644–3652.
[235] H. Alter. "Filler particle size and mechanical properties of polymers". In: *Journal of Applied Polymer Science* 9.4 (1965), pp. 1525–1531.
[236] G. P. Baeza et al. "Network dynamics in nanofilled polymers". In: *Nature Communications* 7 (2016).
[237] Q. Chen et al. "Mechanical reinforcement of polymer nanocomposites from percolation of a nanoparticle network". In: *ACS Macro Letters* 4.4 (2015), pp. 398–402.

[238] S. Toki et al. “Strain-induced crystallization of natural rubber as detected real-time by wide- angle X-ray diffraction technique”. In: *Polymer* 41.14 (2000), pp. 5423–5429.

[239] K. N. Fuller et al. “The effect of low-temperature crystallization on the mechanical behavior of rubber”. In: *Journal of Polymer Science, Part B: Polymer Physics* 42.11 SPEC. ISS. (2004), pp. 2181–2190.

[240] J. S. Bergström and M. C. Boyce. “Large strain time-dependent behavior of filled elastomers”. In: *Mechanics of Materials* 32.11 (2000), pp. 627–644.

[241] E Guth and O Gold. “Viscosity and electroviscous effect of the AgI sol. II. Influence of the concentration of AgI and of electrolyte on the viscosity”. In: *Phys. Rev* 53 (1938), p. 322.

[242] S. Y. Fu et al. “Effects of particle size, particle/matrix interface adhesion and particle loading on mechanical properties of particulate-polymer composites”. In: *Composites Part B: Engineering* 39.6 (2008), pp. 933–961.

[243] E. Gunel and C. Basaran. “Influence of filler content and interphase properties on large deformation micromechanics of particle filled acrylics”. In: *Mechanics of Materials* 57 (2013), pp. 134–146.

[244] M. Huang et al. “The glass transition, segmental relaxations and viscoelastic behaviour of particulate-reinforced natural rubber”. In: *European Polymer Journal* 67 (2015), pp. 232–241.

[245] E. M. Arruda et al. “Effects of strain rate, temperature and thermomechanical coupling on the finite strain deformation of glassy polymers”. In: *Mechanics of Materials* 19.2-3 (1995), pp. 193–212.

[246] L. Nicolais and A. T. Dibenedetto. “Failure criteria for polymeric solids”. In: *Journal of Applied Polymer Science* 15.7 (1971), pp. 1585–1598.

[247] G. Molnár and A. Gravouil. “2D and 3D Abaqus implementation of a robust staggered phase-field solution for modeling brittle fracture”. In: *Finite Elements in Analysis and Design* 130 (2017), pp. 27–38.